



# THE UNIVERSITY *of* EDINBURGH

This thesis has been submitted in fulfilment of the requirements for a postgraduate degree (e.g. PhD, MPhil, DClinPsychol) at the University of Edinburgh. Please note the following terms and conditions of use:

This work is protected by copyright and other intellectual property rights, which are retained by the thesis author, unless otherwise stated.

A copy can be downloaded for personal non-commercial research or study, without prior permission or charge.

This thesis cannot be reproduced or quoted extensively from without first obtaining permission in writing from the author.

The content must not be changed in any way or sold commercially in any format or medium without the formal permission of the author.

When referring to this work, full bibliographic details including the author, title, awarding institution and date of the thesis must be given.

# **Frequency composition of wall shear stress in animal models of atherosclerosis**

**Arunn Sathasivam**



**THE UNIVERSITY  
*of* EDINBURGH**

**Doctor of Philosophy**

**The University of Edinburgh**

**2019**



## **Declaration**

I confirm that the content of this thesis is entirely my own work, unless stated otherwise. I confirm that this work has not been previously submitted for any other degree.

.....



## Acknowledgements

I'd like to dedicate this thesis to my parents for their love and support over the last four years. The decision to leave my life in London was made so much easier knowing that I would always have their support in anything I do. I will always be grateful for the love they have shown, even taking a week away to come to Edinburgh and cook for me while I was in the final month of my write-up.

The supervisor team on this project has been nothing short of amazing. I would like to thank Drs Timm Krüger, Patrick Hadoke, and Peter Hoskins for their advice and support throughout this process. The time they spent reading reports and chapter drafts and discussing the details of my work has really helped me to make this a project that I am proud of. They gave me the motivation I needed when I was struggling, and I will always be grateful. I would also like to thank Dr Goncalo Silva and Professor Rod Hose for the time spent in emails and meetings answering my sometimes, embarrassingly simple questions with patience and clarity.

Thanks also to the thesis examiners, Dr Miguel Bernabeu and Dr Alistair Revell, for their valuable time in reading and critiquing my thesis. I hope it was a pleasurable read. This PhD would not have been possible without the funding and background support so I would like to thank the EPSRC and also the many support staff at the University of Edinburgh for this.

I am thankful for the many flatmates that I have had over these four years. I have truly been lucky to *meet all* of them and they have made the non-academic side of my life in Edinburgh great fun. Special thanks go to Lucas and Eleanor for providing the many welcome distractions from the PhD, either talking about movies and TV series, having meals together, or just walking around the city.

The friends that I have made in Edinburgh have also made this experience a truly special time in my life. First, I would like to thank the PhD students in Timm's group: Rohan, Charles, Yunzhou and Greg for trying to decipher my terrible sketches on the whiteboard and helping me prepare for presentations. The "Gym" group also deserve a special mention: James, Rohan and Davide for putting up with my gym grunts and slow running pace. My colleagues in the School of Engineering have also been a large

part of my life here so I would also like to thank James (another one), Chiara, Eva, Nick, Charithea, Martin, Ricky, Anthony, Anne, and Chris for making Edinburgh so interesting and welcoming. The many pot luck dinners and trips to the pub have been great!

Lastly, I would like to thank my friend Sajeev for helping me start this journey. It was his searches that found this opportunity and his advice that made me take the leap and move to Edinburgh and it has been such an incredible experience.

Arunn Sathasivam  
Edinburgh, Scotland, UK  
16 September 2019

*What we observe is not nature itself, but nature exposed to our method of questioning*  
- Werner Heisenberg

# Abstract

Atherosclerosis and plaque rupture are widely known as multifactorial problems. To isolate the significance of wall shear stress in these problems, the work of this thesis explores the hypothesis that the frequency composition of the wall shear stress signal is associated with the different plaque compositions and disease characteristics in animal models of atherosclerosis.

In this thesis, a lattice Boltzmann simulation tool was developed to test the hypothesis with the basic functionality of an existing code being enhanced for blood flow simulation and wall shear stress calculation. The wall shear stress signals computed from the simulation tool were analysed in terms of the frequency composition to recover the harmonic amplitude and phase information. This information was then used in comparing the different animal models.

Compared to the healthy, non-diseased vessel, disease models are known to result in a decrease in the time-averaged wall shear stress from the reduction in blood flow rate and local complex flow patterns. Further to this, the simulation of these models showed a decrease in the first harmonic amplitude along the length of the vessel. This is a key result of this thesis as the decreased first harmonic amplitude is associated with an increase in the expression of adhesion molecules and proinflammatory factors in endothelial cells. The uniformity in wall shear stress in regions of different plaque type, however, suggests the dominance of circumferential stretch effects over wall shear stress effects in the disease process.

Blood flow simulations in the mouse, rabbit and human vessels were also performed to deduce scaling relationships of the zeroth and first harmonic amplitudes between mammals. The body mass exponent of the first harmonic amplitude was found to be higher than that of the zeroth harmonic amplitude. This suggests an increased significance of the first harmonic component in the wall shear stress signal relative to the zeroth harmonic amplitude in larger mammals. The absence of plaque rupture in the atherosclerotic minipig, however, also suggests the dominance of genomic effects over wall shear stress effects in the disease process.



A key issue in atherosclerosis research is the absence of plaque rupture in the mouse model. The apparent dominance of circumferential stretch and genomic differences shown here suggests that the wall shear stress alone cannot explain the lack of plaque rupture in atherosclerotic mice. How these differences affect plaque composition would be key in understanding the absence of plaque rupture in mouse models and how studies in mice can be applied to benefit human treatments.

## **Lay abstract**

Atherosclerosis is the leading cause of death in the Western world causing patients to suffer from major events like the heart attack and stroke. The disease is characterised by the build-up of a fatty deposit in the walls of blood vessels with a cap of fibrous material. This called structure is called a “plaque”. Heart attack and stroke events are caused by a break in the plaque’s fibrous cap, causing a clot in the blood vessel. An interesting observation is the high probability of some plaques to rupture while others seem more stable and resistant. Considering the mechanics of the plaque, it is clear that the probability of cap disruption is dependent on the plaque’s composition and structure. The key issue in atherosclerosis research is that there is still no clear understanding of the conditions that lead to each type of plaque composition and structure.

Plaque formation commonly occurs at sites of vessel branching and curvature, suggesting ‘disturbed’ blood flow to play a role in the disease. This is also clear from the changes to the function of cells lining the blood vessel walls in response to a force acting on the vessel wall generated by blood flow. This force is known as the wall shear stress and is commonly analysed in terms of its time-averaged value with its time variation being neglected. The time variation is created by the contraction of the heart and was recently shown to be relevant in how the fatty deposit is formed which could be important in the structure and composition of the complete plaque. This thesis explores the hypothesis that the features of the wall shear stress time variation are associated to the different plaque types.

Atherosclerosis has previously been induced in mice where devices have been placed around the blood vessel to create regions of disturbed blood flow. In this thesis, the time variation of wall shear stress was calculated by simulating blood flow under these disturbed flow conditions. Compared to models of the healthy, non-diseased vessel, the simulation of the different mouse models showed decreases in both the time-average and time-varying components of the wall shear stress, properties that are known to result in fat deposition and plaque formation. A key finding of these

simulations is that plaque formation was suggested to also be a result of mechanical and biological factors and not only the blood flow.

Simulations in the vessels of the mouse, rabbit and human showed the ratio of the time-variation to time-average to become larger with increasing animal size. This suggests that the time variation becomes more important in the wall shear stress of larger animals. Simulation results also showed the importance of the time-variation to further increase when looking at a specific region between animals with increasing size.

This study found that, in addition to the decreased time-average, disease models show a decreased time-varying wall shear stress when compared to the healthy, non-diseased vessel. The nature of this relationship between the time-average and time-varying components also changes between species, suggesting differences in how the fatty deposit is formed between species.

Animal models are used extensively in atherosclerosis research but still present difficulties when the information gained is applied to benefit human treatment. Plaques in mice, for example, do not show the rupture event that is seen in humans. This is true even in mouse plaques with similar composition to those that would cause rupture in the human. Understanding why the mouse plaque does not rupture is a key challenge in atherosclerosis research and, while the work of this thesis studies the blood flow as an explanation of this difference, future work should focus on the complete image of the disease including mechanical stresses on the cells and biological differences in cell response.

## List of abbreviations

AHA	American Heart Association
TCFA	thin-cap fibroatheroma
LDL	low-density lipoprotein
SMC	smooth muscle cells
ECM	extracellular matrix
NF- $\kappa$ B	nuclear factor- $\kappa$ B
RBC	red blood cells / erythrocytes
WSS	wall shear stress
TAWSS	time-averaged wall shear stress
OSI	oscillatory shear index
RRT	relative residence time
CFD	computational fluid dynamics
NS	Navier Stokes
LBM	lattice Boltzmann method
BGK	Bhatnagar Gross Krook collision operator
CY	Carreau-Yasuda
PWV	pulse wave velocity



# TABLE OF CONTENTS

<b>ACKNOWLEDGEMENTS.....</b>	<b>III</b>
<b>ABSTRACT .....</b>	<b>V</b>
<b>LAY ABSTRACT .....</b>	<b>VII</b>
<b>LIST OF ABBREVIATIONS .....</b>	<b>IX</b>
<b>1. INTRODUCTION.....</b>	<b>1</b>
1.1 ATHEROSCLEROSIS .....	2
1.2 WALL SHEAR STRESS AND ATHEROSCLEROSIS .....	5
1.3 ANIMAL MODELS IN ATHEROSCLEROSIS .....	7
1.4 HYPOTHESIS AND AIMS .....	10
1.5 THESIS OUTLINE .....	11
<b>2. THEORETICAL BACKGROUND.....</b>	<b>13</b>
2.1 GOVERNING EQUATIONS .....	14
2.2 WALL SHEAR STRESS .....	17
2.3 LOCALISATION METRICS .....	19
2.4 FOURIER SERIES ANALYSIS .....	23
2.5 CONSIDERATIONS IN FOURIER ANALYSIS OF THE WALL SHEAR STRESS SIGNAL.....	26
2.5.1 <i>Multidirectional flow and frequency analysis</i> .....	26
2.5.2 <i>Frequency analysis and normalisation procedures</i> .....	27
2.5.3 <i>Wall shear stress frequency composition and endothelial cells</i> .....	27
2.6 NON-NEWTONIAN FLUID .....	29
2.7 1D MODEL .....	31
2.8 SUMMARY .....	35
<b>3. FLUID SOLVER: LATTICE BOLTZMANN METHOD .....</b>	<b>37</b>
3.1 THE LATTICE BOLTZMANN METHOD .....	37
3.1.1 <i>Overview</i> .....	38
3.1.2 <i>Model implementation</i> .....	41
3.1.3 <i>Model verification</i> .....	42
3.1.4 <i>Model discussion</i> .....	43
3.2 BOUNDARY CONDITIONS .....	45
3.2.1 <i>Boundary conditions in LBM</i> .....	45
3.2.2 <i>Model implementation</i> .....	46

3.2.3	<i>Model discussion</i> .....	48
<b>4.</b>	<b>ADDITIONAL MODELS IN SIMULATING BLOOD FLOW</b> .....	<b>49</b>
4.1	OPEN BOUNDARIES .....	50
4.1.1	<i>Model implementation</i> .....	50
4.1.2	<i>Verification</i> .....	52
4.1.3	<i>Model discussion</i> .....	52
4.2	WALL SHEAR STRESS .....	53
4.2.1	<i>Wall normal vectors</i> .....	53
4.2.2	<i>Wall shear stress</i> .....	56
4.2.3	<i>Model discussion</i> .....	60
4.3	NON-NEWTONIAN FLUID .....	61
4.3.1	<i>Model implementation</i> .....	61
4.3.2	<i>Verification</i> .....	65
4.3.3	<i>Validation of the Newtonian viscosity assumption</i> .....	65
4.3.4	<i>Model discussion</i> .....	67
4.4	1D MODEL .....	67
4.4.1	<i>Model implementation</i> .....	67
4.4.2	<i>Verification</i> .....	69
4.4.3	<i>Model sensitivity analysis</i> .....	71
4.4.4	<i>Model discussion</i> .....	77
4.5	DIMENSIONLESS NUMBERS .....	78
4.6	CONCLUSIONS .....	79
<b>5.</b>	<b>PERIVASCULAR DEVICE MODELS OF ATHEROSCLEROSIS</b> .....	<b>81</b>
	ABSTRACT .....	81
5.1	INTRODUCTION .....	82
5.2	METHODS .....	84
5.2.1	<i>Simulation setup</i> .....	84
5.2.2	<i>Simulations performed</i> .....	86
5.3	RESULTS .....	87
5.3.1	<i>Mesh independence</i> .....	87
5.3.2	<i>Localisation metrics</i> .....	88
5.3.3	<i>Frequency composition</i> .....	98
5.4	DISCUSSION .....	105
5.5	CONCLUSIONS .....	112

<b>6. WALL SHEAR STRESS SIGNAL WITH VARYING BOUNDARY CONDITIONS.....</b>	<b>115</b>
ABSTRACT.....	115
6.1 INTRODUCTION.....	116
6.2 METHODS.....	118
6.2.1 <i>Body force term</i> .....	118
6.2.2 <i>Obtaining dimensionless numbers</i> .....	119
6.2.3 <i>Simulation setup</i> .....	120
6.2.4 <i>Simulations performed</i> .....	121
6.3 RESULTS.....	122
6.3.1 <i>Varying body force signal</i> .....	122
6.3.2 <i>Varying flow dimensionless numbers</i> .....	126
6.4 DISCUSSION .....	134
6.5 CONCLUSIONS .....	139
<b>7. WALL SHEAR STRESS IN THE ARTERIES OF MAMMALS.....</b>	<b>141</b>
ABSTRACT.....	141
7.1 INTRODUCTION.....	142
7.2 METHODS.....	144
7.2.1 <i>Allometric scaling</i> .....	144
7.2.2 <i>Simulation setup</i> .....	148
7.2.3 <i>Simulations performed</i> .....	149
7.3 RESULTS.....	150
7.3.1 <i>Effects of increasing Womersley number</i> .....	150
7.3.2 <i>Peak systolic velocity</i> .....	152
7.3.3 <i>Time-averaged wall shear stress</i> .....	153
7.3.4 <i>Frequency composition</i> .....	155
7.4 DISCUSSION .....	157
7.5 CONCLUSIONS .....	160
<b>8. CONCLUSIONS .....</b>	<b>163</b>
8.1 SUMMARY OF KEY MOTIVATIONS .....	163
8.2 CONCLUSIONS WITH RESPECT TO INDIVIDUAL AIMS .....	164
8.3 FUTURE DIRECTIONS.....	169
8.4 TECHNICAL SPECIFICATIONS.....	171
8.5 KEY FINDINGS .....	171



<b>9. REFERENCES.....</b>	<b>173</b>
---------------------------	------------

# TABLE OF FIGURES

Figure 1.1. Lesion classification system introduced in Virmani <i>et al.</i> (2000) and the proposed sequence of development (Bentzon <i>et al.</i> , 2014). .....	3
Figure 1.2. Analysis of the stress and plaque types in the mouse perivascular cast model of Cheng <i>et al.</i> (2006) .....	9
Figure 2.1 Fluid control volume and stress components acting on the surfaces.....	17
Figure 2.2. The different flow environments over the endothelial cell (circle) typical of a region of disturbed flow and the resulting TAWSS, OSI and transWSS values	22
Figure 2.3. Illustration of the Fourier transform of a square waveform considering the increasing number of harmonic components .....	25
Figure 2.4. Fourier representation of a square waveform function.....	25
Figure 2.5. Experimental measurement of the relative viscosity as a function of the shear rate for human blood.....	30
Figure 2.6. Multiscale representation of the arterial network focussing on a 3D model of the carotid bifurcation .....	33
Figure 3.1. D3Q19 lattice for the lattice Boltzmann method .....	39
Figure 3.2. Verification of the lattice Boltzmann implementation in Womersley flow .....	43
Figure 3.3. Illustration of a simple lattice structure showing the known (solid arrows) and unknown populations (dotted arrows) in the propagation step .....	46
Figure 3.4. Time evolution of the half-way bounceback approach.....	47
Figure 3.5. Staircase approximation of a curved boundary in the half-way bounceback treatment.....	47
Figure 4.1. Illustration of the inlet nodes indicating the unknown $f^-$ (dotted arrows), known $f^+$ , and tangential or zero populations $f_0$ (solid arrows) at the open boundary nodes (green circles) .....	51
Figure 4.2. Illustration of the local averaging method for the computation of the wall normal vector $\mathbf{n}$ (Matyka <i>et al.</i> , 2013).....	54
Figure 4.3. Deviation of the computed wall normal from the analytical value at points around the circumference of the geometry .....	55
Figure 4.4. Wall shear stress plotted as a function of the angular position with different local averaging schemes.....	57
Figure 4.5. Effect of increasing averaging radius, $r$ , on the $L_2$ error norm of wall shear stress (WSS).....	58
Figure 4.6. Effect of increasing pipe diameter, and therefore resolution, on the $L_2$ error norm of the circumferentially averaged wall shear stress (WSS) .....	58
Figure 4.7. Distributions of normalised deviation from the analytical solution of wall shear stress (WSS) with increasing pipe diameter, $D$ .....	59
Figure 4.8. Verification of the Python script for the Newton iterator in relaxation parameter over a range of input values of the first-order momentum flux magnitude $\Pi(1)$ .....	64
Figure 4.9. Significance of the viscosity model assumptions in the simple pipe.....	66

Figure 4.10. Comparison of the impedance spectrum (a) modulus and (b) phase in the ascending aorta computed from the Python implementation and the forward algorithm of John (2004) .....	70
Figure 4.11. Pulse wave velocities (PWV) in the vessels of the arterial network. ....	72
Figure 4.12. Impedance spectrum (a) modulus and (b) phase in the ascending aorta using the empirical fit PWV and Moens-Korteweg PWV .....	73
Figure 4.13. Time-varying pressure computed in the ascending aorta from the Python implementation using the empirical fit PWV and Moens-Korteweg PWV .....	73
Figure 4.14. Impedance spectrum (a) modulus and (b) phase in the ascending aorta computed using the Windkessel parameters of Liu <i>et al.</i> (1989) and Reymond <i>et al.</i> (2009) .....	75
Figure 4.15. Time-varying pressure computed in the ascending aorta from the Python implementation using the Windkessel parameters of Liu <i>et al.</i> (1989) and Reymond <i>et al.</i> (2009) .....	75
Figure 4.16. Comparison of the transfer function computed from the source to the (a) carotid and (b) tibial artery in the Python script and Xiao <i>et al.</i> (2016) .....	76
Figure 5.1. Approximations of the (a) Cheng <i>et al.</i> (2006), (b) Mohri <i>et al.</i> (2014) and (c) Chen <i>et al.</i> (2013) common carotid arteries .....	84
Figure 5.2. Mesh independence study using the distance from cast end to the position of the peak oscillatory shear index (OSI) value .....	88
Figure 5.3. Distribution of the (a) time-averaged wall shear stress (TAWSS), (b) oscillatory shear index (OSI) and (c) relative residence time (RRT) metrics in the (d) conventional direction perivascular cast geometry .....	90
Figure 5.4. Time evolution of the velocity field along a segment of the conventional direction perivascular cast with the solid line indicating the axial position of the peak OSI .....	91
Figure 5.5. Distribution of the (a) time-averaged wall shear stress (TAWSS), (b) oscillatory shear index (OSI) and (c) relative residence time (RRT) metrics in the (d) reversed direction perivascular cast geometry .....	93
Figure 5.6. Time evolution of the velocity field along a segment of the reversed direction perivascular cast.....	94
Figure 5.7. Distribution of the (a) time-averaged wall shear stress (TAWSS), (b) oscillatory shear index (OSI) and (c) relative residence time (RRT) metrics in the (d) tandem stenosis geometry .....	96
Figure 5.8. Time evolution of the velocity field along a segment of the tandem ligation geometry.....	97
Figure 5.9. Time varying waveform of wall shear stress (WSS) over a single cardiac cycle computed from control vessel simulations .....	98
Figure 5.10. Distribution of the first harmonic (a) amplitude and (b) phase of the wall shear stress signal along the length of the (c) tapering perivascular cast geometry. ....	100
Figure 5.11. Frequency composition of the wall shear stress signal at axial positions along the perivascular cast geometry .....	101
Figure 5.12. Distribution of the first harmonic (a) amplitude and (b) phase of the wall shear stress signal along the length of the (c) reversed direction perivascular cast . ....	102

Figure 5.13. Frequency composition of the wall shear stress signal in the upstream and downstream regions of the reversed perivascular cast geometry .....	103
Figure 5.14. Distribution of the first harmonic (a) amplitude and (b) phase of the wall shear stress signal along the length of the (c) tandem stenosis geometry .....	104
Figure 5.15. Frequency composition of the wall shear stress signal at points along the tandem stenosis geometry .....	105
Figure 5.16. Pressure difference computed between the vessel inlet and outlet.....	108
Figure 5.17. Comparison of the frequency composition of the wall shear stress signals in regions showing the (a) thin-cap fibroatheroma and (b) stable-looking plaques.	111
Figure 6.1. Distribution of the (a) normalised time-averaged wall shear stress (TAWSS) and (b) oscillatory shear index (OSI) in simulations of varying body force term in the (c) perivascular tapering cast geometry .....	123
Figure 6.2. (a) First and (b) second harmonic amplitudes of the wall shear stress (WSS) signal compared against the first harmonic amplitude of the body force signal A ..	125
Figure 6.3. Distributions of the (a) normalised time-averaged wall shear stress (TAWSS) and (b) oscillatory shear index (OSI) in the (c) different simulation cases .....	127
Figure 6.4. Distribution of the first harmonic (a) amplitude and (b) phase of the wall shear stress signal along the length of the in the (c) different simulation cases. ....	129
Figure 6.5. Distribution of the second harmonic (a) amplitude and (b) phase of the wall shear stress signal along the length of the (c) S5 perivascular cast geometry .....	130
Figure 6.6. Frequency composition of the wall shear stress signal at axial positions along the S1 perivascular cast geometry .....	131
Figure 6.7. Frequency composition of the wall shear stress signal at axial positions along the S2 perivascular cast geometry .....	132
Figure 6.8. Frequency composition of the wall shear stress signal at axial positions along the S3 perivascular cast geometry .....	132
Figure 6.9. Frequency composition of the wall shear stress signal at axial positions along the S4 perivascular cast geometry .....	133
Figure 6.10. Frequency composition of the wall shear stress signal at axial positions along the S5 perivascular cast geometry .....	133
Figure 7.1. Viscosity model parameters were estimated using an assumed linear scaling law between the mouse and human parameters.....	148
Figure 7.2. First harmonic (a) amplitude and (b) phase of the wall shear stress signal computed in preliminary studies into the effect of the Womersley number. ....	151
Figure 7.3. Allometric relationship of animal body mass with the peak systolic velocity computed from the Carreau-Yasuda viscosity model .....	153
Figure 7.4. Allometric relationship of animal body mass with the time-averaged wall shear stress (TAWSS) computed from the Carreau-Yasuda viscosity model.....	154
Figure 7.5. Allometric relationship of animal body mass with the first harmonic amplitude computed from the Carreau-Yasuda viscosity model .....	156

# LIST OF TABLES

Table 4.1. Carreau-Yasuda viscosity model parameters for the mouse and human. .	66
Table 5.1. Summary of key findings in perivascular device simulations .....	110
Table 6.1. Dimensionless numbers based on the allometric scaling laws discussed above .....	120
Table 6.2. Mouse models of atherosclerosis and implications in terms of PWV ....	138
Table 7.1. Dimensionless numbers based on the allometric scaling laws discussed above .....	147
Table 7.2. Viscosity model parameters based on the allometric scaling laws discussed above .....	147
Table 7.3. Allometric scaling parameters for the peak systolic velocity computed using the Newtonian and Carreau-Yasuda viscosity models. ....	152
Table 7.4. Allometric scaling parameters for the time-averaged wall shear stress computed using the Newtonian and Carreau-Yasuda viscosity models .....	154
Table 7.5. Allometric scaling parameters for the first harmonic amplitude computed using the Newtonian and Carreau-Yasuda viscosity models .....	156

In 2016, cardiovascular disease was identified as the cause of 17.9 million deaths worldwide with heart attacks and strokes contributing to 85% of these deaths (WHO, 2017). The underlying pathology in these clinical events is called atherosclerosis with its name having origins in Greek, meaning “hard gruel”. Due to the high risk of death associated with atherosclerosis, an understanding of the disease mechanisms is keenly sought in order to devise new approaches in prevention, diagnosis and treatment.

Atherosclerosis is characterised by the formation of a fatty lesion, termed “plaque”, in the intimal layer of blood vessels. Studies into the localisation of these plaques in the arterial network have shown a clear predilection for lesion development at branch ostia, bifurcation, and curvature, to suggest the role of blood flow dynamics in the disease process (VanderLaan *et al.*, 2004). By considering the action of blood flow over the vessel wall, the wall shear stress has been implicated in lesion formation with many studies working to characterise the relationship between this force and the response of cells lining the vessel wall (Chiu and Chien, 2011). An interesting, yet somewhat unexplored finding is the differential response of the cells to details of the wall shear stress time-variation (Himburg *et al.*, 2007; Feaver *et al.*, 2013). This thesis, as a whole, works to clarify the significance of this time-variation in regions coincident with plaque formation in animal models of atherosclerosis.

The current chapter presents the motivation for this thesis and the necessary background in pathology along with its relation to wall shear stress. This chapter will first consider atherosclerosis, describing its sequential progression from the initial “fatty streak” to the advanced plaque. Next, the current understanding of wall shear stress will be discussed in terms of its role in plaque formation, progression and rupture. Finally, this introduction will present the hypothesis and aims of the PhD.

## 1.1 Atherosclerosis

Atherosclerosis is a progressive inflammatory disease characterised by the accumulation of lipid-laden foam cells in the intimal layer of a blood vessel. This describes one of three layers in the blood vessel: the intima, media and adventitia. The intima is the innermost layer and comprises a single layer of endothelial cells with an underlying basement membrane. The middle layer, or media, consists of smooth muscle cells (SMCs), circumferentially layered elastin sheets and collagen fibres. The adventitia, consisting mainly of collagen, is the outermost layer. Together, the adventitia and media form the major structural component of the blood vessel, each varying in thickness and composition according to the vessel's function and location. The endothelial cells of the intima form the flow-sensing component of the blood vessel, with complex roles in the regulation of vascular tone, permeability, inflammation and haemostasis.

Atherosclerosis develops over several decades in humans, with lesions progressing through a number of stages (Lusis, 2000; Weissberg, 2000). The development of the lesion through its main types is shown in Figure 1.1. Lesion predilection sites initially show adaptive intimal thickening with outward remodelling (Figure 1.1A), such that the vessel lumen is preserved (Stary *et al.*, 1992). The initial lipid deposit is formed by the infiltration of low-density lipoproteins (LDLs) into the subendothelial space (Getz, 1990).

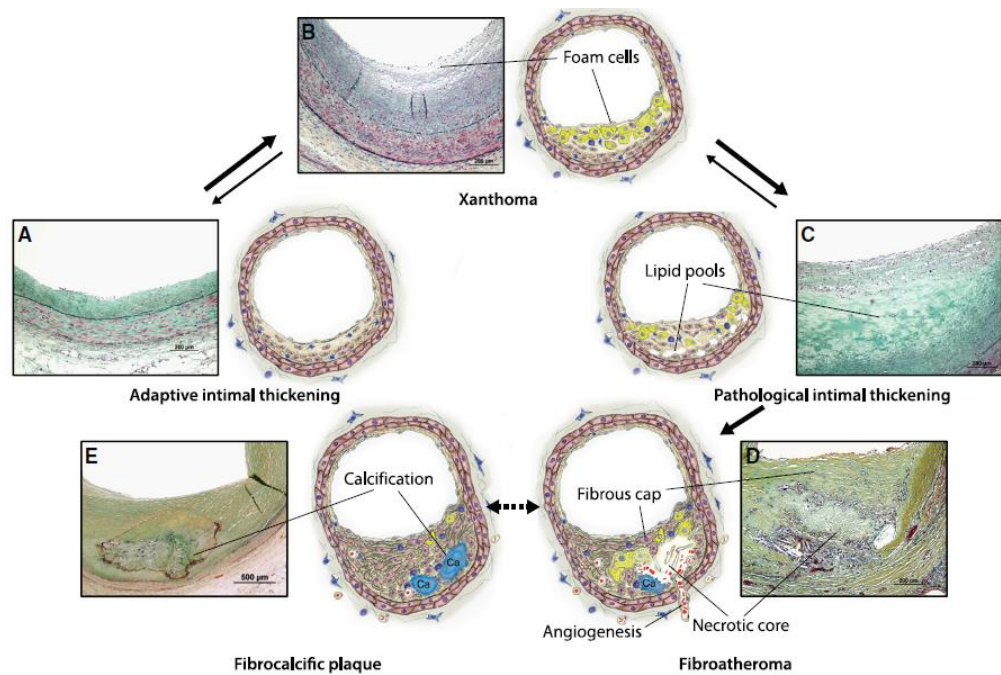


**Figure 1.1. Lesion classification system introduced in Virmani *et al.* (2000) and the proposed sequence of development (Bentzon *et al.*, 2014).** Movat pentachrome stain of histological samples and schematic drawings show plaque characteristics in each lesion type. **A**, Adaptive intimal thickening by smooth muscle cell accumulation in the vessel intima. **B**, Foam cell accumulation showing the intimal xanthoma lesion. **C**, Accumulation of extracellular lipid pools. **D**, Fibroatheroma and necrotic core. Intraplaque neovascularisation is also shown with microvessels developing into the plaque from the vessel adventitial layer. **E**, Fibrocalcific plaque. Figure is taken from Bentzon *et al.* (2014) with permission.

The accumulation and oxidation of LDLs triggers an inflammatory response, with the recruitment of monocytes caused by release of cytokines and proinflammatory mediators (Quinn *et al.*, 1987). Increases in the expression of proinflammatory molecules result in the adhesion of blood-borne monocytes to the endothelial layer and their extravasation into the subendothelial space (Poole and Florey, 1958). The monocytes then differentiate to macrophages and, following the uptake of oxidised LDLs, become foam cells (Figure 1.1B). Foam cell-derived vesicles also promote the migration of smooth muscle cells (SMCs) from the media into the subendothelial space (Niu *et al.*, 2016), where the now-intimal SMCs take on a foam cell-like appearance by oxidised-lipoprotein internalisation. Extracellular lipid pools may also accumulate in this region without gross disruption of the intimal surface (Figure 1.1C). The



persistent stimulation of this inflammatory process leads to the accumulation of these foam cells and lipid-laden SMCs, presenting itself as a “fatty streak” on the intimal surface (Ross, 1993). This is the first macroscopically visible type of lesion in the American Heart Association (AHA) classification scheme (Stary *et al.*, 1994).

At this stage, intimal SMCs proliferate and secrete extracellular matrix (ECM) proteins. Studies have shown the ECM to aid in lipid retention (Schwenke and Carew, 1989a, 1989b), potentially having a role in the site selectivity of plaque formation (Cunningham and Gotlieb, 2004). The continued entry and retention of lipids into the intimal layer results in the formation of the atheroma; the first in the advanced lesion class of the AHA scheme (Stary *et al.*, 1995). Lesion sites also show the disorganisation of intimal SMCs with an accumulation of extracellular lipid particles. The lesion at the atheroma stage still shows minimal infringement into the vessel lumen with the tissue lying between the lipid core and the endothelial surface largely resembling that of the healthy, non-diseased vessel (Stary *et al.*, 1995). Further progression involves the accumulation of collagen in this space. The vessel lumen is preserved by the outward remodelling process, even in the presence of a large neointimal thickening (Glagov *et al.*, 1987). The resulting lesions are known as fibroatheromas (Figure 1.1D) with subclassifications being defined based on their composition and structure. The fibrocalcific plaque shown in Figure 1.1E is an example of this subclassification.

Macrophage cell death results in the formation of the soft, thrombogenic necrotic core and the further recruitment of inflammatory cells (Virmani *et al.*, 2006). Advanced lesions may also show calcifications and intraplaque neovascularisation with thin-walled microvessels developing into the plaque from the vessel’s adventitial layer (Chistiakov *et al.*, 2015). Rupture of these microvessels, termed as an intraplaque haemorrhage, contributes to further deposition of extracellular lipids from the lysed red blood cells.

Plaque rupture leads to exposure of the underlying thrombogenic material, resulting in the formation of the occlusive thrombosis. This is a catastrophic event in disease-progression and is the cause of acute clinical events in the human. A major determinant of this rupture is the cap stress. Tensile stresses on the plaque cap lead to rupture of

the fibrous material only if in excess of the cap's strength. The thin-cap fibroatheroma (TCFA) subclassification is, therefore, of particular importance in human disease considering the reduced cap strength associated with a large necrotic core and thin fibrous cap (Virmani *et al.*, 2000; Slager *et al.*, 2005a, 2005b; Schwartz *et al.*, 2007; Finn *et al.*, 2010; Bentzon *et al.*, 2014).

## 1.2 Wall shear stress and atherosclerosis

Given the site-specificity of lesion formation, blood flow dynamics have long been implicated in atherosclerosis. The wall shear stress (WSS) has received considerable attention in this respect, with it being one of two main forces acting on the vessel endothelium (Hoskins and Hardman, 2009). The WSS is given by the tangential component of fluid stress while the other main force, pressure, is described by the normal component. A detailed introduction into the WSS is provided in Section 2.2. While high WSS was initially thought to be atherogenic through endothelial damage (Fry, 1969), the localisation of lesions in *post mortem* human aortas showed sites of lesion formation to be coincident with regions of low WSS (Caro *et al.*, 1971). Analysis of near-wall flows in vessel models later demonstrated the oscillatory nature of WSS in regions coincident with disease (Ku *et al.*, 1985). These key studies resulted in the widespread use of the low and oscillatory shear stress theory in disease localisation. Despite its popularity, a systematic review of the literature showed a large number of papers failing to support this theory (Peiffer *et al.*, 2013a). This is discussed further in Section 2.3, along with several other metrics that have been proposed in the literature to relate the WSS to lesion formation.

While the details of the WSS-plaque localisation relationship are not fully understood, it is clear that the pattern of WSS is key in regulating the endothelial response. Davies (1995), Malek *et al.* (1999), Cunningham and Gotlieb (2004) and Chiu and Chien (2011) provide excellent reviews of this field. Slager *et al.* (2005a, 2005b) also discuss the role of WSS in the generation and destabilisation of plaques, citing the activity of macrophages in the degradation of the fibrous cap (Lendon *et al.*, 1991). Intrusion of the plaque into the vessel lumen also leads to the disruption of blood flow and varying WSS distributions over the plaque cap. High shear stresses are found at the point of

maximum stenosis while low shear stresses occur in the downstream region. The low shear stresses in this region further contribute to plaque growth by the mechanisms discussed in the above-mentioned review papers. Growth of the necrotic core and degradation of the fibrous cap leads to the formation of the TCFA plaque. While the WSS has shown significance in the activity of SMCs (Chiu *et al.*, 2004a), control of vascular relaxation (Rubanyi *et al.*, 1986) and changes to the endothelial cell cytoskeleton (Davies, 1995; Noria *et al.*, 2004), the major point of relevance to this PhD is the role of WSS in inflammation.

A key marker of inflammation is the expression of NF- $\kappa$ B, a proinflammatory transcription factor. Antibody staining of the atherosclerosis-prone mouse aorta found upregulation of NF- $\kappa$ B in regions coincident with lesion formation, suggesting active inflammation to occur in these regions (Hajra *et al.*, 2000). The WSS also influences adhesion molecule expression on the surface of endothelial cells (Chiu *et al.*, 2004b), with low and oscillatory shear stresses being associated with the increased adhesion and extravasation of inflammatory molecules (Cunningham and Gotlieb, 2004). A finding of great importance to this PhD is the differential expression of these inflammatory markers with variation of the WSS frequency composition, considered now as a time-varying signal (Himburg *et al.*, 2007; Feaver *et al.*, 2013). Feaver *et al.* (2013), in particular, demonstrated a decrease in the expression of NF- $\kappa$ B with increasing zeroth and first harmonic amplitudes. This forms an important result as it establishes a sensitivity of endothelial cells to details of the WSS beyond the categories of “low” and “oscillatory”. The frequency composition of the WSS signal is also a fairly unexplored topic, presenting an interesting avenue for research.

The initiating event in atherogenesis is also not fully understood. While this event is not of particular relevance to this PhD, it still warrants a clear discussion in order to develop a broader understanding of the disease. The current leading theory in the atherosclerosis community is the “response to injury” hypothesis summarised by Ross *et al.* (1977). The initiating mechanism of atherogenesis in this theory was considered to be endothelial denudation or damage. Findings of an intact endothelium over an atheroma-type lesion (Stary *et al.*, 1995), however, suggested the absence of damage at lesion sites. Revisions of the theory now suggest endothelial dysfunction to be the key initiating factor (Ross, 1993).

Endothelial dysfunction may be attributed to a number of causes including hypercholesterolaemia, *diabetes mellitus*, cigarette smoking, genetic predisposition and other environmental factors. These factors, however, are systemic and fail to account for the local nature of lesion formation. The relationship between WSS and atherogenesis has received much attention because of this, showing flow-dependent local increases in LDL residence times (Himburg *et al.*, 2004) and inflammatory response (Davies, 1995; Malek *et al.*, 1999; Cunningham and Gotlieb, 2004; Chiu and Chien, 2011). The “response to retention” theory, on the other hand, proposes the local nature of lesion formation to be attributed to LDL retention (Williams and Tabas, 1995). Mechanisms of retention include the trapping by the ECM (Schwenke and Carew, 1989a, 1989b; Cunningham and Gotlieb, 2004) and ingestion by macrophages. The extravasation of inflammatory molecules into the intimal layer is, therefore, key in retention as it is the initiating event in SMC migration and ECM production. As the distribution and organisation of the endothelial layer is a regulator of vascular permeability and extravasation, the site-specificity of atherosclerosis can also be seen in the change of shape and alignment of endothelial cells in regions of low and oscillatory WSS (Davies, 1995).

### 1.3 Animal models in atherosclerosis

Plaque rupture and the occlusive thrombosis are seen as the key causes of clinical events in humans (Chen *et al.*, 2013). There is, however, an inherent difficulty in studying plaque rupture in humans, the most significant being that the pathology becomes apparent only in targeted diagnostic procedures or after the clinical event. Rupture also occurs in a stochastic manner, making it difficult to identify a sequence of events leading to cap disruption (Cullen *et al.*, 2003). A good animal model of plaque rupture is, therefore, required to develop an understanding of these mechanisms.

Following the works of Ignatowski in 1908, animal models have found use in the design and testing of novel treatments for application to human disease (Daugherty *et al.*, 2009; Konstantinov and Jankovic, 2013). The popularity of animal models is largely due to their low cost in maintenance, ease in genetic manipulation and the rapid

disease progression. Atherosclerosis-prone mouse models, for example, have been shown to develop complex lesions after 10 weeks on a high-fat diet, with 3% of mice showing signs of plaque rupture (Calara *et al.*, 2001). A key issue in atherosclerotic mice is the rarity of these plaque rupture events (Zhou *et al.*, 2001; Schwartz *et al.*, 2007; Finn *et al.*, 2010; Bentzon and Falk, 2010; Bentzon *et al.*, 2014). This rarity is also seen in large animal models of disease (Getz and Reardon, 2012; Shim *et al.*, 2016; Veseli *et al.*, 2017). An inability to study plaque rupture in animal models presents a large barrier to the current knowledge as it is the most critical event in human disease.

In a study of particular importance to this PhD, Cheng *et al.* (2006) showed a dependence of the plaque composition on the pattern of wall shear stress in the mouse (Figure 1.2). The authors used the placement of a perivascular tapering cast to create distinct regions of high, low, and oscillatory WSS along the length of the mouse carotid artery. Nine weeks after cast placement, fibroatheroma plaques were found in regions coincident with low and oscillatory shear stress, with the high shear stress region being well-protected against lesion formation. A key finding of this study was the localisation of a plaque resembling the TCFA to the region of low shear stress while the oscillatory stress region downstream of the cast showed a stable-looking plaque type with a thick fibrous cap and high infiltration of SMCs. However, when considering the mechanical interference, altered circumferential stresses and inflammatory responses (Tropea *et al.*, 2000; Tanaka *et al.*, 2003) caused by cast placement, there is dispute about the significance of differences in WSS pattern to the resulting plaque composition. A clear statement of the WSS's importance relative to these effects is currently missing.

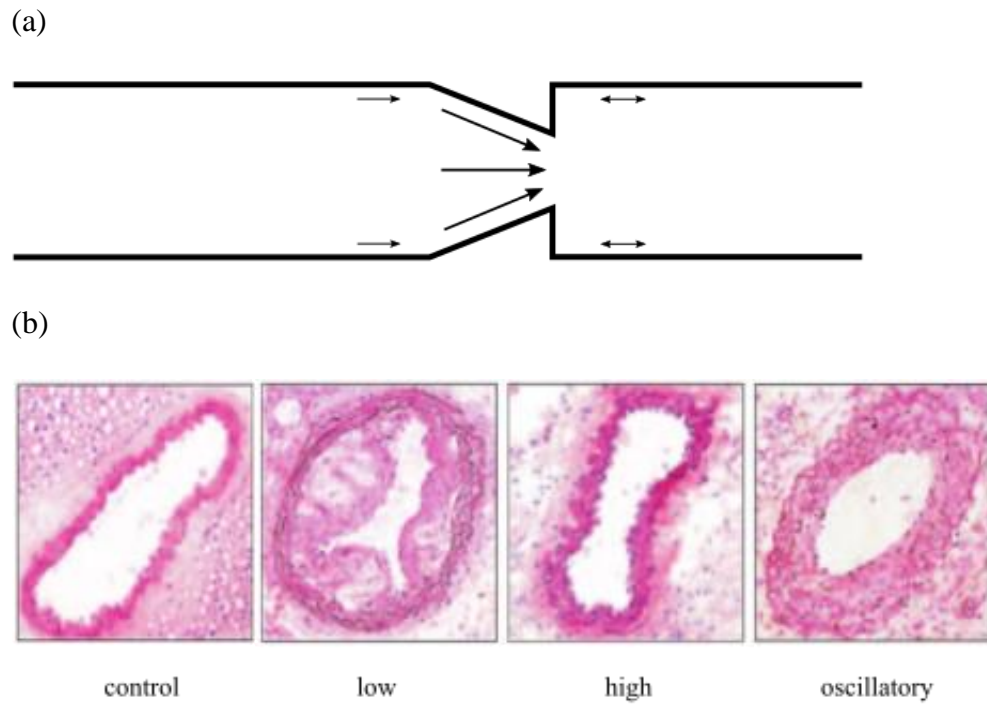


**Figure 1.2. Analysis of the stress and plaque types in the mouse perivascular cast model of Cheng *et al.* (2006).** (a) Schematic representation of the shear stress patterns induced by the perivascular cast. Placement of the cast creates a constrictive effect on the vessel, decreasing the flow rate. This leads to a region of low shear stress upstream of the cast. The tapering of the cast produces a gradually increasing shear stress along the length of the cast, creating a high shear stress region. The pulsatile nature of blood flow and the fluid velocity at the downstream end of the cast creates a region of oscillatory shear stress. The magnitude and direction of wall shear stress are indicated with the size and direction of the arrows in each region. The terms “high”, “low” and “oscillatory” are all referred to in comparison with the control vessel. (b) Histology samples were taken from the carotid arteries of apolipoprotein E deficient mice 9 weeks after cast placement. Plaques resembling the human thin-cap fibroatheroma lesions were induced in the region of low shear stress with a lipid-rich core and a thin overlying fibrous cap. The high shear stress region was shown to be well-protected against plaque formation, similar to the control vessel model. A stable-looking plaque type was found in the oscillatory stress region downstream of the cast with a thick fibrous cap and high infiltration of smooth muscle cells. Figure taken from Cheng *et al.* (2006) with permission.

The ideal animal model of atherosclerosis is one in which the insights gained from the animal studies are translatable to human disease, showing histological similarity and the same response to treatment (Cullen *et al.*, 2003). Considering the importance of the WSS in lesion formation and progression (Section 1.2), the ideal animal model

would, therefore, also bear similarities to humans in terms of the haemodynamic environment and in the endothelial response to this environment. Given the difference in vessel size and heart rate, however, differences in the vessel haemodynamics are expected between the animals (Weinberg and Ethier, 2007; Suo *et al.*, 2007; Cheng *et al.*, 2007; Dawson, 2014).

In order to assess the scalability of insights gained from the animal model, a detailed view of the haemodynamic environment is required. From a fluid dynamics point of view, the haemodynamic environment is sensitive to the flow dimensionless numbers and the waveform of pressure. A clear statement of relationship between these parameters is important in assessing the similarity of the haemodynamic environment between the species.

#### 1.4 Hypothesis and aims

The overarching aim of this work is to further the understanding of atherosclerosis and to clarify the significance of blood flow dynamics in plaque formation, progression and rupture. A number of mouse models exist in the literature in which the common carotid artery has been surgically manipulated, producing atherosclerotic plaques with region-specific composition. The simulations performed in this PhD will, therefore, focus on the wall shear stress signals coincident with each of these regions. This thesis addresses the hypothesis that the frequency composition of the wall shear stress signal is associated to the different plaque compositions and disease characteristics in animal models of atherosclerosis.

The following aims were set out to test the hypothesis:

- 1) Are differences in the wall shear stress frequency composition present across different surgically-manipulated mouse models of atherosclerosis?
- 2) Are the differences in wall shear stress seen between the regions of the perivascular tapering cast mouse model dependent on the input waveforms of pressure?

- 3) Are the differences in wall shear stress seen between the regions of the perivascular tapering cast mouse model dependent on the flow dimensionless numbers?
- 4) Are there differences in the wall shear stress frequency composition in the arteries of different mammals?

## 1.5 Thesis outline

This thesis has been divided into three parts. The first part, presented in Chapters 2, 3 and 4, will deal with the implementation and verification of the numerical method required to address the research aims set out above. Chapter 2 introduces the necessary background needed to understand the modelling choices made in this thesis. Chapters 3 and 4 then deal with the implementation and verification of the numerical method. The 3D lattice Boltzmann (LB) implementation is introduced in Chapter 3. It should be noted that the implementation details described in Chapter 3 are the result of the works of Krüger (2012). Chapter 4 details the implementation and verification of the modules necessary for simulations specific to blood flow in the animal carotid artery. These additional modules were built on top of the Krüger (2012) LB implementation as a part of this thesis.

The second part of the thesis, given in Chapters 5, 6 and 7, addresses the research aims through the simulation of blood flow in the vessels of interest. Research aim 1 is addressed in Chapter 5 in which the wall shear stress signal is analysed in surgically-manipulated mouse models. The implementation of these models is verified against experimentally derived quantities present in the literature. A comparison of the wall shear stress between regions coincident with different plaque characteristics is also presented and discussed. Chapter 6 addresses aims 2 and 3 by simulation of the perivascular cast model with varying input boundary conditions. It should be noted that Chapter 6 provides an exploration into the effects of varying pressure waveform and dimensionless parameters rather than presenting flow cases relevant to any specific animal or biological mechanism causing the variation of these parameters. Chapter 7 addresses aim 4 by simulation of the control vessel in five different



mammals. Novel findings into the difference between species are presented and discussed.

The third, and final, part of this thesis is given in Chapter 8 and presents a discussion of the information gained from this body of work and its relevance to the atherosclerosis community.

### Theoretical background

---

The localisation and progression of atherosclerosis is dependent on the interaction between local mechanical forces and local biological processes (Slager *et al.*, 2005; Chatzizisis *et al.*, 2007; Koskinas *et al.*, 2010; Wentzel *et al.*, 2012). For this reason, the focus of this thesis will be to analyse the local haemodynamics in regions of disease formation. The current chapter presents the necessary background required for this analysis by establishing how the flow field can be studied in terms relevant to inflammation and atherogenesis.

Analysis of the flow field requires the development of a numerical tool that is capable of calculating and visualising fluid flow in a geometry of interest. Fluid flow is described by the Navier-Stokes equations as presented in Section 2.1. By studying the flow field, wall shear stress and atherosclerosis flow metrics can also be computed. Section 2.2 deals with the calculation of the wall shear stress with its interpretation with respect to atherosclerosis being discussed in Section 2.3. Section 2.4 will introduce the Fourier series as a method of quantitatively and qualitatively comparing waveforms of wall shear stress. Section 2.5 presents a discussion of the potential relevance of the wall shear stress frequency composition and comments on the suitability of the analysis method for multidirectional flow.

With blood being a suspension of deformable cells, the shear thinning nature of the fluid must also be considered to retrieve an accurate representation of the flow field. This behaviour and the effective viscosity model are discussed in Section 2.6.

Also, due to the proximity of the vessels of interest to the heart, flow is largely dominated by pulsatile effects and must be modelled as such (Gabriel *et al.*, 2017). This creates a time-varying flow profile which is dependent on several parameters relevant to the network structure of the vascular system. To recover an accurate

representation of the flow field, the time-varying flow profile must also be calculated and implemented properly as “boundary conditions” for the Navier-Stokes equations. The importance of these boundary conditions is discussed further in Section 2.1, and the method used to obtain the flow profiles is also presented in Section 2.7.

## 2.1 Governing equations

Given the relationship between the wall shear stress and atherosclerosis initiation and progression, the accurate calculation of the wall shear stress magnitude and direction is key to this simulation study. As introduced in Chapter 1, the wall shear stress (WSS) is proportional to the near-wall velocity gradient, meaning that an accurate representation of the fluid flow is critical. This can be achieved numerically by solving the Navier-Stokes equations to obtain the velocity field in the fluid domain.

Formulated by G.G. Stokes and M. Navier in the early 19<sup>th</sup> century, the Navier-Stokes (NS) equations are still the most important equations in fluid mechanics. This set of equations is derived from the principle of momentum conservation and is solved together with the continuity equation to describe fluid motion. The continuity equation also represents a key principle in fluid mechanics, the conservation of mass.

By introducing the concept of a finite control volume within a volume of fluid, the continuity and NS equations can be derived. Thinking of fluid motion into and out of the control volume, the mass moving through each of the faces can be evaluated. As mass cannot be created or destroyed, the change of mass in the volume must be equal to the mass fluxes into and out of the system. This principle is expressed as the continuity equation:

$$\frac{\partial \rho}{\partial t} + \nabla \cdot (\rho \mathbf{u}) = 0 \quad (2.1)$$

where  $\rho$  and  $\mathbf{u}$  are the fluid density and velocity, respectively. The time is given by  $t$ .

The Navier-Stokes equations can be derived by thinking of the rate of momentum moving through each of the faces in the control volume. Now considering Newton’s second law of motion, the rate of change of momentum is equal to the sum of the forces applied to the control volume (2.2). The resulting set of equations describe the balance

of inertial, pressure, viscous and external force components applied to the fluid. Each of these components are given sequentially in the lines of equation (2.2). From this derivation process, it is clear that the NS equations describe the conservation of momentum within the control volume.

$$\begin{aligned} \rho \left( \frac{\partial \mathbf{u}}{\partial t} + \mathbf{u} \cdot \nabla \mathbf{u} \right) &= -\nabla p \\ &+ \nabla \cdot (\mu (\nabla \mathbf{u} + (\nabla \mathbf{u})^T) - \lambda (\nabla \cdot \mathbf{u}) \mathbf{I}) \\ &+ \mathbf{F} \end{aligned} \quad (2.2)$$

where  $\mathbf{u}$  is the velocity,  $p$  is the pressure,  $\rho$  is the fluid density and  $\mu$  is the dynamic viscosity.  $\lambda$  is a viscosity term related to the bulk viscosity in compressible fluids.  $\mathbf{F}$  is an external force applied to the fluid system such as gravity.

Assuming incompressibility, the fluid density is taken to be constant and the bulk viscosity term is set to zero. This assumption results in the divergence-free form of the continuity equation (2.3) and the well-known incompressible Navier-Stokes equations:

$$\nabla \cdot \mathbf{u} = 0 \quad (2.3)$$

$$\rho \frac{\partial \mathbf{u}}{\partial t} = -\nabla p + \nabla \cdot (\mu \nabla \mathbf{u}) + \mathbf{F} \quad (2.4)$$

### Boundary conditions

From a mathematical point of view, it is known that partial differential equations such as (2.3) and (2.4) cannot be uniquely determined unless adequate initial and boundary conditions are described. These conditions take the form of mathematical statements and are imposed on a system to identify a solution specific to the fluid flow problem from all possible solutions. From a physical perspective, the boundary conditions also describe the process by which the theory approaches the real-world application through a series of assumptions and idealisations. The conditions are imposed on the fluid boundaries in order to specify some of these assumptions in a simulation domain.

The importance of accurately describing the boundary conditions can be highlighted using the ‘no-slip’ condition, for example. The no-slip condition describes the

assumption that, at a boundary between a fluid and a solid, the fluid velocity is the same as the velocity of the solid. While there are a few exceptions to this condition in nature and industry (Neto *et al.*, 2005), the no-slip condition holds true in many physical cases and is relevant for all simulations performed in this thesis.

Another important type of boundary condition is the description of pressure and/or flow at the inlet and outlet boundaries of the fluid domain. An arbitrary definition of the inlet and outlet conditions may lead to situations where all physical phenomena relevant to the study are missed. Imposing steady flow in atherosclerosis studies for example would fail to capture any fluctuations in wall shear stress caused by the pulsatile nature of blood flow. Hardman *et al.* (2013) also show the importance of specifying the velocity inlet at higher levels of flow complexity. Description of the inlet boundary using the Womersley analytical solution and multidirectional velocity vectors showed significant differences in flow helicity in simulations of the abdominal aortic aneurysm with the multidirectional velocity inlet being assumed as the optimal solution (Hardman *et al.*, 2013). These fluctuations have all been shown to be important in determining the endothelial response and are therefore key to any simulations performed as part of this thesis.

A key part of this discussion is also how flow is imposed in the simulation domain. The choice here is whether to implement a constant pressure difference or a constant flow rate across the system and this is highly dependent on the simulation case. Simulations of arterial blood flow for example are subject to pressure losses through vessel elasticity. This means that the prescription of pressure boundary conditions in a rigid vessel model is not representative of the physical case. Idealisations in geometry, such as those employed in this thesis however, render these boundary condition errors negligible. A key benefit of using pressure boundary conditions in the lattice Boltzmann simulations performed here is the ease with which flow is imposed as a body force. For this reason, the remainder of this thesis will use pressure boundary conditions to describe fluid flow.

The current chapter provides only the necessary background required for this thesis. The study of fluid mechanics is a well-established field providing a number of excellent textbooks; some of which are Batchelor (2000), Landau and Lifshitz (1987)

and Munson *et al.* (2010). A more detailed review of the literature can be found in these books.

## 2.2 Wall shear stress

With the flow field represented by the NS equations, the desired parameters can now be introduced. Arguably the most important parameters in a fluid dynamics study of atherosclerosis are those derived from the traction vector, such as the WSS. The effects of the WSS on endothelial cells and the resulting atherogenic or atheroprotective responses have been presented in Chapter 1. Given its importance throughout this thesis, the current section will provide a complete discussion of the WSS.

The stress tensor  $\sigma_{\alpha\beta}$  can be illustrated by thinking of the fluid control volume in Figure 2.1. The index notation is used here to identify each component of the stress tensor with  $\alpha$  giving the direction of the unit vector normal to the surface and  $\beta$  giving the direction of the stress component. The tensor consists of the normal and tangential (or shear) stress represented by  $\alpha = \beta$  and  $\alpha \neq \beta$ , respectively.

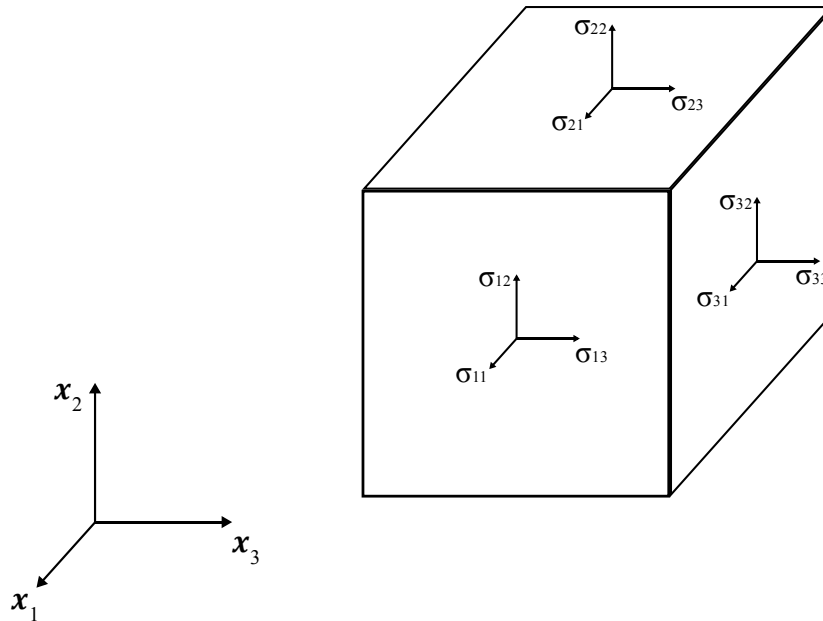


**Figure 2.1 Fluid control volume and stress components acting on the surfaces.** The stresses acting on the surfaces of the control volume can be represented by the stress tensor  $\sigma_{\alpha\beta}$  where  $\alpha, \beta = 1, 2, 3$ . Normal stress components of  $\sigma_{\alpha\beta}$  are given by  $\alpha = \beta$  while the tangential stress components are given by  $\alpha \neq \beta$ .

Initially considering a fluid at rest, only the normal stress components have a non-zero value as there is no shearing motion of the fluid. In this case, the stress tensor is given by equation (2.5) where  $p$  is the local fluid pressure and  $\delta_{\alpha\beta}$  is the Kronecker delta function ( $\delta_{\alpha\beta} = 1$  for  $\alpha = \beta$  and  $\delta_{\alpha\beta} = 0$  for  $\alpha \neq \beta$ ).

$$\sigma_{\alpha\beta} = -\delta_{\alpha\beta}p \quad (2.5)$$

Next, imagining a fluid domain to be composed of several thin layers of fluid, fluid flow requires that these layers move over one another. With this shearing motion, the fluid viscosity becomes important due to intermolecular forces between the fluid layers. The fluid viscosity  $\mu$  describes the resistance to shearing motion. The deviatoric (or viscous) stress tensor  $\sigma'_{\alpha\beta}$  is a result of these intermolecular forces and describes the shearing stress required to create motion in the fluid domain. The total stress, given by equation (2.6), can now be described using the normal and tangential stress components. Also, following the conservation of angular momentum, the tensor is symmetrical about the diagonal, that is  $\sigma_{\alpha\beta} = \sigma_{\beta\alpha}$ .

$$\sigma_{\alpha\beta} = -\delta_{\alpha\beta}p + \sigma'_{\alpha\beta} \quad (2.6)$$

Considering the definition of the deviatoric stress tensor, it is clear that the tensor is related to the deformation of a fluid control volume. This deformation is expressed as the strain rate tensor  $S_{\alpha\beta}$  and is given by equation (2.7). The strain rate tensor is then related to the deviatoric stress tensor by equation (2.8).

$$S_{\alpha\beta} = \frac{1}{2} \left( \frac{\partial u_\alpha}{\partial x_\beta} + \frac{\partial u_\beta}{\partial x_\alpha} \right) \quad (2.7)$$

$$\sigma'_{\alpha\beta} = 2\mu S_{\alpha\beta} \quad (2.8)$$

The traction vector is the sum of the tangential (shear stress on wall) and normal components (pressure on wall) of the stress. This is calculated as the projection of the deviatoric stress tensor onto the wall normal vector  $n_\beta$  (2.9). The vector's tangential component  $\tau_\alpha$  can then be computed by removing the normal component of the

traction vector (2.10). The wall shear stress  $\tau_W$  is taken as the magnitude of the tangential traction vector (2.11).

$$t_\alpha = \sigma'_{\alpha\beta} \cdot n_\beta \quad (2.9)$$

$$\tau_\alpha = t_\alpha - (t_\beta \cdot n_\beta) \cdot n_\alpha \quad (2.10)$$

$$\tau_W = |\tau_\alpha| \quad (2.11)$$

### 2.3 Localisation metrics

With the traction vector and wall shear stress calculated from the flow field, it then becomes necessary to present these quantities in terms relevant to atherosclerosis. A number of flow metrics have been defined by correlating the distribution of atherosclerotic plaques to predictions of wall shear stress from the flow field. These metrics are heavily used in the literature to visualise regions of the arterial network that may be vulnerable to plaque formation through fluid dynamics studies.

While it is known that the wall shear stress influences the location of plaque development (Davies, 1995; Malek *et al.*, 1999; Cunningham and Gotlieb, 2004; Chiu and Chien, 2011), a deeper understanding of the relationship between disease and the spatio-temporal variations of the stress is not known. Identification of regions of interest would allow a detailed analysis to be performed only in these regions, reducing the computational expense associated with post-processing.

#### Time-averaged wall shear stress (TAWSS)

Based on the observation of a high occurrence of plaque formation in regions of wall curvature and branching flows, Caro *et al.* (1971) proposed that low WSS are pro-atherogenic with physiological WSS being protective. Based on this observation, Caro *et al.* (1971) proposed the time-averaged wall shear stress metric:

$$\text{TAWSS} = \frac{1}{T} \int_0^T |\tau_\alpha| dt \quad (2.12)$$

where  $T$  is the pulse period. Thresholds were defined based on the formation of atherosclerotic plaques and the wall shear stresses computed in these regions. These



thresholds are used to identify TAWSS values below which flow is deemed to be pro-atherogenic. Normal values in the healthy human arterial system are 1.0 – 1.5 Pa (Malek *et al.*, 1999; Peiffer *et al.*, 2013a) while pro-atherogenic regions show TAWSS values less than 0.5 Pa (Cunningham and Gotlieb, 2004). Recent studies have also emphasised the importance of high WSS ( $> 3$  Pa) in atherogenesis (Dolan *et al.*, 2013; Eshtehardi *et al.*, 2017).

### Oscillatory shear index (OSI)

The oscillatory shear index (OSI) was introduced to quantify a change in flow direction using the axial component of the tangential traction vector (Ku *et al.*, 1985). An important note here is that the circumferential component of the traction vector is often neglected.

$$OSI = \frac{1}{2} \left( 1 - \frac{\left| \int_0^T \tau_\alpha dt \right|}{\int_0^T |\tau_\alpha| dt} \right) \quad (2.13)$$

Equation (2.13) shows that a non-zero value of the OSI is only obtained in regions of flow reversal. The parameter varies between 0.5 in highly oscillatory flows and 0 in flows where the stress vector is collinear with the time-averaged shear stress (2.12). Considering the denominator in equation (2.13), it can be seen that there is a strong relationship between the oscillatory and low shear stress theories.

### Residence time

Himburg *et al.* (2004) proposed the relative residence time (RRT) metric as a physical interpretation of the OSI. By considering the radial displacement of a near-wall tracer particle away from the vessel wall, the RRT quantifies the time spent by the particle within some small distance from the wall at a given location (2.14). An increased residence time would allow the particle a greater amount of time to migrate across the wall. This is then linked to the progression of atherosclerosis by likening the tracer particle to an inflammatory species. The RRT metric has also been verified through Lagrangian particle tracking methods based on the velocity field (Basciano *et al.*, 2011).

$$RRT \sim [(1 - 2OSI)TAWSS]^{-1} \quad (2.14)$$

From this equation, it can be seen that regions of the vessel presenting highly recirculatory flow and stagnation are expected to return elevated values of RRT. This concept can be visualised by considering flow driven with a sinusoidal pressure gradient with net flow equal to zero. The axial component of the fluid velocity vector would vary sinusoidally, reversing the flow direction and causing a tracer particle to have a net movement of zero in the radial and axial directions. Thinking of the near-wall shear forces, the magnitude of the tangential traction vector would also vary sinusoidally with an OSI value of 0.5. Now considering equation (2.14), this results in an infinite RRT value. A high value of the RRT can also be obtained in regions of low, unidirectional traction vector which may occur as a result of a lower flow rate.

#### Multi-directional wall shear stress

When considering physiological geometries and flows, it becomes obvious that flow is multidirectional; that is, the fluid velocity is variable in all vector components. This would also mean that the tangential traction vector is multidirectional, varying in the axial and circumferential directions on the wall surface. McMillan (1985) proposed these multidirectional flows to be atherogenic with Potter *et al.* (2012) supporting this theory by the analysis of endothelial cells under swirling flow conditions. Following from the varying plaque distributions with age (Sinzinger *et al.*, 1980; Weinberg, 2002), Peiffer *et al.* (2012) proposed that these differences were caused by the varying persistence of multidirectional flows in the aortic arch.

With the OSI metric only quantifying the degree of oscillation in the axial direction, the transverse WSS (transWSS) metric was then proposed to account for the multidirectionality of the traction vector (Peiffer *et al.*, 2013b). The transWSS metric describes the time-average of the traction vector components normal to its time-averaged direction:

$$\text{transWSS} = \frac{1}{T} \int_0^T \left| \vec{\tau} \cdot \left( \vec{n} \times \frac{\int_0^T \vec{\tau} dt}{\left| \int_0^T \vec{\tau} dt \right|} \right) \right| dt \quad (2.15)$$

where  $\vec{n}$  is the vector normal to the geometry surface. The Weinberg group have shown good alignment between lesion prevalence and transWSS in immature and mature rabbits around intercostal branch ostia (Peiffer *et al.*, 2013b; Mohamied *et al.*, 2015).

The capture of information between the TAWSS, OSI and transWSS metrics is highlighted in Figure 2.2.

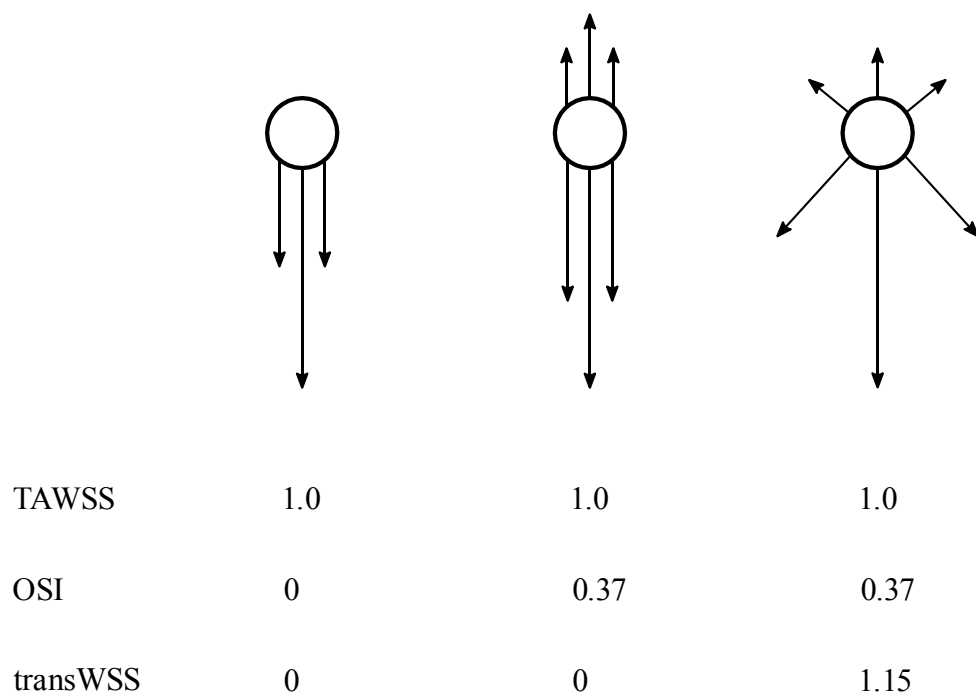


**Figure 2.2. The different flow environments over the endothelial cell (circle) typical of a region of disturbed flow and the resulting TAWSS, OSI and transWSS values.** Each arrow indicates the magnitude and direction of the tangential traction vector at different points in time over the pulse period. The figure highlights the loss of information in the different metrics as multidirectional flows are not captured by the TAWSS and OSI. Redrawn from Mohamied *et al.* (2015) with permission.

### Metric validity

Until recently, the TAWSS and OSI metrics had been regarded as the standard for the definition of development-prone sites in atherosclerosis. A comprehensive review performed by Peiffer *et al.* (2013a) identified that despite many authors following the low/oscillatory shear theory, there is little evidence to support this theory. In fact, the point-to-point comparison of shear stress maps and plaque location failed to prove this theory (Steinman *et al.*, 2002; Wentzel *et al.*, 2005; Gijzen *et al.*, 2007). A study into the accuracy of prediction showed the TAWSS to accurately identify the largest number of plaques among several flow metrics but to also produce the greatest number of false positive results with the greatest percentage accuracy being given by the OSI and RRT metrics (Knight *et al.*, 2010).

With many flow metrics present in the literature, simulation studies have also been used to compare the regions indicated as vulnerable to plaque development, showing some metrics to be numerically equivalent (Lee *et al.*, 2009). Several other metrics have been proposed including the calculation of spatial, temporal and angular gradients of the tangential traction vector (Ojha, 1994; Lei *et al.*, 1996). Another interesting metric is the determination of regions in which the frequency spectrum of the wall shear stress is dominated by the higher harmonics (Himburg and Friedman, 2006).

## 2.4 Fourier series analysis

As discussed in Chapter 1, experimental studies of fluid flow over cultured endothelial cells have shown a dependence of the inflammatory response on the particular frequency composition of the wall shear stress (Himburg *et al.*, 2007; Feaver *et al.*, 2013; Sei *et al.*, 2017). Following this and the pulsatile nature of blood, it becomes necessary to consider the wall shear stress as a time-varying waveform rather than the time-averaged measures used in the literature. The current section will introduce the Fourier series as a method of analysing the time-varying waveforms of wall shear stress. The mathematical tool is used throughout this thesis as a method of comparing wall shear stress waveforms in different models of disease and forms a key component of the analysis method.

The method relies on the property that any periodic function can be expressed in terms of a linear combination of sine and cosine functions:

$$f(t) = a_0 + \sum_{n=-\infty}^{\infty} (a_n \cos(\omega_n t) + b_n \sin(\omega_n t)) \quad (2.16)$$

where a periodic function  $f(t)$  is represented as a Fourier series in terms of coefficients,  $a_n$  and  $b_n$ , and the harmonic identity  $n$ . The angular frequency is given by  $\omega_n = n\omega_0$ , where  $\omega_0 = 2\pi/T$  is the fundamental frequency.

Figure 2.3 shows the approximation of a square wave to achieve a greater degree of accuracy by considering an increasing number of Fourier coefficients. Following Euler's formula, the function can also be expressed as an exponential function with complex Fourier coefficients  $c_n$ :

$$f(t) = \sum_{n=-\infty}^{\infty} c_n e^{i\omega_n t} \quad (2.17)$$

The key purpose of the method is the mapping of a time-dependent function into the frequency domain using the magnitudes and phase angles of the complex Fourier coefficients (Figure 2.4). Physically, the magnitude indicates the strength of the individual frequency components contributing to the waveform while the phase represents the delay of each frequency component in the time domain (2.18). These values can then be used to quantitatively compare different waveforms.

$$c_n = |c_n| e^{i\phi_n} \quad (2.18)$$

From the definition given in (2.17) and the derivation of the coefficients, it can be seen that the zeroth harmonic returns the time-average value of the waveform while the first harmonic represents the component with frequency equal to the measurement period. This is also known as the fundamental frequency and in the case of blood flow, is equal to the pulse frequency. The Python `numpy.fft` package was used throughout this thesis to obtain the Fourier coefficients  $c_n$ .

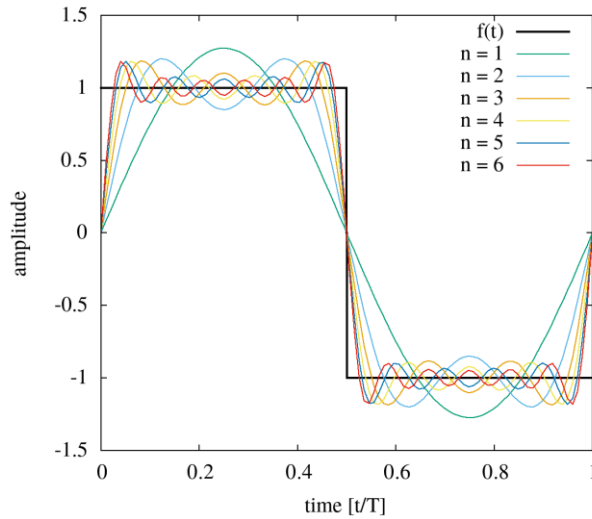
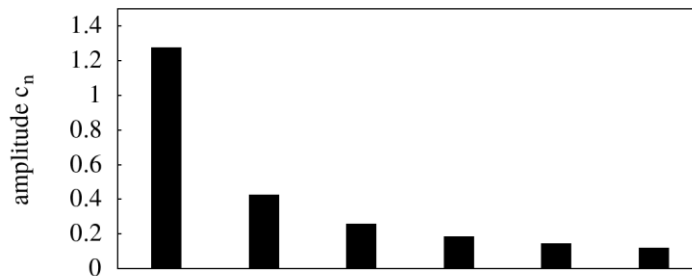


**Figure 2.3. Illustration of the Fourier transform of a square waveform considering the increasing number of harmonic components.** An increasing degree of accuracy is shown in the approximation of  $f(t)$  with an increasing number of harmonic components considered in the Fourier series. Mathematically, the approximation of the curve tends to the true curve as the number of harmonic components tends to infinity.

(a)



(b)

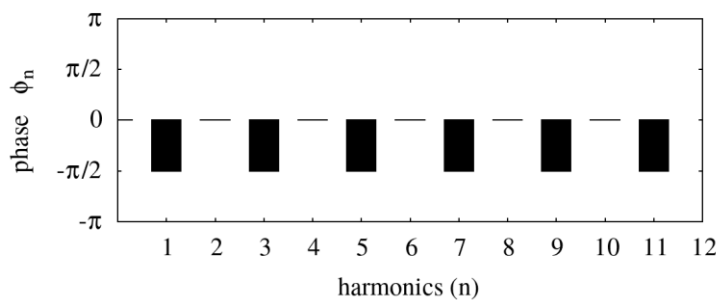


**Figure 2.4. Fourier representation of a square waveform function.** The Fourier (a) amplitudes and (b) phases are given as a function of the harmonic frequencies.

## 2.5 Considerations in Fourier analysis of the wall shear stress signal

### 2.5.1 Multidirectional flow and frequency analysis

Fluid flow in the physiological situation is largely multidirectional as a result of the tortuosity and bifurcations present in the vascular network and the twisting motion of the heart in muscle contraction. McMillan (1985) provides an excellent description of the complex features seen in blood flow. The significance of multidirectional flow features has also been demonstrated in the predisposition for lesions to develop around the rabbit intercostal branch ostia (Sinzing *et al.*, 1980; Weinberg, 2002; Peiffer *et al.*, 2012, 2013; Mohamied *et al.*, 2015), and the shape and alignment of endothelial cells (Potter *et al.*, 2012). Frequency-based WSS studies, however, commonly neglect the circumferential terms and assume a purely axial flow case for the ease of signal comparison (Gelfand *et al.*, 2006; Himburg *et al.*, 2007; Feaver *et al.*, 2013). The responses characterised in these studies are then not representative of the cell responses present in the physical case.

Given the assumption of purely axial flow, the tangential traction vector,  $\vec{\tau}$ , contains only one non-zero quantity in the axial component. Multidirectional flows, however, are defined by non-zero quantities in the axial and circumferential components of  $\vec{\tau}$ . A concern then comes from the inability of frequency spectrum analysis to visualise the signals in an effective and intuitive manner. The following section suggests approaches to deal with the issues raised here.

The multidirectional nature of flow must first be quantified. The transWSS metric (2.15) may be applied for this purpose. This metric describes the time-average of the traction vector components normal to its time-averaged direction. The definition of the “axial” and “circumferential” directions is also complicated by the multidirectional nature of flow in that the direction of  $\vec{\tau}$  changes as a function of time. For this purpose, the modified traction scalar,  $\tau^*(t)$ , is proposed here where the time varying traction vector is projected onto the time-averaged direction  $\hat{\tau}$ :

$$\tau^*(t) = \vec{\tau}(t) \cdot \hat{\tau}, \quad (2.19)$$

where

$$\hat{\tau} := \frac{\int_0^T \vec{\tau} dt}{\left| \int_0^T \vec{\tau} dt \right|} \quad (2.20)$$

Low values of the transWSS indicate flow in which the contributions of multidirectional components are minimal. Frequency decomposition may be performed on the modified traction vector in this case. In high transWSS flows, a frequency-based analysis method would be largely invalid. A full characterisation of the signal would require a frequency-based analysis of the axial and circumferential components of  $\vec{\tau}$ . A frequency-based analysis of the modified traction vector may also be performed with the acknowledgement of its invalidity in regions of local high transWSS.

### 2.5.2 Frequency analysis and normalisation procedures

It is important to note that the frequency composition plots shown throughout this PhD have been normalised with respect to the first harmonic amplitude. The normalisation procedure was used to allow a qualitative comparison between the waveforms computed in different regions. Elevations of a particular harmonic amplitude with respect to the entire spectrum are used to assess differences in the time varying signal. It is, therefore, only relevant to consider the elevations with respect to the entire spectrum and not the values of each amplitude.

### 2.5.3 Wall shear stress frequency composition and endothelial cells

As discussed in Chapter 1, the work of Feaver *et al.* (2013) is of great importance to this PhD. The authors were the first to show a “dose-dependent” response of NF- $\kappa$ B activity to the zeroth and first harmonic amplitudes of the WSS signal. Interestingly, the rate of decrease of NF- $\kappa$ B activity was greater with increase of the first harmonic amplitude when compared to the rate of decrease with increasing zeroth harmonic amplitude. This suggests that the first harmonic amplitude has a greater influence on vascular inflammation than the zeroth harmonic amplitude. Since this study, however, the frequency composition of the WSS signal has not received attention.



Considering the WSS signal in the time domain, in the human, the first harmonic amplitude describes the fluctuation seen on the timescale of 0.8 s. The temporal sensitivity of porcine, bovine and human endothelial cells is given in similar timescales with the earliest detectable response, the activation of ion channels, occurring within seconds of a fluid stress stimulus. The temporal sensitivity of endothelial cells in these large animal models is reviewed in Davies (1995). Fluctuations of the wall shear stress at the higher harmonic frequencies, however, occur on shorter timescales and so, may not be relevant to signalling mechanisms that happen on the scale of seconds. This raises the question of the relevant timescales in endothelial activity.

An important, yet undiscussed, observation from the work of Feaver *et al.* (2013) is the lack of a statistically significant change in NF- $\kappa$ B activity with mutation of the higher harmonic amplitudes ( $n > 1$ ). This suggests that the particular amplitudes of the higher harmonic components are not relevant to the cell's inflammatory response. NF- $\kappa$ B activity did, however, show sensitivity to the presence of these higher harmonic components with an approximately four-fold increase relative to steady flow controls. An interesting result of the Himburg *et al.* (2007) study, with regard to the temporal sensitivity, is the lack of statistical significance of endothelial cell alignment in response to variations in the WSS frequency. Cell alignment also shows a lack of significance when comparing pulsatile and steady flows. This suggests that cell alignment only depends on the time-averaged WSS signal, in contrast to the frequency-dependent response of NF- $\kappa$ B activity.

Another key result from Himburg *et al.* (2007), with regard to the harmonic amplitude, is the downregulation of the proinflammatory molecule, vascular cell adhesion molecule-1 (VCAM-1), in response to a 1 Hz signal whereas the 2 Hz signal resulted in its upregulation. Considering the dose-dependent change of NF- $\kappa$ B activity with the first harmonic amplitude (Feaver *et al.*, 2013), the shift towards the proinflammatory state may be due to the deletion of the 1 Hz frequency component. The 1 Hz frequency component discussed in Himburg *et al.* (2007) is approximately equivalent to the first harmonic component in Feaver *et al.* (2013). The 2 Hz frequency component then correlates to the higher harmonic content given in Feaver *et al.* (2013). This analysis supports the conclusion of Feaver *et al.* (2013) where an increasing first harmonic amplitude is atheroprotective.

It should be noted that the frequency of pulsation also varies between mammals. This is clear from allometric scaling laws (Dawson, 2014; Weinberg and Ethier, 2007) with the human pulse duration being six times greater than that of the mouse. The pulse duration in porcine, bovine and human models are fairly similar. The difference in timescales of pulsatility may then indicate differences in the temporal sensitivity of the animal endothelial cells to a mechanical stimulus. This hypothesis is also suggested by the timescales of recovery in the mouse and human in response to vascular injury models (Seok *et al.*, 2013).

## 2.6 Non-Newtonian fluid

Blood is a non-Newtonian fluid with shear thinning properties. This viscous behaviour arises as a result of red blood cell (RBC) migration, deformation and cell alignment (Galdi, 2008; Robertson *et al.*, 2008; Toksvang and Berg, 2013). The shear-dependent viscosity can be recovered in simulation studies either by the modelling of a particulate suspension or with the use of effective models to estimate the fluid viscosity. Considering the high computational expense and complexity of simulating particle motion and deformation in arterial flows, it is often impractical to simulate blood as a dense suspension. Effective viscosity models on the other hand, can be implemented with relative ease and at low computational expense. Viscosity models commonly take the form of a power law relationship expressing the viscosity as a function of the shear rate. Fit parameters are then used to match the viscous behaviour to physiological data. Phillips and Roberts (2011) provide an excellent review on the different viscosity models available in the literature and their implementation in the lattice Boltzmann framework. The implementation procedure will be discussed in Section 4.3.

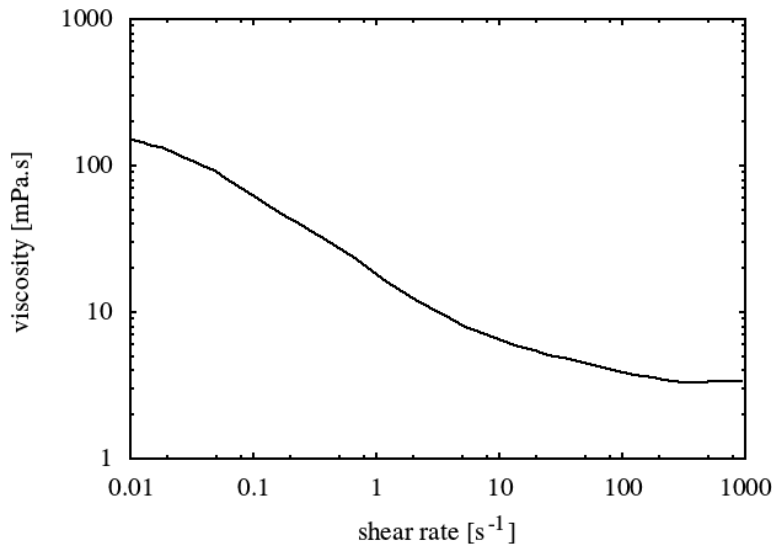


**Figure 2.5. Experimental measurement of the relative viscosity as a function of the shear rate for human blood.** The shear thinning behaviour of blood is demonstrated by the decrease in viscosity with increasing shear rate. Taken from Chien (1970) with permission.

Due to the high shear rates present in the majority of arterial vessels, the shear thinning nature of blood is often neglected. This allows blood to be modelled as a Newtonian fluid with a constant viscosity (Quarteroni *et al.*, 2000). The assumption is commonly justified by the Newtonian plateau at shear rates greater than  $100 s^{-1}$  (Figure 2.5). With arterial shear rates commonly exceeding this shear rate threshold, the fraction of fluid flow experiencing the shear thinning effects is thought to be negligible.

By defining an importance factor parameter using the ratio of apparent viscosity to Newtonian viscosity, Johnston *et al.* (2006) have supported this constant viscosity assumption by showing significance of the viscosity model at the wall only for a small part of the cardiac cycle. Little difference was also shown in the wall shear stress distribution over the length of the artery model. Boyd and Buick (2007) have also supported this assumption for the simulation of a 2D stenosed carotid artery with similar findings in the significance of the viscosity model.

In opposition to this theory, several simulation studies have shown significant differences between the Newtonian and non-Newtonian fluids in both the flow field and shear stress (Gijssen *et al.*, 1999a, 1999b; Artoli and Sequeira, 2006; Wang and

Bernsdorf, 2009). Boyd *et al.* (2007) have also shown a dependence of the velocity field and shear stress on the particular choice of viscosity model. Interestingly, Johnston *et al.* (2004) have shown consistency in the waveform of spatial variation between viscosity models but with differences in the magnitude along the length of the geometry. These differences were found to vanish with increasing inlet velocity as expected considering the increased shear rates. Given the conflict in the validity of the constant viscosity assumption and the importance of the wall shear stress in this study, blood must be modelled as a non-Newtonian fluid with the choice of an adequate viscosity model.

The Carreau-Yasuda (CY) model, equation (2.21), has been chosen in particular as it shows a continuous profile over a range of shear rates. Popular models such as the Casson model, on the other hand, require a viscosity threshold to be applied as an upper bound as the viscosity at low shear rates tends to infinity. The generalised power law model was also seen as a potential choice for the fluid viscosity model. However, negligible differences in the wall shear stress along the length of artery models were found in Johnston *et al.* (2004) while requiring the control of additional parameters and a more complex implementation.

$$\frac{\mu - \mu_{\infty}}{\mu_0 - \mu_{\infty}} = [1 + (\lambda\dot{\gamma})^a]^{-m/a} \quad (2.21)$$

where the fluid viscosity  $\mu$  is calculated from the shear rate  $\dot{\gamma}$ .  $\mu_{\infty}$  and  $\mu_0$  describe the high and low shear rate limits of the viscosity. The characteristic time constant  $\lambda$  and parameters  $m$  and  $a$  are computed empirically to describe the transition region between  $\mu_0$  and  $\mu_{\infty}$ . The shear rate at which the transition occurs is given by the characteristic time constant while the fit parameters,  $m$  and  $a$ , determine the slope of the transition.

## 2.7 1D model

The Navier-Stokes equations, described in Section 2.1, can be solved numerically to compute the flow and pressure fields in the fluid domain. The flow field can then be used to compute the tangential traction vector, a parameter of particular importance in this thesis. As discussed in Section 2.2, the accurate calculation of the traction vector

relies on a physiological representation of the flow field. This is entirely dependent on the specification of physiological boundary conditions, namely those at the inlet and outlet boundaries of the simulation domain. This is the reasoning behind a key problem in the simulation of blood flow.

As a simple illustration of the importance of accurate boundary conditions on the flow field, consider the flow fields resulting from pulsatile and steady flow conditions. Oscillatory components of velocity are absent in the steady flow case leading to a largely different flow field. From this example, it is obvious that the time-variation of blood flow due to the phases of heart contraction must be modelled accurately. In a complex network such as the human arterial system, the vessel geometry and mechanical properties must also be considered. Vessel elasticity, tortuosity, tapering and bifurcation cause the nature of time-variation to also be spatially dependent, changing along the length of a single vessel. These factors significantly complicate the approximation of inlet and outlet boundary conditions and also require an adequate modelling process (Ku, 1997).

The effects of geometrical and mechanical properties of the arterial vasculature can be captured by the 3D modelling of the entire network with an elastic vessel model. However, considering the high computational expense and complexity associated with the 3D simulation of the entire vascular network, it is often impractical to perform this type of calculation. Alternatively, a multiscale model describing lower-dimension representation of flow distribution in the vascular network can be used to provide information for the 3D simulation in a region of interest (Figure 2.6). The multiscale approach provides a computationally cheaper alternative, fully resolving details of the flow field only in the region of interest while computing time-varying waveforms of pressure and flow in the whole vascular network at a lower computational cost.

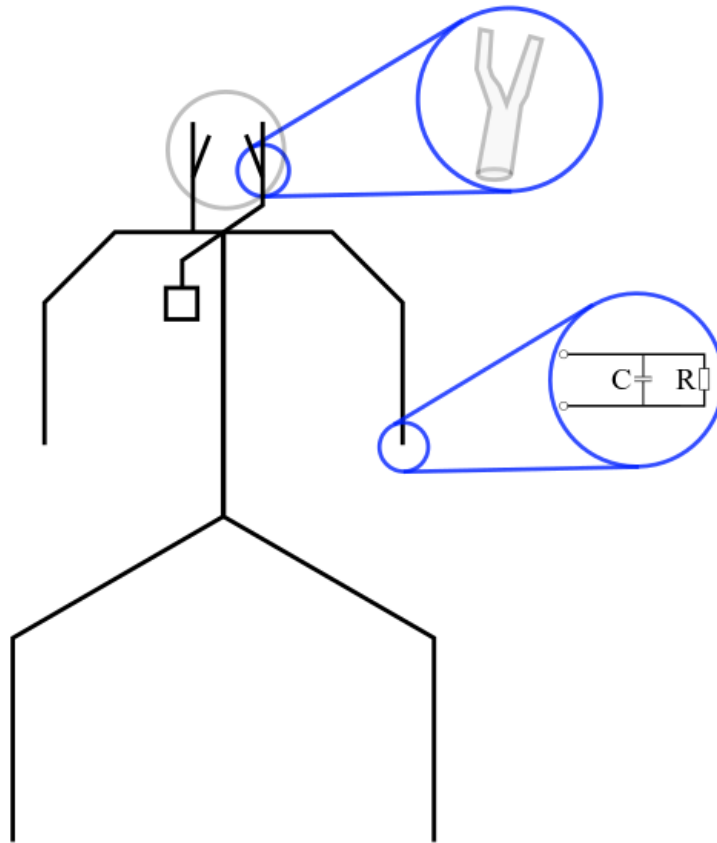


**Figure 2.6. Multiscale representation of the arterial network focussing on a 3D model of the carotid bifurcation.** Pressure and flow waveforms are recovered from a 1D model of the simplified arterial network with terminal vessels ending in a 0D representation of the downstream capillary and venous networks. The 0D models are characterised by the standard two-element Windkessel model with the compliance and peripheral resistance properties of the downstream vessels given by capacitance  $C$  and resistance  $R$ , respectively.

Following the discussion above, the key boundary conditions to be applied at the inlet and outlet boundaries of the simulation domain are waveforms of pressure and flow rate. This information can be computed with the use of relatively simple 1D models. Among the 1D models, the transmission line model has received particular attention because of its simplicity in implementation and low computational cost (Avolio, 1980; Stergiopoulos *et al.*, 1992; John, 2004; de Sá Ferreira *et al.*, 2009; He *et al.*, 2012; Lazovic *et al.*, 2015).

The transmission line model is based on the comparison of the structure and properties of a vessel segment to a section of compliant tubing. This can then be modelled, by

analogy, as a segment of the electrical transmission line where the system is defined by the vessel propagation constant and impedances, both of which are derived from vessel and flow properties. Further details of the compliant tubing analogy and the transmission line models can be found in Avolio (1980), Formaggia and Veneziani (2003) and John (2004).

An important note here is that the electrical transmission line analogy can only be applied to the linearised one-dimensional form of the Navier-Stokes equations (John, 2004; Shi *et al.*, 2011). This means that the convective acceleration term,  $\mathbf{u} \cdot \nabla \mathbf{u}$  must be negligible which is likely to not be the case in the arterial network considering the time-varying profile of pressure and the geometric features of the network. A ‘modelling assumption’ will be applied here as the transmission line approach has been employed successfully in several arterial stenosis studies with correlation in the pressure and flow waveforms between studies (Karamanoglu *et al.*, 1995; John, 2004; Liang *et al.*, 2009; Stroeve *et al.*, 2005; Xiao *et al.*, 2016). A linear description of the system also means that computations can be performed in the frequency domain and allows a comparison to be easily drawn between the inputs and outputs of any 3D simulations.

The key outputs of the model are the vessel impedances and transfer functions. The vessel impedance describes the ratio of pressure drop to flow rate and considers the elastic energy of the vessel walls as well as the viscous resistance of the fluid while the transfer function relates the proximal and distal pressure waveforms in each vessel (van de Vosse and Stergiopulos, 2011). Each parameter is a property of the vessel and flow parameters and so describes the propagation of the pressure and flow through the entire arterial network.

Another key parameter in the description of elastic vessels is the pulse wave velocity (PWV). This parameter gives the velocity of pressure waves travelling through the vascular network and is used in clinical settings as an indicator of vessel stiffness. The pulse wave velocity can also be used in the computation of the vessel impedances and transfer functions in the transmission line model.

In a network of vessel segments connected in series, the transfer function in a vessel of interest is computed as the product of all transfer functions in the series between it

and the source. The product is then related to the outlet pressure of that vessel. The overall transfer function for the right common carotid artery for example, is computed as the product of the transfer functions of the ascending aorta, the brachiocephalic artery and the common carotid artery. Using the source of the arterial system as the pressure output from the left ventricle, the outlet pressure in the right common carotid artery can then be computed. The details of how the input impedance and transfer functions are computed are given in Stroev *et al.* (2005).

Implementation of the 1D model also requires the choice of arterial map to represent the vascular network. The importance of the cerebral vasculature was shown in Reymond *et al.* (2009) indicating flow reversal in the common carotid artery in the absence of an adequate cerebral tree model. Several arterial maps for the human vasculature have been based on the original data of Noordergraaf *et al.* (1963) with modifications later being made to deal with the non-physiological wave reflections in the upper limbs and head (Westerhof and Noordergraaf, 1970; Avolio, 1980). Additional models representing the heart and coronary arteries have also been included in the literature which will not be considered here as their contributions to model flexibility are not relevant to this study (Reymond *et al.*, 2009).

## 2.8 Summary

This chapter presented the theoretical background required for this thesis. In summary, the analysis of blood flow with relevance to atherosclerosis requires the calculation of the wall shear stress. From the definition of the wall shear stress, it is clear that this parameter depends on an accurate description of blood and the flow field. Chapter 3 presents the base implementation of the flow solver while Chapter 4 deals with the implementation and verification of all additional modules required in simulating blood flow.

The points of key relevance in this thesis are the wall shear stress and the analysis of its frequency composition. These concepts are introduced here in Sections 2.2 and 2.4, respectively. The calculation of the wall shear stress is given in Section 4.2 along with an analysis of its limitations.





# Fluid solver: Lattice Boltzmann method

---

Chapter 1 discusses the importance of the wall shear stress in atherosclerosis. The need for a solution to the Navier-Stokes equations then becomes apparent when considering the wall shear stress calculation introduced in Section 2.2. As analytical solutions do not exist for the non-trivial flow cases, the Navier-Stokes equations must be solved numerically. The lattice Boltzmann method is discussed in Section 3.1 as a method of approximating a solution to the Navier-Stokes equations. The flow field is computed in this way for analysis of the local haemodynamics relevant to atherosclerosis studies. The boundary conditions used to describe the no-slip condition at the geometry walls and the periodic boundaries at the inlet and outlet are also discussed in Section 3.2. It should be noted that all implementation details presented in this chapter are the result of the works of Krüger (2012).

### 3.1 The lattice Boltzmann method

Due to the complexity of the Navier-Stokes (NS) equations (Section 2.1), analytical solutions exist only for a few simple cases, steady pipe flows for example. Non-trivial flow cases, such as those with complicated wall geometries and time-dependent flow conditions, require the use of numerical methods to approximate a solution to the NS equations (Landau and Lifshitz, 1987; Batchelor, 2000; Munson *et al.*, 2010). Conventional NS-based methods compute the flow field at the macroscopic scale to recover pressure and velocity in the fluid domain. This pressure and velocity information can also be recovered by solving the flow field at smaller scales by considering the momentum and interaction of the fluid particles in a “bottom-up” approach to fluid modelling (Latt, 2007). One such approach is the use of the lattice

Boltzmann method (LBM) to describe the distribution of fluid particles, thereby approximating a solution to the NS equations (Succi, 2001; Krüger *et al.*, 2017).

### 3.1.1 Overview

The following section aims only to provide the reader with a functional understanding of the LBM and the information necessary for this thesis. The key note in the lattice Boltzmann equation is that the macroscopic behaviour described by the NS equations can be recovered through the definition of the equilibrium distribution (Succi, 2001). For further reading, Krüger *et al.* (2017) provide an excellent account of the history and derivation of the LBM along with the additional considerations needed for its implementation.

The key parameter in the lattice Boltzmann equation (3.1) is the particle distribution function  $f_i$ , also known as the particle population. The quantity represents the density of particles moving with a lattice velocity  $\mathbf{c}_i$  at position  $\mathbf{x}$  and time  $t$  in a regular grid of lattice nodes.

$$f_i(\mathbf{x} + \mathbf{c}_i \Delta t, t + \Delta t) - f_i(\mathbf{x}, t) = \Omega_i(\mathbf{x}, t) + f_i^F(\mathbf{x}, t) \Delta t \quad (3.1)$$

where  $\Delta t$  represents the discrete time step and  $f_i^F$  is used to add external forces such as gravity. The equation describes the collision of particle distributions according to the collision operator  $\Omega_i$ . The post-collision distributions are then streamed from the lattice node at position  $\mathbf{x}$  to the nearest neighbour  $\mathbf{x} + \mathbf{c}_i \Delta t$  along the lattice velocity  $\mathbf{c}_i$ . These velocities are determined by the choice of lattice structure. The structure is defined by the lattice directions  $q$  in a  $d$ -dimensional space with notation  $DdQq$ . A sketch of the D3Q19 lattice is shown in Figure 3.1 with its lattice velocities given by:

$$\mathbf{c}_i = \left( \begin{array}{c|cccccc} 0 & 1 & -1 & 0 & 0 & 0 & 0 \\ 0 & 0 & 0 & 1 & -1 & 0 & 0 \\ 0 & 0 & 0 & 0 & 0 & 1 & -1 \end{array} \middle| \begin{array}{cccccccccccccccc} 1 & -1 & -1 & 1 & -1 & 1 & 1 & -1 & 0 & 0 & 0 & 0 \\ 0 & 0 & -1 & 1 & 0 & 0 & -1 & 1 & -1 & 1 & -1 & 1 \\ 1 & -1 & 0 & 0 & 1 & -1 & 0 & 0 & 1 & -1 & -1 & 1 \end{array} \right) \frac{\Delta \mathbf{x}}{\Delta t}. \quad (3.2)$$

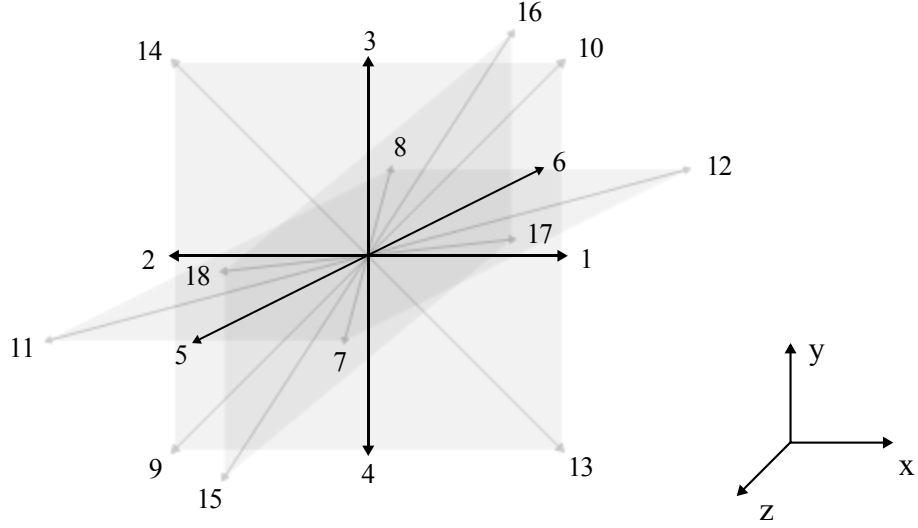


**Figure 3.1. D3Q19 lattice for the lattice Boltzmann method.** The zero velocity  $\mathbf{c}_0 = \mathbf{0}$  is not shown.

The Bhatnagar-Gross-Krook (BGK) collision operator was employed in this implementation to compute the relaxation of populations towards the equilibrium distribution:

$$\Omega_i(\mathbf{x}, t) = -\frac{\Delta t}{\tau} [f_i(\mathbf{x}, t) - f_i^{eq}(\mathbf{x}, t)] \quad (3.3)$$

where  $\tau$  is the relaxation time. Considering the BGK collision operator, the external forcing term is given by:

$$f_i^F(\mathbf{x}, t) = \left(1 - \frac{1}{2\tau}\right) w_i \left( \frac{\mathbf{c}_i \cdot \mathbf{u}}{c_s^2} + \frac{\mathbf{c}_i \cdot \mathbf{u}}{c_s^4} \right) \cdot \mathbf{f} \quad (3.4)$$

with  $\mathbf{f}$  equal to the body force density. The equilibrium distribution is computed from:

$$f_i^{eq} = w_i \rho \left( 1 + \frac{\mathbf{c}_i \cdot \mathbf{u}}{c_s^2} + \frac{(\mathbf{c}_i \cdot \mathbf{u})^2}{2c_s^4} - \frac{\mathbf{u} \cdot \mathbf{u}}{2c_s^2} \right) \quad (3.5)$$

with  $c_s$  being the speed of sound of the model and  $w_i$  describing the lattice weights, both chosen from the particular lattice structure. The D3Q19 lattice structure was employed here because of its stability in the simulation of 3D geometries. From this structure, the speed of sound is  $c_s = \sqrt{1/3} \Delta x / \Delta t$  and lattice weights are defined as

$w_0 = 1/3$ ,  $w_{1-6} = 1/18$  and  $w_{7-18} = 1/36$ .  $\rho$  and  $\mathbf{u}$  describe the macroscopic density and velocity respectively.

Considering the definition of the particle populations, the macroscopic variables of density and momentum density are computed locally from

$$\rho = \sum_{i=0} f_i \quad (3.6)$$

and

$$\rho \mathbf{u} = \sum_{i=0} f_i \mathbf{c}_i + \frac{\Delta t}{2} \mathbf{f} \quad (3.7)$$

respectively where  $\mathbf{f}$  is equal to the body force density.

As a result of the BGK collision operator, the viscosity derived from the LBM is given by the relaxation time as

$$\mu = c_s^2 \rho \left( \tau - \frac{1}{2} \right) \Delta t. \quad (3.8)$$

The deviatoric stress tensor  $\sigma'_{\alpha\beta}$  is also computed from

$$\sigma'_{\alpha\beta} = \left( 1 - \frac{1}{2\tau} \right) \sum_i c_{i\alpha} c_{i\beta} f_i^{neq} \quad (3.9)$$

where  $f_i^{neq} = f_i - f_i^{eq}$  is the non-equilibrium distribution function representing the deviation of the distribution function from its equilibrium state. The calculation of this tensor forms a key part of this thesis as it is used to calculate the traction vector and wall shear stresses (Section 2.2).

The pressure and density in the LBM are related through the equation of state for an ideal gas:

$$p'^* = c_s^2 \rho'^* \quad (3.10)$$

where  $p'^*$  is the deviation from the reference pressure  $p_0^*$  in a system and  $\rho'^*$  is the deviation from the average density  $\rho_0^*$ . Parameters given in lattice units are indicated by the asterisk (\*). A key note in the NS equations is that only pressure gradient is

relevant, rather than a total pressure. This means that the LB density also considers only the deviation from its average.

### 3.1.2 Model implementation

The implementation of the lattice Boltzmann equation requires the initialisation of all related parameters. The populations were initialised to the equilibrium distributions computed from  $\rho^* = 1$  and velocity  $\mathbf{u} = \mathbf{0}$ . A unit conversion step was also performed as part of the initialisation process where physical parameters were scaled to the simulation domain so that the time step  $\Delta t$  and lattice size  $\Delta x$  are both equal to one. The conversion process is described thoroughly in Krüger *et al.* (2017) where all conversion factors are derived in terms of the density, length and time scale conversion factors.

Considering the physical interpretation of the lattice Boltzmann equation, the collision and propagation operations were performed in two steps:

$$f_i^*(\mathbf{x}, t) = f_i(\mathbf{x}, t) - \frac{1}{\tau} [f_i(\mathbf{x}, t) - f_i^{eq}(\mathbf{x}, t)] + f_i^F(\mathbf{x}, t) \Delta t \quad (3.11)$$

and

$$f_i(\mathbf{x} + \mathbf{c}_i \Delta t, t + \Delta t) = f_i^*(\mathbf{x}, t) \quad (3.12)$$

where  $f_i^*$  denotes the post-collision state of the distribution function.

Following initialisation, the computational procedure is given by:

1. Populations were propagated to neighbouring lattice sites along the lattice velocities using equation (3.12).
2. Boundary conditions were applied to compute unknown populations (discussed in Section 3.2).
3. Macroscopic quantities of density and velocity were computed at each lattice node from equation (3.6) and equation (3.7).
4. The deviatoric stress tensor was computed according to equation (3.9)
5. The relaxation of populations towards the equilibrium state was performed through particle collision equation (3.11).
6. Advance to the next time step  $t + \Delta t$  where the process was repeated.

In steady flow simulations, the computational procedure was terminated according to the convergence of the velocity profile to a steady state. The convergence of velocity profiles at times  $t$  and  $t + T$  was determined where the time interval  $T$  was set according to the simulation case. The convergence criterion  $\epsilon$  was determined as:

$$\epsilon = \frac{1}{N} \frac{\sum_N \|u_x(\mathbf{x}, t + T) - u_x(\mathbf{x}, t)\|}{\sum_N \|u_x(\mathbf{x}, t)\|} \quad (3.13)$$

where  $N$  is the number of fluid lattice sites and  $u_x$  indicates the axial component of velocity. Convergence of the velocity to a quasi-steady solution in the pulsatile flow cases was assessed by setting the time interval  $T$  equal to the pulse period.

### 3.1.3 Model verification

The computational procedure given in Section 3.1.2 was adopted from the work of Krüger (2012) and describes the base implementation of the lattice Boltzmann equation. In addition to the verification studies performed in Krüger *et al.* (2009) and Krüger (2012), several simulations have been performed as part of this thesis to verify the functionality of the implementation. Comparison of the fluid velocity and stress profiles showed excellent agreement between the analytical solutions and steady pipe flow simulation results. The  $L_2$  error norm was computed to be less than 2% in a range of simulations with varying radii and relaxation parameters. The error term was computed from:

$$L_2 \text{ error norm} = \sqrt{\frac{\sum (P_S - P_A)^2}{\sum (P_A)^2}} \quad (3.14)$$

where  $P$  is the parameter of interest in the error calculation, velocity in this case, and the subscripts  $S$  and  $A$  represent the simulation and analytical results, respectively.

The implementation was also verified in the case of Womersley flow against the analytical solution obtained from Nash *et al.* (2014). Comparison of the fluid velocity profiles at several points in time showed excellent agreement between the analytical solution and simulation results with an  $L_2$  error norm of less than 2% (Figure 3.2).

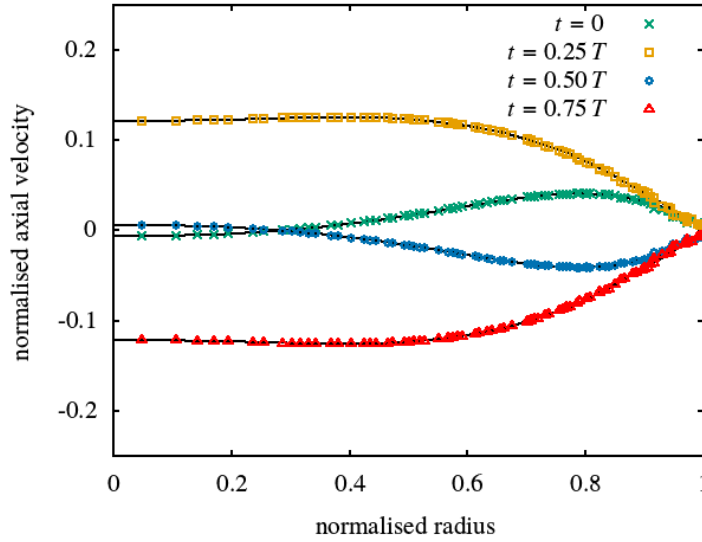


**Figure 3.2. Verification of the lattice Boltzmann implementation in Womersley flow.** A sinusoidal pressure gradient was imposed as a body force with Reynolds and Womersley numbers equal to 135 and 5.94, respectively. Comparisons of the lattice Boltzmann simulation results and the analytical solution are shown at different points in time,  $t$ , over the pulse period,  $T$ . The analytical solutions are shown in solid black lines. Excellent agreement is shown between the simulation results and the analytical solution.

#### 3.1.4 Model discussion

Over the last two decades, LBM has shown increasing popularity in the simulation of biological flows (O'Connor *et al.*, 2016). The method is effective in these applications considering the simplicity of its numerical procedure. This is clear from the description given in Section 3.1.2 where the implementation of the LB equation is straightforward, consisting entirely of simple arithmetic calculations (Chen and Doolen, 1998; Aidun and Clausen, 2010). The relatively “challenging” computation of the method lies in the collision step. This, however, is local and requires no information from neighbouring lattice sites. The only non-local aspect of the method, propagation, is linear and is computationally simple. The simplicity and local nature of the procedure is a major advantage of the lattice Boltzmann method and forms the basis for its use in this thesis.

Relative to computational fluid dynamics (CFD) approaches, the lattice Boltzmann method holds a number of advantages. One such advantage is that there is no need for



potentially expensive meshing processes. The simulation domain is, instead, discretised according to the lattice resolution  $\Delta x$ . A feature of key importance in haemodynamic studies, as in this thesis, is the ease with which the deviatoric stress tensor is computed (3.9). In comparison, conventional CFD methods use an expensive process of computing velocity gradients to calculate components of the stress tensor. The fluid pressure can also be recovered from the density field using the equation of state (3.10). This avoids the need to solve the Poisson equation, a numerically challenging computation in conventional CFD methods (Chen and Doolen, 1998).

The lattice Boltzmann method, however, requires great care in the selection of parameters. Compressibility errors emerging from the Chapman-Enskog multiscale analysis are minimised by control of the fluid velocity, for example. The Chapman-Enskog analysis is used to recover the weakly compressible NS equations from the LB equation (Krüger *et al.*, 2017). As the error terms are a function of the numerical Mach number, all parameters used in the simulations of this thesis were chosen such that the fluid velocity did not exceed 0.07. With the specification of the flow dimensionless numbers and lattice resolution, the simulation timestep is also fixed through this Mach number criteria.

Considering the geometries simulated here, the D2Q9 axisymmetric lattice Boltzmann scheme could be used as an alternative method. Compared to the D3Q19 lattice structure employed in this thesis, implementation of the axisymmetric model would greatly reduce the number of computations and improve the computational efficiency. This is clear from the reduction of the computational domain by a factor of two diameters and the decrease in the number of lattice velocities. Details of the implementation are discussed in Li *et al.* (2010). The 3D lattice structure was used in this thesis to maintain versatility of the model for any future studies where the geometries are not axisymmetric. An important note is that the errors emerging in the treatment of solid boundaries are relevant in both models discussed here (Sections 3.2.3 and 4.2).

This base implementation forms a key component of the thesis as it allows the simulation of fluid flow as a straightforward numerical procedure. The remainder of

the chapter will deal with the implementation of the boundary conditions required to accurately specify the simulation case.

## 3.2 Boundary conditions

As discussed in Section 2.1, boundary conditions form a key component of all fluid dynamics studies. The importance of the boundary conditions and their accurate specification in a simulation study cannot be stressed enough as they are critical in making the solution of the NS equations specific to each modelling case. The specification of inlet and outlet boundary conditions, for example, could mean the difference between the steady and pulsatile flow cases, producing largely different results in the temporal variation of wall shear stress. The following section will deal with the implementation of these boundary conditions in the lattice Boltzmann framework.

### 3.2.1 Boundary conditions in LBM

In conventional fluid dynamics methods, boundary conditions are applied as pressure and velocity conditions at the boundaries of the simulation domain. However, as described in Section 3.1, the LBM operates in terms of the particle populations rather than the macroscopic values of pressure and velocity. This means that the boundary conditions must be prescribed in terms of the particle populations in order to recover the desired macroscopic flow conditions.

The propagation step, shown equation (3.12), involves the streaming of particle populations to neighbouring lattice sites along the lattice velocities. Considering this definition and Figure 3.3, the populations streaming into the fluid domain from boundary nodes are unknown and therefore must be constructed from certain assumptions. Given the importance of the boundary conditions to simulation accuracy and stability, the construction of the unknown populations has received great attention in the lattice Boltzmann community with a large number of potential treatments being proposed. Aidun and Clausen (2010) and Krüger *et al.* (2017) provide excellent reviews of several boundary conditions commonly used in the LBM. A key requirement of the boundary condition is that the desired macroscopic quantities must be recovered from the known and constructed particle populations (Latt *et al.*, 2008).

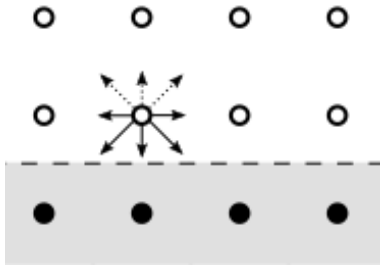


**Figure 3.3. Illustration of a simple lattice structure showing the known (solid arrows) and unknown populations (dotted arrows) in the propagation step.** The boundary (dashed line) separates the solid (grey) and fluid (white) regions. A D2Q9 lattice is shown here to demonstrate that some populations streaming into the fluid nodes (white circles) from solid nodes (black circles) are unknown. Boundary conditions in the LBM must construct these unknown populations from the known information to recover the macroscopic variables at the boundary.

### 3.2.2 Model implementation

Simulation of fluid flow was performed with the use of solid, periodic and open boundary condition implementations.

#### Solid boundary conditions

The no-slip boundary condition present at the solid-fluid interfaces was implemented in all simulations using the standard bounceback scheme. Populations streaming to a solid node were ‘bounced back’ to the node of origin with the opposite lattice velocity (Ginzbourg and Adler, 1994; Ladd, 1994). This implementation was achieved through:

$$f_i(\mathbf{x}, t + \Delta t) = f_i^*(\mathbf{x}, t) \quad (3.15)$$

where  $f_i$  refers to the population with lattice velocity  $\mathbf{c}_i = -\mathbf{c}_i$  (Figure 3.4). Given the simplicity of its implementation, the standard bounceback scheme has become the most popular treatment for solid-fluid interfaces in the lattice Boltzmann community with second-order accuracy being achieved when taking the position of the solid-fluid interface to be located half-way between the solid and fluid nodes (He *et al.*, 1997; Aidun and Clausen, 2010; Krüger *et al.*, 2017). The scheme was implemented as part of Krüger (2012) and has been verified over a number of simulations and studies. A key result of the bounceback scheme is the approximation of the curved and inclined boundaries to a staircase geometry (Figure 3.5).

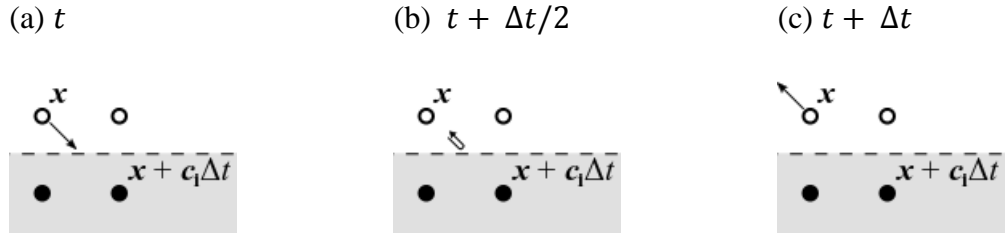


**Figure 3.4. Time evolution of the half-way bounceback approach.** The boundary (dashed line) separates the solid (grey) and fluid (white) regions. The physical no-slip interface is located half way between the fluid nodes (white circles) and solid nodes (black circles) in this approach. (a) At time  $t$ , the post-collision population  $f_i^*$  streams from position  $x$  to the solid node  $x + c_1 \Delta t$ . (b) Bounceback is then applied where the population is ‘bounced back’ with the opposite lattice velocity. (c) This is then assigned to population  $f_i$  at time  $t + \Delta t$  and position  $x$ . In this way, all unknown particle populations at the wall-adjacent node can be constructed from known populations.

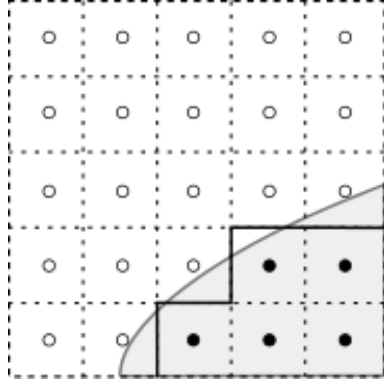


**Figure 3.5. Staircase approximation of a curved boundary in the half-way bounceback treatment.** The lattice discretisation is shown by the dotted lines with lattice nodes represented as circles. The solid region in the physical space (grey area) is approximated to a staircase boundary (solid black lines) in the lattice domain separating the solid lattice sites (black circles) from fluid lattice sites (white circles).

### Periodic boundary conditions

The periodic boundary condition was employed in simulation cases where the inflow and outflow conditions could be assumed to be the same at the inlet and outlet boundaries. With this treatment, post-collision populations leaving the fluid domain at the outlet nodes,  $x + L$ , were streamed back to the inlet nodes,  $x$ , to create the

impression of an infinitely large fluid domain along the axes of periodicity. The periodic boundary condition is given by:

$$f_i^*(\mathbf{x}, t) = f_i^*(\mathbf{x} + \mathbf{L}, t) \quad (3.16)$$

where  $\mathbf{L}$  is the domain size. A simple pipe flow was implemented by setting the axis of periodicity to be only along the axial direction of the pipe. Fluid flow is driven by a body force term implemented in the collision process, given by equation (3.11). The use of periodic boundary conditions was validated in all simulations by comparing the wall shear stress signal upstream and downstream of the geometric manipulations.

### 3.2.3 Model discussion

The specification of the no-slip boundary condition was implemented at all solid-fluid interfaces through the use of the standard bounceback scheme. A known artefact of this method is the approximation of the curved and inclined boundaries to a staircase structure, reducing the accuracy of the solution in the region near the wall. The effect of this approximation on the wall shear stress calculation is discussed further in Section 4.2.

Extensions to the standard bounceback approach have been proposed as a way of reducing the staircase effects by the interpolation of particle populations (Bouzidi *et al.*, 2001; Lallemand and Luo, 2003) and grid refinement in regions where the solutions are expected to change (Filippova and Hanel, 1998). While these proposed extensions show second-order accuracy of the solution, the error caused by the staircase approximation is negligible when considering the errors introduced by geometry simplification and the profiles of pressure and velocity imposed at the inlet and outlet. The errors associated with the staircase approximation were accepted when also considering the significant effort required in reformulating the solid boundary treatment method.

### **Additional models in simulating blood flow**

---

Following the discussion in Chapter 1, it is clear that the wall shear stress plays an important role in the localisation and progression of atherosclerosis. The current chapter therefore aims to develop a numerical tool that is capable of simulating the local haemodynamics in different animal models of atherosclerosis. Using the theoretical background laid out in Chapter 2 and the base lattice Boltzmann method discussed in Chapter 3, the current chapter deals with the implementation and verification of the additional modules required in the analysis of blood flow and calculation of the wall shear stresses.

This chapter details the work performed as part of this thesis including the implementation of an open boundary condition scheme, prescribed at the inlet and outlet. Section 4.1 deals with the specification of this boundary condition with respect to the numerical method. Their implementation in the lattice Boltzmann scheme forms an important task in this thesis given the relationship to simulation stability and accuracy (Succi, 2001; Krüger *et al.*, 2017).

Section 4.2 presents the development and verification of the wall shear stress computation along with the analysis of errors resulting from the wall boundary treatment. Following the discussion in Section 2.6, the shear-thinning nature of blood was also modelled to recover an accurate representation of blood flow. The Carreau-Yasuda model was implemented in Section 4.3 alongside its numerical solution and a robust and efficient method of computing the viscosity from the fluid stress. Again, returning to the importance of the boundary conditions, the flow and pressure prescribed at the inlet and outlet must be accurate and faithful to the physical case in order to recover physiologically relevant information. Section 4.4 deals with the implementation and verification of a 1D model for this purpose. Finally, Section 4.5

discusses the relevant flow dimensionless numbers and the concept of dynamic similarity between simulations and the physical case for simulation validity.

## 4.1 Open boundaries

As discussed in Section 3.2, the periodic boundary condition is employed in the majority of simulations in this thesis considering its efficient implementation and operation. An open boundary treatment is however, required where the assumption of periodic boundaries could not be justified. In this case, the inlet and outlet boundaries were implemented using the regularisation method (Latt *et al.*, 2008). While the specification of any general open boundary condition is discussed in Latt *et al.* (2008) and Krüger *et al.* (2017), a detailed methodology is also provided here given its importance in the lattice Boltzmann scheme.

### 4.1.1 Model implementation

Considering that the implementation of both the density and velocity at the open boundary leads to the mathematical over-specification of the problem, it is only possible to specify either the density or velocity (Krüger *et al.*, 2017). The value of density was imposed at the inlet and outlet to prescribe a desired pressure drop over the length of the geometry. The imposed density was used along with the known populations and moments of  $f_i$  (equations 3.6 and 3.7) to compute the fluid velocity at the boundary. Considering the inlet boundary shown in Figure 4.1, the moments of  $f_i$  were rewritten in terms of the known  $f_+$ , unknown  $f_-$  and tangential or zero populations  $f_0$ :

$$\rho = f_+ + f_- + f_0 \quad (4.1)$$

$$\rho u_x = f_- - f_+. \quad (4.2)$$

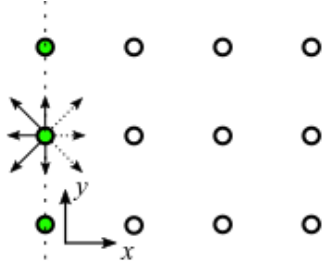


**Figure 4.1. Illustration of the inlet nodes indicating the unknown  $f_-$  (dotted arrows), known  $f_+$ , and tangential or zero populations  $f_0$  (solid arrows) at the open boundary nodes (green circles). The imposed macroscopic quantity (density, in this case) is used with  $f_+$ ,  $f_0$  and the moments of  $f_i$  to compute velocity on the boundary.**

The  $x$ -component of velocity at the inlet was given by:

$$u_x = 1 - \frac{1}{\rho}(f_0 + 2f_+). \quad (4.3)$$

Considering the greater number of unknown populations at the corner nodes, a zeroth-order extrapolation scheme was used to compute the velocity term at these sites. The velocity vector was taken to be equal to that of the neighbouring fluid node in the direction normal to the boundary vector.

The imposed density and computed velocity values were then used to calculate the equilibrium distribution at the open boundaries from equation (3.5). The bounceback of non-equilibrium components (Zou and He, 1997) was used to compute all unknown populations according to:

$$f_i = f_i^{eq} + (f_{\bar{i}} - f_{\bar{i}}^{eq}) \quad (4.4)$$

where the unknown populations  $f_i$  were calculated from the known populations  $f_{\bar{i}}$  and equilibrium distributions. The first-order momentum flux tensor  $\Pi^{(1)}$  was then computed from the non-equilibrium components of the populations on the boundary node as:

$$\Pi^{(1)} = \sum_i c_i c_i f_i^{neq}. \quad (4.5)$$

All pre-collision particle populations on the open boundary were then recomputed from the regularisation method using:



$$f_i(\mathbf{x}, t) = f_i^{eq}(\rho, \mathbf{u}) + \frac{w_i}{2c_s^4} \mathbf{Q}_i : \boldsymbol{\Pi}^{(1)} \quad (4.6)$$

where  $\mathbf{Q}_i = \mathbf{c}_i \mathbf{c}_i - c_s^2 \mathbf{I}$ . A key note in this method is that all populations were overwritten according to the regularisation method, simplifying its implementation in the lattice Boltzmann method. Collision was also performed at all non-solid lattice sites, including at the open boundaries.

#### 4.1.2 Verification

The implementation of the regularisation boundary condition was verified by comparison with the analytical solution of flow in a simple pipe. A parabolic curve was fit to the simulation velocity profile at the axial midpoint. Verification was performed by comparing the coefficient of the quadratic term in the fit curve to the analytical solution showing a good agreement with less than 3% deviation over a range of simulation cases. As a result of the corner node treatment method, a non-zero radial velocity component was also observed in the near-wall regions close to the inlet and outlet boundaries. The magnitudes of these radial velocity components were found to be negligible at less than 0.1% of the axial velocity component. An approximate continuity in the stress profile at the inlet and outlet nodes and the bulk fluid nodes also indicated the correct approximation of the non-equilibrium component of particle populations.

The regularisation method was also verified in Womersley flow by comparing the velocity profile at the axial centre to the analytical solution. As mentioned in Nash *et al.* (2014), simulation results showed good agreement with the analytical solution when allowing for the time taken for the propagation of the pressure wave to the site of velocity output.

#### 4.1.3 Model discussion

The regularisation method was implemented only for the tandem stenosis geometry of Chen *et al.* (2013) where the use of periodic boundary conditions was not possible. The use of periodic boundaries at the inlet and outlet was preferred as it provides a relatively cheap solution in terms of computational effort. This is clear when considering the simplicity of operation. The regularisation method was successfully

implemented and verified in the case of steady and Womersley flows in a simple pipe geometry by imposing profiles of density at the inlet and outlet.

## 4.2 Wall shear stress

The Lattice Boltzmann method is able to describe the flow field by approximating a solution to the Navier-Stokes equations. Conventional fluid dynamics techniques calculate the deviatoric stress tensor from the flow field by computing the strain rate tensor from gradients of the fluid velocity. This process can be computationally demanding as it employs a finite difference method at each position and time. An advantage of the lattice Boltzmann method is that the deviatoric stress tensor  $\sigma'_{\alpha\beta}$  can be computed locally from the non-equilibrium components of the distribution functions (3.9). The traction vector and all subsequent parameters can then be computed from this tensor using the methods detailed in Sections 2.2, 2.3 and 2.4.

### 4.2.1 Wall normal vectors

The challenge in calculating the wall shear stress (WSS) is that both the boundary location and wall normal vector must be known. As discussed in Section 3.2, the half-way bounceback approach approximates curved and inclined geometries to a staircase structure with the solid-fluid boundary located half-way between the solid node and its neighbouring fluid node (Figure 3.5). This approach complicates the determination of normal vectors as the geometry is seen only as voxel data and no additional information about the true normal vector is known. As the half-way bounceback implementation is used throughout this thesis, approximation of the wall normal vector forms a key component of WSS computation.

To solve the problem of wall normal approximation, lattice Boltzmann studies have attempted to quantify the vector using flow (Stahl *et al.*, 2010), geometry (Matyka *et al.*, 2013) and imaging based methods (Hyväluoma *et al.*, 2017). Considering the accuracy and ease of implementation associated with each of these methods, the approach given by Matyka *et al.* (2013) was implemented here to approximate the wall normal vector.

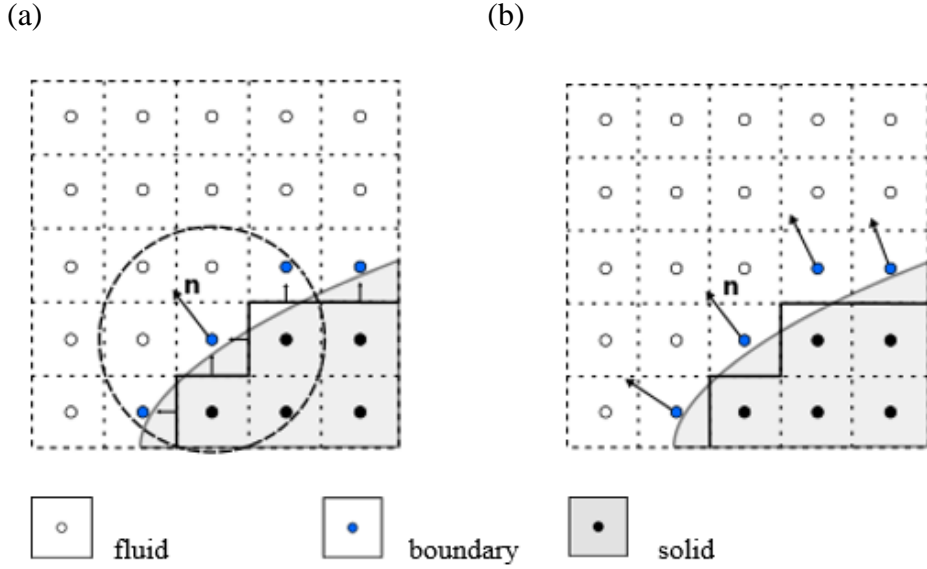


**Figure 4.2. Illustration of the local averaging method for the computation of the wall normal vector  $\mathbf{n}$  (Matyka *et al.*, 2013).** Boundary nodes are identified as lattice nodes with at least one lattice velocity streaming across a physical boundary to a solid node. The staircase normal vectors (short arrows) were defined on the boundary half way between the lattice nodes (solid black lines). (a) An averaging sphere is drawn around the boundary node of interest. (b) The weighted average of the staircase normal vectors is computed to estimate the wall normal vector (long arrow) at each boundary node to characterise the wall surface.

Matyka *et al.* (2013) proposed to compute the wall normal by averaging the normal vectors created by the staircase structure in the neighbouring region. Fluid nodes neighbouring the staircase boundary were redefined as boundary nodes with staircase normal vectors defined on the staircase structure to point into the fluid domain. The weighted average of the staircase normal vectors within a spherical radius of the node was computed as the wall normal vector  $\mathbf{n}$  (Figure 4.2). This average was calculated according to equation (4.7) where  $W_i$  indicates the weighting function and  $\mathbf{b}_i$  indicates the staircase normal vector of the  $i$ -th boundary face.

$$\mathbf{n} = \left( \sum_i W_i \right)^{-1} \sum_i W_i \mathbf{b}_i \quad (4.7)$$

The weighting function was computed as  $W_i = \frac{1}{1 + d_i}$  where  $d_i$  is the distance between the node of interest and the boundary between lattice nodes. It is important to note that

the boundary is located half way between lattice nodes and that this shift is also considered in the calculation of the distance in the weighting function (Figure 4.2).

The approach was tested in the case of a simple pipe by varying the radius of the averaging sphere. The maximum deviation from the analytical normal was used to verify the implementation against results provided in Matyka *et al.* (2013). The fluctuations in angular deviation at points around the circumference is clearly a result of the variation in the staircase arrangement and the property of the analytical normal vectors in a circular cross section to be mirror symmetric about a point on the circumference (Figure 4.3). A zero deviation was found at  $\pm 45$  deg as the staircase normal vectors also show this mirror symmetry property about the node of interest. The points of maximum deviation on the other hand, were found adjacent to  $\pm 45$  deg as the symmetry property is weakest in the neighbouring staircase normal vectors and so the computed wall normal is strongly biased towards a certain direction.

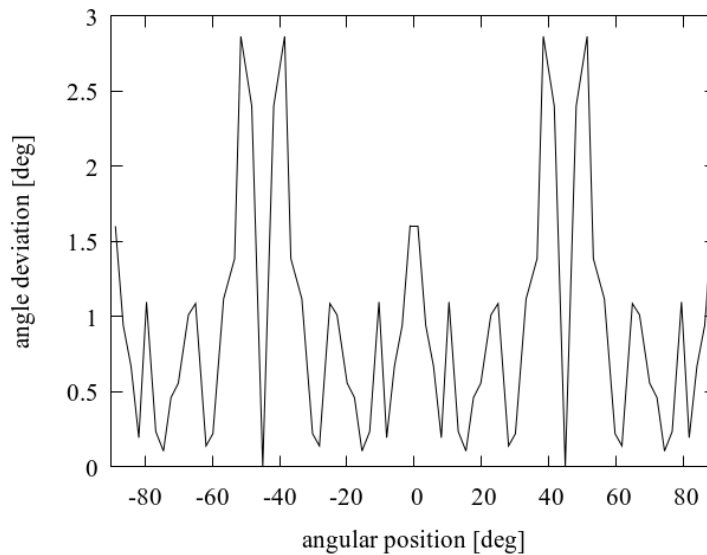


**Figure 4.3. Deviation of the computed wall normal from the analytical value at points around the circumference of the geometry.** Angular deviation was computed in a simple pipe geometry of radius 25 lattice nodes. The wall normal vector was computed using the Matyka *et al* (2013) approach with an averaging sphere radius of 5 lattice nodes. The maximum angle deviation matches that of results reported in Matyka *et al* (2013).

#### 4.2.2 Wall shear stress

Before moving into the discussion of the WSS and its errors, it should be noted that the computed stress is not evaluated directly on the solid-fluid boundary. Rather, it is calculated at the wall-adjacent fluid node which lies approximately one-half lattice site away from the boundary as the deviatoric stress tensor is only available at fluid sites. The ‘one-half’ lattice site difference arises from the halfway bounceback method discussed in Section 3.2. This is a property common to all lattice Boltzmann simulations considering halfway bounceback and so the computed value shall be referred to from this point onwards as the WSS. The analytical solutions of WSS have also been computed to account for this effect.

Considering the analytical solution of the Navier Stokes equations in a simple pipe geometry, the fluid stress is expected to be a function only of the radius and pressure gradient. This leads to a constant value of WSS at all points on the circumference in a pipe geometry. Similarly to Hyväluoma *et al.* (2017) however, the WSS obtained from equation (2.11) shows significant fluctuations at points around the circumference. Simulations performed in this thesis also found negligible differences in the comparison of WSS computed from the Matyka *et al.* (2013) and analytical wall normal vectors. This suggests that the wall normal approximation is irrelevant in the fluctuation of WSS. The distribution of the fluid stress tensor along the radius also found deviation from the analytical solution only in the near-wall region. This indicates that it is the effects of the staircase geometry on the flow field that are being reflected in the deviatoric stress tensor and therefore, in the WSS distribution.

To study the staircase effects on the WSS, the tangential traction vectors were replaced with those computed using a local averaging scheme similar to that of the wall normal calculation. The approach of local WSS averaging has previously been used in Matyka *et al.* (2013) and Hyväluoma *et al.* (2017). The resulting distribution of WSS around the circumference shows a decrease in fluctuation when increasing the averaging sphere radius (Figure 4.4).

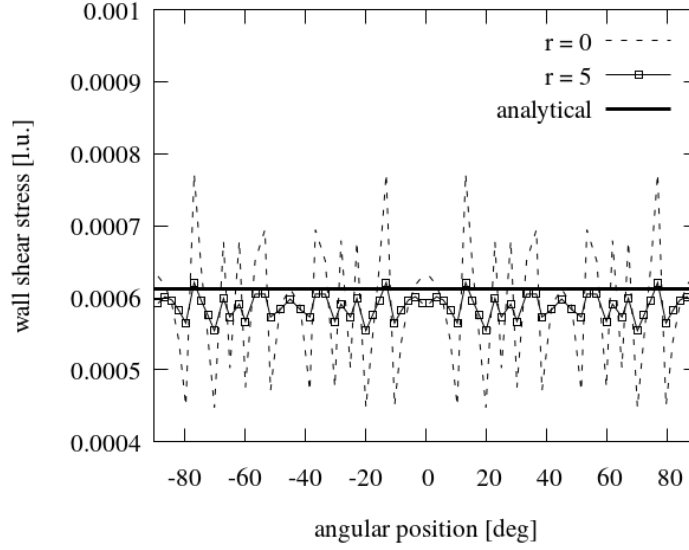


**Figure 4.4. Wall shear stress plotted as a function of the angular position with different local averaging schemes.** The wall shear stress was computed as the magnitude of the tangential traction vector in a simple pipe geometry of 25 lattice unit radius. Increasing the sphere radius,  $r$ , in the local averaging scheme shows a decrease in the fluctuation of the wall shear stress value. The decrease in fluctuation is due to the averaging out of fluctuation of raw wall shear stress values ( $r = 0$ ). The  $L_2$  error norms for the different averaging sphere radii are shown in Figure 4.5.

The  $L_2$  error norm was defined according to equation (4.8) and considers the analytical solution with the one-half lattice site factor mentioned above.

$$L_2 \text{ error norm} = \sqrt{\frac{\sum (WSS_S - WSS_A)^2}{\sum (WSS_A)^2}} \quad (4.8)$$

where the subscripts  $S$  and  $A$  indicate the simulation and analytical values, respectively. The error decreases with an increasing averaging sphere radius and tends towards the error computed from the circumferential average (Figure 4.5). A key note here is that the  $L_2$  error tends towards a non-zero value with increasing averaging sphere radius. This shows that the analytical solution of WSS is not perfectly recovered with the averaging methods, both local and circumferential.

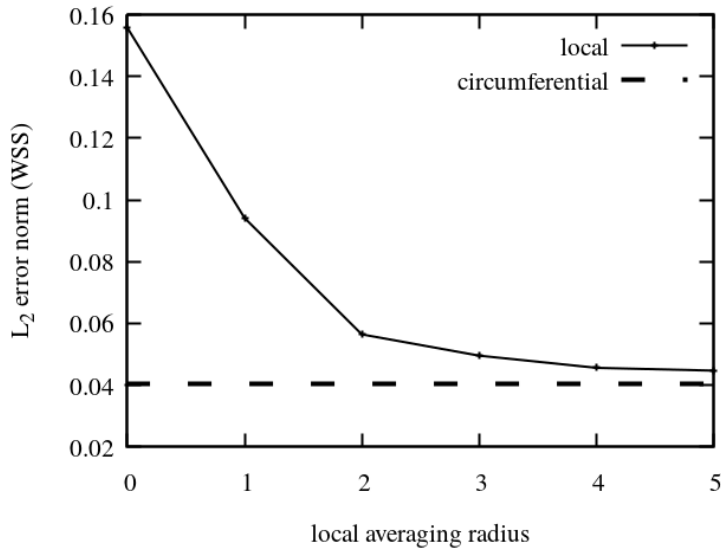


**Figure 4.5. Effect of increasing averaging radius,  $r$ , on the  $L_2$  error norm of wall shear stress (WSS).** A decreasing  $L_2$  norm was found with an increasing radius of the averaging sphere. The  $L_2$  norm tends towards the value computed for the circumferential average which is also non-zero. This suggests that the staircase effects on wall shear stress cannot be completely removed by an averaging method.

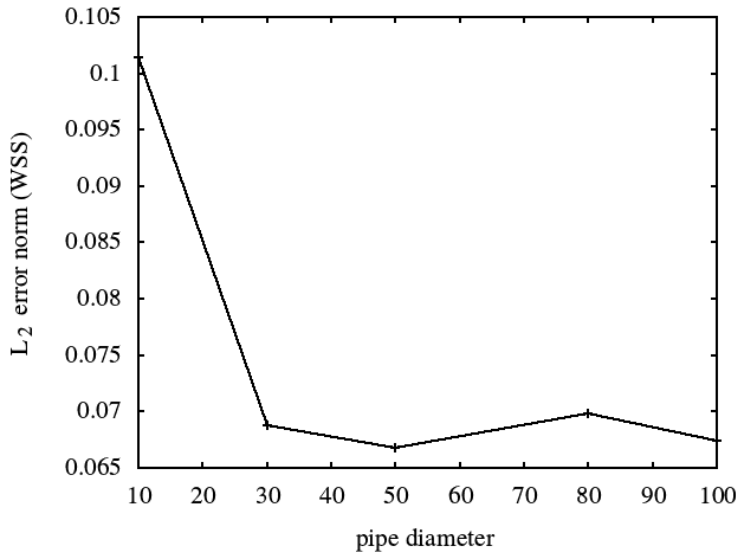


**Figure 4.6. Effect of increasing pipe diameter, and therefore resolution, on the  $L_2$  error norm of the circumferentially averaged wall shear stress (WSS).** Simulations of a simple pipe geometry were performed with  $Re = 10$  and  $\tau = 0.8$  at different resolutions. Flattening of the error curve with increasing resolution shows a zeroth order convergence and that the staircase approximation is always significant in wall shear stress calculation for the considered geometries.

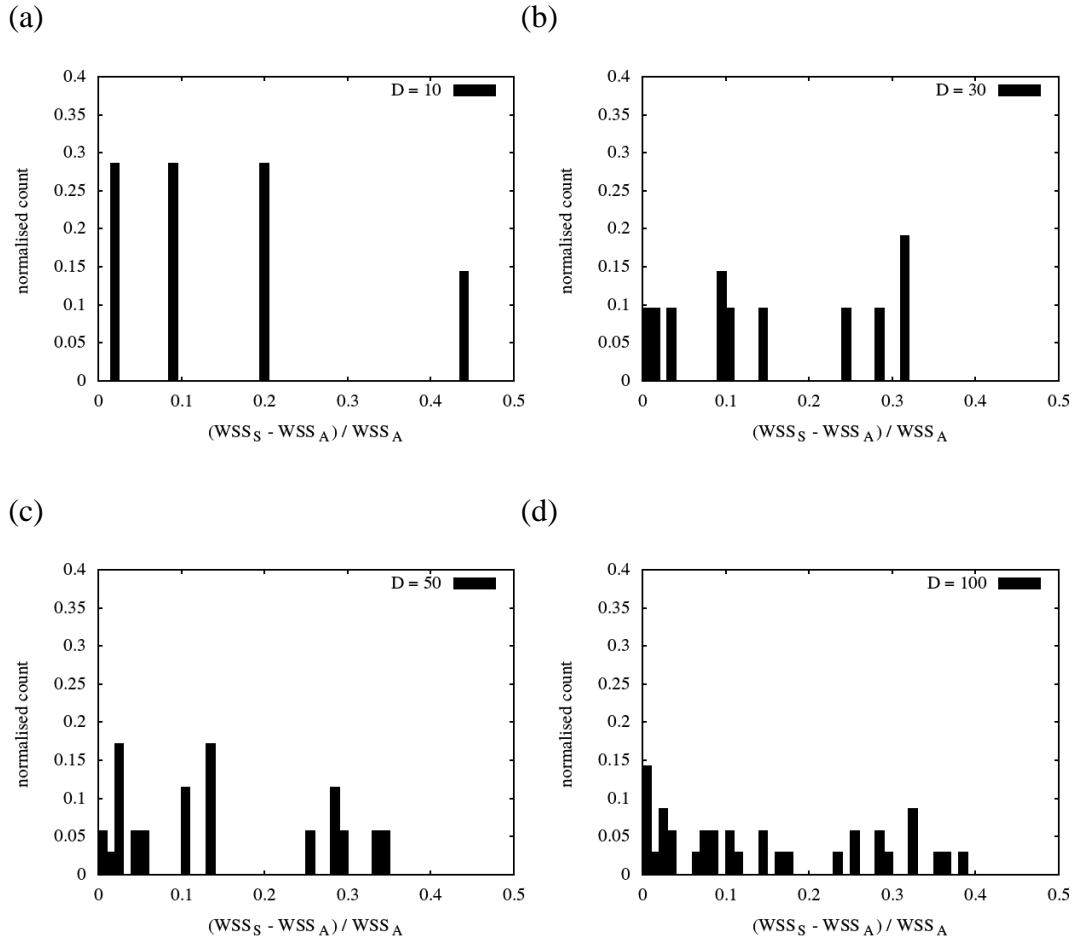


**Figure 4.7. Distributions of normalised deviation from the analytical solution of wall shear stress (WSS) with increasing pipe diameter,  $D$ .** Simulations of a simple pipe geometry were performed with  $Re = 10$  and  $\tau = 0.8$  at pipe diameters (a) 10, (b) 30, (c) 50 and (d) 100 and therefore, at different resolutions. Subscripts S and A indicate simulation and analytical results of wall shear stress, respectively. No averaging scheme was employed for the wall shear stress calculation. Increasing resolution shows an initial shift in the concentration of deviations towards the lower magnitudes before reaching a stable distribution. These properties are reflected in the decrease and subsequent flattening of the  $L_2$  error norm with increasing pipe diameter (Figure 4.6).

The WSS error convergence was assessed in a simple pipe geometry with fixed Reynolds number and relaxation parameter ( $Re = 10$  and  $\tau = 0.8$ ). The channel diameter was increased to simulate an increasing resolution and showed a decrease and subsequent flattening of the error. This indicates a zeroth order convergence of the WSS (Figure 4.6). Referring again to Figure 4.5, it is clear that the magnitude of the zeroth order term is dependent on the choice of WSS averaging method with the errors



shown in Figure 4.6 being computed from the circumferential average. To understand the behaviour of the WSS error, the distribution of normalised deviations was studied at points around the circumference with no averaging scheme (Figure 4.7). The decrease in the  $L_2$  error norm is reflected in the initial shift of the distribution of normalised deviations towards the lower magnitudes. Stability of the distributions at diameters greater than 30 lattice sites also captures the flattening of the  $L_2$  error norm. This flattening behaviour and absence of any convergence was also observed in Hyväluoma *et al.* (2017) with the simulation of a 3D simple pipe geometry.

Kang and Dun (2014) however, show a first order rate of convergence in WSS with increasing resolution for a 2D Poiseuille flow. Here, the assumption of Poiseuille flow in an aligned channel removes any staircase approximation in the geometry. This reduces the observed error to be a factor only of the distance between the physical wall and the wall-adjacent lattice node which clearly reduces with first order rate. It then follows that the convergence of WSS is also first order.

Hyväluoma *et al.* (2017) wrongly attribute the first order convergence behaviour in Kang and Dun (2014) to the use of interpolation-based boundary conditions but the simulations in question use a standard bounceback approach. Instead, the lack of convergence shown in Figure 4.6 and Hyväluoma *et al.* (2017) appears to be purely a result of the staircase approximation. Supporting this observation, Kang and Dun (2014) also show a slight flattening behaviour of the WSS convergence in inclined channel simulations where the staircase approximation again becomes relevant. The lesser degree of flattening in Kang and Dun (2014) may be attributed to the difference in arrangement of the staircase between the 2D inclined channel and the 3D pipes simulated here.

#### 4.2.3 Model discussion

The implementation of the normal vector and WSS calculations was verified against the literature and analytical solutions in a simple pipe geometry. Analysis of the deviatoric stress tensor in the pipe radius was performed showing the fluctuations in WSS to be a result of the staircase approximation at the solid-fluid boundary. This staircase approximation was also found to lead to a zeroth order error term that persists with increasing resolution. Reduction of this error term was achieved through a WSS

averaging scheme. While local averaging methods are recommended for the simulation of complex geometries, the circumferential averaging method will be used in all subsequent calculations considering the axial symmetry of the simulated geometries and the minimal value of error recovered in these cases.

The zeroth order convergence of the bounceback scheme in the simple pipe geometry suggests that the standard bounceback is limited in its use in WSS studies. As mentioned in Section 3.2.3, the interpolated bounceback scheme, discussed in Bouzidi *et al.* (2001), is known to remove the staircase effects and improve simulation accuracy. When considering the velocity error residuals in Poiseuille flow, Nash *et al.* (2014) showed the interpolated bounceback scheme to produce second-order convergence while the standard bounceback implementation gives first-order. Womersley flow simulations also showed a reduction in velocity error residuals with the implementation of the interpolated bounceback scheme (Nash *et al.*, 2014). The errors caused by the staircase effects are accepted considering their small magnitudes and the other, more significant errors introduced in the modelling process such as the geometry simplification. The effects of the geometry simplification are most apparent in the simulations of Chapter 5.

### 4.3 Non-Newtonian fluid

Following the discussion in Section 2.6, it is clear that blood must be modelled as a non-Newtonian fluid with the appropriate shear thinning properties. The Carreau-Yasuda model was implemented for this purpose to compute the viscosity as a function of shear rate. The lattice Boltzmann method again proves advantageous over conventional computational fluid dynamics techniques because of the ease with which this shear rate is computed. Similar to the deviatoric stress tensor discussed in Section 4.2, the shear rate calculation is also entirely local allowing the viscosity to be easily set at each lattice site (Krüger *et al.*, 2009).

#### 4.3.1 Model implementation

An implicit relationship between shear rate and viscosity in the Carreau-Yasuda model (2.21) becomes apparent when considering the viscosity model and Newton's law:

$$\frac{\mu - \mu_\infty}{\mu_0 - \mu_\infty} = \left[ 1 + \left( \lambda \left( \frac{\sigma}{\mu} \right) \right)^a \right]^{-m/a} \quad (4.9)$$

where the fluid viscosity  $\mu$  is expressed in terms of the stress magnitude  $\sigma$  and itself through the shear rate.  $\mu_0$  and  $\mu_\infty$  are the asymptotic limits of the viscosity model,  $\lambda$  is the characteristic time constant and  $m$  and  $a$  are model parameters describing the transition region between  $\mu_0$  and  $\mu_\infty$ . The Carreau-Yasuda model Newton iterator (CY iterator) was implemented to solve this shear rate-viscosity implicit relationship (4.9) from the fluid stress as in Wang and Bernsdorf (2009). The iterative process was terminated when the viscosity had converged within a margin of  $10^{-6}$ . This implementation was initially found to be well-suited for this application as convergence of the local viscosity occurred within 3 iterations at all lattice sites in the test simulation cases.

Initially, the viscosity model was implemented in the lattice Boltzmann method using the stress tensor computed as part of the wall shear stress calculation. By expressing the viscosity model in terms of the fluid stress, a local viscosity was computed by the CY iterator. The computed viscosity was then implemented in the lattice Boltzmann scheme by changing the value of a local relaxation according to equation (3.8). As with any general viscosity model, its implementation in the lattice Boltzmann method is complicated by an implicit relationship between the stress tensor and fluid viscosity. The implicit relationship is clear from equation (3.8) and

$$\tau = \frac{\mu(\sigma(\tau))}{\rho c_s^2} + \frac{1}{2} \quad (4.10)$$

where the functions  $\sigma(\tau)$  and  $\mu(\sigma)$  are given by equation (3.9) in the lattice Boltzmann formulation and the general viscosity model, respectively. In simulation cases with a slow time-evolution of the relaxation parameter, the stress tensor can be computed from the relaxation parameter of the previous time step (Phillips and Roberts, 2011).

The initial approach was found to be unsuitable for parameter sets with increasing difference between the asymptotic limits of the viscosity range. A more robust solution is the application of a Newton iterator to solve the implicit relationship given by equation (4.10). A Python script, specific to the Carreau-Yasuda model, was developed

for this purpose. The script exploits the magnitude of the first-order momentum flux tensor  $\Pi^{(1)}$  as this value is independent of the relaxation parameter and can be easily computed as part of the simulation:

$$\Pi^{(1)} = \left| \sum_i c_{i\alpha} c_{i\beta} f_i^{neq} \right|. \quad (4.11)$$

For clarity, a breakdown of the script is provided here using only a single value of the momentum flux where, in reality, the script inputs a range of values for the momentum flux. The script works on the basis of a Newton iterator for the Carreau Yasuda model within a Newton iterator for the relaxation parameter. The algorithm is given by:

- 1) Set a value for the momentum flux and an initial guess of the relaxation parameter.
- 2) In the relaxation parameter Newton iterator (RP iterator), compute the stress magnitude using equation (3.9) and the values of momentum flux and initial guess relaxation parameter.
- 3) Within the relaxation parameter iterator, compute the viscosity from the stress magnitude using the CY iterator. Given that the CY iterator is within the RP iterator, only one iteration needs to be performed.
- 4) In the RP iterator, compute the relaxation parameter from equation (3.8).
- 5) Compute the next approximation of the relaxation parameter. The iterative process was terminated when the solution had converged within a margin of  $10^{-6}$ .

The iterative process was performed for momentum flux values ranging from  $10^{-10}$  to 1 on a logscale with 100 data points to provide a full range of viscosities. The script was verified by comparing the viscosity profile output from the Python script with some initial guess of the viscosity to the profile computed directly from the Carreau-Yasuda model with a range of stress values (Figure 4.8). The iterative process was well-suited to this application with the speed of relaxation parameter convergence being dependent on the viscosity model parameters and the range of momentum flux values. It should be noted that a converged solution was not achieved for parameter sets with  $m > 0.8$ . The values of  $m$  relevant to this PhD, however, do not exceed this criterion.

The viscosities determined from this script were then read at initialisation of the lattice Boltzmann implementation and, within the simulation at each time step and position, a computed value of the momentum flux was used to calculate a corresponding viscosity. A linear interpolation scheme was used to interpolate between the values of the momentum flux output from the Python script.

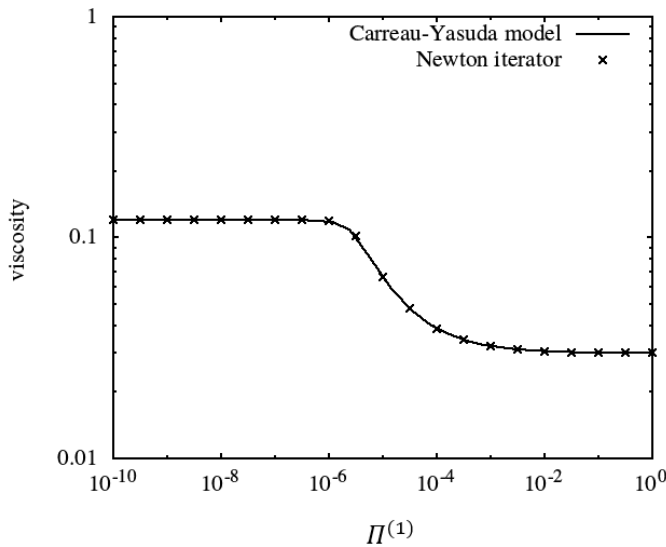


**Figure 4.8. Verification of the Python script for the Newton iterator in relaxation parameter over a range of input values of the first-order momentum flux magnitude  $\Pi^{(1)}$ .** The viscosity model is solved from an initial guess of the relaxation parameter and a range of values of the momentum flux of non-equilibrium components using the mouse Carreau-Yasuda model parameter set. Excellent agreement was found from a comparison of the viscosities computed from the Newton iterator and those output directly from the Carreau-Yasuda model. All parameters are provided in lattice units.

#### 4.3.2 Verification

The viscosity model implementation was tested in the case of steady flow in a simple pipe geometry. Considering that the Carreau-Yasuda model does not have an analytical solution, a numerical integration step was performed. For this purpose, a Python script was developed using the numerical integration tool in the SciPy library. Numerical integration was used on equation (4.12) to compute the fluid velocity, viscosity and local shear rate for verification against the lattice Boltzmann simulation results.

$$\frac{r}{2} \frac{dP}{dx} = \left( \mu_{\infty} + (\mu_0 - \mu_{\infty}) \left[ 1 + \left( \lambda \frac{du}{dr} \right)^a \right]^{-m/a} \right) \frac{du}{dr} \quad (4.12)$$

where  $\frac{dP}{dx}$  is the pressure gradient,  $u$  is the fluid velocity and  $r$  is the distance to the centre of the pipe. Boundary conditions for the numerical integration step were obtained from the velocity and shear rate at the wall. The velocity at the wall was taken as zero by considering the no-slip condition and the wall shear rate was computed from the fluid viscosity at the wall, calculated using an implementation of the Newton iterator with the analytical solution of wall shear stress.

Simulations and numerical integration calculations were performed at different shear rate numbers by using the characteristic time constants to vary the range of viscosities experienced in the fluid. The shear rate number is introduced in Section 4.5. The  $L_2$  error norm was computed from the velocity profiles showing an error of less than 3% over a number of tested parameter sets. This suggests the accurate implementation of the viscosity model in the lattice Boltzmann method.

#### 4.3.3 Validation of the Newtonian viscosity assumption

Comparing the analytical solution of Newtonian flow with the numerical solutions of the mouse and human Carreau-Yasuda viscosity models showed importance of the viscosity assumption only in the velocity profile (Figure 4.9). Viscosity model parameters in the mouse and human are presented in Table 4.1. A comparison of the near-wall velocities showed the wall shear rates to be largely similar, suggesting minimal effect of the Newtonian viscosity assumption on the WSS. This finding proves that the Newtonian viscosity assumption is valid for the purpose of WSS calculation in simulations of steady flow in a straight pipe geometry of constant radius.

The effects of the viscosity model assumption in constriction geometries and pulsatile flows are still not clear.

**Table 4.1. Carreau-Yasuda viscosity model parameters for the mouse and human.** The mouse viscosity parameters were obtained from Bernabeu *et al.* (2014) in which a least square regression fit was performed on mouse viscosity data provided in Vogel *et al.* (2003) and Windberger *et al.* (2003). The human viscosity parameters were obtained from Boyd *et al.* (2007) and Bernabeu *et al.* (2013).

Animal	$\mu_0$ [mPa.s]	$\mu_\infty$ [mPa.s]	$\lambda$ [s]	$m$	$a$
mouse	14.5	3.265	0.1839	0.5864	2.707
human	160	3.5	8.2	0.7872	0.64

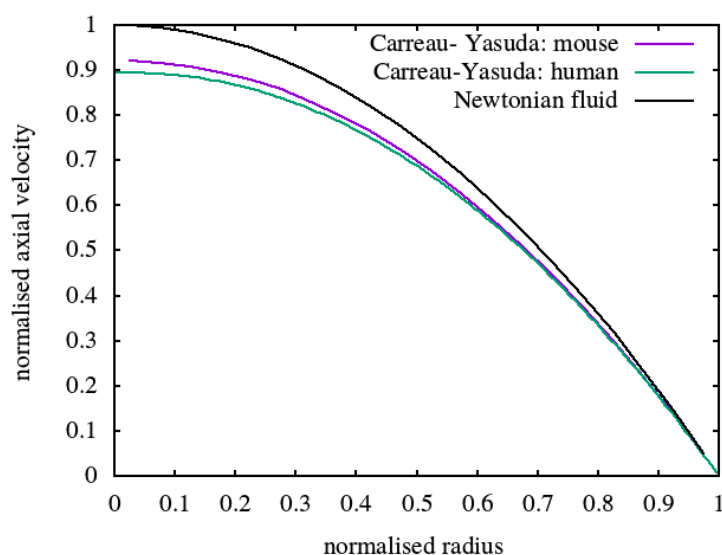


**Figure 4.9. Significance of the viscosity model assumptions in the simple pipe.** Analytical solutions of the Newtonian fluid were compared with the numerical solutions of the Carreau-Yasuda viscosity model with mouse and human parameters.

#### 4.3.4 Model discussion

The Carreau-Yasuda viscosity model was implemented in the lattice Boltzmann method in order to accurately model blood as a non-Newtonian fluid. Benchmarks against a numerical solution were used to verify this implementation showing the accurate calculation of velocity, viscosity and shear rate. Surprisingly, it appears that a numerical solution for the Carreau-Yasuda model has not been previously shown in the literature with the majority of benchmark tests only being shown against simpler power law viscosity models. The numerical solution computed in this thesis shows that the Newtonian viscosity assumption is entirely valid for the calculation of WSS in steady pipe flows.

### 4.4 1D model

In order to recover a physiological representation of flow field, the boundary conditions imposed on the system must describe the physical situation. As discussed in Section 3.2, these boundary conditions are given in the form of pressures and/or flow rates at the open boundaries. A 1D model becomes necessary here as the computation of these waveforms in a higher-dimension model, 3D for example, would prove impractical considering its high computational effort. Experimental measurement of the pressure is also not favoured because of its invasive nature. Following from Section 2.7, the waveforms can be recovered using the 1D transmission line model of a healthy vascular network.

A successful implementation of the model was not achieved in this PhD. The following section discusses the model implementation and an investigation into the possible sources of error.

#### 4.4.1 Model implementation

The implementation and verification of the model was performed in the human vasculature as waveforms of pressure and flow are available at several points along the vascular network from the literature (Liang *et al.*, 2009; Reymond *et al.*, 2009; He *et al.*, 2012). Following the successful implementation of the human model, the mouse arterial network and model parameters can be adapted from Aslanidou *et al.* (2016).



### Model input

As the transmission line model operates in the frequency domain, the input for the model was taken as the Fourier series representation of the time-varying flow waveform. The waveform was taken from John (2004). All unsteady flow computations used only the first eight harmonic components of the waveform as the accuracy of approximation showed negligible difference when further increasing the number of harmonic components (Nichols *et al.*, 1998; Artoli *et al.*, 2002).

### Vascular network model

The human arterial map of this implementation is based on the works by Avolio (1980). As discussed in Section 2.7, the arterial map is based on the original physiological data of Noordergraaf *et al.* (1963) with modifications later being made by Westerhof *et al.* (1969) and Avolio (1980) to deal with non-physiological wave reflections in the upper limbs and head. Reymond *et al.* (2009) also consider the Avolio (1980) network to provide the sufficient level of detail in the cerebral circulation for the recovery of physiological waveforms of pressure and flow. All vessel parameters in the human vasculature were adapted from Avolio (1980), Liu *et al.* (1989) and Reymond *et al.* (2009).

### Computational procedure

A Python script was developed to operate on the human arterial network. The vasculature was implemented as a list of dictionaries with each item in the list containing information about a vessel. The branching structure was established by creating a list within each item to give the identity of vessels immediately downstream. Each vessel was also assigned a generation number containing the number of vessels between it and the source. Following the backwards algorithm of Avolio (1980) and Stroeve *et al.* (2005), the Python script worked backwards in the generation number to characterise each vessel in terms of the impedance and transfer function as introduced in Section 2.7.

The terminal impedances at the peripheral vessels were first computed using the three-element Windkessel model (Westerhof *et al.*, 1971). Vessel impedances were calculated in the branch immediately upstream using the properties of the electrical

transmission line as in Stroev *et al.* (2005). The impedance of vessels where branching occurred was computed by summing the impedances of the downstream vessels in parallel. Once all vessel impedances were known, the transfer functions were computed at all points in the arterial tree. The transfer functions were used to relate the pressure waveform between the upstream and downstream end in each vessel. With this, the pressure waveform at all vessels was recovered by multiplying the transfer functions of the upstream vessels in series. The input impedances were then used to relate the pressure and flow waveforms.

The computation was performed for each harmonic frequency with the zeroth harmonic being approximated by an infinitesimally small constant as in He *et al.* (2012). Frequencies are given by  $n\omega_f$  where  $\omega_f$  is the fundamental frequency and  $n$  is 0.1, 1, 2, ..., 8 with the zeroth component being approximated to 0.1. The value of infinitesimal constant was chosen here to recover a physiological value of the zeroth component of the impedance spectrum.

#### 4.4.2 Verification

The accuracy of the Python implementation was initially assessed in terms of its ability to recover key characteristics of the impedance spectrum in the ascending aorta. These characteristics are given as the steep fall in modulus from the zeroth harmonic to a minimum at 3 Hz and a maximum at 7.5 Hz. The phase waveform is also expected to show a negative value at the lower frequencies with a change of sign at 3 Hz and fluctuation about zero radians at the higher frequencies (Avolio, 1980). Simulations performed with the pulse wave velocity (PWV) computed from the empirical fit relationship (Reymond *et al.*, 2009) were able to crudely match these characteristics with the minimum modulus occurring at approximately 3 Hz and maximum at 6 Hz. The key characteristics of the phase waveform were also recovered from the Python script using an empirical fit PWV (Figure 4.10). Studying the literature models in terms of the frequency of minimum and maximum also suggests an accurate implementation of the Python script as similar frequencies are reported with the different arterial networks and algorithms (Avolio, 1980; John, 2004; He *et al.*, 2012). A comparison of these literature impedance spectra are provided in He *et al.* (2012).

A more detailed comparison of the modulus and phase waveforms with the literature models, however, suggests the inaccurate implementation of the 1D model in the Python script (Figure 4.10). As the impedance spectrum of John (2004) most explicitly captures the key characteristics, its modulus and phase components are shown in all impedance plots as a benchmark spectrum for the Python implementation. The most notable difference in the impedance spectrum is the difference in modulus at the 2-6 Hz frequency range. With its relationship to the pressure and flow waveforms, the input impedance forms a key parameter in the 1D model and must therefore be computed accurately, consistent with the literature and the physiological data.

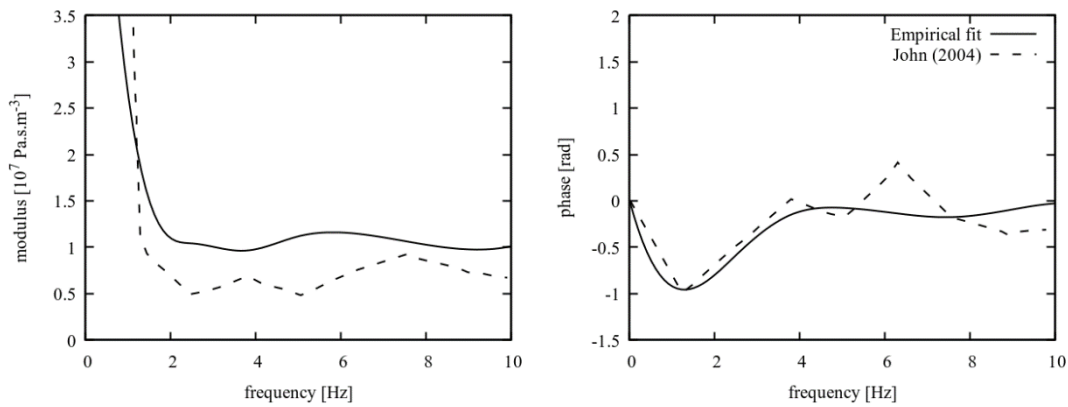


**Figure 4.10. Comparison of the impedance spectrum (a) modulus and (b) phase in the ascending aorta computed from the Python implementation and the forward algorithm of John (2004).** The pulse wave velocity was computed using the empirical fit relation proposed in (Reymond *et al.*, 2009). While the key characteristics of impedance are well-recovered, the difference in magnitudes of the modulus at higher frequencies suggest the inaccurate implementation of the Python script. John (2004) impedance spectrum data was extracted from John (2004) with permission using a plot digitiser tool available at <https://automeris.io/WebPlotDigitizer/>.

#### 4.4.3 Model sensitivity analysis

To understand the possible causes of difference in the impedance spectra, the modelling choices were examined in greater detail. A sensitivity to modelling choices has already been demonstrated in the literature as a simplified arterial network (He *et al.*, 2012) shows differences in the phase components when compared to complete cerebral vasculature models (Avolio, 1980; John, 2004). Again, the reader is referred to He *et al.* (2012) for this comparison of spectra as it is not reproduced here. The difference in phase between the studies could be illustrative of the results of non-physiological wave reflections seen in the models with an inadequate cerebral vasculature model (Westerhof *et al.*, 1969; Avolio, 1980).

As clear from the model implementation and its definition, the PWV is a key parameter in calculating the vessel impedance. The initial Python implementation used the PWV values computed from an empirical fit proposed by Reymond *et al.* (2009) as a similar model would need to be applied in the case of the mouse vasculature (Aslanidou *et al.*, 2016). The empirical fit of Reymond *et al.* (2009) works on an inverse relationship with the lumen diameter and was obtained using a fit algorithm of literature data. Alternatively, the PWV values can be computed from the Moens-Korteweg equation using vessel properties such as the wall thickness, stiffness and lumen radius. An assumption commonly used in the Moens-Korteweg equation is the approximation of the Young's modulus of the central, limb and peripheral vessels to 0.4, 0.8 and 1.6 MPa, respectively (Avolio, 1980; John, 2004; He *et al.*, 2012). While the Moens-Korteweg implementation of PWV shows the same inverse relationship with lumen diameter as the empirical fit, relatively large differences between the two implementations are found at the smaller vessels in the peripheral vasculature (Figure 4.11).

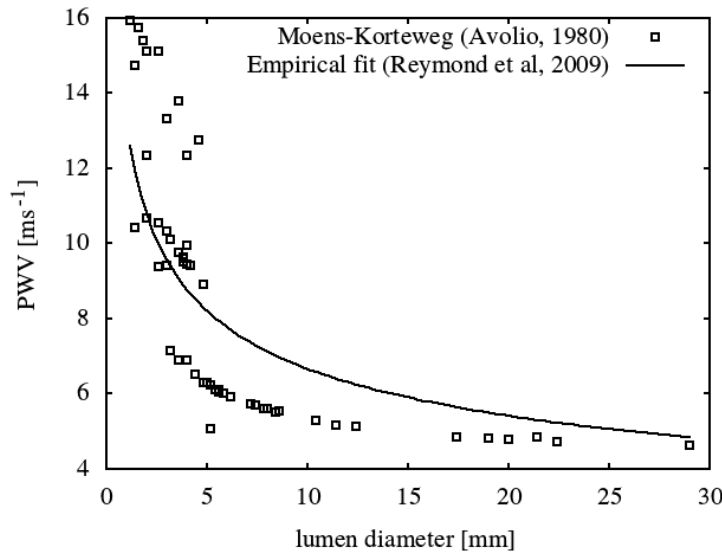


**Figure 4.11. Pulse wave velocities (PWV) in the vessels of the arterial network.** The empirical fit PWV was computed as a function of the mean lumen diameter in Reymond *et al.* (2009) to fit experimental data provided in the literature. The Moens-Korteweg PWV was computed using the fluid density and vessel radius, stiffness and wall thickness given in Avolio (1980).

As expected from the impedance spectrum, the pressure waveforms computed from the Python script also show a sensitivity to the PWV models with a difference of approximately 18 mmHg in the time-averaged component as well as differences in the amplitudes of each frequency component (Figure 4.13).

Considering the better degree of approximation obtained from the Moens-Korteweg PWV at the lower frequencies and its wide use in transmission line models, all following impedance calculations are performed using this calculation method. The pressure waveform computed from the Moens-Korteweg PWV still suggests the effect of an inaccurate implementation in the Python model ranging between 80 and 140 mmHg. The presence of these deviations from the physiological waveform suggests the effect of modelling choices to be elsewhere in the Python implementation.

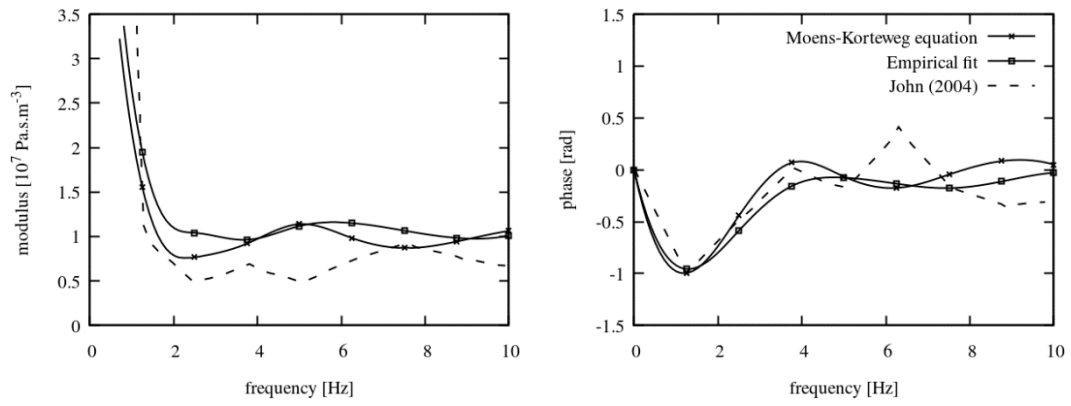


**Figure 4.12. Impedance spectrum (a) modulus and (b) phase in the ascending aorta using the empirical fit PWV and Moens-Korteweg PWV.** The difference in impedance between the PWV models shows a sensitivity to the model choices. Comparing the Moens-Korteweg PWV and John (2004) spectra, a factor of more than 2 difference at 5 Hz also suggests the effect of modelling choices elsewhere in the implementation of the Moens-Korteweg PWV model. John (2004) impedance spectrum data was extracted from John (2004) with permission using a plot digitiser tool available at <https://automeris.io/WebPlotDigitizer/>.

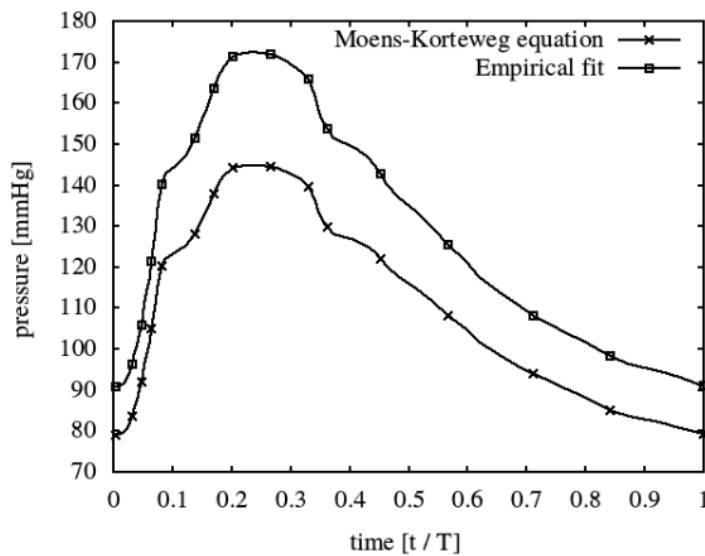


**Figure 4.13. Time-varying pressure computed in the ascending aorta from the Python implementation using the empirical fit PWV and Moens-Korteweg PWV.** The pressure waveform is calculated from the input impedance and the time-varying flow taken from John (2004). The different models of PWV show large differences in the resulting pressure waveform with a visible difference in the mean pressure and amplitude. The difference in mean pressure between the two implementations was approximately 18 mmHg.

Comparing the impedance moduli computed from the Liu *et al.* (1989) and Reymond *et al.* (2009) Windkessel models, a sensitivity to the treatment of peripheral vessels is shown with the most significant differences at 1.25 Hz and 3.75 Hz (Figure 4.14). Both implementations use a three-element Windkessel model with terminal resistance and capacitance. The Windkessel models of the Liu *et al.* (1989) study were designed to represent all upper and lower extremities in a T-tube model of the vasculature while the Reymond *et al.* (2009) study represents each terminal vessel with its own Windkessel model. The small differences in impedance at the higher harmonics despite the difference in the scale of represented vessels suggests that the choice of Windkessel parameters was not the cause of the significant errors shown in Figure 4.12 and Figure 4.13. The differences in the impedance modulus at 1.25 Hz and 3.75 Hz are reflected in the time-varying pressure waveform with a difference of approximately 25 mmHg in the peak pressure (Figure 4.15).

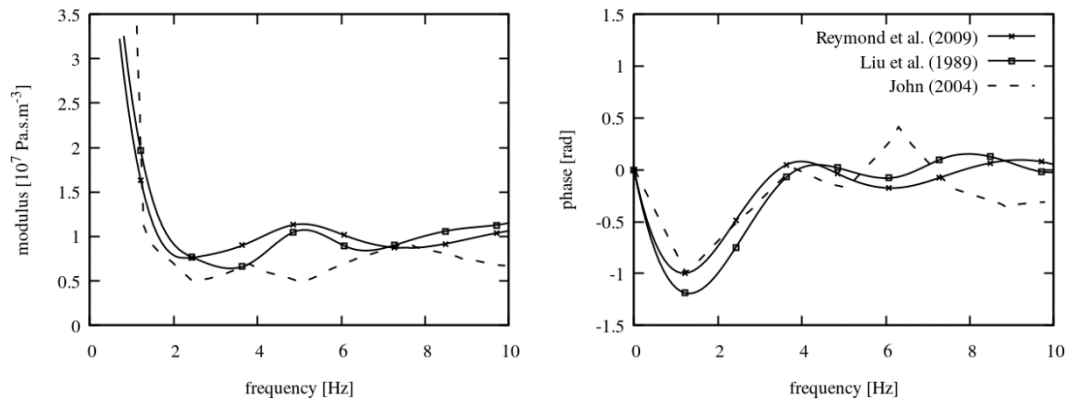


**Figure 4.14. Impedance spectrum (a) modulus and (b) phase in the ascending aorta computed using the Windkessel parameters of Liu *et al.* (1989) and Reymond *et al.* (2009).** Liu *et al.* (1989) use the Windkessel models to represent all upper and lower extremities in a T-tube model of the human vasculature while Reymond *et al.* (2009) represent each terminal vessel with its own Windkessel model. The most significant deviation between the two implementations occurs at 3.75 Hz with all other frequency components showing reasonable similarity. John (2004) impedance spectrum data was extracted from John (2004) with permission using a plot digitiser tool available at <https://automeris.io/WebPlotDigitizer/>.

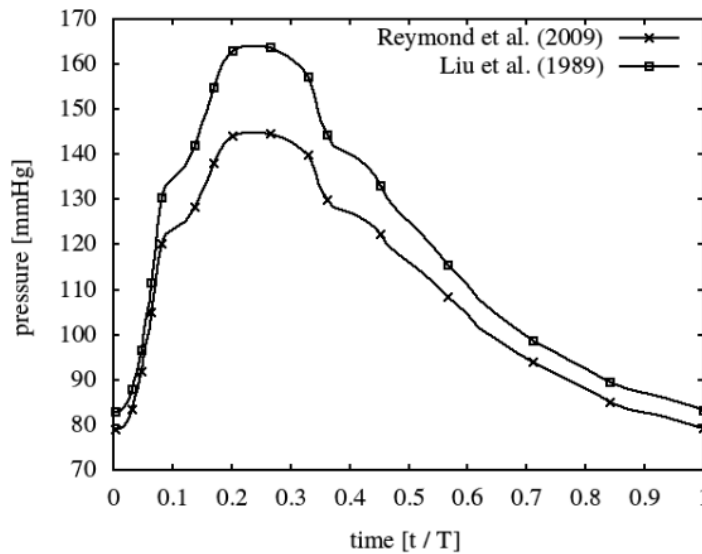
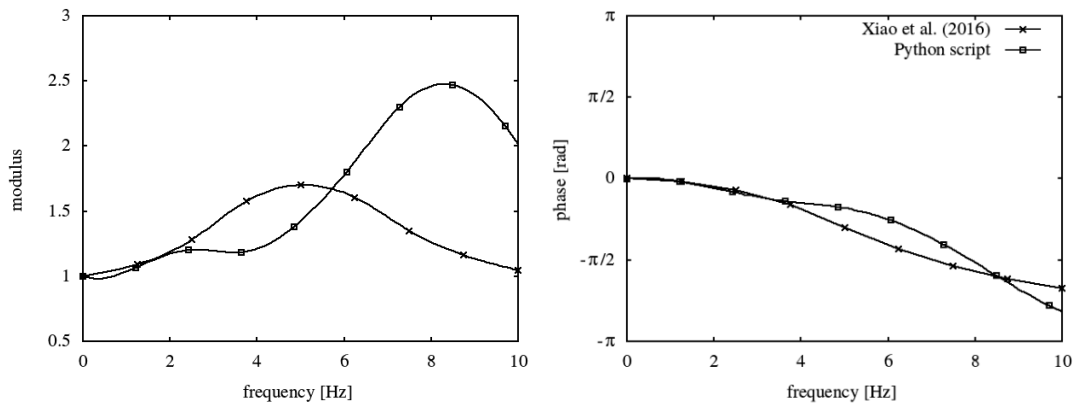


**Figure 4.15. Time-varying pressure computed in the ascending aorta from the Python implementation using the Windkessel parameters of Liu *et al.* (1989) and Reymond *et al.* (2009).** The sensitivity of the 1D model is shown in a difference of 25 mmHg in the peak pressure over a pulse period.



(a)



(b)

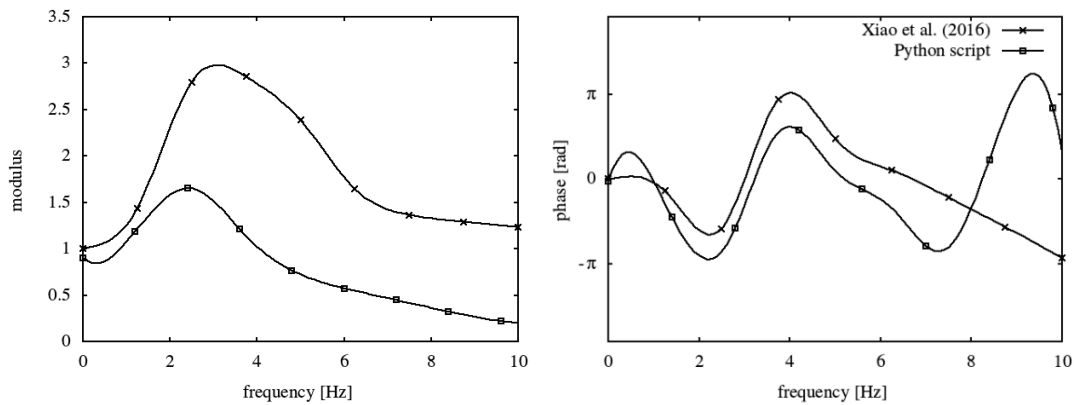


**Figure 4.16. Comparison of the transfer function computed from the source to the (a) carotid and (b) tibial artery in the Python script and Xiao *et al.* (2016).** The modulus (left) and phase (right) components of the transfer functions were computed using the Moens-Korteweg PWV and Reymond *et al.* (2009) Windkessel models at the peripheral vasculature. The trend of increasing phase delay with the distance from the heart is accurately recovered but the differences in the modulus waveform suggests the inaccurate implementation of the Python script. Xiao *et al.* (2012) transfer function data was extracted from Xiao *et al.* (2012) with permission using a plot digitiser tool available at <https://automeris.io/WebPlotDigitizer/>.

As an additional test of the Python implementation, a comparison of the transfer functions computed at the carotid and tibial arteries was also performed with those provided in the literature (de Sá Ferreira *et al.*, 2009; Huanguang Xiao *et al.*, 2016). Considering the elasticity of the vessels, the phase delay of the harmonic components is expected to increase with the distance from the source. While this property is

recovered from the Python script, the waveform of modulus components suggests inaccurate implementation (Figure 4.16). The flow waveforms computed at each vessel are also presented in Reymond *et al.* (2009) for further verification.

#### 4.4.4 Model discussion

A 1D transmission line model was implemented as a Python script to compute waveforms of pressure and flow for use as the boundary conditions of the lattice Boltzmann simulation. The Python model, while recovering the fundamental characteristics of the impedance spectrum, was unable to match the impedance modulus of the physiological spectrum and forward algorithm of John (2004). The modelling sensitivity study showed the impedance computed in the ascending aorta to be dependent on the pulse wave velocity and the treatment of the peripheral vessels. Variation of these parameters was also not able to accurately recover the physical characteristics of the healthy vasculature.

In addition to the sensitivity of the computed parameters to modelling choices, the possibility of a coding error in the Python implementation also exists. The presence of a coding error is suggested by the inability to recover the physical characteristics of the healthy vasculature with the variation of the parameters of the sensitivity study. Considering the complexity of the transmission line model and the arterial network, a substantial effort is required to identify the cause of this error. Due to the time limitations of the thesis, the cause of error will not be explored any further. Rather, it is suggested that the forward algorithm of John (2004) is employed where the zeroth, first and higher harmonic components of the impedance are treated separately.

It should be noted that, while this task will not be explored further in this study, the recovery of realistic pressure and flow waveforms is a key part of all blood flow simulation studies. Instead, the simulations of this thesis will impose a physiological waveform in the carotid artery measured in a healthy subject (Chapter 5) and explore the effect of the different boundary conditions on the wall shear stress (Chapter 6).

## 4.5 Dimensionless numbers

A key consideration in the unit conversion process, discussed in Section 3.1, is that dynamic similarity between the simulation and physical systems must be maintained by matching the relevant dimensionless numbers. The characteristics of blood flow in the arteries can be described entirely by the Reynolds number, Womersley number and Dean number (Ku, 1997). Following the geometry simplification, secondary flows are also neglected in the simulations performed in this thesis. As such, fluid flow is described only through the Reynolds number  $Re$  and Womersley number  $\alpha$ . The shear rate number  $N_{\dot{\gamma}}$  is also presented here given its relevance in non-Newtonian fluid flows.

The Reynolds number describes the ratio of inertial to viscous forces and is defined by

$$Re = \frac{uD}{\nu} \quad (4.13)$$

where  $u$  is the peak axial velocity,  $D$  is the pipe diameter and  $\nu$  is the kinematic viscosity.

The Womersley number is the ratio of pulsatile to viscous forces and is given by

$$\alpha = \frac{D}{2} \sqrt{\frac{\omega}{\nu}} \quad (4.14)$$

where  $\omega = 2\pi f = \frac{2\pi}{T}$  is the angular frequency computed in terms of the frequency  $f$  and pulse period  $T$ .

The shear rate number is a dimensionless number defined to indicate the importance of the shear thinning behaviour of the fluid (Gijssen *et al.*, 1999a). The parameter is expressed in terms of a characteristic shear rate  $\dot{\gamma}_c$  and  $\lambda$  is the characteristic time constant of the Carreau-Yasuda model (2.21):

$$N_{\dot{\gamma}} = \frac{\dot{\gamma}_c}{(1/\lambda)} \quad (4.15)$$

The characteristic shear rate is taken as the wall shear rate  $\dot{\gamma}_w$  computed from the wall shear stress  $\sigma_w$  and the Carreau-Yasuda viscosity limit  $\mu_{\infty}$

$$\dot{\gamma}_w = \sigma_w / \mu_\infty \quad (4.16)$$

Considering the Carreau-Yasuda model, the characteristic time constant defines the shear rate at the transition between the high and low viscosity limits. The physical interpretation of the shear rate number can then be thought of as the ratio of the peak shear rate  $\dot{\gamma}_w$  and the shear rate at the viscosity transition region. With this, the shear rate number indicates ‘how much’ of the viscosity transition is seen by the fluid. From this definition, it is clear that high shear rate number flows behave largely as a Newtonian fluid with viscosity  $\mu = \mu_\infty$ . Low shear rate number flows also behave as a Newtonian fluid with viscosity  $\mu = \mu_0$  while the non-Newtonian behaviour of the fluid is shown at intermediate shear rate numbers.

The parameters relevant to flow in the mouse and human common carotid arteries are given here as an example. Vessel radii for the mouse and human common carotid arteries were taken as 0.245 mm (Aslanidou *et al.*, 2016) and 3 mm (Reymond *et al.*, 2009), respectively. The viscosity parameters were taken at the lower asymptotic limit of the Carreau-Yasuda viscosity model as 3.265 mPa.s (Vogel *et al.*, 2003; Windberger *et al.*, 2003; Bernabeu *et al.*, 2014) and 3.5 mPa.s (Bernabeu *et al.*, 2013; Boyd *et al.*, 2007) for the mouse and human. The peak systolic velocity was estimated as  $0.7 \text{ ms}^{-1}$  in the human (Harloff *et al.*, 2013; Pomella *et al.*, 2017). The same velocity was assumed in the mouse given the consistency expected from allometric scaling laws (Weinberg and Ethier, 2007) and experimental measurements (Khir *et al.*, 2001; Lacy *et al.*, 2001). The mouse and human heart rates were taken as 480 (Aslanidou *et al.*, 2016) and 75 (Reymond *et al.*, 2009) beats per minute. The Reynolds number in the mouse and human are computed from these parameters as 105 and 1200, respectively. The Womersley numbers are also computed from these parameters as 0.96 and 4.94, respectively.

## 4.6 Conclusions

This chapter describes the development, implementation and verification of the additional models required in the study of blood flow with relevance to atherosclerosis. With this, it is possible to compute the local haemodynamic forces in different vessel geometries for the comparison of the WSS signal between disease models, and also

between species. Using this simulation tool, the haemodynamic conditions in regions coincident with different plaque types are induced can be studied for the differences in wall shear stress at plaque initialisation. Following the discussion presented in Chapter 1, the WSS signal is investigated here as an explanation of the differences in plaque characteristics found between species models of atherosclerosis.

Using the base lattice Boltzmann method of Krüger (2012), additional modules were developed as part of this thesis to accurately represent blood as a non-Newtonian fluid, compute the wall shear stress from the flow field, and to calculate and implement physiological flow conditions in the simulation geometry. Comparison of the module outputs to the literature, analytical and numerical solutions showed the accurate implementation of the wall shear stress and viscosity model while the 1D model was unable to recover the required flow conditions.

Numerical solutions of the Carreau-Yasuda viscosity model showed the Newtonian viscosity assumption to be valid in assessing the WSS in steady pipe flows. Considering the local variations in shear rate in regions of bifurcation and constriction, however, the validity of this Newtonian viscosity assumption is still not clear. Simulations of the tapering perivascular cast and tandem stenosis geometry performed in Chapter 5 will, therefore, use the Carreau-Yasuda viscosity model. Following the discussion in Chapter 1, it is clear that the time-varying components of the WSS signal holds importance in the inflammatory response of endothelial cells and atherosclerosis. The effect of the viscosity model assumption with a pulsatile flow waveform is, therefore, characterised in Chapter 7.

A key note in the wall shear stress calculation is the zeroth order error term resulting from the solid boundary treatment method. As discussed in Sections 3.2 and 4.2, these errors are considered to be negligible when accounting for the required idealisation of disease model geometries. Also, due to inaccuracies in the flow conditions recovered from the 1D model, the waveforms of pressure will be approximated from the healthy vessels in the following chapters. An exploration of the effects of the flow conditions will also be performed by approximating the pressure waveform to a simple sinusoidal profile (Chapter 6).

## Perivascular device models of atherosclerosis

---

### Abstract

The wall shear stress has been shown to be a key regulator of endothelial activity (Malek *et al.*, 1999; Cunningham and Gotlieb, 2004; Davies, 2009; Chiu and Chien, 2011) with the expression of inflammatory markers in human and porcine endothelial cells also showing sensitivity to the wall shear stress frequency composition (Himburg *et al.*, 2007; Feaver *et al.*, 2013). An understanding of the local haemodynamic environment is, therefore, needed as the probability of cap disruption is dependent on the plaque compositions resulting from the inflammatory response (Virmani *et al.*, 2000; Slager *et al.*, 2005a, 2005b; Schwartz *et al.*, 2007; Bentzon *et al.*, 2014). The current chapter explores the hypothesis that the different plaque compositions shown in mouse models of atherosclerosis occur in regions experiencing different frequency compositions of the wall shear stress signal.

Simulations were performed here in geometries approximating the mouse models of Cheng *et al.* (2006), Chen *et al.* (2013) and Mohri *et al.* (2014) considering the variety of plaque compositions found in the different regions of each model. Cheng *et al.* (2006), for example, induced the formation of plaques resembling the human thin-cap fibroatheroma and the highly-cellular stable-looking plaque while Chen *et al.* (2013) showed the development of plaques with intraplaque haemorrhage, rupture and luminal thrombosis. Wall shear stress signals computed from the simulations were analysed in terms of their frequency compositions and showed variation of the phase of the first harmonic component along the length of all geometries. A key result of this study is the decrease in the wall shear stress signal zeroth and first harmonic amplitudes of all mouse models relative to the control vessel simulations. While the modulus components of the higher harmonics ( $n > 1$ ) were similar between regions showing thin-cap fibroatheromas in the Cheng *et al.* (2006) and Chen *et al.* (2013)

models, consistency in the higher harmonics along the Chen *et al.* (2013) ligation geometry suggests this to not be the sole factor with relevance to plaque composition. Correlations in the moduli of the frequency components were also not found when comparing the signals in regions showing a stable-looking plaque composition from the Cheng *et al.* (2006) and Chen *et al.* (2013) models. This suggests a lack of comparability between the models.

The key result of this simulation study is the lack of comparability between the Cheng *et al.* (2006) and Chen *et al.* (2013) mouse models. Despite the similarities in mouse genetic background, varied plaque compositions were found between the studies. This conclusion then highlights the significance of mechanical differences between the models.

## 5.1 Introduction

A number of disease models have been studied in the literature in which the flow velocities have been manipulated with the use of perivascular devices and ligations. Manipulation of the vessels was performed to achieve controlled patterns of wall shear stress (WSS) and mechanical stress and showed a dependence of the plaque composition on the nature of these patterns. Winkel *et al.* (2015) provide an excellent review of these devices along with descriptions of the resulting vessel pathologies.

By placing a tapering perivascular cast around the mouse carotid artery, Cheng *et al.* (2006) induced the formation of plaques resembling the lipid-rich thin-cap fibroatheroma (TCFA) in regions upstream of the cast while stable-looking plaques were found in the downstream region. These regions coincide with areas of low shear stress and oscillatory shear stress, respectively. The haemodynamic conditions and the resulting plaque compositions shown in Cheng *et al.* (2006) have been reproduced in several studies; both by the Krams research group (Cheng *et al.*, 2007; Segers *et al.*, 2011; Harrison *et al.*, 2013; Mohri *et al.*, 2014; Pfenniger *et al.*, 2012, 2015; Seneviratne *et al.*, 2015; Pedrigi *et al.*, 2016) and others (Wenning *et al.*, 2014; Fraga-Silva *et al.*, 2015).

The localisation of vulnerable-looking and stable-looking plaques shown in Cheng *et al.* (2006) has also been reiterated by the quantification of macromolecule uptake as a marker of lipid deposition: with a higher uptake in the region immediately upstream of the cast edge compared to the disease site downstream of the cast (Mohri *et al.*, 2014). Interestingly, Mohri *et al.* (2014) also show that reversal of the cast direction produced no statistically significant difference between the uptake peaks at either end of the cast. The tandem stenosis model of Chen *et al.* (2013) also produced different plaque compositions in each region of the vessel including a plaque showing disruption of the fibrous cap. Other regions of the vessel showed plaques with compositions resembling the TCFA and the stable, highly cellular plaque. Reduction of the flow velocity in the partial ligation model also resulted in large complex plaques along the length of the carotid artery (Nam *et al.*, 2009).

The models mentioned above have previously been analysed in terms of the time-averaged WSS showing the coincidence of plaques to regions of low and oscillatory shear stress (Section 2.3). There is, however, a loss of information in the time-averaging process of the current metrics. This loss of information may be reflected in the occurrence of different plaque types in the regions of the vessel showing similar values in the time-averaged metrics. While capturing all temporal and spatial details of the WSS waveform, the frequency composition of the WSS signal has also shown significance to inflammatory markers expressed on the endothelial surface (Himburg *et al.*, 2007; Feaver *et al.*, 2013).

#### Hypothesis and aims:

Considering the role of the inflammatory process in disease development and plaque composition, the current chapter explores the hypothesis that plaques resembling the human TCFA and stable-looking compositions are shown in mouse models of atherosclerosis in regions experiencing different time-varying waveforms of the WSS signal.





**Figure 5.1. Approximations of the (a) Cheng *et al.* (2006), (b) Mohri *et al.* (2014) and (c) Chen *et al.* (2013) common carotid arteries.** The flow direction is from left to right. The tapering casts of the Cheng *et al.* (2006) and Mohri *et al.* (2014) studies reduce the diameter to half of that of the uncasted vessel segments over the length of one vessel diameter. The ligatures of the Chen *et al.* (2013) have diameters equal to a third of the non-ligated vessel.

The hypothesis was addressed in terms of the following aims:

- 1) Are there similarities/differences in the stress waveform between regions showing different plaque compositions in each model?
- 2) Are there similarities/differences in the stress waveform between regions showing similar plaque composition between models?

## 5.2 Methods

To better understand the local haemodynamics in regions with different plaque compositions, simulations have been performed in geometries approximating the mouse carotid artery with a perivascular cast device placed in the conventional (Cheng *et al.*, 2006) and the reversed directions (Mohri *et al.*, 2014). Simulations were also performed in an approximation of the mouse carotid artery with a tandem stenosis by ligation placement (Chen *et al.*, 2013). The geometries are shown in Figure 5.1.

### 5.2.1 Simulation setup

All simulations were performed in 3D using the D3Q19 lattice structure (Section 3.1). The dimensionless numbers governing fluid flow were set using the physiological conditions in the mouse carotid artery. The calculation of the Reynolds and Womersley

numbers is given in Section 4.5. The Reynolds and Womersley numbers were equal to 105 and 0.96, respectively. The system size was chosen following a mesh independence study (Section 5.3.1) such that the vessel radius was represented by 20 lattice nodes. This gives a lattice resolution of  $\Delta x = 12.25 \mu\text{m}$ . The asymptotic lower limit of the lattice Boltzmann relaxation parameter was set to  $\tau_\infty = 0.575$ . The dimensionless numbers were then used to compute a simulation time step of  $\Delta t = 1.15 \mu\text{s}$ . The lattice resolution and relaxation parameter lower limit were chosen such that the peak axial velocity in a simple pipe geometry would not exceed 0.07. These considerations were made in order to minimise error terms created in recovering the Navier Stokes equations from the lattice Boltzmann equation (Section 3.1.4).

The parameters of the mouse Carreau Yasuda viscosity model (2.21) were obtained from Bernabeu *et al.* (2014) where a least squares regression fit was performed on mouse viscosity data provided in Vogel *et al.* (2003) and Windberger *et al.* (2003). These parameters are given as follows:

$$\mu_0 = 14.49 \text{ mPas}, \mu_\infty = 3.265 \text{ mPas}, \lambda = 0.1839 \text{ s}, m = 0.5864, a = 2.707.$$

Following unit conversion, the lattice Boltzmann relaxation parameter was set according to the effective viscosity model to range between  $0.59 < \tau < 0.90$ . Viscosity model parameters were fed into the Python script discussed in Section 4.4 to compute values of the local viscosity as a function of the first-order momentum flux tensor.

The no-slip boundary condition was specified in all simulations using the standard bounceback approach at the geometry walls (Section 3.2). Simulations of the perivascular cast models in Cheng *et al.* (2006) and Mohri *et al.* (2014) were performed with the use of periodic boundaries at the inlet and outlet alongside a body force term imposed at all lattice sites. Simulation of the tandem ligation model, on the other hand, was performed using the regularisation scheme discussed in Section 4.1 with the density deviation term  $\rho'$ . The inlet and outlet density conditions were verified when considering the negligible increase in total system mass over the simulation (Krüger *et al.*, 2009).

Periodic boundary conditions were not employed in the tandem ligation model as the distance between the ligations is greater than the flow development length. The use of

a body force term in this case would recover all flow features before reaching the distal ligation in the geometry, “hiding” any flow effects caused by the proximal ligation. Inlet and outlet boundary conditions are, therefore, more representative of flow behaviour in the tandem ligation model than simulations with periodic boundary conditions.

The pressure waveform measured in the healthy mouse carotid artery was extracted from Artoli and Sequeira (2006) using the plot digitizer function available online at <https://automeris.io/WebPlotDigitizer/>. A curve-fitting method was used to obtain the waveform in terms of a Fourier series in the first eight harmonics. Higher harmonic components were omitted because of their minimal contribution to the accuracy of approximation. The Fourier series was then implemented as the body force term or density fluctuation in the periodic or regularisation schemes, respectively.

### 5.2.2 Simulations performed

The control vessel was simulated as a straight pipe geometry with constant radius. Simulations were also performed in the conventional (Figure 5.1a) and reversed (Figure 5.1b) orientations of the perivascular cast device approximating the geometry to a tapering diameter over the length of the cast, with the remaining length being modelled as a straight pipe with constant diameter. The cast length was taken to be equal to one diameter while tapering to a cross-sectional area of 25% of the control vessel. The simulation of the conventional and reversed cast directions was achieved by reversing the direction of the body force term. Simulations were also performed at a number of lattice sizes as part of a mesh independence study.

The tandem stenosis geometry (Figure 5.1c) was studied by approximating the geometry to a straight channel with sinusoidal constrictions at the positions of ligation. The wavelength of the constriction profile was set to one diameter while reducing the cross-sectional area to 11% of the control vessel at the profile peak. As mentioned above, all simulations were performed with dimensionless numbers approximating the flow conditions in the healthy mouse carotid artery. The flow direction is shown in all results from left to right with model geometries placed in the figure inset where necessary.

As discussed in Section 3.1, simulations were terminated once the velocity profile measured at the geometry axial centre had converged to the profiles measured in the previous pulse period using equation (3.14). The convergence criteria for this termination event was set to  $10^{-5}$ . Once the criteria had been satisfied, the simulation would run for one more pulse period to compute and write all desired observables. Frequency analysis of the wall shear stress signal was performed on the axial component of the circumferentially averaged traction vector (Section 2.4).

## 5.3 Results

The regions of each mouse model of atherosclerosis were analysed in terms of the circumferentially-averaged traction vector, both in relation to the time-averaged shear metrics and to its instantaneous value over the pulse period. A comparison of the frequency composition of the instantaneous values was also performed to identify any potential correlations between the time-varying nature of the wall shear stress and the plaque composition found in the region.

### 5.3.1 Mesh independence

A mesh independence study was performed here to identify the optimal lattice resolution for further simulations. Here, the term “optimal” refers to the balance of accuracy and computational time. The mesh resolution was improved in order to minimise discretisation errors and increase simulation accuracy. The distance between the downstream cast end and the point of peak OSI was monitored in simulations to show mesh independence at a lattice resolution of  $\Delta x = 12.25 \mu\text{m}$  (Figure 5.2). This resolution was used in all simulations of the current chapter.

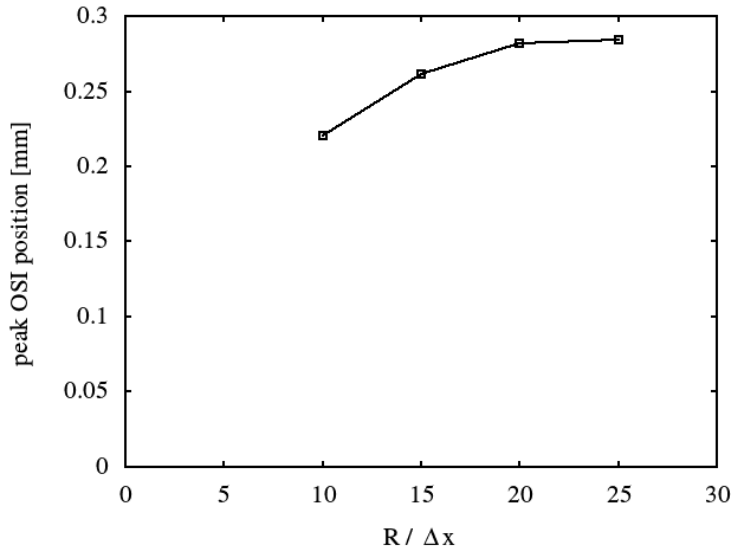


**Figure 5.2. Mesh independence study using the distance from cast end to the position of the peak oscillatory shear index (OSI) value.** Simulations were performed in the conventional direction perivascular cast geometry with a range of lattice resolutions showing convergence of the solution at  $R / \Delta x = 20$ .

### 5.3.2 Localisation metrics

#### Control vessel

The time-averaged wall shear stress (TAWSS) in the control vessel was computed as 15.76 Pa, matching values measured experimentally in Cheng *et al.* (2006) in the contralateral carotid artery. Following expectations, near-zero values of the oscillatory shear index (OSI) and relative residence time (RRT) were also found in the control vessel. For comparison with the literature, the Reynolds number is computed here in terms of the mean axial velocity at peak systole. A Reynolds number of 51 was approximated from the cross-sectionally averaged velocity field. The velocity field was assessed at the peak inflow velocity at  $t/T = 0.38$  where  $t$  is the simulation time and  $T$  is the period length. Pedrigi *et al.* (2016) report a Reynolds number of 40. The small difference in the simulation and literature Reynolds numbers may be attributed to variability between animals. The approximate agreement found between the Reynolds number and wall shear stress and their values reported in Pedrigi *et al.* (2016) and Cheng *et al.* (2006) respectively then suggests the accurate implementation of the simulation model.

### Conventional direction perivascular cast

The results discussed here were computed for a Reynolds number of 28 following the same procedure as in the control vessel. The regions of high, low and oscillatory shear stress identified in Cheng *et al.* (2006) are evident from the TAWSS and oscillatory shear index (OSI) plots (Figure 5.3). It should be noted that the peak value of OSI is due to the near-zero wall shear stress at the cast end and is considered to be an artefact of the geometry idealisation at the sharp downstream cast boundary. The peak RRT at the cast end is also attributed to this OSI value given equation (2.14).

The lowered Reynolds number in comparison with the control vessel indicates a reduced flow rate as suggested in Cheng *et al.* (2006). Following this, a “low” shear stress region was observed upstream of the tapering cast with the TAWSS computed here as 9.18 Pa. This also compares favourably with the value of 10 Pa reported from the Doppler ultrasound measurements of Cheng *et al.* (2006). Constriction of the vessel to a diameter half of that of the control vessel leads to fluid acceleration along the length of the cast in a “high” shear stress region. Simulations performed here show an approximately five-fold increase in the TAWSS over the length of the constriction. Fluid acceleration at the downstream end of the cast seen in the velocity field results in flow separation immediately downstream of the device (Figure 5.4). The separation and recirculation in the downstream region lead to low TAWSS with negative values of the velocity vector axial component along with negative values of the traction vector axial component. The region downstream of the cast is classified as the “oscillatory” shear stress region. The change of direction of the traction vector axial component during the pulse period occurs only at the point of peak OSI found at the end of the recirculation region. Flow then reverts to the direction of the imposed body force. Given the simplicity of the profiles of TAWSS and OSI and the definition of the metric (2.14), the RRT simply mirrors the features of the OSI.

As a method of standardising the length of the recirculation region, the flow behaviour is quantified by the distance between the downstream cast end and the point of peak OSI. The length of this region was computed as 0.282 mm in the conventional direction tapering cast geometry.

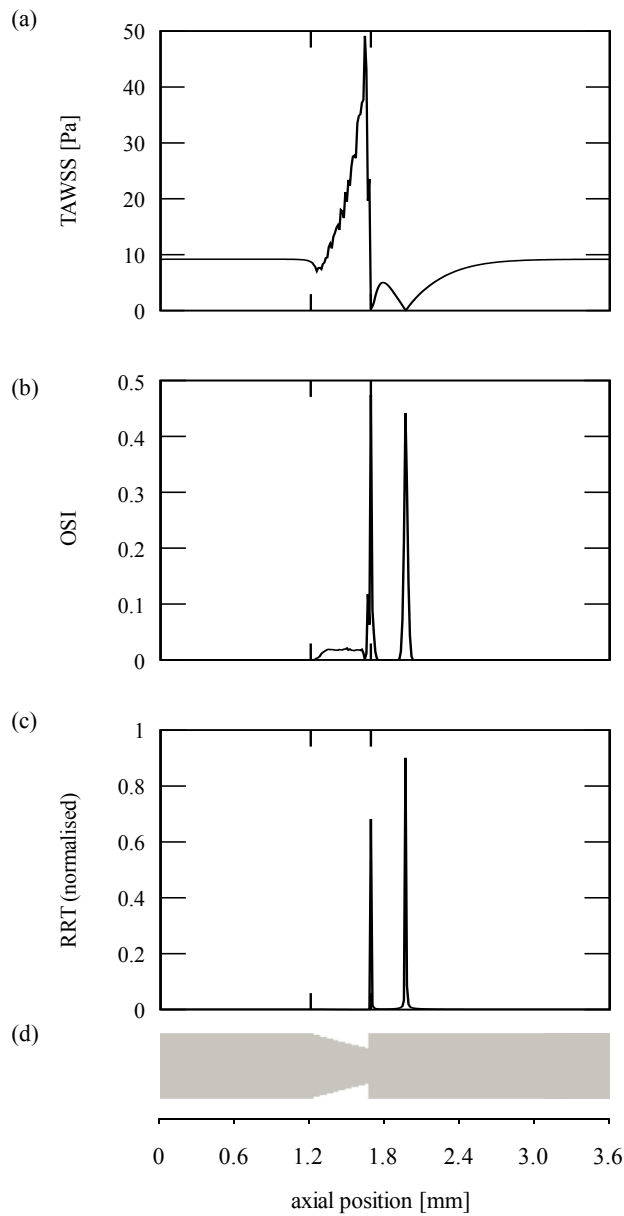


**Figure 5.3. Distribution of the (a) time-averaged wall shear stress (TAWSS), (b) oscillatory shear index (OSI) and (c) relative residence time (RRT) metrics in the (d) conventional direction perivascular cast geometry.** The flow direction is given from left to right. The TAWSS computed in the control vessel is 15.76 Pa. The regions of “high”, “low” and “oscillatory” shear stress can be identified from the shown metrics. Cheng *et al.* (2006) discuss the occurrence of the vulnerable-looking and stable plaque types in the low and oscillatory shear regions along with the absence of plaque formation in the high shear region suggesting a dependence of plaque composition on the pattern of fluid shear stress.

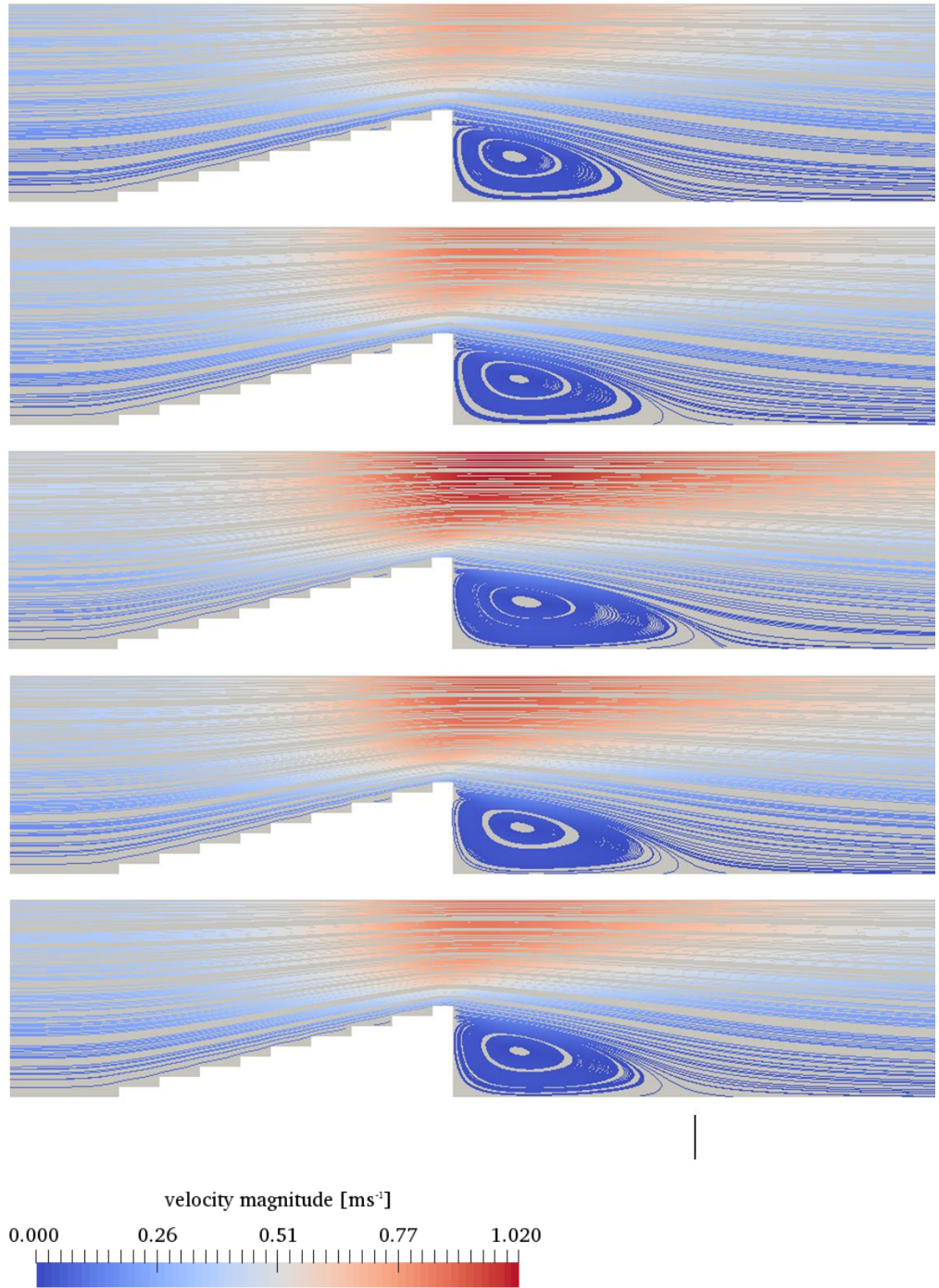


**Figure 5.4.** Time evolution of the velocity field along a segment of the conventional direction perivascular cast with the solid line indicating the axial position of the peak OSI. Flow direction is from left to right. Velocity streamlines are shown at  $t/T = 0.00, 0.20, 0.38, 0.6, 0.8$  (descending figures) where  $t$  is the simulation time and  $T$  is the period length. The peak OSI indicates the position at which the traction vector changes direction over the pulse period with flow reverting to the direction of the imposed body force after this point. The distance from the downstream cast end to the point of peak OSI was computed as 0.282 mm.



### Reversed direction perivascular cast

The results discussed here were computed from the velocity field for a Reynolds number of 29. Consistency between the simulation Reynolds numbers of the reversed and conventional direction tapering casts is due to the geometries have the same diameter constriction. This means that flow in the geometry experience the same flow resistance. The distributions of the time-averaged metrics are shown in Figure 5.5. The lower Reynolds number compared to the control vessel again indicates a low flow rate as a result of the constriction and results in a low TAWSS value. The TAWSS upstream of the region of cast placement was computed as 9.38 Pa compared to 15.76 Pa computed in the control vessel. Fluid acceleration due to the constriction results in elevated shear stress at the entrance region of the cast with a seven-fold increase in the TAWSS. The time-averaged value then stabilises quickly after the downstream cast end as the velocity field also recovers to the pre-constriction state. The peak OSI and RRT values are considered to be artefacts of the geometry idealisation as they occur at the sharp boundary of the cast. It is then clear that there is no “oscillatory” shear stress region considering the low values of OSI (Figure 5.5). This can be seen from the velocity field as fluid flow remains attached to the wall and there is no change of direction of the velocity vector along the length of the geometry (Figure 5.6). The absence of a recirculation region forms a key result of the simulation as it suggests an entirely different flow behaviour than in the conventional direction tapering cast model.

The decrease in TAWSS immediately upstream of the cast device is also a result of the geometry idealisation at the sharp upstream cast boundary shown by the absence of this feature in the Mohri *et al.* (2014) CFD study. The magnitudes of peak wall shear stress in the Mohri *et al.* (2014) CFD study of the conventional and reversed directions, however, suggest an incorrect methodology in their study with values in excess of 250 Pa. Theoretical predictions of the wall shear stress in a 50% diameter constriction suggest an eight-fold increase in the wall shear stress where Mohri *et al.* (2014) show a 25-fold increase.

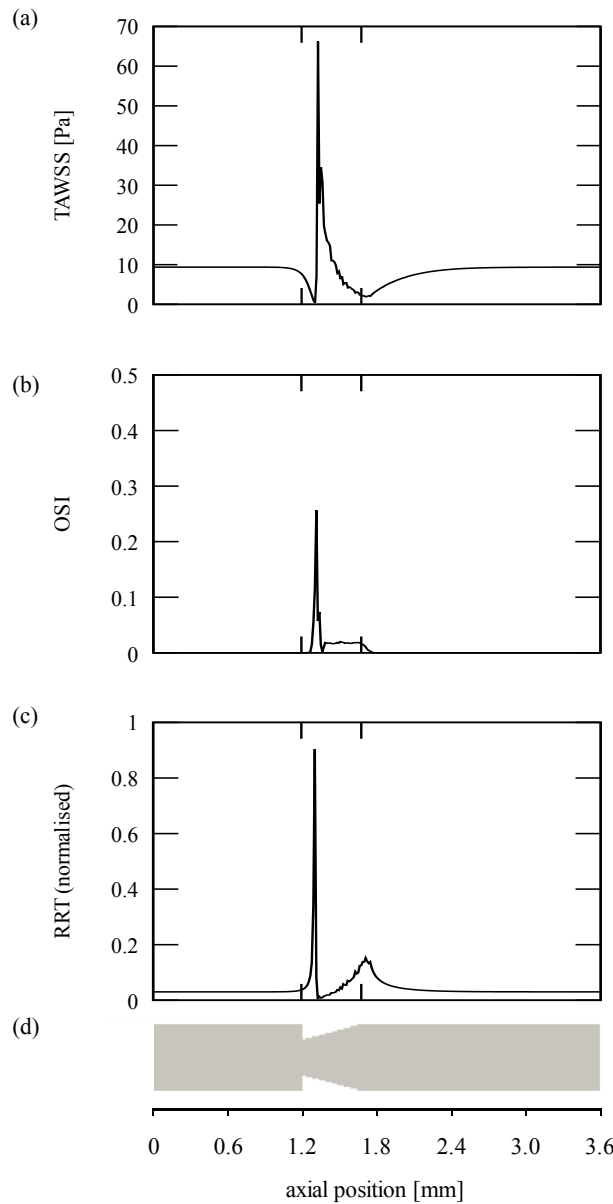


**Figure 5.5. Distribution of the (a) time-averaged wall shear stress (TAWSS), (b) oscillatory shear index (OSI) and (c) relative residence time (RRT) metrics in the (d) reversed direction perivascular cast geometry.** The flow direction is given from left to right. The time-averaged wall shear stress (TAWSS) computed in the control vessel is 15.76 Pa. The peak OSI value again occurs at the sharp cast boundary as a result of the geometry idealisation and so is neglected. The OSI plot then shows no “oscillatory” region as seen in the conventional direction cast geometry. Mohri *et al.* (2014) showed no significant relationship between macromolecule uptake and the regions of the vessel.

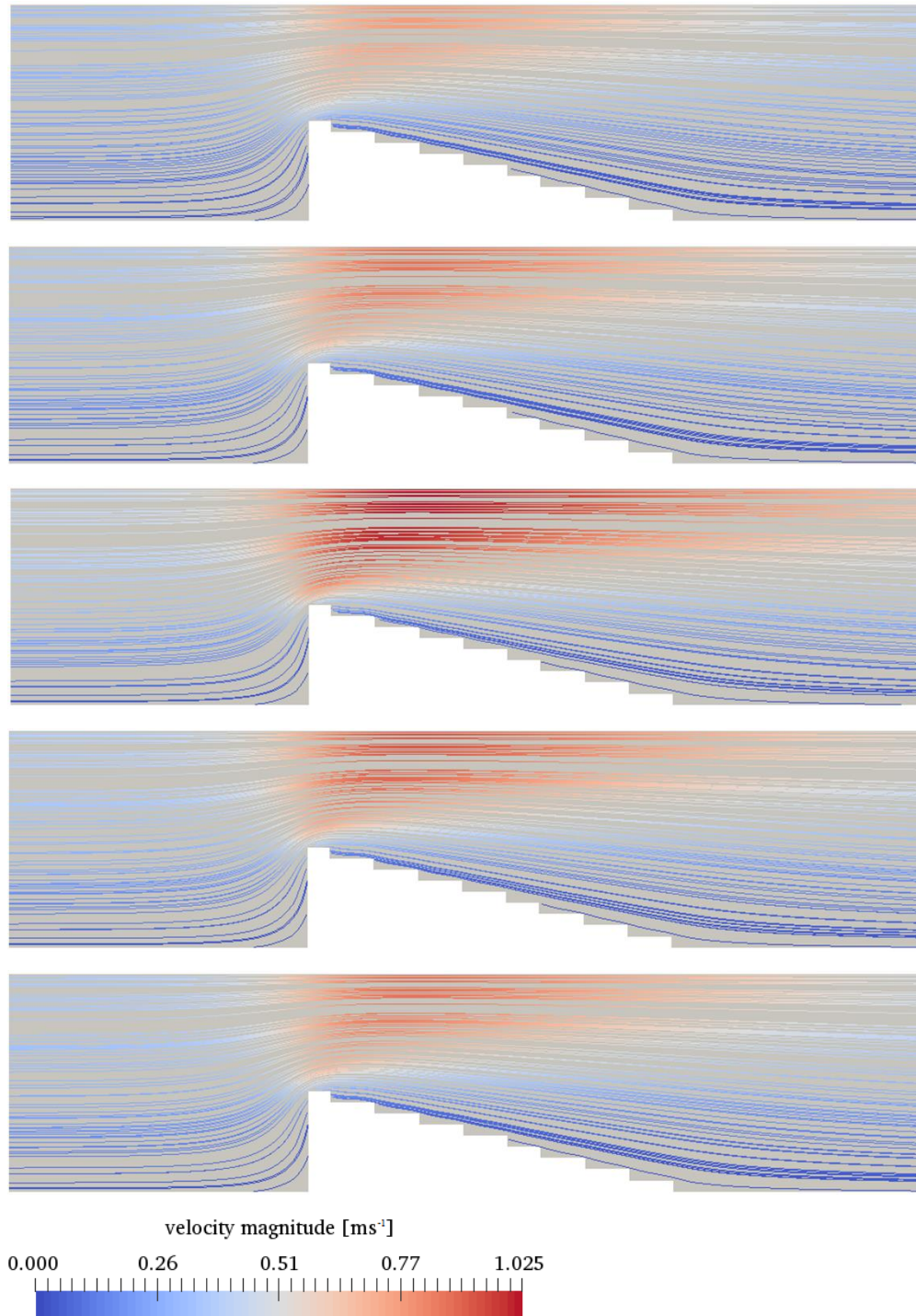


**Figure 5.6. Time evolution of the velocity field along a segment of the reversed direction perivascular cast.** Flow direction is from left to right. Velocity streamlines are shown at  $t/T = 0.00, 0.20, 0.38, 0.6, 0.8$  (descending figures) where  $t$  is the simulation time and  $T$  is the period length. The streamlines show an acceleration phase at the cast throat and no region of flow separation as expected of the geometry.

### Tandem stenosis

The Reynolds number computed from the velocity field in the tandem stenosis geometry is 8. This indicates a significant resistance to flow when compared to the Reynolds number of the control vessel and may be attributed to the vessel ligation to a diameter one-third of that of the control vessel in two locations along the geometry. The pressure drop across the ligations is also greater than that across the tapered cast geometry, explaining the smaller Reynolds number. The wall shear stress was computed in the non-ligated regions as 2.56 Pa with an approximately twenty-fold increase in magnitude occurring at the peak constriction (Figure 5.7). Drops in the TAWSS were found in the regions immediately upstream and downstream of the constriction profiles. Considering the magnitude of the wall shear stresses reported in Chen *et al.* (2013) and those known to occur in the healthy mouse vessel, the CFD simulations performed in the Chen *et al.* (2013) study are also assumed to be incorrect reporting a peak wall shear stress at systole of 1 Pa at the ligation throat.

The axial component of the traction vector showed a small region of recirculation downstream of each ligation. This was reflected in the velocity field taken at peak inflow velocity (Figure 5.8). The peaks in OSI and RRT found immediately upstream of each ligation were attributed to fluctuations in the circumferential components of the tangential traction vector and the low TAWSS (Figure 5.7). The flow field around each ligation was identical. This suggests that periodic boundary conditions may have been used in this simulation rather than the regularisation scheme.

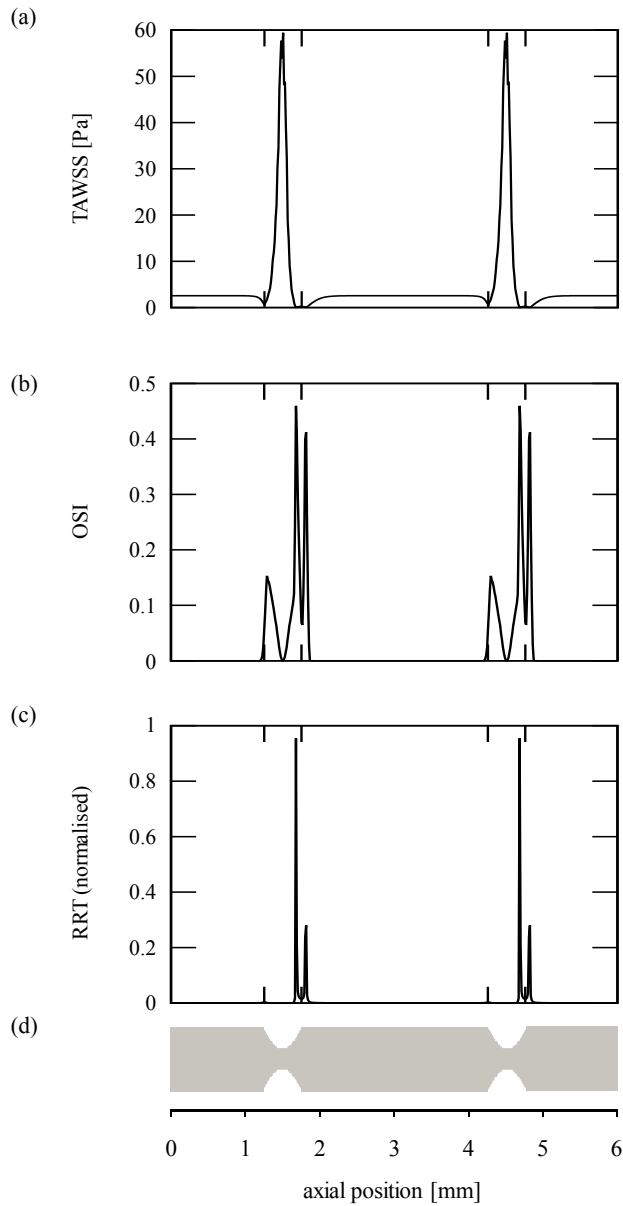


**Figure 5.7. Distribution of the (a) time-averaged wall shear stress (TAWSS), (b) oscillatory shear index (OSI) and (c) relative residence time (RRT) metrics in the (d) tandem stenosis geometry.** The flow direction is given from left to right. The time-averaged wall shear stress (TAWSS) computed in the control vessel is 15.76 Pa. Very low values of the TAWSS were found in the non-ligated regions of 2.56 Pa. Chen *et al.* (2013) demonstrated the occurrence of various plaque types in these regions including a plaque showing disruption of the fibrous cap.

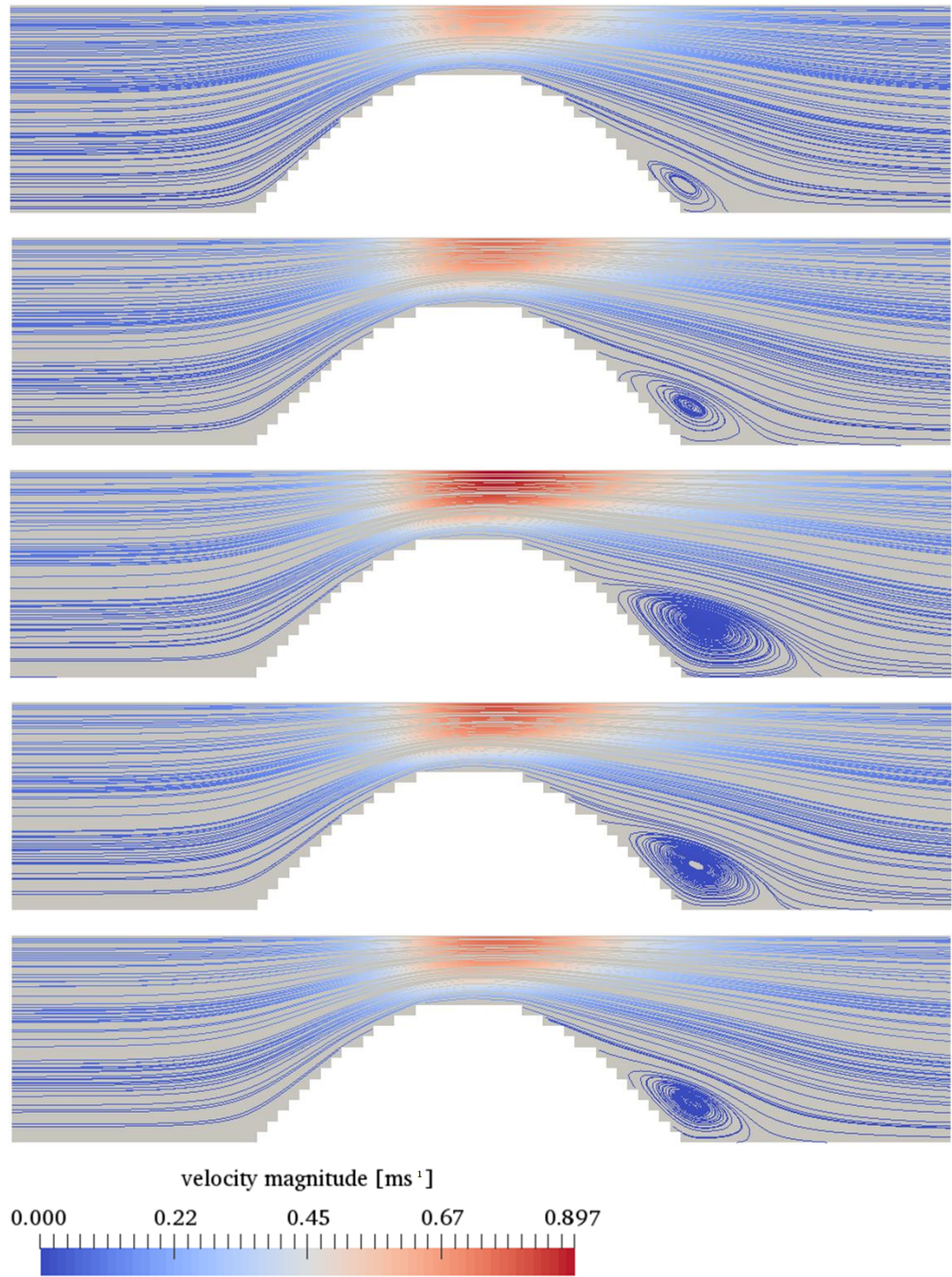


**Figure 5.8. Time evolution of the velocity field along a segment of the tandem ligation geometry.** Flow direction is from left to right. Velocity streamlines are shown at  $t/T = 0.00, 0.20, 0.38, 0.6, 0.8$  (descending figures) where  $t$  is the simulation time and  $T$  is the period length. The vectors suggest fluid acceleration at the point of maximum ligation and a small region of recirculation immediately downstream. The flow field is shown only around the proximal ligation as the velocity profile in regions downstream of the proximal and distal ligations were identical.

### 5.3.3 Frequency composition

A key note in the following results is that only the axial component of the traction vector was studied in terms of its frequency composition. This analysis is valid here for the simulated geometries considering the axial symmetry property and purely axial direction of the inflow driving force terms. The analysis of the traction vector axial component and omission of its circumferential component will be discussed further in Section 2.4. The reader is also referred to Section 2.4 for a description of the Fourier transform amplitudes and phases.

#### Control vessel

As expected from the geometry, the frequency composition of the wall shear stress signal was constant along the length of the control vessel. Variation of the wall shear stress signal is shown in Figure 5.9 with the first harmonic amplitude equal to 2.47 Pa. A key note in the wall shear stress signal is also that its normalised frequency content is largely similar to that of the input pressure waveform.

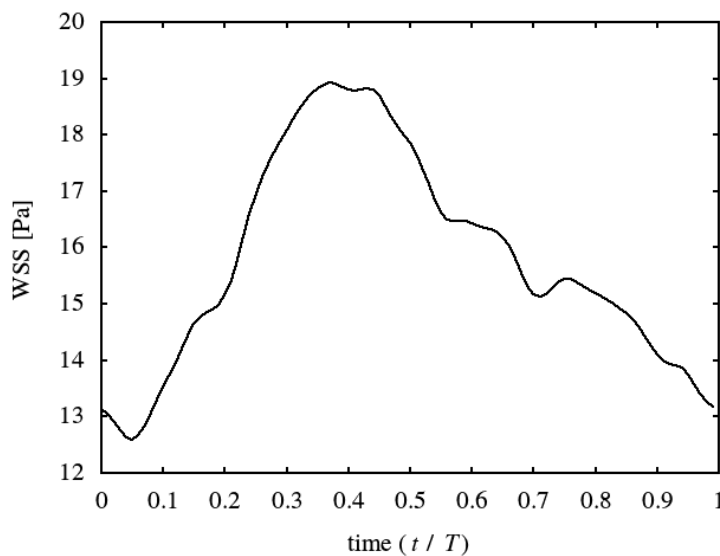


**Figure 5.9. Time varying waveform of wall shear stress (WSS) over a single cardiac cycle computed from control vessel simulations.** The waveform was normalised in time  $t$  over the period  $T$ . Negligible differences were found between the normalised frequency content of the input pressure and output wall shear stress signals.

### Conventional direction perivascular cast

The distribution of the first harmonic amplitude (Figure 5.10) shows a largely similar behaviour to that of the TAWSS (Figure 5.3). The amplitude of the first harmonic in the upstream region was computed as 1.21 Pa also showing an approximately seven-fold increase to the peak value along the length of the cast. The axial position of 3.5 mm shows the recovery of the wall shear stress zeroth (equivalent to the TAWSS) and first harmonic components to values present in the low shear region.

The phase component immediately downstream of the cast indicates a negative value of the first harmonic amplitude with a phase difference of  $\pi$  when compared to the upstream region. The negative value of the first harmonic amplitude can be made clear when thinking of the  $\sin(x)$  and  $-\sin(x)$  curves also showing a phase difference of  $\pi$ .

The frequency composition of the wall shear stress shows similar higher harmonic amplitudes ( $n > 1$ ) in the control vessel and in the high and low shear regions in the conventional direction cast geometry (Figure 5.11). Differences in the waveform are then characterised only by differences in the zeroth (Figure 5.3) and first harmonics (Figure 5.10). This can be visualised by thinking of variations in the zeroth harmonic as the application of a translation operation to the waveform and variations in the first harmonic, as the application of a magnification operation. The high and low shear region waveforms can then be obtained by applying these operations to the control vessel waveform when moving along the high and low shear regions in the perivascular cast geometry.



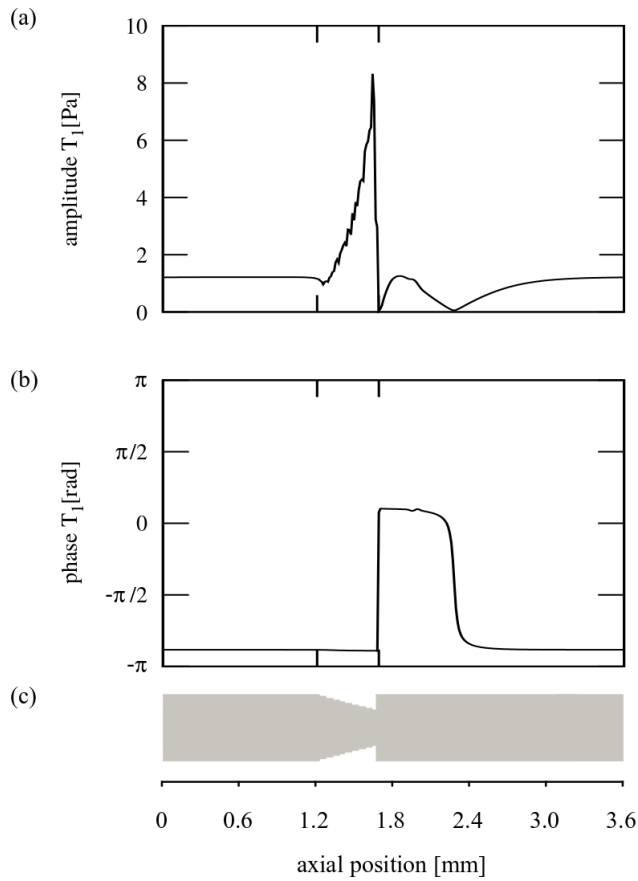


**Figure 5.10. Distribution of the first harmonic (a) amplitude and (b) phase of the wall shear stress signal along the length of the (c) tapering perivascular cast geometry.** The flow direction is given from left to right. The first harmonic amplitude computed in the control vessel is 2.47 Pa. Flow separation is marked by the difference in phase of the first harmonic. The amplitude distribution shows largely similar patterns to the zeroth harmonic (Figure 5.3).

The oscillatory signal given in Figure 5.11 was chosen as a representative waveform of the oscillatory region. All waveforms of the oscillatory region showed a notable difference in the third harmonic of the wall shear stress signal. With this and the TAWSS and first harmonic distributions, the key differences between the low and oscillatory shear regions occur in the zeroth, first and third harmonic components of the wall shear stress signal.

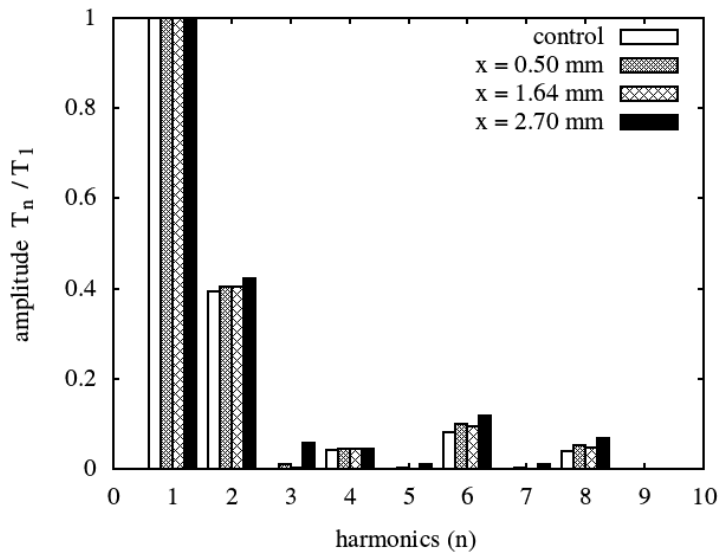


**Figure 5.11. Frequency composition of the wall shear stress signal at axial positions along the perivascular cast geometry.** The waveforms were normalised by the respective first harmonic amplitudes and shown with the wall shear stress signal of the control vessel. Axial positions,  $x$ , were chosen in the geometry to lie in the low, high and oscillatory shear regions. The waveforms of the oscillatory signal are highly variable and so a position was chosen here simply to highlight the difference in waveform from the control, low and high signals. The compositions of the control, low and high waveforms were largely similar. Comparison with the oscillatory waveform shows notable differences in the second and third harmonics.

#### Reversed direction perivascular cast

The magnitude of the first harmonic amplitude was computed as 1.26 Pa in the regions proximal and distal to the cast, as in the conventional direction geometry. The first harmonic amplitude was increased almost ten-fold at the cast throat due to fluid acceleration similar to the TAWSS distribution.

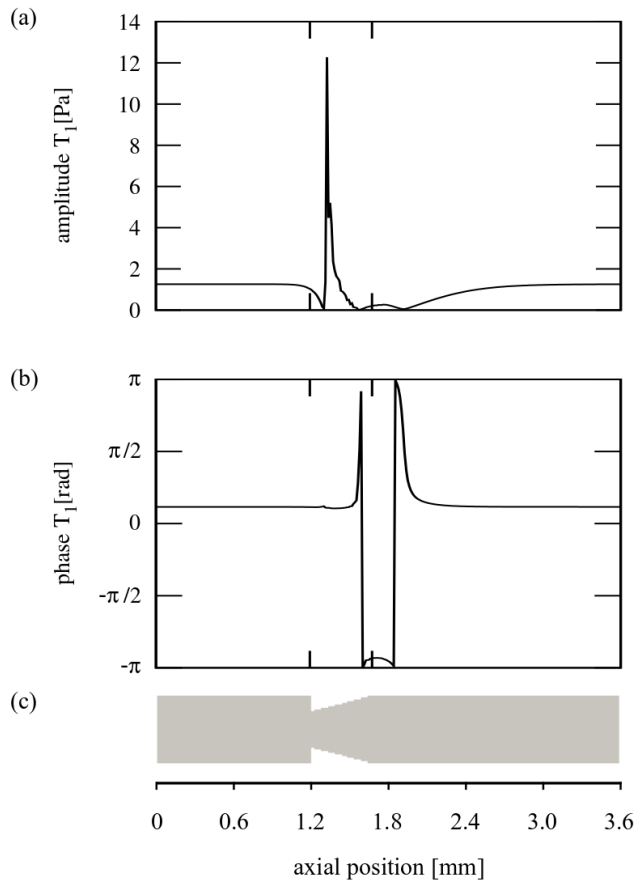


**Figure 5.12. Distribution of the first harmonic (a) amplitude and (b) phase of the wall shear stress signal along the length of the (c) reversed direction perivascular cast.** The flow direction is given from left to right. The first harmonic amplitude computed in the control vessel is 2.47 Pa. The constant value in the phase component shows no separation/reversal of the traction vector component as shown in Figure 5.6. The amplitude distribution shows similar distribution to the zeroth harmonic (Figure 5.5).

Mohri *et al.* (2014) show macromolecule uptake to be relevant only at axial positions within 0.5 mm from the upstream and downstream bounds of the perivascular device. Analysis of the traction vector in the upstream region however, would be significantly affected by the geometry idealisation at the sharp boundary shown in Figure 5.6. The geometry approximation at the downstream cast end is considered to be reasonable due to the gradual change in diameter over the geometry length. The frequency composition of the waveforms computed in these regions are largely similar with minute difference in the third harmonic amplitude.

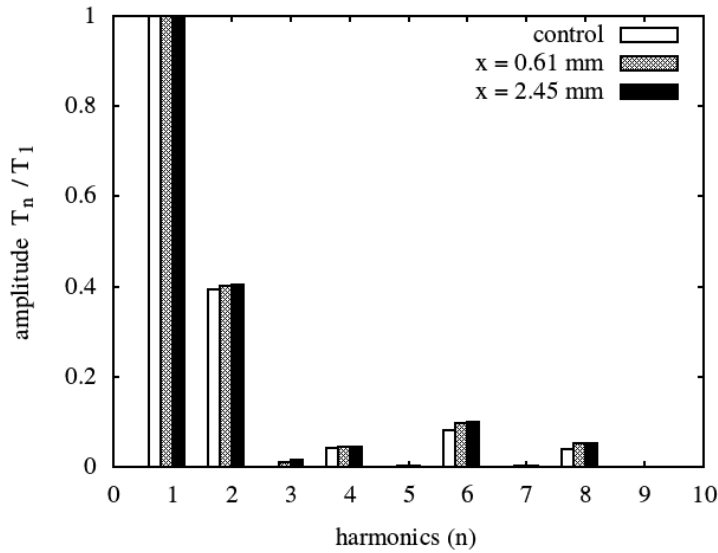


**Figure 5.13. Frequency composition of the wall shear stress signal in the upstream and downstream regions of the reversed perivascular cast geometry.** The waveforms were normalised by the respective first harmonic amplitudes and shown with the wall shear stress signal of the control vessel. Axial positions,  $x$ , were chosen such that the waveforms were representative of the region. Largely similar waveforms were computed in the control vessel and upstream and downstream regions of the cast geometry with small differences in the third harmonic amplitude.

### Tandem stenosis

As in the perivascular cast simulations, the distribution of the first harmonic amplitude (Figure 5.14) was largely similar to that of the TAWSS (Figure 5.7). This is clear from the peaks of the first harmonic amplitude at points of maximum constriction, showing an approximately 25-fold increase in amplitude from the non-ligated regions. The magnitude of the first harmonic amplitude was computed as 0.32 Pa in the non-ligated regions. As with the zeroth harmonic amplitude, drops in the amplitude were found in the regions immediately upstream and downstream of the constriction profiles. Changes in the phase component of the signal were found in the region immediately downstream of each constriction profile. The change of phase indicates the change of direction of the traction vector axial component as in the conventional direction tapering cast simulations. The small decrease in the phase in non-ligated regions was a result of the regularisation boundary condition as a phase delay is created from the propagation of velocity information along the geometry.

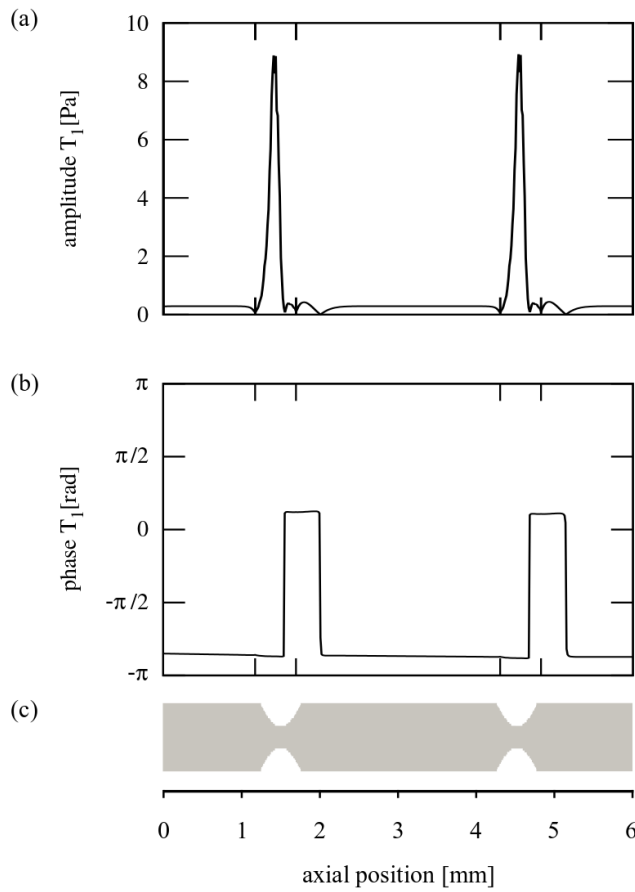


**Figure 5.14. Distribution of the first harmonic (a) amplitude and (b) phase of the wall shear stress signal along the length of the (c) tandem stenosis geometry.** The flow direction is given from left to right. The first harmonic amplitude computed in the control vessel is 2.47 Pa. The first harmonic amplitude in non-ligated vessel segments was computed as 0.32 Pa.

A key result of the frequency analysis in the tandem stenosis geometry is the consistency of the waveform composition along the length of the geometry (Figure 5.15). The vessel segments identified in Chen *et al.* (2013) showed differences from the control vessel signal only in the zeroth and first harmonic amplitudes with no differences in signal between the segments.

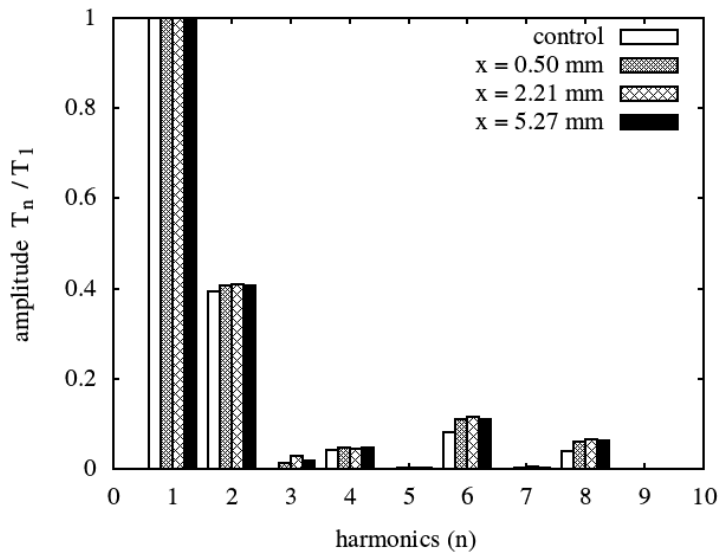


**Figure 5.15. Frequency composition of the wall shear stress signal at points along the tandem stenosis geometry.** The waveforms were normalised by the respective first harmonic amplitudes and shown with the wall shear stress signal of the control vessel. Wall shear stress signals were analysed at various axial positions,  $x$ , from vessel segments identified in Chen *et al.* (2013). Largely consistent profiles of wall shear stress were found at all axial positions within the geometry also showing similarity with the control vessel signal.

## 5.4 Discussion

The current chapter explores the hypothesis that plaques resembling the human TCFA and stable-looking compositions are observed in regions experiencing different local haemodynamic conditions in the atheroprone mouse. A key note throughout this PhD is that the frequency composition of the wall shear stress details all spatial and temporal characteristics of the signal in its most raw form. The information is given as a time-varying signal, devoid of any time-averaging steps used in the commonly applied shear metrics. This allows for a thorough comparison of the wall shear signal without any loss of information. The importance of the signal's frequency composition has also been demonstrated through the differential expression of several inflammatory markers under the variation of the zeroth and first harmonic components in Himburg *et al.* (2007) and Feaver *et al.* (2013). The reader is referred to Section 2.4 for a description of the frequency domain analysis and the interpretation of the harmonic amplitude and phase.

It is known that the placement of perivascular devices diminishes the value of the zeroth harmonic (TAWSS) compared to the control vessel signal. Further to this, simulations performed in this chapter also indicate the reduced value of the first harmonic amplitude relative to the control vessel signal. Feaver *et al.* (2013) demonstrate the sensitivity of endothelial cells to the zeroth and first harmonic amplitudes through the expression of NF- $\kappa$ B, a proinflammatory transcription factor. Increasing zeroth and first harmonic amplitudes were shown to decrease the expression of this pathway, shifting the endothelial cells towards the atheroprotective state. Following this, the low zeroth and first harmonic amplitudes form a key result of this chapter as plaque formation was found to occur in all regions coincident with these wall shear stresses.

In a study of particular importance to this PhD, Cheng *et al.* (2006) proposed the dependence of plaque composition on the pattern of wall shear stress. Stable plaque types were found to occur in the oscillatory shear stress region while the TCFA plaque developed in the low shear stress region. Cheng *et al.* (2006) define oscillatory shear stress simply using the bidirectional nature of the traction vector with no further analysis of the wall shear stress signal, while the low shear stress region is defined by the upstream reduction of blood flow due to the tapering geometry. As mentioned above, simulations performed in this chapter show decreased values of the zeroth and first harmonic amplitudes, compared with the control vessel, in both regions. Additionally, the zeroth and first harmonic amplitudes were found to be lower throughout the oscillatory region relative to the low shear stress region. Signals normalised with respect to the first harmonic also show an increased contribution of the third harmonic amplitude in the oscillatory signal relative to the low shear stress signal. This suggests the amplitude of the zeroth, first and third harmonic amplitudes to be important to plaque composition as opposed to the simple low or oscillatory classifications of Cheng *et al.* (2006).

In addition to the amplitude differences discussed above, simulations showed a first harmonic phase difference between the low and oscillatory shear stress regions in the perivascular cast model. The imposed body force is related to the vessel circumferential strain by thinking of the vessel dilation caused by propagation of the blood pressure waveform. The phase difference in the wall shear stress signal then suggests an out-of-phase relationship between wall shear stress and circumferential strain. This stress phase angle has previously been noted in CFD studies of the stenosed coronary artery with the expression of NF- $\kappa$ B being increased in regions coincident with an out-of-phase WSS-strain relationship (Torii *et al.*, 2009; Amaya *et al.*, 2015).

The importance of differences in both the WSS signal and the out-of-phase stress-strain relationship can be considered in terms of set-point theory where disturbance from homeostatic conditions results in vascular remodelling (Baeyens *et al.*, 2015). In this light, placement of perivascular devices causes deviation from the WSS signal and stress-strain relationship “healthy” set points and leads to a pro-inflammatory state.

An important observation from the Chen *et al.* (2013) study is the occurrence of both the TCFA and stable-looking plaque types in vessel segments experiencing the same TAWSS. Further to this, simulations performed in this chapter demonstrate a consistency of the signal frequency composition among all vessel segments. This finding then forms a key result of this chapter, indicating the effects of factors other than wall shear stress to contribute towards the plaque composition. One such factor is thought to be the circumferential tensile stress given the clear segmentation of the vessel into regions of distinct pressures (Figure 5.16). In support of this suggestion, the tensile stress is also a known contributor in atherosclerosis showing significance to cap disruption and plaque compositional changes (Slager *et al.*, 2005; Akyildiz *et al.*, 2014; Gijzen and Migliavacca, 2014). As mentioned above, the pressure is thought to correspond to the circumferential strain and tensile stress considering its relationship to vessel dilation. In addition to this segmentation of the vessel by tensile stress, each plaque type found in the tandem stenosis model is clearly localised to the regions of tensile stress. The geometry segmentation in tensile stress is also shown in Chen *et al.* (2013) through analysis of the blood pressure.



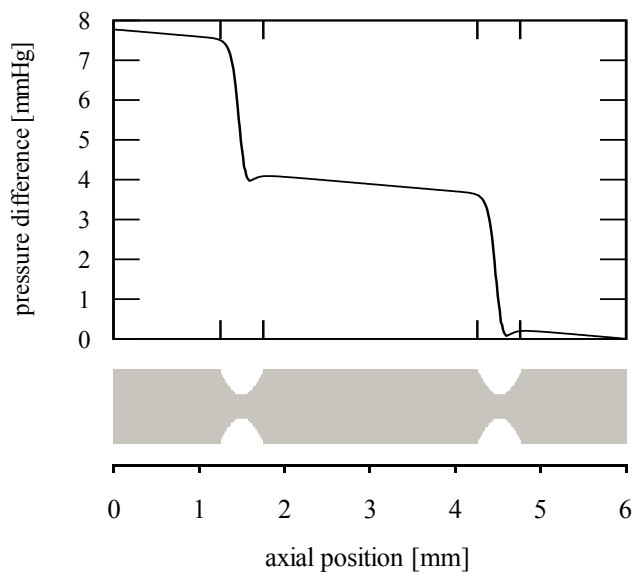


**Figure 5.16. Pressure difference computed between the vessel inlet and outlet. The pressure difference is thought to correspond to the circumferential tensile stress considering its relationship to vessel dilation.** Pressure drops are found at the ligation throats showing clear segmentation of the vessel to each region of circumferential tensile stress. The segmented regions also correspond to regions of different plaque type in the atheroprone mouse (Chen *et al.*, 2013).

A key result of the Mohri *et al.* (2014) study is the lack of statistical significance in macromolecule uptake between the regions upstream and downstream of the reversed cast model. Considering the direct relationships proposed between lipid uptake and TAWSS, it is expected that similar profiles of wall shear stress would result in regions of equal uptake (Olgac *et al.*, 2009; Nouri *et al.*, 2015). Consistency of the wall shear stress signal in these regions further suggests the effects of factors other than the wall shear stress with respect to macromolecule uptake. A lack of statistical significance despite the pressure drop across the tapering cast also indicates at least one more factor with relevance to macromolecule uptake. The variation in vessel thickness and localisation of macromolecule uptake only at the cast boundaries may suggest the effect of mechanical interference from cast placement (Mohri *et al.*, 2014). The resulting macromolecule uptake in the reversed cast model may then be the cumulative effect of these factors.

The TCFA plaque was found upstream of the tapering cast (Cheng *et al.*, 2006) while Chen *et al.* (2013) show its development in the region between ligations. Again, simulations show both models to produce the plaque in a region of low TAWSS and first harmonic amplitude when compared to the control vessel. The zeroth and first harmonic amplitudes were however, lower in the tandem stenosis geometry. The higher harmonic amplitudes ( $n > 1$ ) also show consistency in the waveform between models in the regions showing TCFA plaques (Figure 5.17a). The stable plaque, on the other hand, was found downstream of the tapering cast (Cheng *et al.*, 2006) while Chen *et al.* (2013) show its development in the region downstream of both ligations. Simulations again show a lower zeroth and first harmonic amplitude in the regions of the stable plaque in the tandem stenosis model compared to the perivascular cast model. The details of the waveform shown in the higher harmonics ( $n > 1$ ) were also different between the models (Figure 5.17b). The findings discussed here are summarised in Table 5.1.

The occurrence of the stable plaque type in regions of different wall shear stress suggests the “cumulative effect” mentioned above. Also considering the different degrees of constriction between the Cheng *et al.* (2006) and Chen *et al.* (2013) models, different magnitudes of the pressure drop are expected between the models. The cumulative effect of mechanical constriction and alteration of the flow field then suggests a lack of comparability between the different atherosclerosis models.

**Table 5.1. Summary of key findings in perivascular device simulations.** Results of the perivascular device models are discussed relative to the control vessel simulations where the zeroth and first harmonic amplitudes were computed as 15.76 Pa and 2.47 Pa, respectively.

Citation	TCFA	Cellular plaque	Cap disruption
(Cheng <i>et al.</i> , 2006)	<ul style="list-style-type: none"> <li>• Reduced zeroth harmonic amplitude WSS[0] = 9.18 Pa</li> <li>• Reduced first harmonic amplitude WSS[1] = 1.21 Pa</li> <li>• Normalised higher harmonic content similar to control signal</li> <li>• First harmonic phase component is consistent with the control vessel</li> </ul>	<ul style="list-style-type: none"> <li>• Reduced zeroth harmonic amplitude Variable in oscillatory stress region</li> <li>• Reduced first harmonic amplitude Variable in oscillatory stress region</li> <li>• Elevated third harmonic amplitude relative to control signal</li> <li>• Elevated first harmonic phase component relative to control vessel</li> </ul>	<ul style="list-style-type: none"> <li>• Not found</li> </ul>
(Chen <i>et al.</i> , 2013)	<ul style="list-style-type: none"> <li>• Reduced zeroth harmonic amplitude WSS[0] = 2.56 Pa</li> <li>• Reduced first harmonic amplitude WSS[1] = 0.32 Pa</li> <li>• Normalised higher harmonic content similar to control signal</li> <li>• Colocalised with region of moderate circumferential stretch</li> </ul>	<ul style="list-style-type: none"> <li>• Reduced zeroth harmonic amplitude WSS[0] = 2.56 Pa</li> <li>• Reduced first harmonic amplitude WSS[1] = 0.32 Pa</li> <li>• Normalised higher harmonic content similar to control signal</li> <li>• Colocalised with region of minimum circumferential stretch</li> </ul>	<ul style="list-style-type: none"> <li>• Reduced zeroth harmonic amplitude WSS[0] = 2.56 Pa</li> <li>• Reduced first harmonic amplitude WSS[1] = 0.32 Pa</li> <li>• Normalised higher harmonic content similar to control signal</li> <li>• Colocalised with region of peak circumferential stretch</li> </ul>

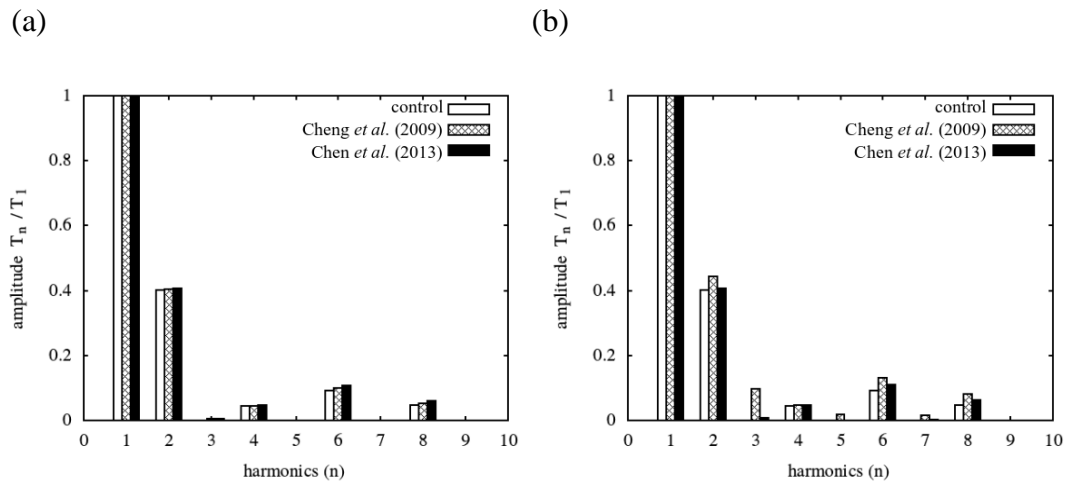


**Figure 5.17. Comparison of the frequency composition of the wall shear stress signals in regions showing the (a) thin-cap fibroatheroma and (b) stable-looking plaques.** The zeroth and first harmonic amplitudes of the tandem stenosis model (Chen *et al.*, 2013) were found to be lower than in the tapering cast model (Cheng *et al.*, 2006). The higher harmonic amplitudes ( $n > 1$ ) show largely similar wall shear stress signals in the regions where vulnerable-looking plaques were formed. The frequency composition of the signal in regions where stable plaque types were different with the most apparent difference in the third harmonic amplitude. Differences are expected in the mechanical environment between the two models suggesting a lack of comparability.

### Study limitations

The major limitation of this chapter and PhD is the approximation of model geometries to the idealised case. The importance of this approximation is seen across the fluid dynamics literature as the accuracy of the flow field is largely dependent on the accuracy of the geometry model. Approximations were made in terms of both the vessel axial symmetry and the perivascular cast boundaries. These assumptions were made considering the lack of accurate vessel geometry data and the simplicity in processing the frequency composition of the wall shear stress signal.

The inaccuracy in the axial symmetry approximation is highlighted by Mohri *et al.* (2014) by defining the vessel asymmetry through a shape index. The index parameter shows significant deviation from the axially symmetrical cross-section along the length of the cast, most significantly at the cast throat. The cast boundary approximation is also clear when considering the upstream end of the reversed

direction perivascular cast with the sharp edge cast boundary. Comparison with the CFD study of Mohri *et al.* (2014) shows the effect of this approximation with the simulations performed here showing a non-physical drop in TAWSS.

A 1D vascular network model coupled together with the disease model could be used to generate physiologically representative boundary conditions in each simulation case. The lack of a verified and complete 1D model (Section 4.4) therefore forms a key limitation of this chapter. This necessitates the approximation of the pressure waveform in disease models to that of the healthy mouse carotid artery. The impact of this approximation is explored in Chapter 6 with simulations aiming to characterise a relationship between the input pressure waveform and the computed wall shear stress signal.

It should also be noted that the studied models may themselves be flawed in reporting differences in plaque composition as a result purely of the wall shear stress or mechanical effects. In reality, a number of processes may be relevant. The restriction of vessel motion or placement of the perivascular devices has been shown to produce atherogenic effects with the differing levels of inflammatory markers being dependent on the choice of perivascular device (Tropea *et al.*, 2000; Tanaka *et al.*, 2003). While the non-constrictive controls and sham-operated groups represent an excellent step in isolating the effects of each model, there is a great difficulty in decoupling all possible contributors of the disease. The discussion presented here aims to highlight the complexity of each atherosclerosis model and the implementation of vessel manipulation devices. Despite the numerous complicating factors, simulations performed here consistently demonstrate the plaque formation in regions of low zeroth and first harmonic amplitudes.

## 5.5 Conclusions

The numerical tool implemented and developed in Chapters 3 and 4 was applied to geometries approximating published mouse models of atherosclerosis. Surgical manipulations described in these mouse models cause local differences in the wall shear stress that have been shown to be important in the resulting plaque composition. Following from studies in the literature showing the dependence of inflammatory

markers on the frequency composition of the wall shear stress signal, simulations were performed here to test the hypothesis that different plaque compositions shown in the mouse models occur in regions experiencing different time-varying waveforms of the wall shear stress signal.

The conclusions of this chapter are expressed in terms of the aims set out in the introduction:

- 1) *Are there similarities/differences in the stress waveform between regions showing different plaque compositions in each model?*

Differences were found in the frequency composition of the wall shear stress signal between regions showing the TCFA and stable plaque types in the conventional direction perivascular cast geometry. More specifically, the wall shear stress signal obtained from simulations showed differences in the zeroth, first and third harmonic amplitudes between the regions of different plaque composition.

The tandem stenosis geometry, on the other hand, showed consistent profiles of wall shear stress in all regions. Each segment of this model showed different plaque types including the TCFA and stable-looking plaques. Characteristics of human disease were also observed in the region upstream of the ligations.

The reversed direction perivascular cast also showed similar profiles in the wall shear stress signal at the upstream and downstream regions of the cast device where no statistically significant difference was found in the uptake of a labelled macromolecule.

- 2) *Are there similarities/differences in the stress waveform between regions showing similar plaque composition between models?*

The TCFA plaque type was found in the conventional direction perivascular cast (Cheng *et al.*, 2006) and tandem stenosis (Chen *et al.*, 2013) studies. Simulations found the higher harmonic components ( $n > 1$ ) of the signal in these regions to be equal to that of the control vessel with differences only in the zeroth and first harmonic amplitude. It should be noted that the zeroth and first harmonic amplitudes of the vulnerable-looking plaque in the tandem stenosis geometry were lower than those of the perivascular cast geometry.

The stable plaque type was found in the conventional direction perivascular cast (Cheng *et al.*, 2006) and tandem stenosis (Chen *et al.*, 2013) studies. Referring again to the consistency of the wall shear stress signal along the length of the tandem stenosis geometry, differences were found in the frequency composition of the wall shear stress signal between regions showing the stable plaque type.

From this chapter, it can be concluded that the wall shear stress alone, even in its most raw form of the time-varying profile, cannot be used to predict plaque compositions where mechanical effects such as the circumferential tensile stress are also relevant and variable. This is highlighted by the simulation of the tandem stenosis geometry where only the blood pressure was found to vary between vessel segments. Changes in blood pressure can be related to differences in the circumferential tensile stress on the vessel wall. Comparability between models may also be hindered by the difference in pressure drop along the perivascular device and the mechanical or inflammatory effects of the placement of the device itself.

Considering the variability in mechanical and inflammatory effects between the different models, subsequent chapters aim to make this constant by studying only the conventional direction tapering cast geometry. With this, the mechanical effects of confinement can be considered to be constant. The wall shear stress is studied in this case with Chapter 6 dealing with the effects of the input pressure waveform and Chapter 7 looking at the effects of varying dimensionless numbers as would be found across different mammalian species.

## Chapter 6

# Wall shear stress signal with varying boundary conditions

---

### Abstract

Wall shear stress is a parameter of key interest in a number of fluid dynamics studies because of known relationships to endothelial activity and cardiovascular disease (Davies, 1995; Ku, 1997; Malek *et al.*, 1999; Cunningham and Gotlieb, 2004; Chiu and Chien, 2011). The relevance of these studies, however, is highly dependent on the validity of the conditions applied at simulation boundaries. The effect of these flow conditions on the time-averaged wall shear stress has been explored in several simulation studies. The Womersley flow analytical solution also shows a dependence of fluid flow on the time variation of the input flow waveform. The time variation is of particular importance to this PhD considering the relevance of the wall shear stress frequency composition to the endothelial cell inflammatory response (Himburg *et al.*, 2007; Feaver *et al.*, 2013). The frequency composition is also able to capture all spatial and temporal details of the wall shear stress signal. The current chapter, therefore, aims to explore the hypothesis that the wall shear stress frequency composition found in regions of the mouse perivascular cast model is dependent on the flow conditions applied at the simulation inlet and outlet boundaries.

Simulations were performed in geometries approximating the Cheng *et al.* (2006) perivascular tapering cast with varying waveforms of the body force term and dimensionless numbers. The perivascular cast geometry was used to create three distinct regions of high, low and oscillatory wall shear stress patterns. A key result of the varying waveform study is the linear relationship between the first harmonic amplitudes of imposed body force and computed wall shear stress in all regions. The gradient of this linear relationship varied between each region. A quadratic relationship



was also found between the body force first harmonic amplitude and the wall shear stress second harmonic amplitude. These second harmonic amplitudes became noticeable only in the oscillatory region. A key result of the dimensionless numbers study is the approximate consistency of the wall shear stress higher harmonic terms ( $n > 1$ ) in the high and low shear stress regions between all models. The distribution of the zeroth and first harmonic amplitudes were also found to vary between models with the length of the recirculation region increasing with the Reynolds and Womersley numbers.

It should be noted that the studies performed here provide only an exploration into the effects of a varying body force term and dimensionless parameters rather than presenting flow cases relevant to any specific animal or biological mechanism that may cause the variation of these parameters. The simulations did not model the physical cases in the interest of lower computational cost. The findings of this study may, however, be extrapolated to animal models with variability of the body force waveforms being a result of vascular tone regulation (O'Rourke and Yaginuma, 1984; Nichols *et al.*, 1998; Stroeve *et al.*, 2005) and arterial stiffening with aging (Mikael *et al.*, 2017). The variability of dimensionless numbers can also be seen between mammals of different size (Weinberg and Ethier, 2007; Dawson, 2014).

## 6.1 Introduction

Flow dimensionless numbers are a key determinant of fluid flow. As discussed in Section 4.6, the Reynolds number describes the ratio of inertial to viscous forces and the Womersley number gives the ratio of pulsatile to viscous forces. The two dimensionless numbers given here are key in defining blood flow and are necessary in achieving dynamic similarity between the physical situation and any experiment or simulation. The significance of these parameters to the wall shear stress (WSS) has been shown throughout the literature in the development and transport of vortical structures in stenosis and aneurysm models (Buchanan *et al.*, 2000; Banerjee *et al.*, 2012; Asgharzadeh and Borazjani, 2016).

The applicability of simulations to the physical situation is also determined by the time variation of pulsatile effects (Gabriel *et al.*, 2017). The time-varying nature of the flow

profile is created by the phases of heart contraction, and changes along the length of the arterial network as a result of vessel elasticity, bifurcations, tapering, and tortuosity (Ku, 1997). The importance of this flow rate time variation to the velocity profile and WSS is obvious from the analytical solution of the Womersley equation which was initially derived by Helps and McDonald (1954) and Womersley (1954).

The analytical solution of the Womersley equation can be expressed in terms of the Fourier decomposition of the flow rate and the Reynolds and Womersley numbers (Salsac *et al.*, 2006). This shows a clear dependence of the WSS time variation on these parameters. The accurate specification of these parameters is, therefore, key in the recovery of a physiologically relevant flow field and WSS. The analytical solution for WSS is given as a function of time  $t$  by:

$$\text{WSS}(t) = \text{Re} \left( \frac{G_0}{2} + \sum_{n=1}^{\infty} \frac{G_n}{2} F(\alpha_n) e^{-in\omega t} \right) \quad (6.1)$$

where  $G_n$  are the Fourier coefficients of the pressure gradient and  $n$  is the identity of the harmonic component.  $\text{Re}$  denotes the Reynolds number,  $\alpha_n = R\sqrt{n\omega/\nu}$  is the Womersley number relevant to each harmonic frequency component.  $R$  is the pipe radius,  $\omega$  is the frequency of oscillation and  $\nu$  is the kinematic viscosity.  $F(\alpha_n)$  is the Womersley function and is given by:

$$F(\alpha_n) = \frac{2}{i^{3/2}\alpha_n} \frac{J_1(i^{3/2}\alpha_n)}{J_0(i^{3/2}\alpha_n)} \quad (6.2)$$

where  $J_0$  and  $J_1$  are the Bessel functions of first kind with order 0 and 1 respectively. The analytical solution was reproduced here from Salsac *et al.* (2006). Considering the importance of these parameters in obtaining a physiologically relevant WSS signal, an exploration of the flow field sensitivity to the flow rate signal and dimensionless numbers is required in geometries relevant to atherosclerosis.

Hypothesis and aims:

The current chapter explores the hypothesis that the WSS frequency compositions found in the perivascular cast geometry are related to the flow conditions applied at the simulation boundaries. The work of this chapter is, in part, motivated by the lack of a functioning 1D model (Section 4.4). The lack of accurate boundary conditions necessitates an understanding of how the input boundary conditions are related to the output wall shear stress signal. The following aims were set out to address this hypothesis:

- 1) Are the current atherosclerosis localisation metrics able to identify the differences in the waveform of wall shear stress with varying body force signal?
- 2) Are the differences in wall shear stress signal shown between regions of the mouse perivascular model dependent on the imposed flow boundary conditions?

## 6.2 Methods

To better understand the physical effects relevant to fluid flow and their relationships with the WSS, a number of simulations were performed with varying input boundary conditions. Specifically, the effects of the body force term and dimensionless numbers were explored. The perivascular cast device of Cheng *et al.* (2006) was adopted in each simulation to create local variations in flow dynamics. It should be noted that the simulations performed in this chapter aim only to provide an exploration of the physical effects relevant to WSS and do not represent the flow cases of any specific animal model. The simulations did not model the physical situations in the interest of lower computational cost.

### 6.2.1 Body force term

A time-varying body force  $f_x(t)$  was applied at all lattice sites using:

$$f_x(t) = F(1 + A \cos(\omega t)), \quad (6.3)$$

where the axial component of the body force is given by the time-averaged magnitude,  $F$ , and oscillation amplitude,  $A$ . The body force was chosen to follow a simple cosine

function to develop an initial understanding of how the term is related to the WSS and how this relationship varies within the perivascular cast geometry.

### 6.2.2 Obtaining dimensionless numbers

Dimensionless numbers were computed from a model adapted from allometric scaling theory (Dawson, 2014). In mammals, allometric scaling laws are used to estimate haemodynamic parameters as a function of the animal body weight (Weinberg and Ethier, 2007). While this study does not concern physical animal models, hypothetical body masses were selected in order to obtain the dimensionless numbers from allometric scaling. The scaling laws are given in the form:

$$P = aM^b \quad (6.4)$$

where the parameter of interest  $P$  varies with the body mass  $M$  in a power law function with constant  $a$  and body mass exponent  $b$ . This topic is discussed further in Chapter 7.

Body masses were chosen to be equally distributed on a logscale between 0.025 kg and 75 kg. The Reynolds numbers corresponding to these body masses were chosen to be 40 and 360. The Womersley numbers were also chosen as 0.8 and 4.2, respectively. The limits of the Reynolds and Womersley numbers were computed from the cross-sectionally averaged velocity field in the mouse (Pedrigi *et al.*, 2016) and human (Milner *et al.*, 1998). These limits were chosen for the purpose of designing simulations with a relatively low computational cost. With the assumptions of body mass, Reynolds number and Womersley number, the constants and body mass exponents were found for the dimensionless numbers. The body mass exponents of the Reynolds number and Womersley number were computed as 0.27 and 0.21, respectively. The body masses relevant to each model were then used to estimate values of the Reynolds number and Womersley number in each simulation model (Table 6.1).

**Table 6.1. Dimensionless numbers based on the allometric scaling laws discussed above.** The Reynolds number,  $Re$ , and Womersley number,  $\alpha$ , were computed as a function of a hypothetical body mass,  $M$ , for use in the dimensionless numbers study.

Simulation name	Body mass $M$ [kg]	$Re$	$\alpha$
S1	0.025	40	0.80
S2	1	110	1.72
S3	3.5	155	2.23
S4	20	250	3.20
S5	75	360	4.20

### 6.2.3 Simulation setup

The simulation setup was largely similar to that of Chapter 5 with key differences being in the choice of the body force term and simulation parameters. A Newtonian viscosity model was also implemented in all cases. The simulation relaxation parameter and pipe diameter were chosen to achieve a peak axial velocity less than 0.07. This upper limit of peak axial velocity was used in order to minimise errors coming from the truncation of equilibrium populations (3.5).

Solid boundaries were treated with the standard bounceback approach detailed in Section 3.2. The periodic boundary condition was employed at the inlet and outlet boundaries alongside the time-varying body force term applied at all lattice sites. The time-varying body force term was chosen according to the specific investigation with the effects of the body force term being studied using equation (6.3) and the dimensionless number studies using the pressure waveform measured in the healthy mouse carotid artery, taken from Artoli and Sequeira (2006). This mouse pressure waveform was used in the latter study as the effects of varying dimensionless number on the higher harmonics would not be apparent if only studying the simple body force term of equation (6.3).

#### 6.2.4 Simulations performed

Many of the simulations were performed in geometries approximating the tapering cast model of Cheng *et al.* (2006) with the cast causing a constriction of the pipe diameter to half of that of the uncast regions. The cast length was taken to be equal to the pipe diameter. The tapering cast geometry was implemented to create regions of local flow dynamics that have been shown in Chapter 5 to produce variations in WSS over the length of the geometry. The studies of this chapter may be divided into two separate investigations; one looking at the effect of a varying body force term on the wall shear stress and the other looking at the effect of flow dimensionless numbers.

Simulations performed to explore the effects of the body force term differed only in the choice of the  $A$  parameter. The mean Reynolds and Womersley numbers were kept constant in these simulations at 40 and 0.8, respectively, through control of  $F$  and  $\omega$ . The  $A$  parameter was chosen to vary between 0.025 and 0.125 with an interval of 0.025.

The effects of the flow dimensionless numbers were investigated through variation of the Reynolds and Womersley numbers using the allometric scaling method discussed above. The simulated dimensionless numbers are presented in Table 6.1 and were specified through the choice of pipe diameter, fluid viscosity, peak axial velocity and period duration. The geometry axial length was varied in each simulation to ensure flow recovery downstream of the tapering cast, validating the use of periodic boundary conditions in each case (Section 3.2). Simulation results presented in the perivascular cast studies were normalised with respect to the values computed in the control geometry. This was modelled as a straight pipe with constant radius.

As in Chapter 5, simulations were terminated once the velocity profile measured at the geometry axial centre had converged to the profile measured in the previous period (3.14). The convergence criteria for this termination event was set to  $10^{-4}$ . Once the criteria had been satisfied, the simulation would run for one more period to compute and write all desired observables. Frequency analysis of the WSS signal was performed on the axial component of the circumferentially averaged traction vector (Section 2.4).

## 6.3 Results

The regions of each model were analysed in terms of the circumferentially-averaged traction vector, both in relation to the time-averaged shear metrics and its instantaneous value over the oscillation period. This analysis is valid here for the simulated geometries considering the axial symmetry property and purely axial direction of the body force terms. The frequency analysis to be discussed here also considers only the axial component of the tangential traction vector. A comparison of the frequency composition was performed to identify any potential relationships between the input flow conditions and the computed WSS signal in the regions of the perivascular cast model. The analysis of the traction vector axial component and omission of its circumferential component will be discussed further in Chapter 2.4.

As the simulation cases do not relate to a physical case, no unit conversion was applied. The wall shear stresses were, instead, normalised with respect to the value computed in the control geometry. The relative residence time is not shown here considering the simple relationship between it and the oscillatory shear stress, as shown in the localisation metrics plots of Chapter 5.

### 6.3.1 Varying body force signal

#### Localisation metrics

The definition of each metric as a time-average of the tangential traction vector suggests uniformity in their distributions across all input body force studies. This was shown in the lattice Boltzmann simulations with absolute consistency of the time-averaged wall shear stress (TAWSS) metric in all regions of the geometry (Figure 6.1). The oscillatory shear index (OSI) and relative residence time (RRT) metrics showed minimal differences in the region downstream of the cast. This difference in OSI was attributed to minute fluctuations, of magnitude  $10^{-19}$  lattice units, in the circumferential component of the traction vector. Given their small magnitudes, the fluctuations are considered to be an artefact of the numerical method. These fluctuations were found to be different between simulation cases, resulting in the varied OSI magnitudes. Differences in the RRT metric (not shown) are also clearly a result of these fluctuations when considering equation (2.14).

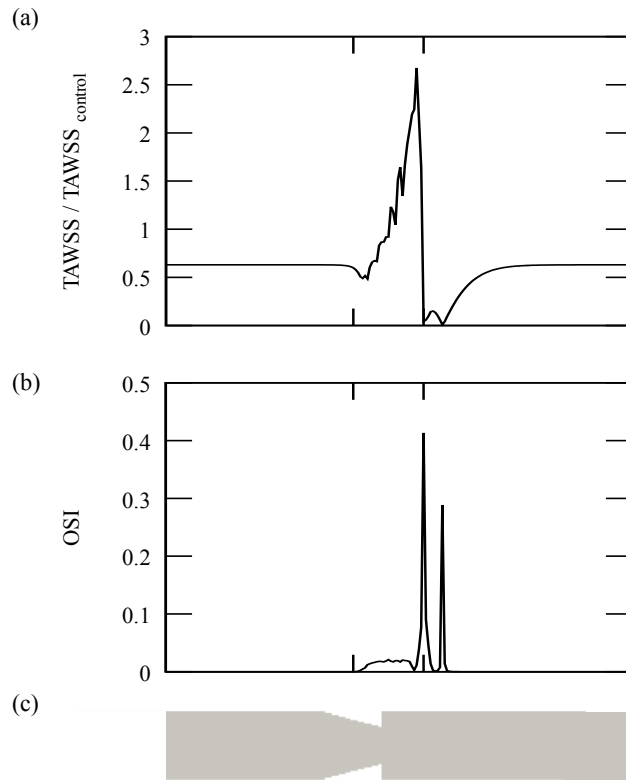


**Figure 6.1. Distribution of the (a) normalised time-averaged wall shear stress (TAWSS) and (b) oscillatory shear index (OSI) in simulations of varying body force term in the (c) perivascular tapering cast geometry.** The TAWSS was normalised against the value computed in the control geometry simulations (TAWSS<sub>control</sub>) showing a decreased TAWSS in the low shear stress region. The flow direction is from left to right and the vertical bold lines on the plot axes indicate the start and end positions of the tapering device. All body force simulations showed consistency in the time-averaged metrics and so are not reproduced. The TAWSS and OSI distributions are computed here for  $Re = 40$  and  $\alpha = 0.8$ .



### Frequency composition

Simulations showed consistency of the WSS first harmonic phase component between all body force studies. This result was expected as the phase information of the body force signal was also kept constant. The WSS harmonic amplitudes, on the other hand, varied between all simulations. Much of the discussion here neglects frequency components with magnitude less than 1% of the first harmonic amplitude. Following this filtering method, a comparison of the WSS signal in the different shear regions showed varying levels of complexity in the waveform. This “complexity” was characterised by the frequency composition of the WSS signal and the number of harmonics returned from the analysis. The WSS waveform in the high and low stress regions showed the same degree of complexity as the body force waveform in all simulated cases, with a non-zero value occurring only in the first harmonic amplitude. WSS signals with increased complexity were found in regions downstream of the peak OSI, showing an additional non-zero second harmonic amplitude.

The key result of this study is the relationships found between the harmonic components of the signals in each region. Figure 6.2a shows the linear relationship of the first harmonic amplitudes of body force and WSS. A quadratic relationship was also drawn between the WSS second harmonic amplitude and the body force first harmonic amplitude (Figure 6.2b). The linear and quadratic functions relating input to output were found to be region-specific. The linear gradient was constant at axial positions across the low shear stress region and varied in the oscillatory shear stress region. The second derivative of the quadratic function also decreased with increasing distance from the peak OSI. Both relationships were supported by the intercept and vertex parameters of the linear and quadratic curves, respectively. The linear regression fit curve of the WSS first harmonic amplitude found a y-intercept of approximately zero. The vertex of the quadratic curve in the WSS second harmonic amplitude also occurred approximately at the xy intercept. This result was expected considering that the axis intercept relates to a body force first harmonic amplitude of zero.

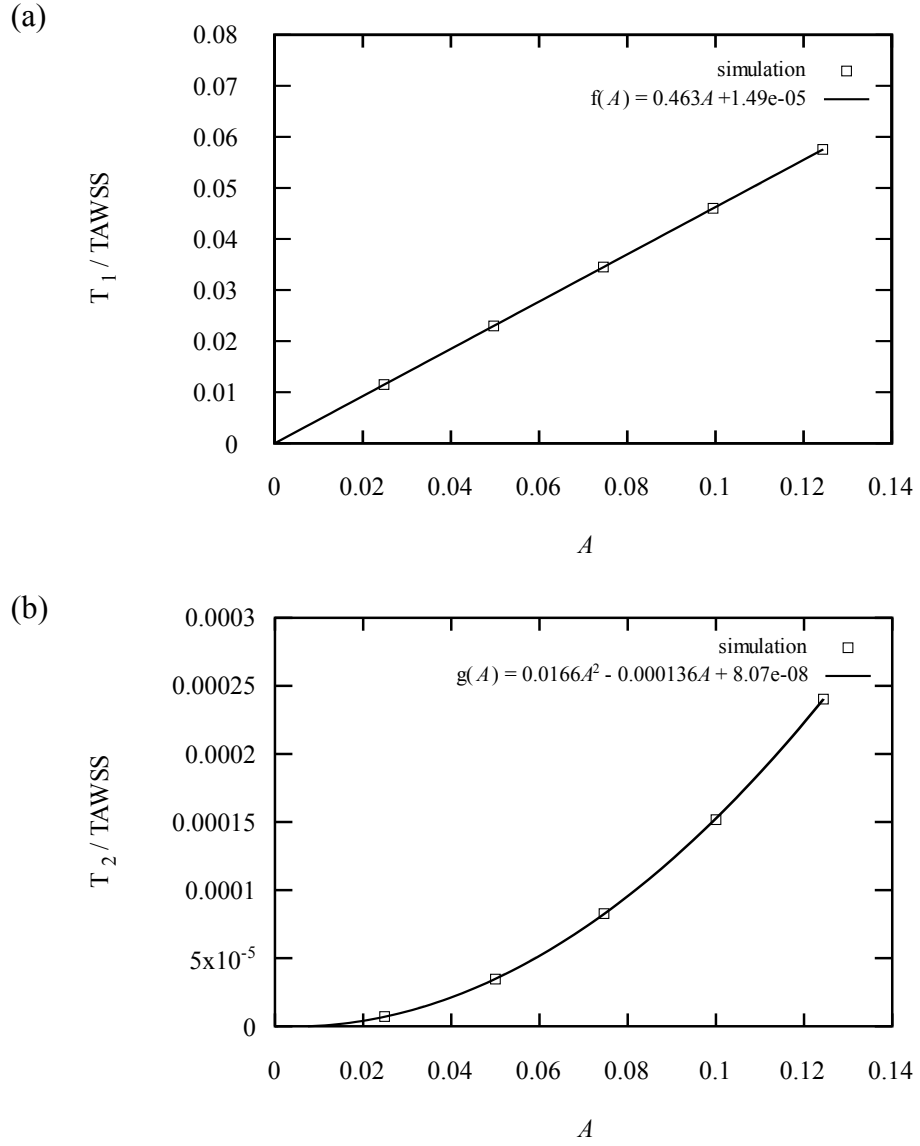


**Figure 6.2. (a) First and (b) second harmonic amplitudes of the wall shear stress (WSS) signal compared against the first harmonic amplitude of the body force signal  $A$ .** Harmonic amplitudes were normalised against the time-averaged wall shear stress (TAWSS). The key result of this study is shown by a least squares regression fit. Linear and quadratic relationships were found in the WSS first and second harmonic amplitudes, respectively. The gradient of the linear relationship was constant among axial positions in the low shear stress region and varied in the oscillatory region. The second derivative of the quadratic relationship varied among axial positions in the oscillatory region, decreasing in magnitude with increasing distance downstream of the cast. Simulations were performed with  $\text{Re} = 40$ ,  $\alpha = 0.8$  and  $A$  varying between 0.025 and 0.125 with an interval of 0.025.

The occurrence of the non-zero second harmonic amplitudes was attributed to differences in the flow field caused by the geometry. This is clear from the Womersley flow analytical solution as the analytical WSS signal in a straight pipe is a function of the Fourier coefficients of the input pressure signal (Salsac *et al.*, 2006). Fourier coefficients of the body force term higher than the first harmonic component are set to zero through equation 6.3. This means that the higher Fourier coefficients of the WSS signal are expected to be zero in the absence of the constriction.

### 6.3.2 Varying flow dimensionless numbers

#### Localisation metrics

All simulation models showed placement of the perivascular cast to result in clear regions of low, high and oscillatory shear stress similar to the mouse model of Cheng *et al.* (2006). This is shown in the distribution of the TAWSS and OSI metrics for the S1, S2, S3, S4 and S5 models (Figure 6.3). The distribution of these regions is thoroughly discussed in Section 5.3 in the case of the mouse model with the aid of Figure 5.3 and Figure 5.4 and will not be repeated here.

A key difference between the metrics in each model is the length between the downstream cast end and the position of peak OSI. This is indicative of the length of the oscillatory region and its increase is explained by the increasing Reynolds number. This increase in length is expected considering the increased significance of inertial effects in fluid flow. Relative to simulations in the control geometry, the TAWSS computed in the high shear stress region also showed an increase with increasing Reynolds and Womersley numbers between all dimensionless number simulations. This is seen as an effect of the Reynolds number as the difference in fluid inertia between the cast and control geometry simulations also increases with Reynolds number. The consistency found in the relative TAWSS in the low shear stress region is a result of the normalisation procedure with respect to the control geometry. The consistency of the decrease in TAWSS in this region suggests the flow reduction caused by the tapering cast to be constant regardless of changes to the flow dimensionless numbers.

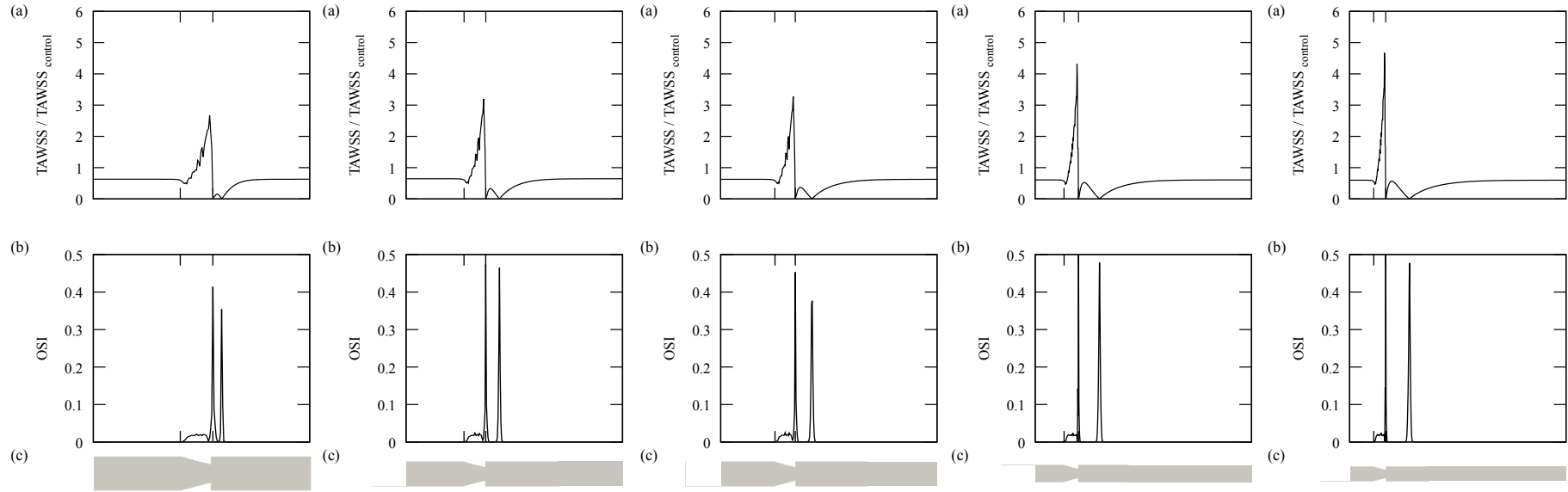


**Figure 6.3. Distributions of the (a) normalised time-averaged wall shear stress (TAWSS) and (b) oscillatory shear index (OSI) in the (c) different simulation cases.** Simulation cases S1-S5 are shown left to right. The flow direction is from left to right and the vertical lines on the plot axes indicate the start and end positions of the tapering device. The TAWSS was normalised against the value computed in the control geometry simulations ( $TAWSS_{control}$ ). The flow dimensionless numbers are given in Table 6.1. The axial length of each geometry was controlled to allow a sufficient flow development length downstream of the tapering cast.

### Frequency composition

The distributions of the first harmonic amplitude and phase were computed along the length of the S1, S2, S3, S4 and S5 models (Figure 6.4). As with the localisation metrics presented above, the distribution of the first harmonic components also showed segmentation of the geometry into the low, high and oscillatory shear stress regions. A key note is that flow is shown to have recovered in all simulations with the first and second harmonic amplitudes recovering to the pre-constriction values before the geometry outlet (Figure 6.4 and Figure 6.5). The reader is referred to Section 2.4 for a description of the Fourier transform amplitudes and phases.

A key difference between simulations was found in the first and second harmonic amplitudes downstream of the tapering cast. An increase in these harmonic amplitudes in the oscillatory region above that of the low shear stress region becomes apparent only with increasing Reynolds and Womersley numbers. This is an important result as it suggests an entirely different flow environment in the downstream region of models of larger Reynolds and Womersley numbers with magnitudes of flow reversal not seen in the other models. In addition to this, the length downstream of the cast end before recovery to the upstream value increased with increasing Reynolds and Womersley numbers.

The rate of increase in first harmonic amplitude in the high shear stress showed an increase with larger Reynolds and Womersley numbers. This is thought to be a result of the same Reynolds number effects discussed with regard to the localisation metrics. Relative to the TAWSS, the first harmonic amplitude computed in the low shear stress region also showed a decrease with increasing Reynolds and Womersley numbers. This effect is due to the Womersley number increase and is explored further in Chapter 7.

The phase component was also shown to vary between simulations as a result of the Womersley number effects. This is most clearly seen in the low shear stress region. When considering the phase between models, it is important to note the periodicity of the phase component meaning the equivalence of values at  $-\pi$  and  $\pi$ . This periodicity is also clearly seen in the sudden change in the phase component along the length of the cast in the S3 model (Figure 6.4b).

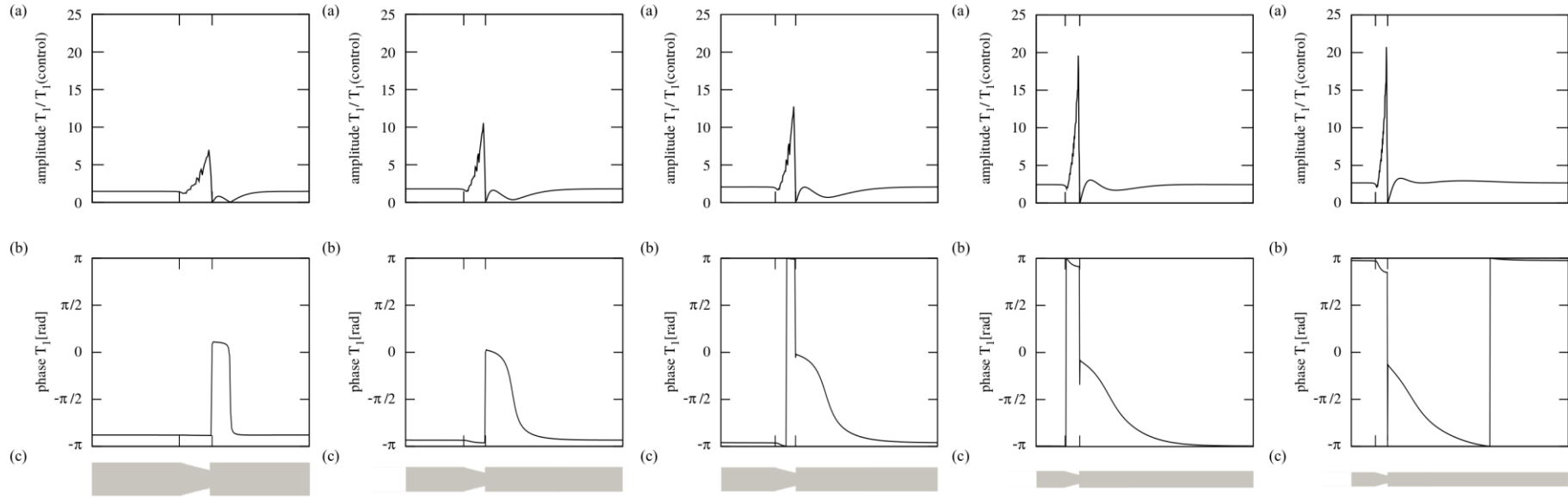


**Figure 6.4. Distribution of the first harmonic (a) amplitude and (b) phase of the wall shear stress signal along the length of the in the (c) different simulation cases.** Simulation cases S1-S5 are shown left to right. The flow direction is from left to right and the vertical lines on the plot axes indicate the start and end positions of the tapering device. The first harmonic amplitude was normalised against the value computed in the control geometry simulations. The flow dimensionless numbers are given in Table 6.1.

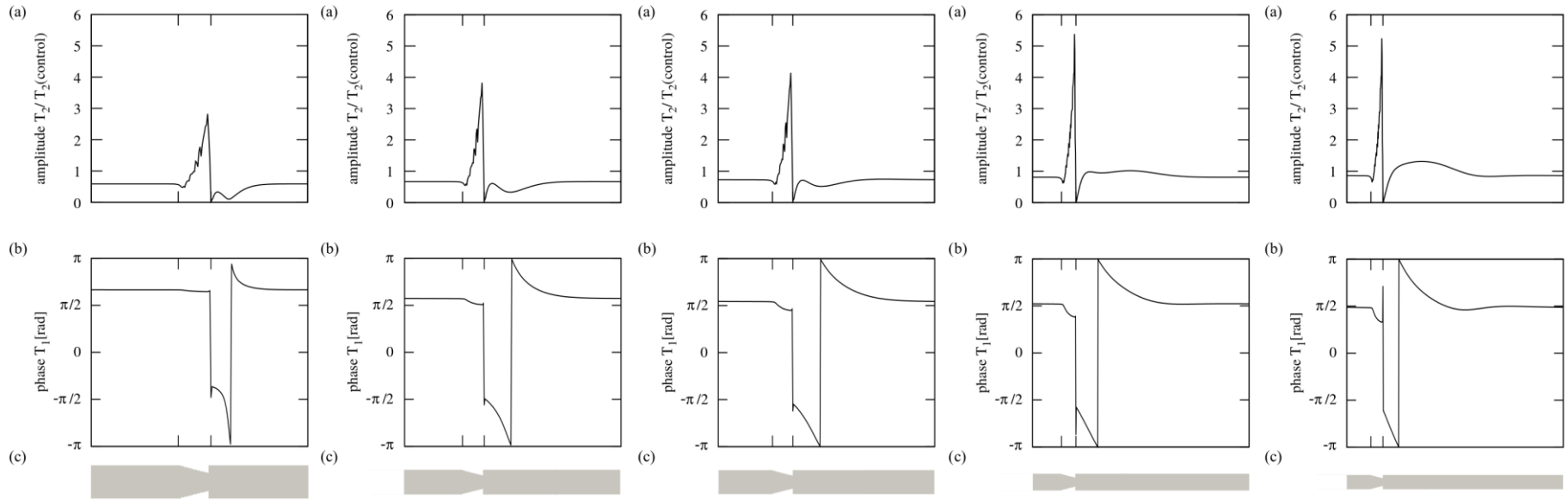


**Figure 6.5. Distribution of the second harmonic (a) amplitude and (b) phase of the wall shear stress signal along the length of the (c) S5 perivascular cast geometry.** The flow direction is from left to right and the vertical bold lines on the plot axes indicate the start and end positions of the tapering device. The first harmonic amplitude was normalised against the value computed in the control geometry simulations. The flow dimensionless numbers are given in Table 6.1.

The frequency composition of the WSS signals were computed in the S1 (Figure 6.6), S2 (Figure 6.7), S3 (Figure 6.8), S4 (Figure 6.9) and S5 (Figure 6.10) models. While the harmonic amplitudes varied throughout the oscillatory region, the figures presented here are illustrative of the typical differences in amplitude between the high, low, control and oscillatory shear stress regions.

An important finding of the mouse perivascular cast geometry is the similarity in higher harmonic amplitudes ( $n > 1$ ) in the high, low and control signals. Differences between the signals in the mouse geometry were shown only in the distributions of the zeroth and first harmonic amplitudes. In this regard, the key result of the dimensionless number simulations is the increasing second harmonic amplitude with increasing Reynolds and Womersley numbers in the oscillatory region. Considering the physical interpretation of the zeroth and first harmonic amplitudes, the similarity in the higher harmonics means that the signals in the low and high WSS regions differ only by the translation and magnification operations due to the variation of the zeroth and first harmonic amplitudes respectively. Differences in the second harmonic amplitude in the oscillatory region represents further variation in WSS signal.

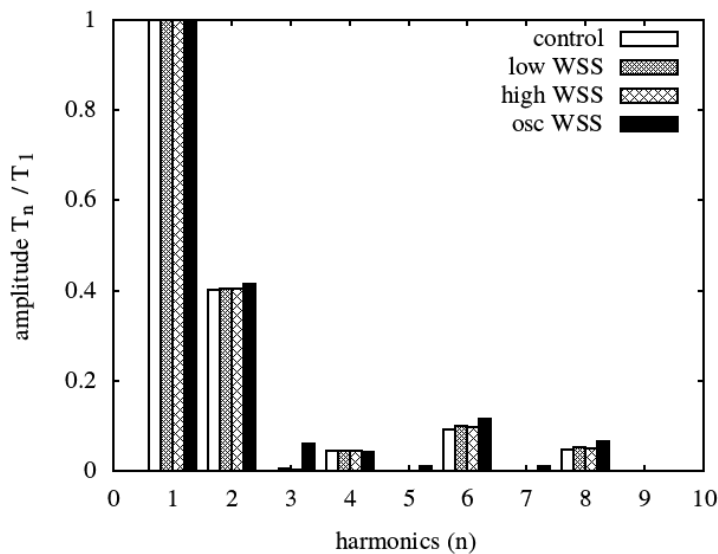


**Figure 6.6. Frequency composition of the wall shear stress signal at axial positions along the S1 perivascular cast geometry.** The waveforms were normalised by the respective first harmonic amplitudes and shown with the wall shear stress signal of the control geometry. Axial positions were chosen in the geometry to lie in the low, high and oscillatory shear stress regions.



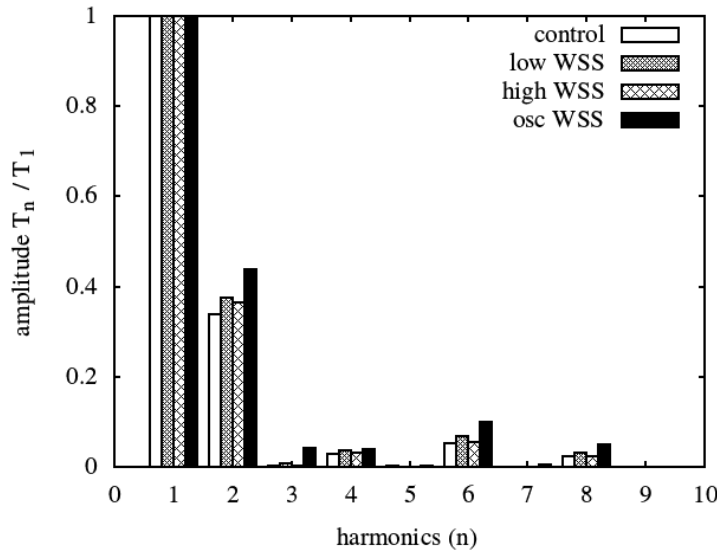


**Figure 6.7. Frequency composition of the wall shear stress signal at axial positions along the S2 perivascular cast geometry.** The waveforms were normalised by the respective first harmonic amplitudes and shown with the wall shear stress signal of the control geometry. Axial positions were chosen in the geometry to lie in the low, high and oscillatory shear regions.

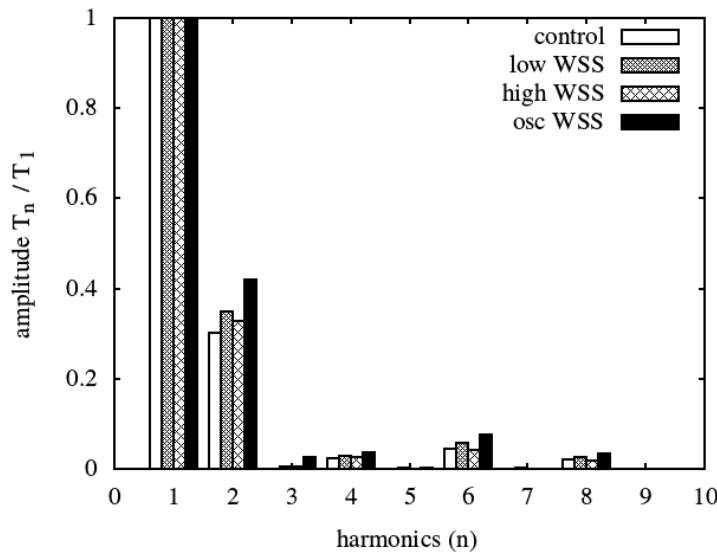


**Figure 6.8. Frequency composition of the wall shear stress signal at axial positions along the S3 perivascular cast geometry.** The waveforms were normalised by the respective first harmonic amplitudes and shown with the wall shear stress signal of the control geometry. Axial positions were chosen in the geometry to lie in the low, high and oscillatory shear regions.

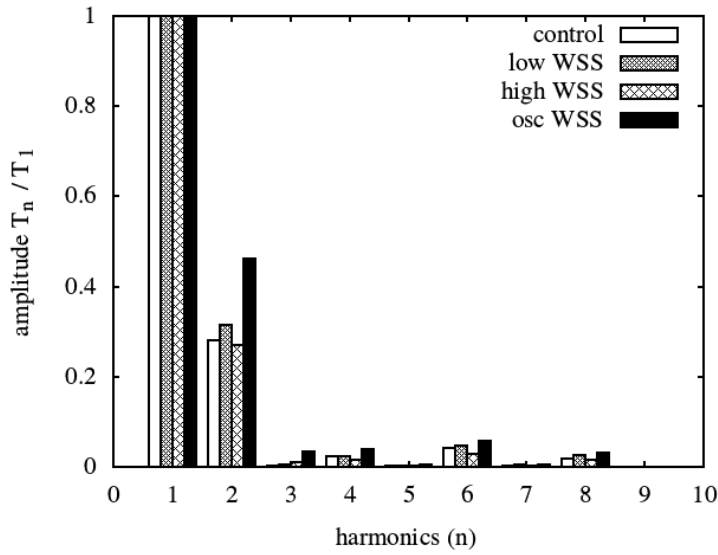


**Figure 6.9. Frequency composition of the wall shear stress signal at axial positions along the S4 perivascular cast geometry.** The waveforms were normalised by the respective first harmonic amplitudes and shown with the wall shear stress signal of the control geometry. Axial positions were chosen in the geometry to lie in the low, high and oscillatory shear regions.

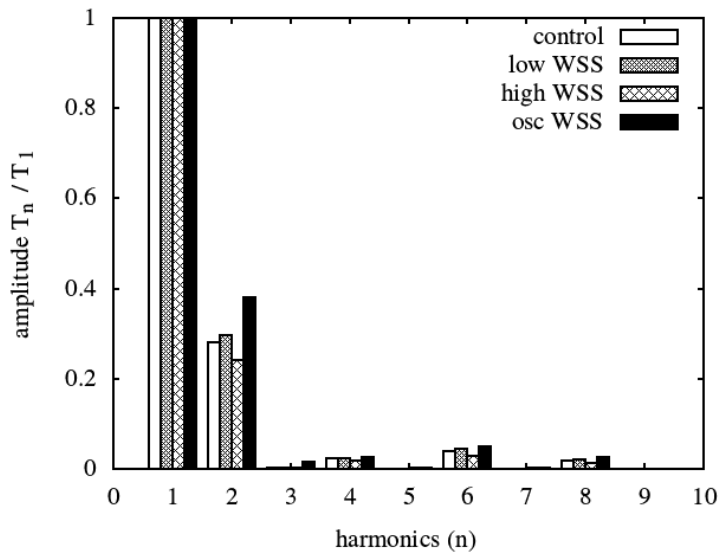


**Figure 6.10. Frequency composition of the wall shear stress signal at axial positions along the S5 perivascular cast geometry.** The waveforms were normalised by the respective first harmonic amplitudes and shown with the wall shear stress signal of the control geometry. Axial positions were chosen in the geometry to lie in the low, high and oscillatory shear regions.

## 6.4 Discussion

The definition of flow conditions at the simulation boundaries forms a significant challenge in fluid dynamics studies. The current chapter, therefore, works to clarify the effect of varying body force signals and dimensionless numbers on the WSS signal computed in the regions of the perivascular cast model approximated from Cheng *et al.* (2006).

A key result of this work is the appearance of clear scaling laws relating the components of the input and output waveforms. Simulations studying the effects of varying body force used a signal consisting only of the first harmonic. The computed WSS signals showed linear relationships between the first harmonic amplitudes of the body force and WSS signals. The gradients of these linear relationships were found to be region-specific in the perivascular cast geometry with approximate consistency throughout the low shear stress region and variation in the oscillatory shear stress region.

The analytical Womersley solution predicts the linear relationship for frequency components present in the input signal in a simple pipe. The relationship predicted by the analytical solution is, however, proportional only to the Reynolds and Womersley numbers (equation 6.1). The variation of the linear gradient and appearance of the higher harmonic terms in the oscillatory region suggests the effect of the constriction geometry. The gradients of the higher harmonic terms are also a function of position in the oscillatory region, decreasing with increasing distance from the cast end. These findings are attributed to the flow acceleration and WSS oscillation caused by the geometry taper and pulsatile flow nature.

The appearance of frequency components not present in the input is a common phenomenon throughout fluid dynamics studies of turbulent and transitional flows. The von Kármán vortex street is an example of this where the steady flow of a fluid around an obstacle can lead to oscillating flow structures downstream of the obstacle. This is an effect of the Reynolds number as inertial effects cause separation of the fluid from the rear-end of the obstacle and the oscillatory shedding of vortices from the top and bottom end of the obstacle. The oscillatory properties of the vortex street are also dependent on the Reynolds number.

Simulations investigating the effects of the body force signal were performed at Reynolds and Womersley numbers equal to 40 and 0.8 respectively. An additional simulation (S1) was performed at the same dimensionless numbers using the pressure waveform measured in the healthy mouse carotid artery (Artoli and Sequeira, 2006). As in the mouse simulations of Chapter 5, comparison of the WSS frequency composition between the control and oscillatory regions in this simulation showed elevation of the third harmonic amplitude. Elevations in the second harmonic amplitude was also suggested from simulations with higher dimensionless numbers. The consistency in elevation of the higher harmonic components in the oscillatory region suggests the extension of scaling relationships to complex waveforms.

Another key result of this chapter is the change in distribution of the zeroth, first and second harmonic amplitudes with increasing Reynolds and Womersley numbers. Comparison of the higher harmonic amplitudes between simulations in each region, however, showed consistency. This suggests the particular WSS frequency composition to be a function, mainly, of the geometry when normalised by the first harmonic amplitude. The differences in the amplitudes of the frequency composition are also suggested to be a function of the Reynolds and Womersley numbers.

#### Extrapolation to animal models

A key note throughout this chapter is that the simulations are not representative of any specific animal model or any biological mechanism that may lead to an altered arterial flow rate waveform. The simulations were not performed in animal models of the perivascular cast because of the large computational times needed. Taking the human common carotid artery as an example, blood flow is defined by a Reynolds number of 1200 and Womersley number of 4.494. The accurate use of periodic boundary conditions also requires a sufficient development length downstream of the cast. Following the numerical study of Durst *et al.* (2005), this would result in a geometry axial length of approximately 850 diameters. Simulation of the human perivascular cast geometry is, therefore, impractical. This forms a major limitation of this chapter as a comparison of the WSS signals in the perivascular cast model of large animals would provide a deeper understanding of blood flow haemodynamics in the animals. The potential need for this work is discussed in Chapter 7. The results of this chapter

can, however, be extrapolated to animal models as variation of the body force waveform may be seen from changes to the pulse wave velocity (PWV) discussed in Section 4.4.

With increased PWV, the forward-travelling pressure waves are propagated faster. These waves are reflected back sooner and alter the arterial pressure waveform by combination with the forward-travelling waves of the following pulse period (O'Rourke and Yaginuma, 1984; Nichols *et al.*, 1998; van de Vosse and Stergiopulos, 2011; Pereira *et al.*, 2015). The remainder of this discussion will deal with the possible biological mechanisms leading to altered PWV and arterial pressure waveforms in animal models of atherosclerosis.

In order to study the mechanisms relevant to the development and progression of the atherosclerotic plaque, a number of methods have been proposed to induce disease in the mouse model. Table 6.2 provides a list of mouse models with their expected effects on the PWV. These include the manipulation of the mouse genetic background (Veseli *et al.*, 2017) and the placement of a perivascular device to manipulate fluid flow (Winkel *et al.*, 2015). Arterial stiffness has also shown a relationship with vascular aging, with differences in structural composition between young and elderly vessels (Mikael *et al.*, 2017). These models are expected to produce varying effects on the vessel properties and, based on the theories of pulse wave propagation and wave reflection discussed above, will lead to different time-varying waveforms of flow and pressure.

Feaver *et al.* (2013) have shown a sensitivity of endothelial cells to the zeroth and first harmonic amplitudes through the activity of various inflammatory markers including NF- $\kappa$ B, a pro-inflammatory transcription factor. Increases in Reynolds and Womersley numbers are also seen in mammals with increasing body size according to allometric scaling (Weinberg and Ethier, 2007; Dawson, 2014). Taken together with the work of Feaver *et al.* (2013), the results of this chapter clearly highlight the role of dimensionless numbers in the localisation of inflammation. This is shown when considering the effect of dimensionless numbers on vessel haemodynamics and the predilection sites common in each animal model. Compared to the human, small animal models show differences in plaque localisation with a lack of coronary lesions

in the mouse (Nakashima *et al.*, 1994; Hu *et al.*, 2005) and only modest plaque formations in the rabbit abdominal aorta (Fan and Watanabe, 2000). The hypercholesterolaemic pig, on the other hand, shows similar predilection sites to the human with lesions forming in the abdominal aorta and proximal segments of the coronary arteries (Hamamdzic and Wilensky, 2013; Al-Mashhadi *et al.*, 2018).

Differences in vascular tone are also regulated through the action of the endothelial and vascular smooth muscle cells, involving the complex action and interaction of the cells and several vasoactive components (Cunningham and Gotlieb, 2004; Sandoo *et al.*, 2010; Mallat *et al.*, 2017). A special mention is made of the use of angiotensin II because of its function in the Cheng *et al.* (2006) study. Here, infusion of angiotensin II resulted in an increased occurrence of intraplaque haemorrhages compared to the control group in regions upstream of the perivascular cuff. The infusion was used to test the hypothesis that increased blood pressure shifts the plaque type towards a more-vulnerable composition. However, in addition to the increased average blood pressure, the change in vascular tone would also result in differences in the time-varying waveforms of pressure and flow, as explained by the pulse wave velocity. It should be noted that vasoactive substances such as angiotensin II do not only affect vascular tone and pressure waveforms but also play complex roles in the inflammatory process (Schmidt-Ott *et al.*, 2000; Cunningham and Gotlieb, 2004). It remains possible that the shift towards the vulnerable plaque composition seen in Cheng *et al.* (2006) is largely a result of these changes to the inflammatory process.

**Table 6.2. Mouse models of atherosclerosis and implications in terms of PWV.**

Citation	Mechanism	Comments	Implications for PWV
(Cheng <i>et al.</i> , 2006)	Tapering cast placed around the carotid artery	Oscillatory shear stress region downstream of cast with development of a stable-looking plaque. Low shear stress region upstream of the cast with development of a vulnerable-looking plaque.	Reduction in cross-sectional area (Mohri <i>et al.</i> , 2014) leads to an increased PWV Changes in wave reflection properties at the site of cast placement
(Cheng <i>et al.</i> , 2006)	Angiotensin infusion	Shifts plaque to a more vulnerable state with increased number of intraplaque haemorrhages	Vasoconstriction as a method of regulating flow rate leads to increased PWV
(Chen <i>et al.</i> , 2013)	Tandem ligation	Ruptured, vulnerable-looking and stable plaque types were described in the different regions of the carotid artery model.	Reduction in cross-sectional area leads to an increased PWV Changes in wave reflection properties at the site of ligation
(Calara <i>et al.</i> , 2001)	Ageing	Observed plaque rupture and coronary thrombosis in long-term HFD study.	Changes in vessel composition with ageing process resulting in increased vessel stiffness
(Van der Donckt <i>et al.</i> , 2015)	Elastin fragmentation	Spontaneous plaque rupture with several disease characteristics resembling human lesions.	Changes in vessel composition leading to decreased vessel stiffness

## 6.5 Conclusions

The numerical tool developed and implemented in Chapters 3 and 4 was applied to the perivascular cast geometry approximated from Cheng *et al.* (2006). The effect of boundary conditions on the WSS was explored through the simulation of varying body force signals and the dimensionless numbers governing pulsatile flow. The body force was modelled as a varying first harmonic amplitude with fixed Reynolds and Womersley numbers. The dimensionless numbers study varied the Reynolds and Womersley numbers while keeping the time-variation of the body force signal constant. The WSS was analysed in terms of its frequency composition considering its ability to capture all spatial and temporal details of the WSS signal.

The conclusions of this chapter are expressed in terms of the aims set out in the introduction:

- 1) *Are the current atherosclerosis localisation metrics able to identify the differences in the waveform of wall shear stress with varying body force signal?*

The time-averaged WSS metrics showed zero sensitivity to the body force signal. Minute fluctuations in the OSI and RRT metrics found at the point of peak OSI were attributed to negligible numerical errors in the simulation.

- 2) *Are the differences in wall shear stress signal shown between regions of the mouse perivascular model dependent on the imposed flow boundary conditions?*

The wall shear stress signal computed in the perivascular cast geometry showed a dependence on both the frequency composition of the imposed body force signal and the dimensionless numbers. This dependence is shown in the analytical Womersley solution for pulsatile flow in a straight pipe geometry. Further to this, clear region-specific scaling laws were computed in the perivascular cast model approximated from Cheng *et al.* (2006) with linear scaling of the first harmonic amplitudes of the body force and WSS signals. A quadratic scaling was also found between the first harmonic amplitude of the



body force signal and a WSS second harmonic amplitude emerging in the oscillatory region downstream of the cast.

Extension of the body force signal to the arterial pressure waveform measured in the mouse carotid artery (Artoli and Sequeira, 2006) showed elevations in the higher harmonic composition ( $n > 1$ ) of WSS between the regions. This suggests the extension of this scaling law between the lower and higher harmonic components. The presence and extrapolation of these scaling laws means that the WSS signals can be predicted for specific geometries.

Considering the results discussed here, an interesting experiment would be to study the effects of the vessel haemodynamics on the endothelial cells of different animals. This study could be performed in a hypothetical environment where the cardiac output of different animals could be controlled at will. In this way, mammalian endothelial cells could be exposed to signals of varying zeroth and first harmonic amplitudes. Exposing the human arterial network to the vessel haemodynamics of mice, for example, could be used to verify the predilection sites of atherosclerosis.

From this chapter, it can be concluded that the WSS signal shows a region-specific dependence on the input body force signal and dimensionless numbers. The most apparent relationship between the dimensionless numbers and WSS distribution is the elongation of the recirculation region with increasing inertial effects. The increasing Womersley number also resulted in a phase delay between the body force and WSS signals. While the simulations do not represent any animal model or biological mechanism, the findings discussed here can be extrapolated to animal models as the increase in Reynolds and Womersley numbers is shown by allometric scaling methods. Chapter 7 discusses the significance of these relationships in animal models.

# Wall shear stress in the arteries of mammals

---

### Abstract

Considering the role of haemodynamics in plaque formation, progression, and rupture (Cunningham and Gotlieb, 2004; Slager *et al.*, 2005a, 2005b; Cheng *et al.*, 2006; Davies, 2009; Chiu and Chien, 2011), a complete analysis of the wall shear stress is essential in understanding the rupture event in humans and the absence thereof in mice (Zhou *et al.*, 2001; Schwartz *et al.*, 2007). Following allometric scaling laws, the difference in body mass between the mouse and human is expected to cause differences in the wall shear stress time-variation as a result of large differences in the dimensionless numbers governing fluid flow. The inflammatory response of human and porcine endothelial cells has also shown a sensitivity to the time-variation of the wall shear stress signal (Himburg *et al.*, 2007; Feaver *et al.*, 2013). The current chapter, therefore, aims to explore the hypothesis that the difference in animal size across mammals is related to the frequency composition of the time-varying wall shear stress.

In the present work, simulations were performed in a straight vessel segment approximating the healthy common carotid artery of several different species. The mouse, rabbit and human models were chosen alongside hypothetical animal1 and animal2 models such that the body masses were equally distributed on a logscale between the mouse and human. The dimensionless numbers and simulation parameters relevant to each animal were approximated from allometric scaling laws (Dawson, 2014). The wall shear stress signal was analysed in terms of its frequency composition and showed a decrease of the zeroth and first harmonic amplitudes with increasing animal body size. A key result of this study is the difference in scaling relationships computed in the zeroth and first harmonic amplitudes. This showed decreasing significance of the time-varying component in the signal with increasing animal body

size. The shear-thinning nature of blood, simulated with the Carreau-Yasuda viscosity model, also showed negligible significance in this relationship. Assumptions made of the fluid viscosity affected only the peak systolic velocity.

Using the computed allometric scaling laws, estimation of the wall shear stress signal in the minipig suggests consistency with the signal found in the human. The scaling laws computed here show the zeroth and first harmonic amplitudes to be almost equal between the two species. The rare occurrence of plaque rupture in atherosclerotic minipigs despite haemodynamic similarities with humans, suggests the influence of factors other than wall shear stress in plaque rupture. This conclusion then highlights the significance of genomic or circumferential stretch differences between the species. The effects of these genomic or circumferential stretch differences may also be relevant in the absence of plaque rupture in the atherosclerotic mouse.

## 7.1 Introduction

Since the early 1900s, animal models have been studied extensively in order to formulate an understanding of atherosclerosis and its underlying mechanisms (Konstantinov and Jankovic, 2013). A wealth of knowledge has been gained from these studies with novel treatments being devised and tested for application in human disease. The popularity of animal models comes from the ability to control key disease risk factors such as diet, genetic susceptibility and environmental contributors (Daugherty, 2002; Lee *et al.*, 2017). Mice do not develop atherosclerotic lesions, even when fed a high-fat diet (Paigen *et al.*, 1987). Following the availability of genetically-altered mice with a greater susceptibility to lesion development, however, the number of publications in the field of murine atherosclerosis has seen a remarkable increase (Daugherty *et al.*, 2009). Veseli *et al.* (2017) provide an excellent review of mouse models of atherosclerosis, nicely summarising methods of disease induction and the resulting plaque characteristics. Getz and Reardon (2012) and Shim *et al.* (2016) also provide excellent reviews of large animal models of atherosclerosis, detailing their advantages and limitations.

Hypercholesterolaemia can be induced in the mouse by the knockout of genes affecting cholesterol homeostasis and endocytosis of the cholesterol-rich low-density

lipoprotein (LDL). Deficiency of the Apolipoprotein E (ApoE) glycoprotein or LDL receptor by gene knockout is commonly employed in mice to cause significant changes in the plasma lipid profile (Piedrahita *et al.*, 1992; Plump *et al.*, 1992; Ishibashi *et al.*, 1993, 1994). This effect triggers lipid accumulation in the arterial wall, leading to chronic inflammatory repair processes consistent with the “response to injury” hypothesis presented in Ross (1993). Arterial inflammation and lipid accumulation in the mouse creates lesions with several similarities to human atherosclerosis; most importantly, in the sequential progression from xanthoma to the advanced lesion (Nakashima *et al.*, 1994).

The occlusive thrombosis is seen as the cause of clinical events in the human and so is key in creating a complete animal model (Chen *et al.*, 2013). The absence of plaque rupture and thrombosis, therefore, forms a major limitation of murine models of atherosclerosis (Zhou *et al.*, 2001; Schwartz *et al.*, 2007; Bentzon and Falk, 2010; Finn *et al.*, 2010; Bentzon *et al.*, 2014). It is important to note that the work in this PhD will adhere to the terminology defined in Schwartz *et al.* (2007) in which plaque rupture refers only to situations where disruption of the fibrous cap leads to exposure of the necrotic core. The superimposed thrombosis then forms from the exposure of thrombogenic material in the necrotic core to blood flow. A matter of particular interest to this PhD is the absence of rupture and occlusive thrombosis in mice, even in lesions resembling the rupture-prone thin-cap fibroatheroma (TCFA) seen in humans.

Computational fluid dynamics studies and allometric scaling arguments have shown the magnitudes of the time-averaged wall shear stress (TAWSS) to be twenty-times higher in the mouse than in the human (Greve *et al.*, 2006; Suo *et al.*, 2007; Weinberg and Ethier, 2007; Cheng *et al.*, 2007). This is an interesting observation as, despite the differences in TAWSS magnitude, the vascular networks of mice still show localisation of plaques to regions predicted by relatively low and oscillatory shear stress (Suo *et al.*, 2007). Given the difference in vessel size and heart rate with animal size, the Reynolds and Womersley numbers that are key in defining fluid flow are also expected to vary greatly between animals (Suo *et al.*, 2007; Weinberg and Ethier, 2007; Trachet *et al.*, 2009). Variability in the blood aggregation properties and flexibility of red blood cells also causes differences in blood viscosity between species (Windberger *et al.*, 2003; Windberger and Baskurt, 2007). A change to the frequency

composition of the wall shear stress (WSS) signal then becomes clear when considering fluid flow to be more inertial and pulsatile in larger animals. The differences in WSS signal frequency composition between animals presents an interesting research topic given their importance to the expression of inflammatory markers (Himburg *et al.*, 2007; Feaver *et al.*, 2013).

Hypothesis and aims:

The current chapter explores the hypothesis that the difference in animal size across mammals is related to the frequency composition of the time-varying wall shear stress.

The following aims were set out to test the hypothesis:

- 1) Are there similarities/differences in the frequency composition in the control vessel of animals of different body size?
- 2) Is the viscosity model relevant to the computed wall shear stress signals in the common carotid artery?

## 7.2 Methods

To better understand the local haemodynamics in the arteries of mammals, simulations were performed in straight pipe segments approximating the healthy common carotid artery in five different animal models. The dimensionless numbers defining the flow conditions in each animal model were approximated from the animal body weight using allometric scaling laws (Dawson, 2014). Viscosity model parameters were also approximated from the animal body weight using an assumed linear scaling relationship.

### 7.2.1 Allometric scaling

Between mammals, variation of haemodynamic parameters has previously been shown to occur in relation to the animal body mass through allometric scaling. A key result of this scaling theory is the idea that the cardiovascular system of all mammals follows the same general “design” (West *et al.*, 1999; Dawson, 2014). The design appears to be optimized to account, most importantly, for the animal’s body size. From an engineering perspective, an increasing body size demands a larger heart as a greater volume of blood needs to be pumped a greater distance to reach the organs. In larger

mammals, the greater heart size means an increased blood volume in the ventricles and so, a greater amount of time is required in each contraction to clear the fluid. This is reflected in the decreasing heart rate with increasing body size. The larger body sizes also demand greater vessel lengths. From the Hagen-Poiseuille equation, the greater vessel lengths result in an increased vascular resistance. Again, considering the Hagen-Poiseuille equation, the vessel radius can be used as a mechanism of regulating this undesirable increase in vascular resistance.

The logic-based arguments presented here were shown experimentally to follow scaling laws in the cardiac mass (Prothero, 1979), heart rate (Westerhof, 1994) and vessel diameter (Holt *et al.*, 1981). An interesting result is that the scaling relationships also satisfy the metabolic demands of the animal through the heart rate parameter (Schmidt-Nielsen, 1984; Westerhof and Elzinga, 1993) while maintaining a turbulence-free environment through regulation of the Reynolds number. Combinations of the base parameters discussed here are used in allometric scaling arguments to determine the relationships between several other parameters and the body mass (Weinberg and Ethier, 2007).

Measurements of haemodynamic parameters, such as the WSS, can then be extrapolated between animals of different species without the need for invasive measurements (Greve *et al.*, 2006; Weinberg and Ethier, 2007). These relationships are defined through allometric scaling laws:

$$f = a_c M^b \quad (7.1)$$

where the parameter of interest  $f$  is given in terms of the animal body mass  $M$ , the body mass exponent  $b$  and a constant  $a_c$ .

The allometric scaling laws were employed here to estimate values of the dimensionless numbers relevant to each animal model. As discussed in Section 4.5, the dimensionless numbers form a key set of parameters in simulation studies as they govern the nature of fluid flow. Dynamic similarity between simulations and the physical case is also necessary to ensure that simulations are representative of flow in the arteries.

Five simulation cases were used with animal body masses chosen to be equally distributed on a logscale between the mouse and human parameters (Table 6.1). These simulation cases include the mouse, rabbit and human and hypothetical animal models termed “animal1” and “animal2”. All values relevant to the mouse and human were computed from physical parameters obtained from the literature. The Reynolds and Womersley numbers were computed in Section 4.5 and used to calculate the constants and body mass exponents for the dimensionless numbers. The body mass exponents of the Reynolds number and Womersley number were computed as 0.30 and 0.19 respectively. The body masses of the animals were then used to estimate values of the Reynolds number and Womersley number for use in each simulation model.

Scaling arguments commonly assume a constant viscosity model by considering the high shear rate numbers present in the aorta (Section 4.5). Given the uncertainty in the literature regarding the validity of a constant viscosity assumption (Section 2.5), the simulations performed here will employ the Carreau-Yasuda viscosity model (equation 2.17). A comparison of model parameters between the mouse and human, however, shows differences in the asymptotic limits of each viscosity model. This is explained by the varying aggregation and flexibility properties between the mouse and human red blood cells (Amin and Sirs, 1985; Windberger *et al.*, 2003; Windberger and Baskurt, 2007). While the low shear rate viscosity data provided Windberger and Baskurt (2007) showed no correlation with animal body mass, a linear scaling law was applied here in order to estimate the viscosity model parameters. Each parameter of the Carreau-Yasuda viscosity model was estimated by linear interpolation between the mouse (Vogel *et al.*, 2003; Windberger *et al.*, 2003) and human (Boyd *et al.*, 2007; Bernabeu *et al.*, 2013) parameter sets. The resulting viscosity-shear rate relationships are shown in Figure 7.1 with the parameters being presented in physical units in Table 7.2.

**Table 7.1. Dimensionless numbers based on the allometric scaling laws discussed above.** The Reynolds number,  $Re$ , and Womersley number,  $\alpha$ , were approximated from the allometric scaling laws using the animal body mass  $M$ . Simulation parameters of spatial,  $\Delta x$ , and temporal,  $\Delta t$ , resolution were computed according to the dimensionless numbers. Hypothetical animal models, animal1 and animal2, were created to achieve equal distribution of animal body masses between the mouse and human on a logscale.

Animal	Body mass $M$ [kg]	$Re$	$\alpha$	$\Delta x$ [mm]	$\Delta t$ [ $\mu s$ ]
mouse	0.025	105	0.96	0.01225	1.15
animal1	1	323	1.96	0.0311	2.87
rabbit	3.5	472	2.49	0.0329	3.17
animal2	20	803	3.48	0.331	2.84
human	75	1200	4.49	0.025	2.50

**Table 7.2. Viscosity model parameters based on the allometric scaling laws discussed above.** A linear interpolation between literature-based values of the mouse and human viscosity models was performed by body mass to obtain viscosity parameters. A description of viscosity model parameters is given in Section 2.5. Hypothetical animal models, animal1 and animal2, were created to achieve equal distribution of animal body masses between the mouse and human on a logscale.

Animal	Body mass $M$ [kg]	$\mu_0$ [mPa.s]	$\mu_\infty$ [mPa.s]	$\lambda$ [s]	$m$	$a$
mouse	0.025	14.5	3.265	0.1839	0.5864	2.707
animal1	1	16.4	3.268	0.2881	0.5890	2.680
rabbit	3.5	21.2	3.276	0.5554	0.5957	2.611
animal2	20	53.3	3.328	2.320	0.6399	2.156
human	75	160	3.5	8.2	0.7872	0.64



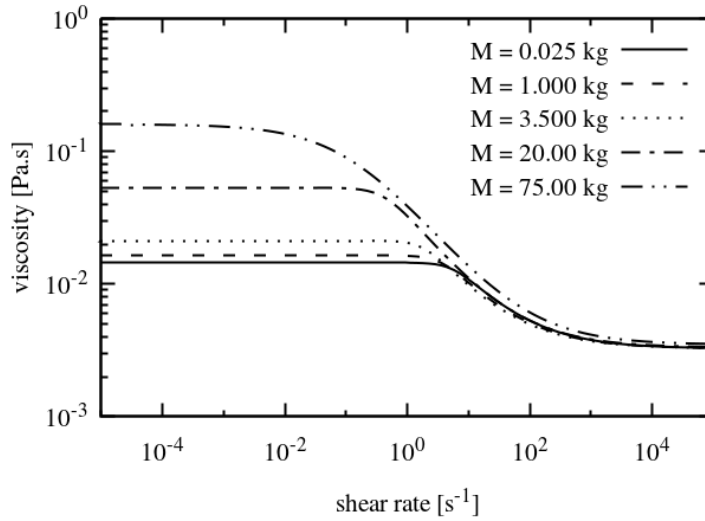


**Figure 7.1. Viscosity model parameters were estimated using an assumed linear scaling law between the mouse and human parameters.** The body mass,  $M$ , was used in a linear interpolation for values of each viscosity model parameter in the Carreau-Yasuda viscosity model.

### 7.2.2 Simulation setup

The simulation setup was largely similar to that used in Chapter 5 with key differences being the choice of parameters. Models were defined according to each animal body mass with the dimensionless numbers calculated from the allometric scaling relationships discussed above. The lattice resolution and lower limit of the relaxation parameter were then chosen such that the peak axial velocity in a simple pipe geometry would not exceed 0.07 in lattice units. These considerations were made in order to minimise errors resulting from the truncation of equilibrium populations (equation 3.5). The resulting parameter sets are given in Table 6.1.

Viscosity model parameters were computed in physical units using the scaling relationship as described above (Table 7.2). Following the unit conversion step, viscosity model parameters were obtained in lattice units for use in the simulation. The viscosity model parameters were then fed into the Python script discussed in Section 4.3 to compute values of the local viscosity as a function of the first-order momentum flux tensor.

Solid boundaries were treated with the standard bounceback approach detailed in Section 3.2. The periodic boundary condition was employed at the inlet and outlet boundaries alongside a time-varying body force term applied at all lattice sites. The frequency composition of the body force term was obtained from a curve-fitting method using the normalised pressure profile measured in the healthy mouse carotid artery (Artoli and Sequeira, 2006). Consistency of the pressure waveform was assumed across all models given the similarity of flow and pressure waveforms in the ascending aorta of different animals (Noordergraaf *et al.*, 1979). The body force term was obtained by multiplying the frequency composition with a body force amplitude derived from the Newtonian assumption and the analytical solution of velocity.

### 7.2.3 Simulations performed

All simulations were performed in the straight pipe geometry with constant radius.

Preliminary simulations were performed to study the effects of an increasing Womersley number on the WSS signal. A sinusoidal body force term was implemented with each simulation having a different period of oscillation to model flows with varying Womersley number.

Simulations were performed with the Newtonian and non-Newtonian viscosity models in each animal model. The dimensionless numbers were varied to capture features of blood flow relevant to the common carotid artery.

As in Chapter 5, simulations were terminated once the velocity profile measured at the geometry axial centre had converged with the profiles measured in the previous pulse period (equation 3.14). The convergence criterion for this termination event was set to  $10^{-5}$ . Once the criterion had been satisfied, the simulation would run for one more pulse period to compute and write all desired observables. Frequency analysis of the WSS signal was performed on the axial component of the circumferentially averaged traction vector (Section 2.4).

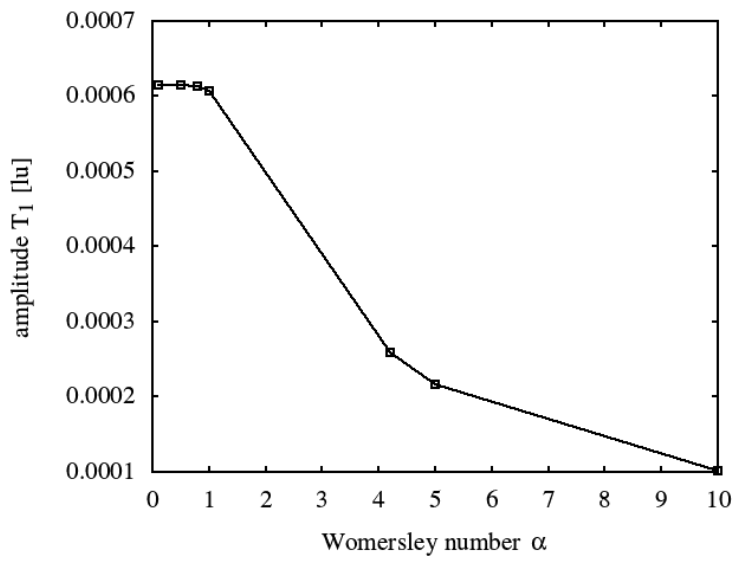
## 7.3 Results

Each animal model was analysed in terms of the circumferentially-averaged traction vector, both in relation to the time-averaged shear metrics and its instantaneous value over the pulse period. A comparison of the frequency composition of the instantaneous values was also performed to identify any potential differences in the time-varying nature of the WSS between the animal models of disease. The reader is referred to Section 2.4 for an overview of the Fourier series amplitude and phase components.

### 7.3.1 Effects of increasing Womersley number

Preliminary simulations into the effects of the Womersley number on the flow field were performed in a simple pipe geometry. Control of the Womersley number was achieved through variation of the pulse period  $T$  with a sinusoidal body force profile. A known result of the increasing Womersley number is the phase lag between the WSS and body force signals. This result is clear from the definition of the Womersley number (4.14) as increasing frequencies of pulsation mean shorter times for the development of the parabolic velocity profile. Further to this, the simulations performed here also showed a decrease in the first harmonic amplitude in the WSS signal with increasing Womersley number (Figure 7.2). The effect can also be explained by the decreased period of oscillation preventing the full development of the parabolic velocity profile. The decreased first harmonic amplitude is then clear from the reduction in wall shear rate.

(a)



(b)

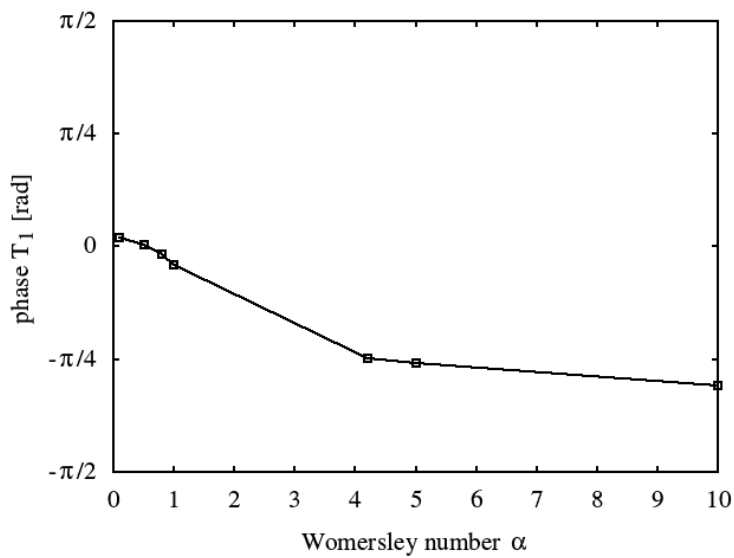


**Figure 7.2. First harmonic (a) amplitude and (b) phase of the wall shear stress signal computed in preliminary studies into the effect of the Womersley number.** A sinusoidal body force was simulated in a simple pipe of constant radius. The Womersley number  $\alpha$  was varied through control of pulse period  $T$ . Increasing the Womersley number resulted in a decrease of first harmonic amplitude with an increasing phase delay between the body force signal and the resulting wall shear stress signal.

### 7.3.2 Peak systolic velocity

The allometric scaling arguments of Schmidt-Nielsen (1984) and Weinberg and Ethier (2007) show consistency of the peak systolic velocity among all mammals. This was found in experimental measurements taken in the mouse and human aortas in Lacy *et al.* (2001) and Khir *et al.* (2001), respectively. Simulations performed in this study also support the allometric scaling argument with a near-zero body mass exponent. The computed velocities were also approximately constant around  $0.7 \text{ ms}^{-1}$  (Figure 7.3), showing good agreement with the velocities measured in the literature.

As with the steady flow simulations shown in Figure 4.9, the use of the Carreau-Yasuda viscosity model showed an approximately 10% decrease in peak velocity relative to the Newtonian viscosity assumption. This result was consistent across all animals. The near-zero body mass exponent was also found with the Newtonian viscosity assumption suggesting the use of a constant viscosity approximation to be valid in pulsatile flow through a simple pipe geometry.

**Table 7.3. Allometric scaling parameters for the peak systolic velocity computed using the Newtonian and Carreau-Yasuda viscosity models.** Viscosity model parameters were obtained assuming a linear interpolation of viscosity model parameters between those available in the literature for the mouse and human. Simulation Reynolds and Womersley numbers were obtained from allometric scaling laws derived from the values computed for the mouse and human. Consistency of the body mass exponents with both the Newtonian and non-Newtonian viscosities suggest that blood can be modelled as a Newtonian fluid.

	$a_c$	$b$	$R^2$
Newtonian	0.6927	-0.03	0.95
Non-Newtonian	0.7853	-0.019	0.94

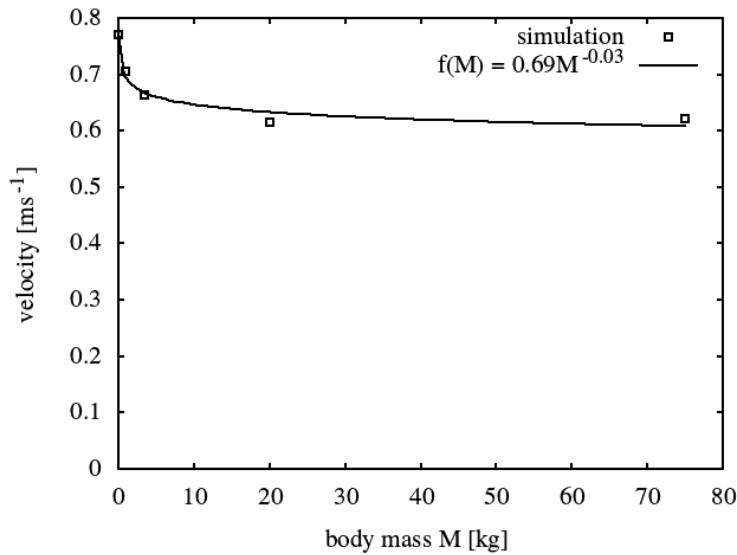


**Figure 7.3. Allometric relationship of animal body mass with the peak systolic velocity computed from the Carreau-Yasuda viscosity model.** The body mass exponent was computed from simulation results as  $b = -0.03$  with  $R^2 = 0.95$ . Simulations were performed in the control vessel with the Reynolds and Womersley numbers computed through allometric scaling laws and the viscosity model parameters being estimated from a linear scaling relationship. The small body mass exponent and approximate consistency of the velocity around  $0.7 \text{ ms}^{-1}$  indicate simulation validity.

### 7.3.3 Time-averaged wall shear stress

The body mass exponent of the time-averaged wall shear stress (TAWSS) computed from the allometric scaling arguments is  $-0.375$  (Weinberg and Ethier, 2007). Greve *et al.* (2006) show strong agreement with these results from magnetic resonance imaging data in the mouse, rat, dog and human. The body mass exponent of the TAWSS computed from simulations performed here was  $-0.3$  (Figure 7.4 and Table 7.4). The slight difference in value is attributed to the difference in the body mass exponent of the Reynolds and Womersley numbers between allometric scaling arguments and those used in the simulations performed here. The exponents used here were interpolated from the Reynolds and Womersley numbers computed in the mouse and human carotid arteries in Section 4.5. The viscosity model showed negligible effect on the TAWSS with the same body mass exponents being computed from Newtonian and Carreau-Yasuda models.

From a physical perspective, the decrease in TAWSS with increasing animal size shown in Figure 7.4 is entirely expected. This is most clear if looking at the Newtonian viscosity assumption where there is a constant peak velocity across mammals. A constant peak velocity while increasing the vessel radius results in decreased magnitudes in the shear rate profiles. Following from the definition of the WSS (2.8), the lower shear rates result in lower shear stresses.

**Table 7.4. Allometric scaling parameters for the time-averaged wall shear stress computed using the Newtonian and Carreau-Yasuda viscosity models.** Viscosity model parameters were obtained assuming a linear interpolation of viscosity model parameters between those available in the literature for the mouse and human. Simulation Reynolds and Womersley numbers were obtained from allometric scaling laws derived from the values computed for the mouse and human.

	$a_c$	$b$	$R^2$
Newtonian	5.1637	-0.3	1
Non-Newtonian	5.1392	-0.3	1

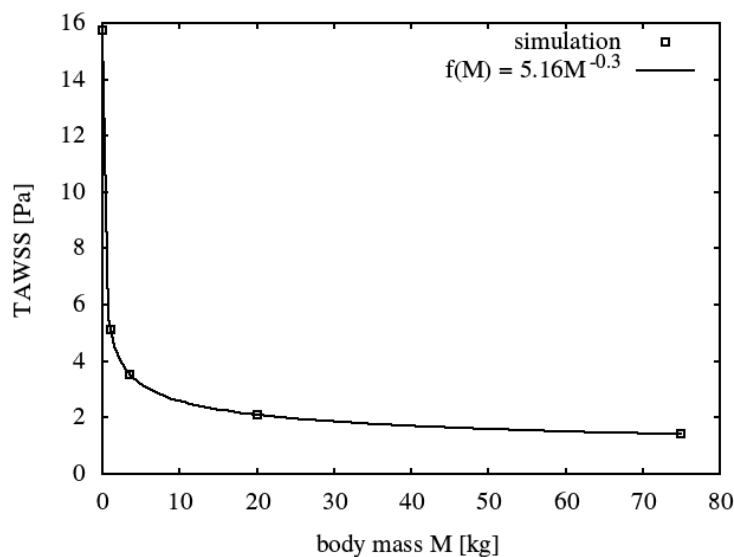


**Figure 7.4. Allometric relationship of animal body mass with the time-averaged wall shear stress (TAWSS) computed from the Carreau-Yasuda viscosity model.** The body mass exponent was computed from simulation results as  $b = -0.3$  with  $R^2 = 1$ . Simulations were performed in the control vessel with the Reynolds and Womersley numbers computed through allometric scaling laws and the viscosity model parameters being estimated from a linear scaling relationship.

#### 7.3.4 Frequency composition

The body mass exponent of the first harmonic amplitude was computed from the simulations performed here as -0.41 (Figure 7.5 and Table 7.5). This forms a key result of the control vessel simulations as the body mass exponents of the zeroth (TAWSS) and first harmonic amplitudes are different. The difference in body mass exponents shows that, relative to the TAWSS values in each animal, the first harmonic amplitude decreases in significance in the WSS signal with increasing animal size. This is clear from the ratios of first harmonic amplitude and TAWSS values taken at specific body masses. Simulations into the effects of increasing Womersley number (Section 7.3.1) also support this difference as the purely sinusoidal body force resulted in a consistently near-zero TAWSS while showing a decreasing first harmonic amplitude (Figure 7.2).

The difference in body mass exponents is in agreement with the allometric scaling arguments of Weinberg and Ethier (2007). The body mass exponent of the temporal gradient of WSS was computed in Weinberg and Ethier (2007) as -0.625 as the ratio of the TAWSS and pulse period body mass exponents. The temporal gradient of WSS is defined as the rate of change of WSS from minimum to maximum within a pulse period. In comparison with the allometric scaling arguments of other parameters, the argument for the temporal gradient serves as a weak approximation for the body mass exponent. This is acknowledged in Weinberg and Ethier (2007) as the temporal gradient of shear stress varies non-linearly with the Womersley number.

Normalisation of the signals with respect to the first harmonic amplitude showed consistency of the higher frequency components between all animals. This forms another key result of the study as it shows the body mass exponent of the first harmonic amplitude to be equal to that of all harmonic components, and therefore, also to the temporal gradient. The difference between the body mass exponent presented in Weinberg and Ethier (2007) and that computed here may be explained by the Womersley number effect discussed above and the difference in dimensionless number body mass exponents discussed in Section 7.3.3.

As in Figure 7.2, the first harmonic phase becomes increasingly negative with increasing body mass. This is attributed to the increasing Womersley number and



shows an increasing time delay between the body force and WSS signals. The first harmonic phase also showed negligible difference between the Newtonian and non-Newtonian viscosity models.

Interestingly, following a comparison of the allometric scaling parameters (Table 7.5), the viscosity model was also found to be insignificant in the first harmonic amplitude calculation. This suggests the near-wall shear rate to not be affected by the shear-thinning nature of blood.

**Table 7.5. Allometric scaling parameters for the first harmonic amplitude computed using the Newtonian and Carreau-Yasuda viscosity models.** Viscosity model parameters were obtained assuming a linear interpolation of viscosity model parameters between those available in the literature for the mouse and human. Simulation Reynolds and Womersley numbers were obtained from allometric scaling laws derived from the values computed for the mouse and human.

	$a_c$	$b$	$R^2$
Newtonian	0.6168	-0.408	0.99
Non-Newtonian	0.6069	-0.410	0.99

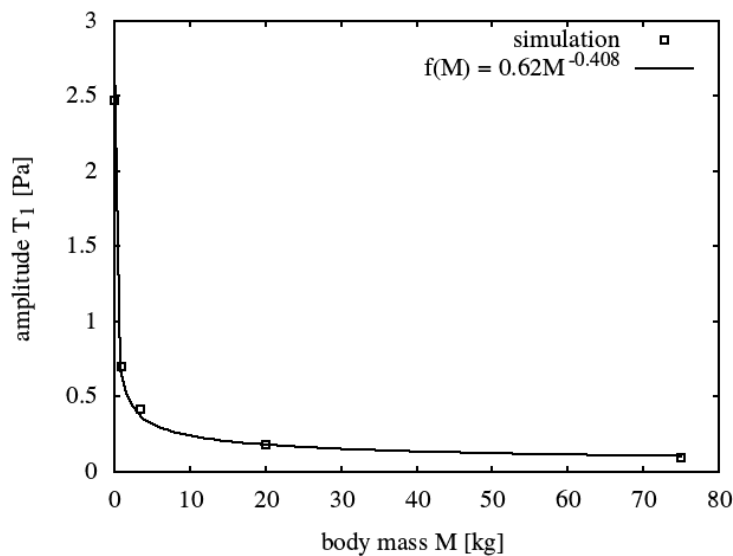


**Figure 7.5. Allometric relationship of animal body mass with the first harmonic amplitude computed from the Carreau-Yasuda viscosity model.** The body mass exponent was computed from simulation results as  $b = -0.408$  with  $R^2 = 0.99$ . Simulations were performed in the control vessel with the Reynolds and Womersley numbers computed through allometric scaling laws and the viscosity model parameters being estimated from a linear scaling relationship.

## 7.4 Discussion

The current chapter explores the hypothesis that body size in mammals is related to the frequency composition of the WSS signal. A key issue in atherosclerosis research is the rarity of plaque rupture and thrombosis in animal models of the disease, limiting studies into plaque instability. The differences in these plaque characteristics are explored here in terms of the wall shear stress signal given its role in the inflammatory response of endothelial cells (Himburg *et al.*, 2007; Feaver *et al.*, 2013).

Further to the allometric scaling of the TAWSS (Greve *et al.*, 2006; Weinberg and Ethier, 2007), simulations performed in the control vessels also showed an allometric scaling relationship of the first harmonic amplitude. This forms an interesting result of this chapter as the relative difference between the scales indicates decreasing significance of the time-varying component in the WSS signal. While this result is also suggested by the allometric scaling arguments of Weinberg and Ethier, (2007), the body mass exponents computed in the present study also account for the non-linear scaling of shear rates with the Womersley number. As the signal was computed in the control vessel model, the simulations performed here represent the WSS in a healthy, non-diseased vessel. The importance of this decreasing significance to the endothelial response, however, is unknown and presents an interesting avenue for future work.

The approximate consistency of the body mass exponents between the Newtonian and non-Newtonian viscosity models showed the constant viscosity assumption to be valid in simulating blood flow in straight channels. The effect of the viscosity model was only shown in the peak axial velocity and shows negligible importance in the study of WSS. This finding is also supported considering the high shear rate numbers (Section 4.6) of 1050 and 3827 computed in the mouse and human, respectively.

A key result of the scaling laws presented in this chapter is the similarities in the zeroth and first harmonic amplitudes between those computed in the human and estimated in the minipig model. The body mass of the minipig was taken to be 50 kg. Simulations in the control models also suggest consistency in the higher harmonics ( $n > 1$ ) between the two species. From this, the WSS signals can be considered to be equal between the minipig and human. A potential future study is the comparison of the inflammatory response of these animals in an *in vitro* application of the “healthy” WSS waveform.

A clear effect of genomic differences between species would be shown if the endothelial response of the minipig and human cells were different under an approximately identical WSS waveform. The genomic differences would then provide an explanation for the lack of fatal rupture in the minipig (Getz and Reardon, 2012; Shim *et al.*, 2016; Veseli *et al.*, 2017), and by extension, in the atherosclerotic mouse.

A recent finding of great interest in this discussion is the localisation of vulnerable-looking plaques to regions of low and oscillatory shear stress in the minipig (Hoogendoorn *et al.*, 2018) and human (Timmins *et al.*, 2017) coronary arteries. Simulations performed in Hoogendoorn *et al.* (2018) showed regions of low and oscillatory WSS to coincide with regions of highly-vulnerable plaques with signs of intraplaque haemorrhage, calcification and previous non-fatal plaque rupture. A similar pattern of disease progression was found in the human coronary arteries with plaques shifting to a more vulnerable-looking composition in regions of low and oscillatory shear stress (Timmins *et al.*, 2017). The significance of this result is clear when considering the reversal of this localisation pattern in the mouse perivascular cast model of Cheng *et al.* (2006). This pattern reversal is currently believed to be due to the mechanical interference caused by cast placement. An alternative explanation based on the findings of this thesis, however, is the effect of the decreased significance of the time-varying component in the minipig and human compared to the mouse.

#### Plaque rupture in the literature

An observation from the literature is the lack of extensive intraplaque neovascularisation in the atherosclerotic mouse model (Getz and Reardon, 2012; Veseli *et al.*, 2017). Formation of the thin-walled microvessels leads to the extravasation of red blood cells and intraplaque haemorrhage (Chistiakov *et al.*, 2015). The cholesterol released from RBC phagocytosis also leads to the formation of cholesterol crystals in the plaque core (Kolodgie *et al.*, 2003) while the released haemoglobin creates a stronger oxidative environment (Potor *et al.*, 2013). These factors all contribute greatly to plaque instability (Virmani *et al.*, 2005). When considering plaque hypoxia to be a driving factor in intraplaque neovascularisation (Sluimer *et al.*, 2009), it is clear that plaque size is a key regulator of this mechanism. As the plaque size is limited by the vessel size, it then follows that neovascularisation

is governed by the animal vessel size, thereby providing an explanation of the lack of neovessel formation in the mouse and rabbit. It should be noted, however, that the atherosclerotic minipig model also rarely shows plaque rupture (Getz and Reardon, 2012; Shim *et al.*, 2016; Veseli *et al.*, 2017).

The occurrence of plaque rupture and thrombosis has also been debated in the literature. Bond and Jackson (2011) argue that absence of the thrombosis in mouse models does not definitively prove the absence of its formation, but instead, may be due to the clearance of the thrombosis by pressure perfusion or fibrinolytic processes. Despite this argument, the current consensus is that plaque rupture and thrombosis are extremely rare in mice. The advanced plaque characteristics and rupture have, however, been triggered by mechanical injury (Sasaki *et al.*, 2006), increased circumferential stress (Chen *et al.*, 2013) and genetic manipulation further to the ApoE knockout (Gough *et al.*, 2006; Van der Donckt *et al.*, 2015). Gough *et al.* (2006) and Van der Donckt *et al.* (2015) achieve plaque rupture by overexpression of matrix metalloprotease-9 and mutation of the fibrillin-1 gene, respectively. These mechanisms result in elastin degradation in the extracellular matrix and cause rupture by thinning of the fibrous cap. The applicability of these mechanisms to human atherosclerosis is currently unclear.

### Study limitations

The major limitation of the current study is the assumption of fully-developed flow in the animal carotid arteries. Blood flow in the carotid arteries is known to be largely multidirectional with circumferential components of velocity arising from the curvature of the aortic arch and the twisting of the left ventricle in contraction (McMillan, 1985). This multidirectional flow behaviour results in axial and circumferential components of the tangential traction vector. The interpretation of this information in the frequency domain requires further work, as discussed in Section 2.5.

The high Reynolds number and branching from the aortic arch also causes a skewing of the carotid artery velocity profile (Ford *et al.*, 2008). In a comparison of inlet flow boundary conditions, Hardman *et al.* (2013) showed a great sensitivity to the assumption of fully-developed flow with the skewed velocity profiles producing more

complex flow streamlines when compared to the Womersley solution velocity profiles. Despite this sensitivity, the assumption of fully-developed flow was made given the absence of the complete three-component velocity inlet data and the complexity associated with WSS signal analysis.

While the absolute values of the zeroth and first harmonic amplitudes may be affected by the multidirectional nature of flow, the result of a decreasing zeroth and first harmonic amplitude with increasing animal size is expected to remain valid. The decrease is explained by the increasing radius and consistency of the peak systolic velocity between animals which causes the decrease of near-wall shear rates. It then follows that the result of the decreasing significance of the time-varying components in the WSS signal is also valid.

The approximation of viscosity model parameters from a linear interpolation forms a limitation of this study. This assumption was made necessary by a lack of Carreau-Yasuda viscosity model data in the rabbit and hypothetical animal models. A change in the properties of the viscosity transition were also expected between the animals given the difference found between the mouse and human parameter sets. The choice of parameters, however, was found to be irrelevant in the simulation of a pipe segment as the viscosity model showed negligible effects on the computed WSS.

## 7.5 Conclusions

The numerical tool developed and implemented in Chapters 3 and 4 was applied to several animals to identify any differences in the local haemodynamics between the mouse and human. The different animal models were specified through the choice of dimensionless numbers obtained from allometric scaling laws. The “healthy” non-diseased vessels were modelled as a pipe segment of constant radius and the effect of the non-Newtonian viscosity model was investigated. Given the importance of the WSS time-variation in the inflammatory response, simulations were performed here to test the hypothesis that the signal’s frequency composition is related to the animal’s body size.

The conclusions of this chapter are expressed in terms of the aims set out in the introduction:

- 1) *Are there similarities/differences in the frequency composition in the control vessel of animals of different body size?*

The WSS signals computed in the control vessels of animals of increasing body size show clear differences in the frequency composition.

In addition to known differences in the TAWSS, simulations performed here also showed a decrease in the first harmonic amplitude with increasing animal body size. An allometric scaling law was computed from this decrease with a body mass exponent different to that of the exponent computed for the TAWSS. The difference in exponent shows the time-varying nature of the signal to become more pronounced in the waveform of larger animals.

- 2) *Is the viscosity model relevant to the computed wall shear stress signals in the common carotid artery?*

Negligible differences were found in the zeroth and first harmonic amplitudes between the Carreau-Yasuda and Newtonian viscosity models. Negligible differences were also found in the first harmonic phase components between the viscosity models.

A 10% decrease in the peak systolic velocity was found in the Carreau-Yasuda simulations of all animals relative to the Newtonian assumption, similar to that of the steady flow numerical solutions (Figure 4.9).

For the purposes of atherosclerosis studies in a straight vessel segment, the use of a constant viscosity assumption was found to be valid.

From this chapter, it can be concluded that the frequency composition of the WSS signal is dependent on the animal body size. An interesting note here is that the time-variance of the signal becomes more significant with increasing animal size. While the frequency component amplitudes are expected to vary within each animal (Cheng *et al.*, 2007a), the result is expected to be relevant throughout the arterial network of the animal. An exploration of this decreasing significance on the inflammatory response

of different animals would be key in furthering an understanding of the differences between species.

A key conclusion of this study is also the apparent significance of genomic and circumferential stretch differences in plaque rupture between the species. The scaling laws computed here show consistency of the local haemodynamics between the human and minipig models. The rare occurrence of plaque rupture in the atherosclerotic minipig despite this similarity in WSS then suggests the influence of factors other than the WSS in plaque rupture. The known genomic and circumferential stretch differences between the animal species may provide an explanation here to the lack of plaque rupture in animal models.

The current chapter presents the conclusions of this PhD. An overview of the key motivations is, first, provided in Section 8.1 to orientate the reader. Section 8.2 then discusses the conclusions with regard to specific aims and their relevance to the scalability of mouse and human atherosclerosis. The future directions emerging from this PhD and the simulation technical details are given in Sections 8.3 and 8.4 respectively. Finally, the key findings of the study are summarised in Section 8.5.

#### 8.1 Summary of key motivations

Atherosclerosis is an inflammatory condition by which lipid-laden foam cells accumulate in the intimal layer of a blood vessel (Lusis, 2000; Weissberg, 2000). The infiltration of low-density lipoproteins into the subendothelial space serves as a stimulus for blood-borne monocyte extravasation (Poole and Florey, 1958). Differentiation of the monocytes into macrophages causes migration of smooth muscle cells into the intimal layer (Niu *et al.*, 2016). Uptake of the lipoproteins by macrophages and the now-intimal smooth muscle cells leads to the growth of an intimal lipid deposit. This inflammatory process, under persistent stimulus, results in the formation of the atherosclerotic plaque (Ross, 1993).

Rupture of the atherosclerotic plaque leads to exposure of the underlying thrombogenic material and the formation of an occlusive thrombosis. This is a key cause of clinical events in the human. The rarity of plaque rupture and thrombosis, therefore, is a major limitation of atherosclerotic mouse models (Zhou *et al.*, 2001; Schwartz *et al.*, 2007; Bentzon and Falk, 2010; Finn *et al.*, 2010; Bentzon *et al.*, 2014). Given the popularity of murine models in atherosclerosis research, an explanation for the lack of rupture in the atherosclerosis-prone mouse is keenly sought in order to



gauge the applicability of insights gained from the mouse to human disease. Future treatments may also benefit from this explanation as it clarifies which components of cell function need to be controlled in order to induce a situation similar to that seen in the mouse where the heart attack and stroke are extremely rare. This need for understanding serves as the key motivation for this PhD.

Plaque formation has shown a clear predilection for vessel segments coincident with low and oscillatory wall shear stress (Caro *et al.*, 1971; Ku *et al.*, 1985; Himburg *et al.*, 2004). Endothelial cells lining the vessel wall have also shown a shift towards the proinflammatory state in response to these wall shear stresses. Davies (1995), Malek *et al.* (1999), Cunningham and Gotlieb (2004) and Chiu and Chien (2011) provide excellent reviews of this field. In a study of particular importance to this PhD, Cheng *et al.* (2006) found the composition of the atherosclerotic plaque to be dependent upon the pattern of wall shear stress in atherosclerosis-prone mice. Plaque composition is of key relevance to this work as it determines the stress threshold beyond which plaque rupture occurs (Virmani *et al.*, 2000; Slager *et al.*, 2005a, 2005b; Schwartz *et al.*, 2007; Finn *et al.*, 2010; Bentzon *et al.*, 2014). The work of this PhD, therefore, explores the vessel haemodynamics in mice and humans as a potential explanation for the lack of plaque rupture in atherosclerotic mice. Interestingly, Himburg *et al.* (2007) and Feaver *et al.* (2013) demonstrated a sensitivity in the expression of inflammatory markers to the frequency composition of the wall shear stress, now considered as a time-varying signal. This PhD addressed the hypothesis that the frequency composition of the wall shear stress signal is associated to the different plaque compositions and disease characteristics in animal models of atherosclerosis.

## 8.2 Conclusions with respect to individual aims

A number of aims were set out in the introduction in order to test this hypothesis. The conclusions of this PhD are expressed in terms of these aims:

- 1) *Are differences in the wall shear stress frequency composition present across different surgically manipulated mouse models of atherosclerosis?*

Simulations performed in Chapter 5 showed that the use of surgical manipulations in published mouse models of atherosclerosis created clear

reductions in the zeroth and first harmonic amplitudes along the length of the manipulated vessel. A proinflammatory condition was also suggested by the out-of-phase stress-strain relationship found in the simulations (Qiu and Tarbell, 2000; Torii *et al.*, 2009; Amaya *et al.*, 2015; Sinha *et al.*, 2016).

Regions coincident with plaques resembling the human thin-cap fibroatheroma or the stable-looking cellular plaque in the Cheng *et al.* (2006) study showed different frequency compositions with elevation of the third harmonic amplitude in the region showing the cellular plaque type. Simulation of the Chen *et al.* (2013) tandem ligation, however, showed consistency of the signal among the regions coincident with different plaque compositions. The contrasting findings between the two studies may be explained by the different mechanical stresses induced by each surgical manipulation. The mechanical stresses discussed here refer to constraint effects and the circumferential stretch induced by the pressure waveform. The regions of the different plaque compositions also showed a clear segmentation according to the vessel mechanical stresses.

The present work highlights the importance of mechanical stresses in plaque composition and is a key result of this study. Differences in the mechanical stresses mean that there is a lack of comparability between the various published models of surgical manipulation in mouse atherosclerosis.

#### Relevance to the comparison of human and murine atherosclerosis:

The dependence of plaque characteristics on the mechanical stresses arising from surgical manipulation is shown in the present work. The perivascular device also causes a mechanical constraint on the vessel wall and induces a proinflammatory response (Tanaka *et al.*, 2003). Considering the absence of surgical manipulation in human atherosclerosis, it then follows that there is an entirely different mechanical and inflammatory environment in the mouse and human. This suggests a poor scalability of the insights gained from surgically manipulated models of murine atherosclerosis to the human disease.

An interesting observation from the literature is the opposite localisation pattern in minipig (Hoogendoorn *et al.*, 2018) and human (Timmins *et al.*, 2017) coronary arteries to that found in the surgically manipulated mouse

model (Cheng *et al.*, 2006). The minipig and human coronary arteries were devoid of any manipulation and showed localisation of the thin-cap fibroatheroma and stable-looking plaque type to regions of oscillatory shear stress and low shear stress, respectively. The opposite pattern of localisation is found in the mouse tapering cast model of Cheng *et al.* (2006). The conclusion drawn from the present work is supported by this finding as the opposite localisation pattern suggests the effect of differences in the mechanical environment between surgically manipulated and unmanipulated vessels. Genomic differences between the species may also play a role in the opposite localisation pattern.

2) *Are the differences in wall shear stress seen between the regions of the perivascular tapering cast mouse model dependent on the input waveforms of pressure?*

Simulation of simple pressure waveforms in the tapering cast geometry (Chapter 6) showed clear region-specific scaling relationships between the frequency compositions of pressure and wall shear stress signals.

The imposed body force waveform consisted of a single harmonic component. Linear relationships were found between the first harmonic amplitudes of the wall shear stress signal and the imposed body force waveform. A second harmonic component was found in the oscillatory region with its amplitude given by a quadratic relationship with the body force first harmonic amplitude. Emergence of the second harmonic amplitude in the oscillatory shear stress region from a simple body force signal input provides a basis for differences in the higher harmonics seen with the complex waveforms measured in the healthy carotid artery.

The presence of these clear scaling relationships means that the wall shear stress signals may be predictable from the input body force waveform for certain geometries without the need for simulation. Sensitivity of the wall shear stress frequency composition to vascular tone and vessel diameter can also be implied considering the expected changes in arterial pressure waveform and the scaling relationships derived from the simulations.

Relevance to the comparison of human and murine atherosclerosis:

The simulations performed in this work only provide an exploration of the effects of varying body force terms on the wall shear stress signal rather than representing flow cases in any specific animal. These findings can, however, be extrapolated to animal studies when considering the changes expected in arterial pressure waveform with the different vessel diameters and vascular tone between models.

As the common carotid artery diameter in the human is approximately 12 times greater than that of the mouse, differences in the arterial pressure waveform are expected between the mouse and human. Considering the scaling relationships found in this study, it then follows that the wall shear stress frequency composition is different between the mouse and human. This suggests a poor scalability of the insights gained from murine models of atherosclerosis to the human disease.

- 3) *Are the differences in wall shear stress seen between the regions of the perivascular tapering cast mouse model dependent on the flow dimensionless numbers?*

The distribution of the first harmonic amplitude indicated entirely different flow environments in the regions downstream of the cast between simulations with increasing Reynolds and Womersley numbers (Chapter 6). The wall shear stress higher harmonic components ( $n > 1$ ) showed an approximate region-specific consistency between simulations when normalised against the first harmonic amplitude.

Relevance to the comparison of human and murine atherosclerosis:

The simulations performed as part of this study did not represent any specific animal model. The emergence of a varied first harmonic amplitude distribution may, however, be extrapolated to animal models when thinking of the increase in the dimensionless numbers with increasing animal body mass.

A comparison of the dimensionless numbers between the mouse and human shows a factor of 10 difference in Reynolds number and a factor of 5 difference in the Womersley number. The increasing dimensionless parameters then

indicate differences in vessel haemodynamics between the mouse and human. This suggests a poor scalability of insights gained from murine atherosclerosis to the human disease.

4) *Are there differences in the wall shear stress frequency composition in the arteries of different mammals?*

The wall shear stress signals computed in different mammals showed reduction of the zeroth and first harmonic amplitudes with increasing animal body mass (Chapter 7).

A key finding of this work was the difference in the rate of change of the zeroth and first harmonic amplitudes. This showed the time-varying component of the signal to decrease in significance with respect to the time-averaged component with an increasing animal body mass. The wall shear stress higher harmonic components ( $n > 1$ ) were largely similar between animal models when normalised against the first harmonic amplitude. The increasing Womersley number, with animal body mass, also resulted in an increased phase difference between the pressure and wall shear stress signals.

The results were shown in simulations of a control geometry segment and represent blood flow in the disease-free common carotid artery of an animal. This shows the “healthy” wall shear stress signal to be different between mammals of different body size.

Relevance to the comparison of human and murine atherosclerosis:

A key result of this study is the allometric scaling laws defined for the wall shear stress signal computed in the mammals. Estimation of the wall shear stress signal in the atherosclerotic minipig suggests consistency in the signal between the minipig and human models. The rarity of plaque rupture in the minipig then suggests the effect of a parameter other than the vessel haemodynamics in atherosclerosis and plaque rupture. This conclusion highlights the significance of mechanical or genomic differences between the species. It then follows that there is poor scalability of the insights gained from the atherosclerotic mouse to the human disease.

### 8.3 Future directions

A number of open questions have been developed as a result of this PhD. Points 1-3 indicate fundamental questions that would further the understanding of the differences in murine and human atherosclerosis. Points 4 and 5 refer to the more technical aspects of the simulation tool and are required for a more accurate simulation of the flow field in the mouse and human models.

- 1) *Are the endothelial cell responses to circumferential strain consistent between the different models of surgically manipulated blood vessel in the atherosclerosis-prone mouse?*

The results of Chapter 5 showed similarity in the local haemodynamic waveforms between regions coincident with different plaque compositions in the tandem stenosis geometry of Chen *et al.* (2013). The pressure drop across the geometry suggests differences in the circumferential strain between regions of the model. A characterisation of the endothelial responses to the circumferential strain may provide an insight into the significance of mechanical differences between regions showing different plaque compositions.

- 2) *Are the endothelial cell responses consistent between mammals under their respective “healthy” wall shear stress signals?*

The findings of Chapter 7 showed differences in the vessel haemodynamics between the mouse and the human. The frequency analysis performed in this PhD provides a full characterisation of the temporal variation of the wall shear stress in a straight, non-diseased vessel. A clear effect of the genomic differences between species would be shown if the responses of endothelial cells to their respective “healthy” wall shear stress signals were different.

A number of studies exist in the literature in which the inflammatory behaviour of cultured endothelial cells is characterised in response to steady, pulsatile or oscillatory flows. The nature of pulsatility, however, does not mirror that seen in the vessels of the animal from which the cell was derived. The mouse endothelial cells are commonly exposed to time-averaged wall shear stress

values found in the human, for example. These studies have been reviewed in Davies (1995) and Chiu and Chien (2011).

The Blackman group provided a number of studies in which the responses of human umbilical vein endothelial cells to human atheroprotective wall shear stress signals were characterised using a cone-and-plate flow device (Blackman *et al.*, 2002; Feaver *et al.*, 2013). The extension of the present work may take a similar form to that of the Blackman studies using the full characterisation of the healthy wall shear stress signals computed here on cell cultures from the respective animal.

3) *Are there similarities/differences in the temporal response to a mechanical stimulus between murine and human endothelial cells?*

The activation of potassium ion channels is taken as the initiation of signalling and is the fastest detectable response in large animal endothelial cells. This occurs on the timescale of seconds. The temporal sensitivity of bovine, porcine and human endothelial cells have been reviewed in Davies (1995). Considering the difference in timescales between the mouse and human pulse period, the temporal sensitivity of murine endothelial cells may differ from that of the large animal models. A key difference in disease progression between the atherosclerosis-prone mouse and human is also the timescale within which lesions form. An understanding of the temporal sensitivity of murine endothelial cells may provide insights into this difference in disease progression timescale.

4) *Implementation of the verified 1D transmission line model*

A key component of furthering the simulation tool is the implementation of physiologically relevant boundary conditions. This would require a verified implementation of the 1D transmission line model discussed in Sections 2.7 and 4.4. The model would provide the flow and pressure waveforms relevant to a vessel in the healthy vascular network.

5) *Can the arterial pressure waveforms in different surgically manipulated vessel models be approximated from the healthy carotid artery in the mouse?*

Constriction of the vessel by surgical manipulation leads to increases in vascular resistance. Alteration of the arterial pressure waveform is also expected due to wave reflections at the constriction (O'Rourke and Yaginuma, 1984; Nichols *et al.*, 1998; van de Vosse and Stergiopulos, 2011; Pereira *et al.*, 2015). Additional models are required to recover boundary conditions relevant to flow through the surgically manipulated geometries.

Li (2006) described the use of a 1D circuit to represent a stenosis in an implementation of the transmission line model. An iterative tuning method was applied together with 3D simulations to calculate parameters of the 1D circuit to model the properties of the stenosis in terms of resistance, capacitance and inductance. The 1D circuit parameters were applied to the transmission line model to recover waveforms of pressure and flow to account for the stenosis. A similar method may be applied to the simulations performed in this PhD to recover boundary conditions for use at the inlet and outlet for each model.

## 8.4 Technical specifications

A key point of discussion in any fluid dynamics study is the computational effort required in simulation. This is quantified in terms of the computational time and was computed as 4 hours in the mouse tapering cast simulations and 9 days in the human control vessel simulations. All simulations were performed on a single processor of an Intel Core i7-4790 desktop machine. The computer was equipped with 15.6 GB of RAM and eight cores running at 3.6 GHz.

## 8.5 Key findings

A major question in the atherosclerosis community is the scalability of insights gained from atherosclerotic mouse models to the human disease considering the rarity of plaque rupture in atherosclerosis-prone mice. In this regard, the key finding of this PhD is the difference in vessel haemodynamics between the mouse and human. Consistency of the wall shear stress signal between that computed in the human and



estimated in the atherosclerotic minipig, however, suggest the dominance of factors other than wall shear stress in plaque rupture. The simulations performed here support this conclusion as a dependence of plaque composition is shown in response to circumferential stretch. The significance of the genomic differences between the species is also highlighted through the simulation of various animal models.

To conclude, the scalability of insights gained from the murine studies to human disease is limited on three counts: the differences in vessel haemodynamics, the sensitivity of plaque composition to circumferential stretch, and genomic differences between the species. This thesis works to isolate the significance of haemodynamics in this multifactorial problem and shows no evidence to suggest that the wall shear stress alone can explain the lack of plaque rupture in atherosclerotic mice. A complete picture of atherosclerosis and plaque rupture cannot be achieved without an understanding of all factors involved, both individually and cumulatively.

- 
- Aidun, C.K., Clausen, J.R., 2010a. Lattice-Boltzmann method for complex flows. *Annual Review of Fluid Mechanics* 42, 439–472. <https://doi.org/10.1146/annurev-fluid-121108-145519>
- Aidun, C.K., Clausen, J.R., 2010b. Lattice-Boltzmann method for complex flows. *Annual Review of Fluid Mechanics* 42, 439–472. <https://doi.org/10.1146/annurev-fluid-121108-145519>
- Akyildiz, A.C., Speelman, L., Gijzen, F.J.H., 2014. Mechanical properties of human atherosclerotic intima tissue. *Journal of Biomechanics, SI: Plaque Mechanics* 47, 773–783. <https://doi.org/10.1016/j.jbiomech.2014.01.019>
- Al-Mashhadi, A.L., Poulsen, C.B., von Wachenfeldt, K., Robertson, A.-K., Bentzon, J.F., Nielsen, L.B., Thygesen, J., Tolbod, L.P., Larsen, J.R., Moestrup, S.K., Frendeus, B., Mortensen, B., Drouet, L., Al-Mashhadi, R.H., Falk, E., 2018. Diet-induced abdominal obesity, metabolic changes, and atherosclerosis in hypercholesterolemic minipigs. *J. Diabetes Res.* 6823193. <https://doi.org/10.1155/2018/6823193>
- Amaya, R., Pierides, A., Tarbell, J.M., 2015. The interaction between fluid wall shear stress and solid circumferential strain affects endothelial gene expression. *PLOS ONE* 10, e0129952. <https://doi.org/10.1371/journal.pone.0129952>
- Amin, T., Sirs, J., 1985. The blood rheology of man and various animal species. *Quarterly Journal of Experimental Physiology and Cognate Medical Sciences* 70, 37–49. <https://doi.org/10.1113/expphysiol.1985.sp002895>
- Artoli, A.M., Hoekstra, A.G., Sloot, P.M.A., 2002. 3D pulsatile flow with the lattice Boltzmann BGK method. *Int. J. Mod. Phys. C* 13, 1119–1134. <https://doi.org/10.1142/S0129183102003826>
- Artoli, A.M., Sequeira, A., 2006. Mesoscopic simulations of unsteady shear-thinning flows, in: Alexandrov, V.N., VanAlbada, G.D., Sloot, P.M.A. (Eds.), *Computational Science - Iccs 2006, Pt 2, Proceedings*. Springer-Verlag Berlin, Berlin, pp. 78–85.
- Asgharzadeh, H., Borazjani, I., 2016. Effects of Reynolds and Womersley numbers on the hemodynamics of intracranial aneurysms. *Comput. Math. Method Med.* 7412926. <https://doi.org/10.1155/2016/7412926>
- Aslanidou, L., Trachet, B., Reymond, P., Fraga-Silva, R.A., Segers, P., Stergiopoulos, N., 2016. A 1D model of the arterial circulation in mice. *ALTEx-Altern. Anim. Exp.* 33, 13–28. <https://doi.org/10.14573/altex.1507071>
- Avolio, A., 1980. Multi-branched model of the human arterial system. *Med. Biol. Eng. Comput.* 18, 709–718. <https://doi.org/10.1007/BF02441895>

- Baeyens, N., Nicoli, S., Coon, B.G., Ross, T.D., Van den Dries, K., Han, J., Lauridsen, H.M., Mejean, C.O., Eichmann, A., Thomas, J.-L., Humphrey, J.D., Schwartz, M.A., 2015. Vascular remodeling is governed by a VEGFR3-dependent fluid shear stress set point. *eLife* 4, e04645. <https://doi.org/10.7554/eLife.04645>
- Banerjee, M.K., Ganguly, R., Datta, A., 2012. Effect of pulsatile flow waveform and Womersley number on the flow in stenosed arterial geometry [WWW Document]. *International Scholarly Research Notices*. <https://doi.org/10.5402/2012/853056>
- Basciano, C., Kleinstreuer, C., Hyun, S., Finol, E.A., 2011. A relation between near-wall particle-hemodynamics and onset of thrombus formation in abdominal aortic aneurysms. *Ann. Biomed. Eng.* 39, 2010–2026. <https://doi.org/10.1007/s10439-011-0285-6>
- Batchelor, G.K., 2000. *An introduction to fluid dynamics*. Cambridge University Press, Cambridge.
- Bentzon, J.F., Falk, E., 2010. Atherosclerotic lesions in mouse and man: is it the same disease? *Curr. Opin. Lipidol.* 21, 434–440. <https://doi.org/10.1097/MOL.0b013e32833ded6a>
- Bentzon, J.F., Otsuka, F., Virmani, R., Falk, E., 2014. Mechanisms of plaque formation and rupture. *Circulation Research* 114, 1852–1866. <https://doi.org/10.1161/CIRCRESAHA.114.302721>
- Bernabeu, M.O., Jones, M.L., Nielsen, J.H., Krüger, T., Nash, R.W., Groen, D., Schmieschek, S., Hetherington, J., Gerhardt, H., Franco, C.A., Coveney, P.V., 2014. Computer simulations reveal complex distribution of haemodynamic forces in a mouse retina model of angiogenesis. *Journal of The Royal Society Interface* 11, 20140543. <https://doi.org/10.1098/rsif.2014.0543>
- Bernabeu, M.O., Nash, R.W., Groen, D., Carver, H.B., Hetherington, J., Krueger, T., Coveney, P.V., 2013. Impact of blood rheology on wall shear stress in a model of the middle cerebral artery. *Interface Focus* 3, 20120094. <https://doi.org/10.1098/rsfs.2012.0094>
- Blackman, B.R., Garcia-Cardena, G., Gimbrone, M.A., 2002. A new in vitro model to evaluate differential responses of endothelial cells to simulated arterial shear stress waveforms. *J. Biomech. Eng.-Trans. ASME* 124, 397–407. <https://doi.org/10.1115/1.1486468>
- Bond, A.R., Jackson, C.L., 2011. The fat-fed apolipoprotein E knockout mouse brachiocephalic artery in the study of atherosclerotic plaque rupture. *J. Biomed. Biotechnol.* 379069. <https://doi.org/10.1155/2011/379069>
- Bouzidi, M., Firdaouss, M., Lallemand, P., 2001. Momentum transfer of a Boltzmann-lattice fluid with boundaries. *Phys. Fluids* 13, 3452–3459. <https://doi.org/10.1063/1.1399290>
- Boyd, J., Buick, J.M., 2007. Comparison of Newtonian and non-Newtonian flows in a two-dimensional carotid artery model using the lattice Boltzmann method. *Physics in Medicine and Biology* 52, 6215–6228. <https://doi.org/10.1088/0031-9155/52/20/009>
- Boyd, J., Buick, J.M., Green, S., 2007. Analysis of the Casson and Carreau-Yasuda non-Newtonian blood models in steady and oscillatory flows using the lattice Boltzmann method. *Phys. Fluids* 19, 093103. <https://doi.org/10.1063/1.2772250>

- Buchanan, J.R., Kleinstreuer, C., Comer, J.K., 2000. Rheological effects on pulsatile hemodynamics in a stenosed tube. *Computers & Fluids* 29, 695–724. [https://doi.org/10.1016/S0045-7930\(99\)00019-5](https://doi.org/10.1016/S0045-7930(99)00019-5)
- Calara, F., Silvestre, M., Casanada, F., Yuan, N., Napoli, C., Palinski, W., 2001. Spontaneous plaque rupture and secondary thrombosis in apolipoprotein E-deficient and LDL receptor-deficient mice. *J. Pathol.* 195, 257–263. <https://doi.org/10.1002/path.915>
- Caro, C., Fitzgerald, J.M., Schroter, R., 1971. Atheroma and arterial wall shear - Observation, correlation and proposal. *Proceedings of the Royal Society Series B-Biological Sciences* 177, 109–+. <https://doi.org/10.1098/rspb.1971.0019>
- Chatzizisis, Y.S., Coskun, A.U., Jonas, M., Edelman, E.R., Feldman, C.L., Stone, P.H., 2007. Role of endothelial shear stress in the natural history of coronary atherosclerosis and vascular remodeling - Molecular, cellular, and vascular behavior. *J. Am. Coll. Cardiol.* 49, 2379–2393. <https://doi.org/10.1016/j.jacc.2007.02.059>
- Chen, S., Doolen, G.D., 1998. Lattice Boltzmann method for fluid flows. *Annual Review of Fluid Mechanics* 30, 329–364. <https://doi.org/10.1146/annurev.fluid.30.1.329>
- Chen, Y.-C., Bui, A.V., Diesch, J., Manasseh, R., Hausding, C., Rivera, J., Haviv, I., Agrotis, A., Htun, N.M., Jowett, J., Hagemeyer, C.E., Hannan, R.D., Bobik, A., Peter, K., 2013. A novel mouse model of atherosclerotic plaque instability for drug testing and mechanistic/therapeutic discoveries using gene and microRNA expression profiling. *Circ.Res.* 113, 252–265. <https://doi.org/10.1161/CIRCRESAHA.113.301562>
- Cheng, C., Helderma, F., Tempel, D., Segers, D., Hierck, B., Poelmann, R., van Tol, A., Duncker, D.J., Robbers-Visser, D., Ursem, N.T.C., van Haperen, R., Wentzel, J.J., Gijzen, F., van der Steen, A.F.W., de Crom, R., Krams, R., 2007a. Large variations in absolute wall shear stress levels within one species and between species. *Atherosclerosis* 195, 225–235. <https://doi.org/10.1016/j.atherosclerosis.2006.11.019>
- Cheng, C., Tempel, D., van Haperen, R., de Boer, H.C., Segers, D., Huisman, M., van Zonneveld, A.J., Leenen, P.J.M., van der Steen, A., Serruys, P.W., de Crom, R., Krams, R., 2007b. Shear stress-induced changes in atherosclerotic plaque composition are modulated by chemokines. *J. Clin. Invest.* 117, 616–626. <https://doi.org/10.1172/JCI28180>
- Cheng, C., Tempel, D., van Haperen, R., van der Baan, A., Grosveld, F., Daemen, M., Krams, R., de Crom, R., 2006. Atherosclerotic lesion size and vulnerability are determined by patterns of fluid shear stress. *Circulation* 113, 2744–2753. <https://doi.org/10.1161/CIRCULATIONHA.105.590018>
- Chien, S., 1970. Shear dependence of effective cell volume as a determinant of blood viscosity. *Science* 168, 977–. <https://doi.org/10.1126/science.168.3934.977>
- Chistiakov, D.A., Orekhov, A.N., Bobryshev, Y.V., 2015. Contribution of neovascularization and intraplaque haemorrhage to atherosclerotic plaque progression and instability. *Acta Physiol.* 213, 539–553. <https://doi.org/10.1111/apha.12438>
- Chiu, J.J., Chen, L.J., Chen, C.N., Lee, P.L., Lee, C.I., 2004a. A model for studying the effect of shear stress on interactions between vascular endothelial cells and

- smooth muscle cells. *J. Biomech.* 37, 531–539. <https://doi.org/10.1016/j.jbiomech.2003.08.012>
- Chiu, J.-J., Chien, S., 2011. Effects of disturbed flow on vascular endothelium: Pathophysiological basis and clinical perspectives. *Physiol. Rev.* 91, 327–387. <https://doi.org/10.1152/physrev.00047.2009>
- Chiu, J.J., Lee, P.L., Chen, C.N., Lee, C.I., Chang, S.F., Chen, L.J., Lien, S.C., Ko, Y.C., Usami, S., Chien, S., 2004b. Shear stress increases ICAM-1 and decreases VCAM-1 and E-selectin expressions induced by tumor necrosis factor-alpha in endothelial cells. *Arterioscler. Thromb. Vasc. Biol.* 24, 73–79. <https://doi.org/10.1161/01.ATV.0000106321.63667.24>
- Cullen, P., Baetta, R., Bellosta, S., Bernini, F., Chinetti, G., Cignarella, A., von Eckardstein, A., Exley, A., Goddard, M., Hofker, M., Hurt-Camejo, E., Kanfers, E., Kovanen, P., Lorkowski, S., McPheat, W., Pentikainen, M., Rauterberg, J., Ritchie, A., Staels, B., Weitkamp, B., de Winther, M., 2003. Rupture of the atherosclerotic plaque - Does a good animal model exist? *Arterioscler. Thromb. Vasc. Biol.* 23, 535–542. <https://doi.org/10.1161/01.ATV.0000060200.73623.F8>
- Cunningham, K.S., Gotlieb, A.I., 2004. The role of shear stress in the pathogenesis of atherosclerosis. *Lab Invest* 85, 9–23. <https://doi.org/10.1038/labinvest.3700215>
- Daugherty, A., 2002. Mouse models of atherosclerosis. *The American Journal of the Medical Sciences* 323, 3–10. <https://doi.org/10.1097/00000441-200201000-00002>
- Daugherty, A., Lu, H., Howatt, Deborah A., Rateri, Debra L., 2009. Modes of defining atherosclerosis in mouse models: Relative merits and evolving standards, in: DiPetrillo, K. (Ed.), *Cardiovascular Genomics, Methods in Molecular Biology™*. Humana Press, pp. 1–15. [https://doi.org/10.1007/978-1-60761-247-6\\_1](https://doi.org/10.1007/978-1-60761-247-6_1)
- Davies, P.F., 2009. Hemodynamic shear stress and the endothelium in cardiovascular pathophysiology. *Nat Clin Pract Cardiovasc Med* 6, 16–26. <https://doi.org/10.1038/ncpcardio1397>
- Davies, P.F., 1995. Flow-mediated endothelial mechanotransduction. *Physiol. Rev.* 75, 519–560.
- Dawson, T., 2014. Allometric relations and scaling laws for the cardiovascular system of mammals. *Systems* 2, 168–185. <https://doi.org/10.3390/systems2020168>
- de Sá Ferreira, A., Filho, J.B., Cordovil, I., de Souza, M.N., 2009. Three-section transmission-line arterial model for noninvasive assessment of vascular remodeling in primary hypertension. *Biomedical Signal Processing and Control* 4, 2–6. <https://doi.org/10.1016/j.bspc.2008.07.001>
- Dolan, J.M., Kolega, J., Meng, H., 2013. High wall shear stress and spatial gradients in vascular pathology: a review. *Ann Biomed Eng* 41, 1411–1427. <https://doi.org/10.1007/s10439-012-0695-0>
- Durst, F., Ray, S., Unsal, B., Bayoumi, O.A., 2005. The development lengths of laminar pipe and channel flows. *J. Fluids Eng.-Trans. ASME* 127, 1154–1160. <https://doi.org/10.1115/1.2063088>
- Eshtehardi, P., Brown, A.J., Bhargava, A., Costopoulos, C., Hung, O.Y., Corban, M.T., Hosseini, H., Gogas, B.D., Giddens, D.P., Samady, H., 2017. High wall

- shear stress and high-risk plaque: an emerging concept. *Int J Cardiovasc Imaging* 33, 1089–1099. <https://doi.org/10.1007/s10554-016-1055-1>
- Fan, J., Watanabe, T., 2000. Cholesterol-fed and transgenic rabbit models for the study of atherosclerosis. *J. Atheroscler. Thromb.* 7, 26–32.
- Feaver, R.E., Gelfand, B.D., Blackman, B.R., 2013. Human haemodynamic frequency harmonics regulate the inflammatory phenotype of vascular endothelial cells. *Nat Commun* 4, 1525. <https://doi.org/10.1038/ncomms2530>
- Filippova, O., Hanel, D., 1998. Grid refinement for lattice-BGK models. *J. Comput. Phys.* 147, 219–228. <https://doi.org/10.1006/jcph.1998.6089>
- Finn, A.V., Nakano, M., Narula, J., Kolodgie, F.D., Virmani, R., 2010. Concept of vulnerable/unstable plaque. *Arteriosclerosis, Thrombosis, and Vascular Biology* 30, 1282–1292. <https://doi.org/10.1161/ATVBAHA.108.179739>
- Ford, M.D., Xie, Y.J., Wasserman, B.A., Steinman, D.A., 2008. Is flow in the common carotid artery fully developed? *Physiol. Meas.* 29, 1335–1349. <https://doi.org/10.1088/0967-3334/29/11/008>
- Formaggia, L., Veneziani, A., 2003. Reduced and multiscale models for the human cardiovascular system, Lecture notes VKI, Lecture Series 2003-07, Brussels.
- Fraga-Silva, R.A., Montecucco, F., Costa-Fraga, F.P., Nencioni, A., Caffa, I., Bragina, M.E., Mach, F., Raizada, M.K., Santos, R.A.S., da Silva, R.F., Stergiopulos, N., 2015. Diminazene enhances stability of atherosclerotic plaques in ApoE-deficient mice. *Vasc. Pharmacol.* 74, 103–113. <https://doi.org/10.1016/j.vph.2015.08.014>
- Fry, D., 1969. Certain chemorheologic considerations regarding blood vascular interface with particular reference to coronary artery disease. *Circulation* 40, IV38-. <https://doi.org/10.1161/01.CIR.40.5S4.IV-38>
- Gabriel, S.A., Ding, Y., Feng, Y., 2017. Quantifying the influence of oscillatory flow disturbances on blood flow. *J. Theor. Biol.* 430, 195–206. <https://doi.org/10.1016/j.jtbi.2017.07.008>
- Galdi, G.P., 2008. Mathematical problems in classical and non-Newtonian fluid mechanics, in: *Hemodynamical Flows, Oberwolfach Seminars*. Birkhäuser Basel, pp. 121–273. [https://doi.org/10.1007/978-3-7643-7806-6\\_3](https://doi.org/10.1007/978-3-7643-7806-6_3)
- Gelfand, B.D., Epstein, F.H., Blackman, B.R., 2006. Spatial and spectral heterogeneity of time-varying shear stress profiles in the carotid bifurcation by phase-contrast MRI. *J. Magn. Reson. Imaging* 24, 1386–1392. <https://doi.org/10.1002/jmri.20765>
- Getz, G., 1990. The involvement of lipoproteins in atherogenesis - Evolving concepts. *Ann. N.Y. Acad. Sci.* 598, 17–28. <https://doi.org/10.1111/j.1749-6632.1990.tb42272.x>
- Getz, G.S., Reardon, C.A., 2012. Animal models of atherosclerosis. *Arterioscler. Thromb. Vasc. Biol.* 32, 1104–+. <https://doi.org/10.1161/ATVBAHA.111.237693>
- Gijsen, F.J.H., Allanic, E., van de Vosse, F.N., Janssen, J.D., 1999a. The influence of the non-Newtonian properties of blood on the flow in large arteries: unsteady flow in a 90° curved tube. *Journal of Biomechanics* 32, 705–713. [https://doi.org/10.1016/S0021-9290\(99\)00014-7](https://doi.org/10.1016/S0021-9290(99)00014-7)
- Gijsen, F.J.H., Migliavacca, F., 2014. Plaque mechanics. *J. Biomech.* 47, 763–764. <https://doi.org/10.1016/j.jbiomech.2014.01.031>

- Gijssen, F.J.H., van de Vosse, F.N., Janssen, J.D., 1999b. The influence of the non-Newtonian properties of blood on the flow in large arteries: steady flow in a carotid bifurcation model. *Journal of Biomechanics* 32, 601–608. [https://doi.org/10.1016/S0021-9290\(99\)00015-9](https://doi.org/10.1016/S0021-9290(99)00015-9)
- Gijssen, F.J.H., Wentzel, J.J., Thury, A., Lamers, B., Schuurblers, J.C.H., Serruys, P.W., Van der Steen, A.F., 2007. A new imaging technique to study 3-D plaque and shear stress distribution in human coronar arter bifurcations in vivo. *J. Biomech.* 40, 2349–2357. <https://doi.org/10.1016/j.jbiomech.2006.12.007>
- Ginzbourg, I., Adler, P., 1994. Boundary flow condition analysis for the 3-Dimensional lattice Boltzmann model. *J. Phys. II* 4, 191–214.
- Glagov, S., Weisenberg, E., Zarins, C.K., Stankunavicius, R., Kolettis, G.J., 1987. Compensatory enlargement of human atherosclerotic coronary arteries. *N. Engl. J. Med.* 316, 1371–1375. <https://doi.org/10.1056/NEJM198705283162204>
- Gough, P.J., Gomez, I.G., Wille, P.T., Raines, E.W., 2006. Macrophage expression of active MMP-9 induces acute plaque disruption in apoE-deficient mice. *J. Clin. Invest.* 116, 59–69. <https://doi.org/10.1172/JCI25074>
- Greve, J.M., Les, A.S., Tang, B.T., Draney Blomme, M.T., Wilson, N.M., Dalman, R.L., Pelc, N.J., Taylor, C.A., 2006. Allometric scaling of wall shear stress from mice to humans: quantification using cine phase-contrast MRI and computational fluid dynamics. *Am. J. Physiol. Heart Circ. Physiol.* 291, H1700–1708. <https://doi.org/10.1152/ajpheart.00274.2006>
- Hajra, L., Evans, A.I., Chen, M., Hyduk, S.J., Collins, T., Cybulsky, M.I., 2000. The NF-kappa B signal transduction pathway in aortic endothelial cells is primed for activation in regions predisposed to atherosclerotic lesion formation. *Proc. Natl. Acad. Sci. U. S. A.* 97, 9052–9057. <https://doi.org/10.1073/pnas.97.16.9052>
- Hamamdzcic, D., Wilensky, R.L., 2013. Porcine models of accelerated coronary atherosclerosis: Role of diabetes mellitus and hypercholesterolemia [WWW Document]. *Journal of Diabetes Research*. <https://doi.org/10.1155/2013/761415>
- Hardman, D., Semple, S.I., Richards, J.M.J., Hoskins, P.R., 2013. Comparison of patient-specific inlet boundary conditions in the numerical modelling of blood flow in abdominal aortic aneurysm disease. *International Journal for Numerical Methods in Biomedical Engineering* 29, 165–178. <https://doi.org/10.1002/cnm.2535>
- Harloff, A., Zech, T., Wegent, F., Strecker, C., Weiller, C., Markl, M., 2013. Comparison of Blood Flow Velocity Quantification by 4D Flow MR Imaging with Ultrasound at the Carotid Bifurcation. *American Journal of Neuroradiology* 34, 1407–1413. <https://doi.org/10.3174/ajnr.A3419>
- Harrison, M., Smith, E., Ross, E., Krams, R., Segers, D., Buckley, C.D., Nash, G.B., Rainger, G.E., 2013. The role of platelet-endothelial cell adhesion molecule-1 in atheroma formation varies depending on the site-specific hemodynamic environment significance. *Arteriosclerosis, Thrombosis, and Vascular Biology* 33, 694–701. <https://doi.org/10.1161/ATVBAHA.112.300379>
- He, W., Xiao, H., Liu, X., 2012. Numerical simulation of human systemic arterial hemodynamics based on a transmission line model and recursive algorithm. *J. Mech. Med. Biol.* 12, 1250020. <https://doi.org/10.1142/S0219519411004587>

- He, X., Zou, Q., Luo, L.-S., Dembo, M., 1997. Analytic solutions of simple flows and analysis of nonslip boundary conditions for the lattice Boltzmann BGK model. *J Stat Phys* 87, 115–136. <https://doi.org/10.1007/BF02181482>
- Helps, E.P., McDonald, D.A., 1954. Arterial blood flow calculated from pressure gradients. *J. Physiol. (Lond.)* 124, 30–31P.
- Himburg, H.A., Dowd, S.E., Friedman, M.H., 2007. Frequency-dependent response of the vascular endothelium to pulsatile shear stress. *Am. J. Physiol. Heart Circ. Physiol.* 293, H645–653. <https://doi.org/10.1152/ajpheart.01087.2006>
- Himburg, H.A., Friedman, M.H., 2006. Correspondence of low mean shear and high harmonic content in the porcine iliac arteries. *J Biomech Eng* 128, 852–856. <https://doi.org/10.1115/1.2354211>
- Himburg, H.A., Grzybowski, D.M., Hazel, A.L., LaMack, J.A., Li, X.-M., Friedman, M.H., 2004. Spatial comparison between wall shear stress measures and porcine arterial endothelial permeability. *American Journal of Physiology - Heart and Circulatory Physiology* 286, H1916–H1922. <https://doi.org/10.1152/ajpheart.00897.2003>
- Holt, J.P., Rhode, E.A., Holt, W.W., Kines, H., 1981. Geometric similarity of aorta, venae cavae, and certain of their branches in mammals. *Am. J. Physiol.* 241, R100–104.
- Hoogendoorn, A., Kok, A.M., Hartman, E.M.J., Casadonte, L., Peters, I., Witberg, K., Visser-te Lintel Hekkert, M., van Gaalen, K., Ligthart, J., Drouet, L., van der Heiden, K., Gijzen, F.J.H., Duncker, D.J., van der Steen, A.F.W., Wentzel, J.J., 2018. The influence of shear stress metrics on plaque progression in an adult hypercholesterolemic pig model: multimodality imaging, biomechanics and histology, in: *The 13th International Symposium. Presented at the Biomechanics in Vascular Biology and Cardiovascular Disease*, Emory University, Atlanta.
- Hoskins, P.R., Hardman, D., 2009. Three-dimensional imaging and computational modelling for estimation of wall stresses in arteries. *Br J Radiol* 82 Spec No 1, S3–17. <https://doi.org/10.1259/bjr/96847348>
- Hu, W., Polinsky, P., Sadoun, E., Rosenfeld, M.E., Schwartz, S.M., 2005. Atherosclerotic lesions in the common coronary arteries of ApoE knockout mice. *Cardiovascular Pathology* 14, 120–125. <https://doi.org/10.1016/j.carpath.2005.02.004>
- Hyväluoma, J., Niemi, V., Thapaliya, M., Turtola, E., Järnstedt, J., Timonen, J., 2017. Lattice Boltzmann simulation of flow-induced wall shear stress in porous media. *Transp Porous Med* 1–16. <https://doi.org/10.1007/s11242-017-0967-0>
- Ishibashi, S., Brown, M., Goldstein, J., Gerard, R., Hammer, R., Herz, J., 1993. Hypercholesterolemia in low-density lipoprotein receptor knockout mice and its reversal by adenovirus-mediated gene delivery. *J. Clin. Invest.* 92, 883–893. <https://doi.org/10.1172/JCI116663>
- Ishibashi, S., Goldstein, J., Brown, M., Herz, J., Burns, D., 1994. Massive xanthomatosis and atherosclerosis in cholesterol-fed low-density lipoprotein receptor-negative mice. *J. Clin. Invest.* 93, 1885–1893. <https://doi.org/10.1172/JCI117179>
- John, L.R., 2004. Forward electrical transmission line model of the human arterial system. *Med. Biol. Eng. Comput.* 42, 312–321. <https://doi.org/10.1007/BF02344705>



- Johnston, B.M., Johnston, P.R., Corney, S., Kilpatrick, D., 2006. Non-Newtonian blood flow in human right coronary arteries: Transient simulations. *J. Biomech.* 39, 1116–1128. <https://doi.org/10.1016/j.jbiomech.2005.01.034>
- Johnston, B.M., Johnston, P.R., Corney, S., Kilpatrick, D., 2004. Non-Newtonian blood flow in human right coronary arteries: steady state simulations. *J. Biomech.* 37, 709–720. <https://doi.org/10.1016/j.jbiomech.2003.09.016>
- Kang, X., Dun, Z., 2014. Accuracy and grid convergence of wall shear stress measured by lattice Boltzmann method. *International Journal of Modern Physics C* 25, 1450057. <https://doi.org/10.1142/S0129183114500570>
- Karamanoglu, M., Gallagher, D., Avolio, A., O'Rourke, M., 1995. Pressure wave-propagation in a multibranched model of the human upper-limb. *Am. J. Physiol.-Heart Circul. Physiol.* 269, H1363–H1369.
- Khiri, A.W., Henein, M.Y., Koh, T., Das, S.K., Parker, K.H., Gibson, D.G., 2001. Arterial waves in humans during peripheral vascular surgery. *Clin. Sci.* 101, 749–757.
- Knight, J., Olgac, U., Saur, S.C., Poulikakos, D., Marshall Jr, W., Cattin, P.C., Alkadhi, H., Kurtcuoglu, V., 2010. Choosing the optimal wall shear parameter for the prediction of plaque location—A patient-specific computational study in human right coronary arteries. *Atherosclerosis* 211, 445–450. <https://doi.org/10.1016/j.atherosclerosis.2010.03.001>
- Kolodgie, F.D., Gold, H.K., Burke, A.P., Fowler, D.R., Kruth, H.S., Weber, D.K., Farb, A., Guerrero, I.J., Hayase, M., Kutys, R., Narula, J., Finn, A.V., Virmani, R., 2003. Intraplaque hemorrhage and progression of coronary atheroma. *N. Engl. J. Med.* 349, 2316–2325. <https://doi.org/10.1056/NEJMoa035655>
- Konstantinov, I.E., Jankovic, G.M., 2013. Alexander I. Ignatowski: A pioneer in the study of atherosclerosis. *Tex. Heart Inst. J.* 40, 247–249.
- Koskinas, K.C., Feldman, C.L., Chatzizisis, Y.S., Coskun, A.U., Jonas, M., Maynard, C., Baker, A.B., Papafaklis, M.I., Edelman, E.R., Stone, P.H., 2010. Natural history of experimental coronary atherosclerosis and vascular remodeling in relation to endothelial shear stress. *Circulation* 121, 2092–U42. <https://doi.org/10.1161/CIRCULATIONAHA.109.901678>
- Krüger, T., 2012. Computer simulation study of collective phenomena in dense suspensions of red blood cells under shear. Vieweg+Teubner Verlag, Wiesbaden.
- Krüger, T., Kusumaatmaja, H., Kuzmin, A., Shardt, O., Silva, G., Viggien, E.M., 2017. Lattice Boltzmann method: Principles and practice, in: *Lattice Boltzmann Method: Principles and Practice*. Springer International Publishing Ag, Cham, pp. 1–694.
- Krüger, T., Varnik, F., Raabe, D., 2009. Shear stress in lattice Boltzmann simulations. *Physical Review E* 79. <https://doi.org/10.1103/PhysRevE.79.046704>
- Ku, D., Giddens, D., Zarins, C., Glagov, S., 1985. Pulsatile flow and atherosclerosis in the human carotid bifurcation - Positive correlation between plaque location and low and oscillating shear stress. *Arteriosclerosis* 5, 293–302.
- Ku, D.N., 1997. Blood flow in arteries. *Annual Review of Fluid Mechanics* 29, 399–434. <https://doi.org/10.1146/annurev.fluid.29.1.399>
- Lacy, J.L., Nanavaty, T., Dai, D., Nayak, N., Haynes, N., Martin, C., 2001. Development and validation of a novel technique for murine first-pass

- radionuclide angiography with a fast multiwire camera and tantalum 178. *J Nucl Cardiol* 8, 171–181. <https://doi.org/10.1067/mnc.2001.112135>
- Ladd, A., 1994. Numerical simulations of particulate suspensions via a discretized Boltzmann-equation .1. Theoretical foundation. *J. Fluid Mech.* 271, 285–309. <https://doi.org/10.1017/S0022112094001771>
- Lallemand, P., Luo, L.S., 2003. Lattice Boltzmann method for moving boundaries. *J. Comput. Phys.* 184, 406–421. [https://doi.org/10.1016/S0021-9991\(02\)00022-0](https://doi.org/10.1016/S0021-9991(02)00022-0)
- Landau, L.D., Lifshitz, E.M., 1987. *Fluid Mechanics*. Pergamon Press, Oxford.
- Latt, J., 2007. *Hydrodynamic limit of lattice Boltzmann equations*. University of Geneva.
- Latt, J., Chopard, B., Malaspinas, O., Deville, M., Michler, A., 2008. Straight velocity boundaries in the lattice Boltzmann method. *Phys. Rev. E* 77, 056703. <https://doi.org/10.1103/PhysRevE.77.056703>
- Lazovic, B., Mazic, S., Zikich, D., Zikic, D., 2015. The mathematical model of the radial artery blood pressure waveform through monitoring of the age-related changes. *Wave Motion* 56, 14–21. <https://doi.org/10.1016/j.wavemoti.2015.02.001>
- Lee, S.-W., Antiga, L., Steinman, D.A., 2009. Correlations among indicators of disturbed flow at the normal carotid bifurcation. *J Biomech Eng* 131, 061013–061013. <https://doi.org/10.1115/1.3127252>
- Lee, Y.T., Lin, H.Y., Chan, Y.W.F., Li, K.H.C., To, O.T.L., Yan, B.P., Liu, T., Li, G., Wong, W.T., Keung, W., Tse, G., 2017. Mouse models of atherosclerosis: a historical perspective and recent advances. *Lipids Health Dis.* 16, 12. <https://doi.org/10.1186/s12944-016-0402-5>
- Lei, M., Kleinstreuer, C., Truskey, G.A., 1996. A focal stress gradient-dependent mass transfer mechanism for atherogenesis in branching arteries. *Medical Engineering & Physics* 18, 326–332. [https://doi.org/10.1016/1350-4533\(95\)00045-3](https://doi.org/10.1016/1350-4533(95)00045-3)
- Lendon, C.L., Davies, M.J., Born, G.V.R., Richardson, P.D., 1991. Atherosclerotic plaque caps are locally weakened when macrophages density is increased. *Atherosclerosis* 87, 87–90. [https://doi.org/10.1016/0021-9150\(91\)90235-U](https://doi.org/10.1016/0021-9150(91)90235-U)
- Li, M., 2006. *Numerical simulation of blood flow and vessel wall stresses in stenosed arteries (Doctor of Philosophy)*. University of Edinburgh.
- Li, Q., He, Y.L., Tang, G.H., Tao, W.Q., 2010. Improved axisymmetric lattice Boltzmann scheme. *Phys. Rev. E* 81, 056707. <https://doi.org/10.1103/PhysRevE.81.056707>
- Liang, F., Takagi, S., Himeno, R., Liu, H., 2009. Multi-scale modeling of the human cardiovascular system with applications to aortic valvular and arterial stenoses. *Med. Biol. Eng. Comput.* 47, 743–755. <https://doi.org/10.1007/s11517-009-0449-9>
- Liu, Z., Shen, F., Yin, F., 1989. Impedance of arterial system simulated by viscoelastic T-tubes terminated in Windkessels. *Am. J. Physiol.* 256, H1087–H1099.
- Lusis, A.J., 2000. Atherosclerosis. *Nature* 407, 233–241. <https://doi.org/10.1038/35025203>
- Malek, A.M., Alper, S.L., Izumo, S., 1999. Hemodynamic shear stress and its role in atherosclerosis. *JAMA-J. Am. Med. Assoc.* 282, 2035–2042. <https://doi.org/10.1001/jama.282.21.2035>

- Mallat, R.K., John, C.M., Kendrick, D.J., Braun, A.P., 2017. The vascular endothelium: A regulator of arterial tone and interface for the immune system. *Crit. Rev. Clin. Lab. Sci.* 54, 458–470. <https://doi.org/10.1080/10408363.2017.1394267>
- Matyka, M., Koza, Z., Mirosław, L., 2013. Wall orientation and shear stress in the lattice Boltzmann model. *Computers & Fluids* 73, 115–123. <https://doi.org/10.1016/j.compfluid.2012.12.018>
- McMillan, D.E., 1985. Blood flow and the localization of atherosclerotic plaques. *Stroke* 16, 582–587. <https://doi.org/10.1161/01.STR.16.4.582>
- Mikael, L. de R., Paiva, A.M.G. de, Gomes, M.M., Sousa, A.L.L., Jardim, P.C.B.V., Vitorino, P.V. de O., Euzébio, M.B., Sousa, W. de M., Barroso, W.K.S., 2017. Vascular aging and arterial stiffness. *Arq. Bras. Cardiol.* 109, 253–258. <https://doi.org/10.5935/abc.20170091>
- Milner, J.S., Moore, J.A., Rutt, B.K., Steinman, D.A., 1998. Hemodynamics of human carotid artery bifurcations: Computational studies with models reconstructed from magnetic resonance imaging of normal subjects. *Journal of Vascular Surgery* 28, 143–156. [https://doi.org/10.1016/S0741-5214\(98\)70210-1](https://doi.org/10.1016/S0741-5214(98)70210-1)
- Mohamied, Y., Rowland, E.M., Bailey, E.L., Sherwin, S.J., Schwartz, M.A., Weinberg, P.D., 2015. Change of direction in the biomechanics of atherosclerosis. *Annals of Biomedical Engineering* 43, 16–25. <https://doi.org/10.1007/s10439-014-1095-4>
- Mohri, Z., Rowland, E.M., Clarke, L.A., De Luca, A., Peiffer, V., Krams, R., Sherwin, S.J., Weinberg, P.D., 2014. Elevated uptake of plasma macromolecules by regions of arterial wall predisposed to plaque instability in a mouse model. *PLoS ONE* 9, e115728. <https://doi.org/10.1371/journal.pone.0115728>
- Munson, B.R., Young, D.F., Okiishi, T.H., Huebsch, W.W., 2010. *Fundamental of fluid mechanics*, Sixth edition. ed. John Wiley and Sons Inc., Asia.
- Nakashima, Y., Plump, A.S., Raines, E.W., Breslow, J.L., Ross, R., 1994. ApoE-deficient mice develop lesions of all phases of atherosclerosis throughout the arterial tree. *Arterioscler. Thromb.* 14, 133–140.
- Nam, D., Ni, C.-W., Rezvan, A., Suo, J., Budzyn, K., Llanos, A., Harrison, D., Giddens, D., Jo, H., 2009. Partial carotid ligation is a model of acutely induced disturbed flow, leading to rapid endothelial dysfunction and atherosclerosis. *Am. J. Physiol.-Heart Circul. Physiol.* 297, H1535–H1543. <https://doi.org/10.1152/ajpheart.00510.2009>
- Nash, R.W., Carver, H.B., Bernabeu, M.O., Hetherington, J., Groen, D., Krueger, T., Coveney, P.V., 2014. Choice of boundary condition for lattice-Boltzmann simulation of moderate-Reynolds-number flow in complex domains. *Phys. Rev. E* 89, 023303. <https://doi.org/10.1103/PhysRevE.89.023303>
- Neto, C., Evans, D.R., Bonaccorso, E., Butt, H.-J., Craig, V.S.J., 2005. Boundary slip in Newtonian liquids: a review of experimental studies. *Rep. Prog. Phys.* 68, 2859. <https://doi.org/10.1088/0034-4885/68/12/R05>
- Nichols, W., O'Rourke, M., Vlachopoulos, C., 1998. *McDonald's blood flow in arteries*, Sixth Edition: Theoretical, experimental and clinical principles. CRC Press, 4th ed. Edward Arnold, London.
- Niu, C., Wang, X., Zhao, M., Cai, T., Liu, P., Li, J., Willard, B., Zu, L., Zhou, E., Li, Y., Pan, B., Yang, F., Zheng, L., 2016. Macrophage foam cell-derived

- extracellular vesicles promote vascular smooth muscle cell migration and adhesion. *J Am Heart Assoc* 5. <https://doi.org/10.1161/JAHA.116.004099>
- Noordergraaf, A., Li, J.K.-J., Campbell, K.B., 1979. Mammalian hemodynamics : A new similarity principle. *Journal of Theoretical Biology* 79, 485–489. [https://doi.org/10.1016/0022-5193\(79\)90239-X](https://doi.org/10.1016/0022-5193(79)90239-X)
- Noordergraaf, A., Verdouw, D., Boom, H.B., 1963. The use of an analog computer in a circulation model. *Prog Cardiovasc Dis* 5, 419–439.
- Noria, S., Xu, F., McCue, S., Jones, M., Gotlieb, A.I., Langille, B.L., 2004. Assembly and reorientation of stress fibers drives morphological changes to endothelial cells exposed to shear stress. *Am. J. Pathol.* 164, 1211–1223. [https://doi.org/10.1016/S0002-9440\(10\)63209-9](https://doi.org/10.1016/S0002-9440(10)63209-9)
- Nouri, M., Jalali, F., Karimi, G., Zarrabi, K., 2015. Image-based computational simulation of sub-endothelial LDL accumulation in a human right coronary artery. *Computers in Biology and Medicine* 62, 206–221. <https://doi.org/10.1016/j.combiomed.2015.04.013>
- O'Connor, J., Day, P., Mandal, P., Revell, A., 2016. Computational fluid dynamics in the microcirculation and microfluidics: what role can the lattice Boltzmann method play? *Integr. Biol.* 8, 589–602. <https://doi.org/10.1039/c6ib00009f>
- Ojha, M., 1994. Wall shear stress temporal gradient and anastomotic intimal hyperplasia. *Circ. Res.* 74, 1227–1231.
- Olgac, U., Poulikakos, D., Saur, S.C., Alkadhi, H., Kurtcuoglu, V., 2009. Patient-specific three-dimensional simulation of LDL accumulation in a human left coronary artery in its healthy and atherosclerotic states. *Am. J. Physiol. Heart Circ. Physiol.* 296, H1969–1982. <https://doi.org/10.1152/ajpheart.01182.2008>
- O'Rourke, M., Yaginuma, T., 1984. Wave reflections and the arterial pulse. *Arch. Intern. Med.* 144, 366–371. <https://doi.org/10.1001/archinte.144.2.366>
- Paigen, B., Morrow, A., Holmes, P.A., Mitchell, D., Williams, R.A., 1987. Quantitative assessment of atherosclerotic lesions in mice. *Atherosclerosis* 68, 231–240. [https://doi.org/10.1016/0021-9150\(87\)90202-4](https://doi.org/10.1016/0021-9150(87)90202-4)
- Pedrigi, R.M., Mehta, V.V., Bovens, S.M., Mohri, Z., Poulsen, C.B., Gsell, W., Tremoleda, J.L., Towhidi, L., de Silva, R., Petretto, E., Krams, R., 2016. Influence of shear stress magnitude and direction on atherosclerotic plaque composition. *R. Soc. Open Sci.* 3, 160588. <https://doi.org/10.1098/rsos.160588>
- Peiffer, V., Rowland, E.M., Cremers, S.G., Weinberg, P.D., Sherwin, S.J., 2012. Effect of aortic taper on patterns of blood flow and wall shear stress in rabbits: Association with age. *Atherosclerosis* 223, 114–121. <https://doi.org/10.1016/j.atherosclerosis.2012.04.020>
- Peiffer, V., Sherwin, S.J., Weinberg, P.D., 2013a. Does low and oscillatory wall shear stress correlate spatially with early atherosclerosis? A systematic review. *Cardiovascular Research* cvt044. <https://doi.org/10.1093/cvr/cvt044>
- Peiffer, V., Sherwin, S.J., Weinberg, P.D., 2013b. Computation in the rabbit aorta of a new metric - the transverse wall shear stress - to quantify the multidirectional character of disturbed blood flow. *Journal of Biomechanics* 46, 2651–2658. <https://doi.org/10.1016/j.jbiomech.2013.08.003>
- Pereira, T., Correia, C., Cardoso, J., 2015. Novel methods for pulse wave velocity measurement. *J Med Biol Eng* 35, 555–565. <https://doi.org/10.1007/s40846-015-0086-8>

- Pfenniger, A., Meens, M.J., Pedrigi, R.M., Foglia, B., Sutter, E., Pelli, G., Rochemont, V., Petrova, T.V., Krams, R., Kwak, B.R., 2015. Shear stress-induced atherosclerotic plaque composition in ApoE(-/-) mice is modulated by connexin37. *Atherosclerosis* 243, 1–10. <https://doi.org/10.1016/j.atherosclerosis.2015.08.029>
- Pfenniger, A., Wong, C., Sutter, E., Cuhlmann, S., Dunoyer-Geindre, S., Mach, F., Horrevoets, A.J., Evans, P.C., Krams, R., Kwak, B.R., 2012. Shear stress modulates the expression of the atheroprotective protein Cx37 in endothelial cells. *J. Mol. Cell. Cardiol.* 53, 299–309. <https://doi.org/10.1016/j.yjmcc.2012.05.011>
- Phillips, T.N., Roberts, G.W., 2011. Lattice Boltzmann models for non-Newtonian flows. *IMA J Appl Math* 76, 790–816. <https://doi.org/10.1093/imamat/hxr003>
- Piedrahita, J.A., Zhang, S.H., Hagaman, J.R., Oliver, P.M., Maeda, N., 1992. Generation of mice carrying a mutant apolipoprotein E gene inactivated by gene targeting in embryonic stem cells. *Proc Natl Acad Sci U S A* 89, 4471–4475.
- Plump, A.S., Smith, J.D., Hayek, T., Aalto-Setälä, K., Walsh, A., Verstuyft, J.G., Rubin, E.M., Breslow, J.L., 1992. Severe hypercholesterolemia and atherosclerosis in apolipoprotein E-deficient mice created by homologous recombination in ES cells. *Cell* 71, 343–353. [https://doi.org/10.1016/0092-8674\(92\)90362-G](https://doi.org/10.1016/0092-8674(92)90362-G)
- Pomella, N., Wilhelm, E.N., Kolyva, C., González-Alonso, J., Rakobowchuk, M., Khir, A.W., 2017. Common Carotid Artery Diameter, Blood Flow Velocity and Wave Intensity Responses at Rest and during Exercise in Young Healthy Humans: A Reproducibility Study. *Ultrasound in Medicine & Biology* 43, 943–957. <https://doi.org/10.1016/j.ultrasmedbio.2016.12.018>
- Poole, J.C., Florey, H.W., 1958. Changes in the endothelium of the aorta and the behaviour of macrophages in experimental atheroma of rabbits. *J Pathol Bacteriol* 75, 245–251.
- Potor, L., Banyai, E., Becs, G., Soares, M.P., Balla, G., Balla, J., Jeney, V., 2013. Atherogenesis may involve the prooxidant and proinflammatory effects of ferryl haemoglobin. *Oxidative Med. Cell. Longev. UNSP* 676425. <https://doi.org/10.1155/2013/676425>
- Potter, C.M.F., Schobesberger, S., Lundberg, M.H., Weinberg, P.D., Mitchell, J.A., Gorelik, J., 2012. Shape and compliance of endothelial cells after shear stress in vitro or from different aortic regions: scanning ion conductance microscopy study. *PLoS ONE* 7, e31228. <https://doi.org/10.1371/journal.pone.0031228>
- Prothero, J., 1979. Heart-weight as a function of body-weight in mammals. *Growth* 43, 139–150.
- Qiu, Y.C., Tarbell, J.M., 2000. Interaction between wall shear stress and circumferential strain affects endothelial cell biochemical production. *J. Vasc. Res.* 37, 147–157. <https://doi.org/10.1159/000025726>
- Quarteroni, A., Tuveri, M., Veneziani, A., 2000. Computational vascular fluid dynamics: problems, models and methods. *Computing and Visualization in Science* 2, 163–97. <https://doi.org/10.1007/s007910050039>
- Quinn, M., Parthasarathy, S., Fong, L., Steinberg, D., 1987. Oxidatively modified low-density lipoproteins - a potential role in recruitment and retention of monocyte

- macrophages during atherogenesis. *Proc. Natl. Acad. Sci. U. S. A.* 84, 2995–2998. <https://doi.org/10.1073/pnas.84.9.2995>
- Reymond, P., Merenda, F., Perren, F., Rüfenacht, D., Stergiopulos, N., 2009. Validation of a one-dimensional model of the systemic arterial tree. *Am. J. Physiol. Heart Circ. Physiol.* 297, H208–222. <https://doi.org/10.1152/ajpheart.00037.2009>
- Robertson, A.M., Sequeira, A., Kameneva, M.V., 2008. Hemorheology, in: *Hemodynamical Flows, Oberwolfach Seminars*. Birkhäuser Basel, pp. 63–120.
- Ross, R., 1993. The pathogenesis of atherosclerosis - a perspective for the 1990s. *Nature* 362, 801–809. <https://doi.org/10.1038/362801a0>
- Ross, R., Glomset, J., Harker, L., 1977. Response to injury and atherogenesis. *Am J Pathol* 86, 675–684.
- Rubanyi, G., Romero, J., Vanhoutte, P., 1986. Flow-induced release of endothelium-derived relaxing factor. *Am. J. Physiol.* 250, 1145–1149.
- Salsac, A.-V., Sparks, S.R., Chomaz, J.-M., Lasheras, J.C., 2006. Evolution of the wall shear stresses during the progressive enlargement of symmetric abdominal aortic aneurysms. *J. Fluid Mech.* 560, 19–51. <https://doi.org/10.1017/S00221120060036X>
- Sandoo, A., van Zanten, J.J.C.S.V., Metsios, G.S., Carroll, D., Kitas, G.D., 2010. The endothelium and its role in regulating vascular tone. *Open Cardiovasc Med J* 4, 302–312. <https://doi.org/10.2174/1874192401004010302>
- Sasaki, T., Kuzuya, M., Nakamura, K., Cheng, X.W., Shibata, T., Sato, K., Iguchi, A., 2006. A simple method of plaque rupture induction in apolipoprotein E-deficient mice. *Arterioscler. Thromb. Vasc. Biol.* 26, 1304–1309. <https://doi.org/10.1161/01.ATV.0000219687.71607.f7>
- Schmidt-Nielsen, K., 1984. *Scaling: Why is animal size so important?* Cambridge University Press.
- Schmidt-Ott, K.M., Kagiya, S., Phillips, M.I., 2000. The multiple actions of angiotensin II in atherosclerosis. *Regulatory Peptides*, 20th Anniversary Celebratory Special Issue 93, 65–77. [https://doi.org/10.1016/S0167-0115\(00\)00178-6](https://doi.org/10.1016/S0167-0115(00)00178-6)
- Schwartz, S.M., Galis, Z.S., Rosenfeld, M.E., Falk, E., 2007. Plaque rupture in humans and mice. *Arterioscler. Thromb. Vasc. Biol.* 27, 705–713. <https://doi.org/10.1161/01.ATV.0000261709.34878.20>
- Schwenke, D., Carew, T., 1989a. Initiation of atherosclerotic lesions in cholesterol-fed rabbits .1. Focal increases in arterial LDL concentration precede development of fatty streak lesions. *Arteriosclerosis* 9, 895–907. <https://doi.org/10.1161/01.ATV.9.6.895>
- Schwenke, D., Carew, T., 1989b. Initiation of atherosclerotic lesions in cholesterol-fed rabbits .2. Selective retention of LDL Vs selective increases in LDL permeability in susceptible sites of arteries. *Arteriosclerosis* 9, 908–918. <https://doi.org/10.1161/01.ATV.9.6.908>
- Segers, D., Lipton, J.A., Leenen, P.J.M., Cheng, C., Tempel, D., Pasterkamp, G., Moll, F.L., de Crom, R., Krams, R., 2011. Atherosclerotic plaque stability is affected by the chemokine CXCL10 in both mice and humans. *International Journal of Inflammation* 2011, e936109. <https://doi.org/10.4061/2011/936109>
- Sei, Y.J., Ahn, S.I., Virtue, T., Kim, T., Kim, Y., 2017. Detection of frequency-dependent endothelial response to oscillatory shear stress using a microfluidic

- transcellular monitor. *Sci Rep* 7, 10019. <https://doi.org/10.1038/s41598-017-10636-z>
- Seneviratne, A.N., Cole, J.E., Goddard, M.E., Park, I., Mohri, Z., Sansom, S., Udalova, I., Krams, R., Monaco, C., 2015. Low shear stress induces M1 macrophage polarization in murine thin-cap atherosclerotic plaques. *J. Mol. Cell. Cardiol.* 89, 168–172. <https://doi.org/10.1016/j.yjmcc.2015.10.034>
- Seok, J., Warren, H.S., Cuenca, A.G., Mindrinos, M.N., Baker, H.V., Xu, W., Richards, D.R., McDonald-Smith, G.P., Gao, H., Hennessy, L., Finnerty, C.C., Lopez, C.M., Honari, S., Moore, E.E., Minei, J.P., Cuschieri, J., Bankey, P.E., Johnson, J.L., Sperry, J., Nathens, A.B., Billiar, T.R., West, M.A., Jeschke, M.G., Klein, M.B., Gamelli, R.L., Gibrán, N.S., Brownstein, B.H., Miller-Graziano, C., Calvano, S.E., Mason, P.H., Cobb, J.P., Rahme, L.G., Lowry, S.F., Maier, R.V., Moldawer, L.L., Herndon, D.N., Davis, R.W., Xiao, W., Tompkins, R.G., 2013. Genomic responses in mouse models poorly mimic human inflammatory diseases. *Proc. Natl. Acad. Sci. U. S. A.* 110, 3507–3512. <https://doi.org/10.1073/pnas.1222878110>
- Shi, Y., Lawford, P., Hose, R., 2011. Review of zero-D and 1-D models of blood flow in the cardiovascular system. *Biomed. Eng. Online* 10, 33. <https://doi.org/10.1186/1475-925X-10-33>
- Shim, J., Al-Mashhadi, R.H., Sorensen, C.B., Bentzon, J.F., 2016. Large animal models of atherosclerosis - new tools for persistent problems in cardiovascular medicine. *J. Pathol.* 238, 257–266. <https://doi.org/10.1002/path.4646>
- Sinha, R., Le Gac, S., Verdonchot, N., van den Berg, A., Koopman, B., Rouwkema, J., 2016. Endothelial cell alignment as a result of anisotropic strain and flow induced shear stress combinations. *Sci Rep* 6, 29510. <https://doi.org/10.1038/srep29510>
- Sinzing, H., Silberbauer, K., Auerswald, W., 1980. Quantitative investigation of sudanophilic lesions around the aortic ostia of human fetuses, newborn and children. *Blood Vessels* 17, 44–52.
- Slager, C.J., Wentzel, J.J., Gijzen, F.J.H., Thury, A., van der Wal, A.C., Schaar, J.A., Serruys, P.W., 2005a. The role of shear stress in the destabilization of vulnerable plaques and related therapeutic implications. *Nat Clin Pract Cardiovasc Med* 2, 456–464. <https://doi.org/10.1038/ncpcardio0298>
- Slager, C.J., Wentzel, J.K., Gijzen, F.J.H., Schuurbiers, J.C.H., van der Wal, A.C., van der Steen, A.F.W., Serruys, P.W., 2005b. The role of shear stress in the generation of rupture-prone vulnerable plaques. *Nat. Clin. Pract. Cardiovasc. Med.* 2, 401–407. <https://doi.org/10.1038/ncpcardio0274>
- Sluimer, J.C., Kolodgie, F.D., Bijnens, A.P.J.J., Maxfield, K., Pacheco, E., Kutys, B., Duimel, H., Frederik, P.M., van Hinsbergh, V.W.M., Virmani, R., Daemen, M.J.A.P., 2009. Thin-walled microvessels in human coronary atherosclerotic plaques show incomplete endothelial junctions: Relevance of compromised structural integrity for intraplaque microvascular leakage. *Journal of the American College of Cardiology* 53, 1517–1527. <https://doi.org/10.1016/j.jacc.2008.12.056>
- Stahl, B., Chopard, B., Latt, J., 2010. Measurements of wall shear stress with the lattice Boltzmann method and staircase approximation of boundaries. *Computers & Fluids* 39, 1625–1633. <https://doi.org/10.1016/j.compfluid.2010.05.015>

- Sary, H., Blankenhorn, D., Chandler, A., Glagov, S., Insull, W., Richardson, M., Rosenfeld, M., Schaffer, S., Schwartz, C., Wagner, W., Wissler, R., 1992. A definition of the intima of human arteries and of its atherosclerosis-prone regions. *Circulation* 85, 391–405.
- Sary, H., Chandler, A., Glagov, S., Guyton, J., Insull, W., Rosenfeld, M., Schaffer, S., Schwartz, C., Wagner, W., Wissler, R., 1994. A definition of initial, fatty streak, and intermediate lesions of atherosclerosis. *Circulation* 89, 2462–2478.
- Sary, H.C., Chandler, A.B., Dinsmore, R.E., Fuster, V., Glagov, S., Insull, W., Rosenfeld, M.E., Schwartz, C.J., Wagner, W.D., Wissler, R.W., 1995. A definition of advanced types of atherosclerotic lesions and a histological classification of atherosclerosis. *Circulation* 92, 1355–1374. <https://doi.org/10.1161/01.CIR.92.5.1355>
- Steinman, D.A., Thomas, J.B., Ladak, H.M., Milner, J.S., Rutt, B.K., Spence, J.D., 2002. Reconstruction of carotid bifurcation hemodynamics and wall thickness using computational fluid dynamics and MRI. *Magn. Reson. Med.* 47, 149–159. <https://doi.org/10.1002/mrm.10025>
- Stergiopoulos, N., Young, D.F., Rogge, T.R., 1992. Computer simulation of arterial flow with applications to arterial and aortic stenoses. *J Biomech* 25, 1477–1488.
- Stroev, P.V., Beech-Brandt, J.J., Easson, W.J., Hoskins, P.R., 2005. Estimation of wall shear stress using a multi-branched model of the human arterial system, in: T.A. Kowalewski (Ed.), *Blood Flow Modelling and Diagnostics*.
- Succi, S., 2001. *The lattice Boltzmann equation for fluid dynamics and beyond*. Oxford University Press, Oxford.
- Suo, J., Ferrara, D.E., Sorescu, D., Guldborg, R.E., Taylor, W.R., Giddens, D.P., 2007. Hemodynamic shear stresses in mouse aortas - Implications for atherogenesis. *Arterioscler. Thromb. Vasc. Biol.* 27, 346–351. <https://doi.org/10.1161/01.ATV.0000253492.45717.46>
- Tanaka, K., Sata, M., Hirata, Y., Nagai, R., 2003. Diverse contribution of bone marrow cells to neointimal hyperplasia after mechanical vascular injuries. *Circ.Res.* 93, 783–790. <https://doi.org/10.1161/01.RES.0000096651.13001.B4>
- Timmins, L.H., Molony, D.S., Eshtehardi, P., McDaniel, M.C., Oshinski, J.N., Giddens, D.P., Samady, H., 2017. Oscillatory wall shear stress is a dominant flow characteristic affecting lesion progression patterns and plaque vulnerability in patients with coronary artery disease. *J. R. Soc. Interface* 14, 20160972. <https://doi.org/10.1098/rsif.2016.0972>
- Toksvang, L.N., Berg, R.M.G., 2013. Using a classic paper by Robin Fåhræus and Torsten Lindqvist to teach basic hemorheology. *Advances in Physiology Education* 37, 129–133. <https://doi.org/10.1152/advan.00009.2013>
- Torii, R., Wood, N.B., Hadjiloizou, N., Dowsey, A.W., Wright, A.R., Hughes, A.D., Davies, J., Francis, D.P., Mayet, J., Yang, G.-Z., Thom, S.A.M., Xu, X.Y., 2009. Stress phase angle depicts differences in coronary artery hemodynamics due to changes in flow and geometry after percutaneous coronary intervention. *Am. J. Physiol.-Heart Circul. Physiol.* 296, H765–H776. <https://doi.org/10.1152/ajpheart.01166.2007>
- Trachet, B., Swillens, A., Van Loo, D., Casteleyn, C., De Paepe, A., Loeys, B., Segers, P., 2009. The influence of aortic dimensions on calculated wall shear stress in



- the mouse aortic arch. *Comput. Methods Biomech. Biomed. Eng.* 12, 491–499. <https://doi.org/10.1080/10255840802695445>
- Tropea, B.I., Schwarzacher, S.P., Chang, A., Asvar, C., Huie, P., Sibley, R.K., Zarins, C.K., 2000. Reduction of aortic wall motion inhibits hypertension-mediated experimental atherosclerosis. *Arterioscler. Thromb. Vasc. Biol.* 20, 2127–2133.
- van de Vosse, F.N., Stergiopulos, N., 2011. Pulse wave propagation in the arterial tree, in: Davis, S.H., Moin, P. (Eds.), *Annual Review of Fluid Mechanics*, Vol 43. Annual Reviews, Palo Alto, pp. 467–499.
- Van der Donckt, C., Herck, V., L, J., Schrijvers, D.M., Vanhoutte, G., Verhoye, M., Blockx, I., Van Der Linden, A., Bauters, D., Lijnen, H.R., Sluimer, J.C., Roth, L., Hove, V., E, C., Fransen, P., Knaapen, M.W., Hervent, A.-S., Keulenaer, D., W, G., Bult, H., Martinet, W., Herman, A.G., Meyer, D., R.y, G., 2015. Elastin fragmentation in atherosclerotic mice leads to intraplaque neovascularization, plaque rupture, myocardial infarction, stroke, and sudden death. *Eur Heart J* 36, 1049–1058. <https://doi.org/10.1093/eurheartj/ehu041>
- VanderLaan, P.A., Reardon, C.A., Getz, G.S., 2004. Site specificity of atherosclerosis - Site-selective responses to atherosclerotic modulators. *Arterioscler. Thromb. Vasc. Biol.* 24, 12–22. <https://doi.org/10.1161/01.ATV.0000105054.43931.f0>
- Veseli, B.E., Perrotta, P., De Meyer, G.R.A., Roth, L., Van der Donckt, C., Martinet, W., De Meyer, G.R.Y., 2017. Animal models of atherosclerosis. *Eur. J. Pharmacol.* 816, 3–13. <https://doi.org/10.1016/j.ejphar.2017.05.010>
- Virmani, R., Burke, A.P., Farb, A., Kolodgie, F.D., 2006. Pathology of the vulnerable plaque. *Journal of the American College of Cardiology, Detection of Vulnerable Plaques* 47, C13–C18. <https://doi.org/10.1016/j.jacc.2005.10.065>
- Virmani, R., Kolodgie, F.D., Burke, A.P., Farb, A., Schwartz, S.M., 2000. Lessons from sudden coronary death - A comprehensive morphological classification scheme for atherosclerotic lesions. *Arterioscler. Thromb. Vasc. Biol.* 20, 1262–1275.
- Virmani, R., Kolodgie, F.D., Burke, A.P., Finn, A.V., Gold, H.K., Tulenko, T.N., Wrenn, S.P., Narula, J., 2005. Atherosclerotic plaque progression and vulnerability to rupture - Angiogenesis as a source of intraplaque hemorrhage. *Arterioscler. Thromb. Vasc. Biol.* 25, 2054–2061. <https://doi.org/10.1161/01.ATV.0000178991.71605.18>
- Vogel, J., Kiessling, I., Heinicke, K., Stallmach, T., Ossent, P., Vogel, O., Aulmann, M., Frietsch, T., Schmid-Schönbein, H., Kuschinsky, W., Gassmann, M., 2003. Transgenic mice overexpressing erythropoietin adapt to excessive erythrocytosis by regulating blood viscosity. *Blood* 102, 2278–2284. <https://doi.org/10.1182/blood-2003-01-0283>
- Wang, D., Bernsdorf, J., 2009. Lattice Boltzmann simulation of steady non-Newtonian blood flow in a 3D generic stenosis case. *Computers & Mathematics with Applications, Mesoscopic Methods in Engineering and Science* 58, 1030–1034. <https://doi.org/10.1016/j.camwa.2009.02.020>
- Weinberg, P.D., 2002. Disease patterns at arterial branches and their relation to flow. *Biorheology* 39, 533–537.
- Weinberg, P.D., Ethier, C.R., 2007. Twenty-fold difference in hemodynamic wall shear stress between murine and human aortas. *J Biomech* 40, 1594–1598. <https://doi.org/10.1016/j.jbiomech.2006.07.020>

- Weissberg, P., 2000. Atherogenesis: current understanding of the causes of atheroma. *Heart* 83, 247–252. <https://doi.org/10.1136/heart.83.2.247>
- Wenning, C., Kloth, C., Kuhlmann, M.T., Jacobs, A.H., Schober, O., Hermann, S., Schaefers, M.A., 2014. Serial F-18-FDG PET/CT distinguishes inflamed from stable plaque phenotypes in shear-stress induced murine atherosclerosis. *Atherosclerosis* 234, 276–282. <https://doi.org/10.1016/j.atherosclerosis.2014.03.008>
- Wentzel, J.J., Chatzizisis, Y.S., Gijzen, F.J.H., Giannoglou, G.D., Feldman, C.L., Stone, P.H., 2012. Endothelial shear stress in the evolution of coronary atherosclerotic plaque and vascular remodelling: current understanding and remaining questions. *Cardiovascular Research* cvs217. <https://doi.org/10.1093/cvr/cvs217>
- Wentzel, J.J., Gijzen, F.J.H., Schuurbijs, J.C.H., Krams, R., Serruys, P.W., De Feyter, P.J., Slager, C.J., 2005. Geometry guided data averaging enables the interpretation of shear stress related plaque development in human coronary arteries. *J. Biomech.* 38, 1551–1555. <https://doi.org/10.1016/j.jbiomech.2004.06.022>
- West, G.B., Brown, J.H., Enquist, B.J., 1999. The fourth dimension of life: fractal geometry and allometric scaling of organisms. *Science* 284, 1677–1679.
- Westerhof, N., 1994. Heart period is proportional to body length. *Cardioscience* 5, 283–285.
- Westerhof, N., Bosman, F., De Vries, C.J., Noordergraaf, A., 1969. Analog studies of the human systemic arterial tree. *Journal of Biomechanics* 2, 121–143. [https://doi.org/10.1016/0021-9290\(69\)90024-4](https://doi.org/10.1016/0021-9290(69)90024-4)
- Westerhof, N., Elzinga, G., 1993. Why smaller animals have higher heart rates. *Adv. Exp. Med. Biol.* 346, 319–323.
- Westerhof, N., Elzinga, G., Sipkema, P., 1971. Artificial arterial system for pumping hearts. *J. Appl. Physiol.* 31, 776–+.
- Westerhof, N., Noordergraaf, A., 1970. Arterial viscoelasticity: A generalized model. *Journal of Biomechanics* 3, IN15–IN16. [https://doi.org/10.1016/0021-9290\(70\)90036-9](https://doi.org/10.1016/0021-9290(70)90036-9)
- WHO, 2017. Cardiovascular diseases (CVDs). Technical report fact sheet.
- Williams, K.J., Tabas, I., 1995. The response-to-retention hypothesis of early atherogenesis. *Arterioscler Thromb Vasc Biol* 15, 551–561.
- Windberger, U., Bartholovitsch, A., Plasenzotti, R., Korak, K.J., Heinze, G., 2003. Whole blood viscosity, plasma viscosity and erythrocyte aggregation in nine mammalian species: reference values and comparison of data. *Exp. Physiol.* 88, 431–440.
- Windberger, U., Baskurt, O.K., 2007. Comparative hemorheology, in: Baskurt, O. K., Hardeman, M.R., Rampling, M.W., Meiselman, H.J. (Eds.), *Handbook of Hemorheology and Hemodynamics*. Ios Press, Amsterdam, pp. 267–285.
- Winkel, L.C., Hoogendoorn, A., Xing, R., Wentzel, J.J., Van der Heiden, K., 2015. Animal models of surgically manipulated flow velocities to study shear stress-induced atherosclerosis. *Atherosclerosis* 241, 100–110. <https://doi.org/10.1016/j.atherosclerosis.2015.04.796>
- Womersley, J., 1954. Flow in the larger arteries and its relation to the oscillating pressure. *J. Physiol.-London* 124, P31–P32.

- Xiao, Hanguang, Avolio, A., Huang, D., 2016. A novel method of artery stenosis diagnosis using transfer function and support vector machine based on transmission line model: A numerical simulation and validation study. *Comput. Meth. Programs Biomed.* 129, 71–81. <https://doi.org/10.1016/j.cmpb.2016.03.005>
- Xiao, Hanguang, Avolio, A., Zhao, M., 2016. Modeling and hemodynamic simulation of human arterial stenosis via transmission line model. *J. Mech. Med. Biol.* 16, 1650067. <https://doi.org/10.1142/S0219519416500676>
- Zhou, J., Moller, J., Danielsen, C.C., Bentzon, J., Ravn, H.B., Austin, R.C., Falk, E., 2001. Dietary supplementation with methionine and homocysteine promotes early atherosclerosis but not plaque rupture in apoE-deficient mice. *Arterioscler. Thromb. Vasc. Biol.* 21, 1470–1476. <https://doi.org/10.1161/hq0901.096582>
- Zou, Q.S., He, X.Y., 1997. On pressure and velocity boundary conditions for the lattice Boltzmann BGK model. *Phys. Fluids* 9, 1591–1598. <https://doi.org/10.1063/1.869307>